In Situ Synchrotron X-Ray Characterisation and Modelling of Pitting Corrosion of Stainless Steel

By

Seyed Majid Ghahari

A thesis submitted to the University of Birmingham for the degree of DOCTOR OF PHILOSOPHY

School of Metallurgy and Materials
University of Birmingham
February 2012

Abstract

Pit propagation in stainless steels under electrochemical control was investigated using *in situ* synchrotron X-ray microtomography, which was used to confirm that the lacy covers commonly found for pits in stainless steels grow through perforation of the metal surface by upward growth of rapidly dissolving lobes from the main pit.

In situ synchrotron X-ray radiography has been used to observe the evolution of 2D pits growing at the edge of stainless steel foils under electrochemical control in chloride solutions. Pit growth shape, kinetics and stability under current and potential control at various bulk chloride concentrations have been studied. It was found that the pit depth tends to grow under diffusion control, whereas lateral development is influenced by solution conductivity. The impact of the perforated cover on the pit growth and stability was examined and its formation was found to be similar to the observations from 3D by X-ray microtomography.

A method for extracting the key dissolution kinetic parameters from radiographs has been developed. The local anodic current density along the boundary of a pit was directly measured from the rate of advance of the pit into the metal. Then the local metal ion concentration and potential drop inside the pit cavity was back-calculated using transport equations and the requirement to maintain charge neutrality, establishing the relationship between local current density, interfacial potential and metal ion concentration in the solution.

The predictive model for pit propagation in stainless steel developed by Laycock and co-workers[*] was examined, its sensitivity to key growth parameters was evaluated, and a modified version of the model was developed based on the kinetic parameters extracted from the radiographic measurements.

---

[*] Laycock, N.J., J.S. Noh, S.P. White, and D.P. Krouse, *Computer simulation of pitting potential measurements.* Corrosion Science, 2005. **47**(12): p. 3140-3177.

Many people have assisted me on carrying out this work, which was sponsored by the Nuclear Decommissioning Authority (NDA), UK.

It was my great fortune to have Dr Alison Davenport as my advisor. I cannot adequately express my gratitude for her everlasting support, criticisms, motivations… and also for sending me on so many foreign trips.

I would like to specially thank my co-advisor, Professor Trevor Rayment (Diamond Light Source, UK), for his insightful and valuable thoughts on the project.

I am extremely indebted to Dr Donal Krouse (Industrial Research Ltd, NZ) for his tremendous support and contribution to this project. Working with him was full of learning and the most enjoyable experience I have ever had…

I am particularly grateful to Dr Nick Laycock (Quest Integrity Group, NZ) and Dr Cristiano Padovani (NDA) for their invaluable suggestions, comments and support.

I highly acknowledge the help from Dr Thomas Suter (EMPA, Switzerland), Dr Marco Stampanoni, Dr Federica Marone and Dr Rajmund Mokso (Swiss Light Source).

Thanks to all my friends with whom I have enjoyed studying here: Mehdi, Josh, April, Mahrez, Andy, Gavin, Liya, Wayne and Ali …

… and thanks to my lovely family for their support and patience.

Dedicated to Neda, Sohrab, Ashkan, Mostafa, Meysam, Amir… and all my brothers and sisters who lost their lives for the sake of a bit of freedom in Iran after the disputed election in June 2009...

Contents

Table of symbols

Symbol	Definition
A	Area of actively corroding pit surface
C_{i}	Concentration of species i
C_{b}	Metal ion concentration at the pit bottom
C_{crit}	Critical concentration of metal ions required for propagation
C_{m}	Metal ion concentration at the pit mouth
C_{M}	Metal ion concentration
C_{sat}	Saturation concentration of metal ions
D_{i}	Diffusion coefficient for species i
DC	Product of diffusion coefficient and metal ion concentration
E	Electrode or interfacial potential
E_{app}	Applied potential
E_{b}	Breakdown potential
E_{pit}	Pitting potential
E_{rep}	Repassivation potential
E_{prot}	Protection potential
F	Faraday’s constant
h	Salt film thickness
i	Current density
i_{a}	Anodic current density from metal dissolution
i_{c}	Cathodic current density
i_{crit}	Critical current density for passivation
i_{lim}	Limited anodic current density
$i.x$	Pit stability product
M	Molar mass of metal
n	Normal direction to pit surface
N_i	Molar flux of species i
R	Gas constant
r	Pit radius
s	Metal foil thickness
T	Absolute temperature
t	Time
t_{ind}	Pitting induction time
w	Pit mouth size
x	Pit depth
z_{i}	Charge of species i
α	Salt film precipitation rate
γ	Geometrical factor
θ	Angle between the pit axis to the pit mouth
Λ	Area of pit cavity
μ	Molar density of salt film
ν	Pit boundary velocity
ρ	Metal density
σ	Solution conductivity
τ	Solution thickness in electrochemical cell
ϕ	Potential drop in solution

1 Introduction

It is planned to store intermediate level radioactive waste (ILW) in the UK in the stainless steel containers suitable for deep geological disposal. It is essential to ensure that the containers' integrity is maintained during the interim storage, which may last for several centuries depending on the eventual disposal option. Austenitic stainless steel grades 304L and 316L are the most common materials proposed for radioactive waste containers in the UK. The main deterioration mechanisms that may limit the lifetime of ILW containers during storage are likely to be localised corrosion or stress corrosion cracking under atmospheric conditions [1]. These may develop due to the deposition of chlorides from marine aerosols during storage periods in coastal facilities. Current plans are that ILW containers will remain in surface stores for a period up to a hundred years or longer before final disposal in a geological disposal facility (GDF) [2]. After emplacement in a GDF, there may be a further period of exposure to atmospheric conditions. The nature of any operational environment and the duration of any such periods have not yet been decided and will depend on future decisions on disposal concepts. However, it is possible that waste containers will be required to retain sufficient integrity for a further, potentially long, period. Therefore, it is essential to understand the growth mechanisms and kinetics of localised corrosion in order to predict the extent of damage that may develop over long timescales [3, 4].

Experimental observations on a prototype waste container and on corrosion coupons exposed for about 5-10 years in an inland, inactive building have shown that little damage is developed over such timescales at the levels of chloride contamination measured in the building [3, 5]. Pitting was observed to occur only to a very small extent (generally less than 5-10 μm deep). It is possible, however, that in coastal locations and over longer timescales, the deposition of chlorides may reach higher levels and induce more significant damage. Given that the timescales for storage are not easily accessible with direct experimental observations, it is important to develop and validate models for the prediction of corrosion damage over relatively long timescales.

Pitting corrosion of stainless steel has been studied for decades, the mechanism of pit propagation is generally well understood [6] and a few predictive models have been proposed [7, 8]. However, understanding the kinetics and prediction of the pitting process is still controversial mainly due to the stochastic nature and nano-scale of initiation events and also the extremely rapid propagation rate (up to few μm per second) immediately after initiation [9]. Moreover, these studies have been mainly focused under full immersion conditions and less attention has been paid to the atmospheric nature of pitting [10]. The eventual aim is to extend these models to atmospheric corrosion conditions. However, before this can be achieved, it is necessary to validate them for full immersion conditions to determine that they provide a robust basis for the more complex geometry found for atmospheric corrosion.

In the present study, synchrotron X-ray imaging methods have been developed to measure the evolution of pits *in situ* in real time for comparison with numerical simulations based on finite element modelling. The results of the synchrotron measurements are used to demonstrate the ability of the model to reproduce fundamental characteristics of pitting propagation as well as to refine its quantitative capabilities. Preliminary work focuses on pits growing in stainless steel 304 under full immersion conditions under potentiostatic or galvanostatic control. The results provide a basis for future work exploring atmospheric corrosion conditions found in typical interim waste stores[2, 4]. Stainless steel 304L is often used for the lid of waste containers and evaluating its long term performance is likely to represent a conservative case for other parts of the waste containers made in more corrosion resistant grades (e.g. 316L).

2 Literature review

2.1 Stainless steels

Stainless steels owe their corrosion resistance to the presence of more than ~11% chromium, which forms a self-healing ‘passive film’ on the surface that provides corrosion resistance over a wide range of conditions. Stainless steels are often classified as austenitic (face-centred cubic), ferritic (body-centred cubic), or martensitic (body-centred tetragonal or cubic). Alloys containing both austenite and ferrite are referred to as ‘duplex’ [11]. The 300 series austenitic stainless steels are defined by the compositional modifications to 18/8(18% Cr-8% Ni) stainless steels. Addition of Mo is the one of the well-known modification to improve pitting and crevice corrosion resistance [11].

2.2 Pitting corrosion in stainless steels

Stainless steels have a naturally formed passive layer on the surface that greatly reduces the rate of corrosion. However, the thin passive layer is very susceptible to localised attack in the presence of chloride or halide anions. Localised corrosion can occur in the form of pitting or crevice corrosion.

Pitting corrosion of metals is one of the most destructive forms of corrosion producing a distinct morphology. Pitting occurs on passive metals in halide solutions. Pits may propagate as single cavity or form morphologies that are more complex than the hemispherical shape that generally provides a basis for modelling [12].

The most conventionally measured parameters of pitting corrosion are the breakdown potential E_b or pitting potential E_pit and the protection potential, E_prot, also known as repassivation potential E_rep [13]. These potentials were first determined by Pourbaix *et al.* [14] by applying cyclic polarization to the sample in a solution containing halide ions. Figure 2-1 shows the schematic diagram of a cyclic polarization of stainless steel sample in halide containing solution and how these potentials are defined. The increase in current density at E_pit is the result of stable pit growth. With pit initiation and growth, the corroding surface area and the total current demand increases. As the potential is reversed back to E_rep, the pit stops growing. Pourbaix showed that E_b was the lowest potential at which a stable pit can initiate and E_rep is the lowest potential at which a growing pit can continue to propagate. It was proposed by Starr *et al.* [15] that either "deactivation" or "repassivation" could be responsible for the pit death at E_{prot}. If the potential is lowered to the value at which the metal is thermodynamically immune to corrosion, then pit is deactivated. However, if a fresh passive film is formed within the pit, the pit is repassivated. They showed that an Fe-12%Cr underwent either deactivation or repassivation depending on the pH.

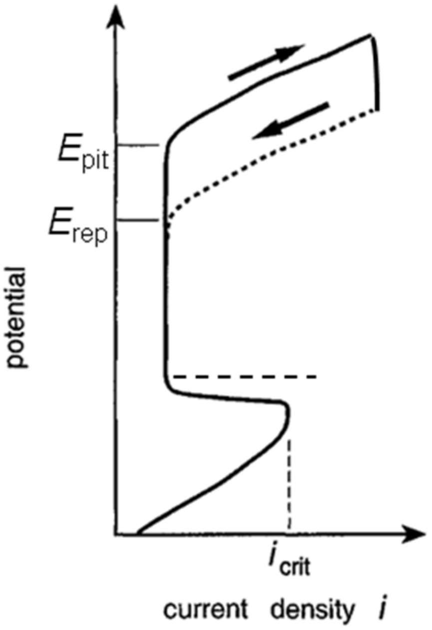

Figure 2-1- Schematic diagram of applied potential vs. current density during cyclic polarization of stainless steel sample in halide containing solution representing the definition of E_{rep} and E_{pit} [13].

It has been shown that even at potentials below E_b, pits can initiate and grow for very short periods before undergoing passivation. These short lived micro-scale pits are known as "metastable" pits [16], whereas "stable" pits can grow indefinitely. However, as metastable pitting necessitates breakdown of the passive film at potentials below E_b, the noticeable breakdown potential is often identified as the pitting potential, E_{pit}. Therefore, the transition from metastable to stable status is considered to occur at E_{pit}.

It is commonly accepted that the pitting potential (E_{pit}) is determined by the solution composition within the pit which prevents pit passivation. Although the mechanism of stable pit growth appears to be well defined, processes leading to the breakdown of the passive film that occurs prior to the development of stable growing pits remain the subject of much discussion [17].

The induction time, t_{ind}, is another parameter in evaluating pitting corrosion [18, 19]. The time period from establishing a set of desired conditions until the pit starts stable propagation is referred to as t_{ind}; either the time elapse from introduction of chloride ions into the system that is held under corrosion region or the time measured following stepping the potential into the desired value from open circuit potential. In more severe conditions, t_{ind} is shorter [20].

Pitting corrosion has been widely studied for many decades and details are available in books [21, 22], review papers [6, 23] and conference proceedings [24-35]. Fundamental studies have typically focused on one of the following stages of the pitting process: the earliest stages of passive film breakdown (pit initiation), the growth of metastable pits, and the growth of stable pits [6, 21]. Each of these stages is discussed below.

2.2.1 Pit initiation

There are many theories of pit initiation on stainless steel focusing on passive film penetration, film breaking, or adsorption [6]. However, for commercial stainless steels, manganese sulphide (MnS) inclusions have been identified as the main pit initiation sites [36-45]. Macro and micro-electrochemical experiments performed by Webb *et al*. indicated that chloride ions catalysed dissolution of inclusions and caused metastable pits leading to rapid temporary periods during which the pH decreased to values as low as zero. Also, large and shallow MnS inclusions failed to initiate pits while narrow and deep oriented ones consistently showed the onset of pitting [46-49].

2.2.2 Pit propagation

Pit propagation requires continuous high rate anodic dissolution within the pit cavity at potentials above E_{pit}. Pits are net anodes: most of the cathodic reactions occurs on the passive surface (under natural immersion) or at the counter electrode (under potential control). Studies have shown that cathodic reactions occurring within the pit only supply less than 5% of the anodic current demand of the pit [50, 51].

In a study of the mechanism of pitting in tin in neutral solutions, Hoar [52] was the first to suggest that a local chemistry different from the bulk solution is required within the developing pit. Later, it was shown that the different local chemistry within the pit may also be accompanied by a potential difference between the pit bottom and the passive surface [53]. A pH as low as ~ 0.13 [54, 55] has been reported from the direct measurements of the anolyte in corroding pits of stainless steel in near neutral bulk solutions.

Galvele [56] was the first who proposed a model to quantify the dependence of the pitting potential with the chloride bulk solution. He simply showed that the pitting potential is independent of the passive film properties but does depend on the propagation stability of the early pits and established a fundamental test for the pit stability [57]. He assumed that the cracks on the passive film would expose the bare metal into the bulk solution, and therefore calculated the condition under which dissolution would be stable within the crack.

He developed a one-dimensional pit model (shown in Figure 2-2) assuming that metal (Me) dissolution at the pit interface followed by a hydrolysis reaction (Equation 2.2) inside the pit would lead to acidification of the pit bottom. By assuming these reactions, the real situation is simplified as the further complicated reactions and hydrolysis are ignored. He also ignored the effects of migration on the transport of ions by assuming the bulk solution as a supporting electrolyte. Therefore, the flux of species, N_i (mol.cm^{-2}.s^{-1}) was given by Fick's 1st law (Equation 2-3) in which D_i is the diffusivity (cm^{2}.s^{-1}), and C_i is the concentration of species.

$$\mathrm{Me} \Leftrightarrow \mathrm{Me}^{n+} + \mathrm{n}\, e^{-} \qquad \textbf{Equation 2.1}$$

$$2\mathrm{Me}^{n+} + \mathrm{H_2O} + \mathrm{OH}^{-} \Leftrightarrow 2\mathrm{Me}\,(\mathrm{OH})^{(n-1)+} + \mathrm{H}^{+} \qquad \textbf{Equation 2.2}$$

$$N_\mathrm{i} = -\, D_\mathrm{i}\, \mathrm{d}C_\mathrm{i}/\mathrm{d}x \qquad \textbf{Equation 2.3}$$

Galvele solved the transport equations assuming steady state conditions from the pit mouth (x=0) to the pit bottom (x) and produced plots of C_i as a function of the product $i.x$, where i is the pit current density and x is the pit depth. Figure 2-3 shows the calculated concentration of Fe, Fe(OH)$^{+}$ and H^{+} as a function of $i.x$ product for a pit in iron. The cross sign on H^{+} concentration demonstrates the critical pH (pH$_\mathrm{crit}$) that segregates the passive region from corrosion based on the work of Pourbaix [58]. Therefore, it was possible to determine the critical $i.x$ value at which the pH at the pit bottom was lower than pH$_\mathrm{crit}$ and the pit propagation is stable. For a certain length of crack in the passive layer (x), then he simply described the pitting potential (E_pit) as the potential at which the current density in pit gives the $i.x$ product that produces pH$_\mathrm{crit}$.

Assuming this basic principle, he was able to describe the dependence of E_{pit} on the bulk solution and inhibitors [59, 60].

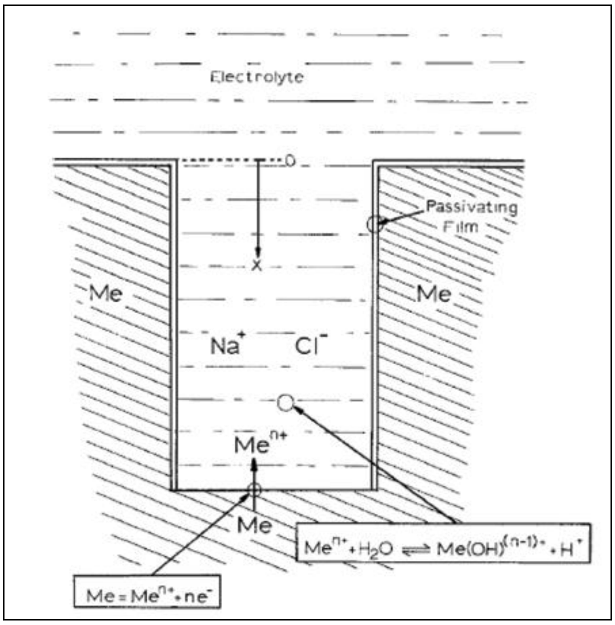

Figure 2-2- simplified pit geometry in Galvele's model of local dissolution [56]

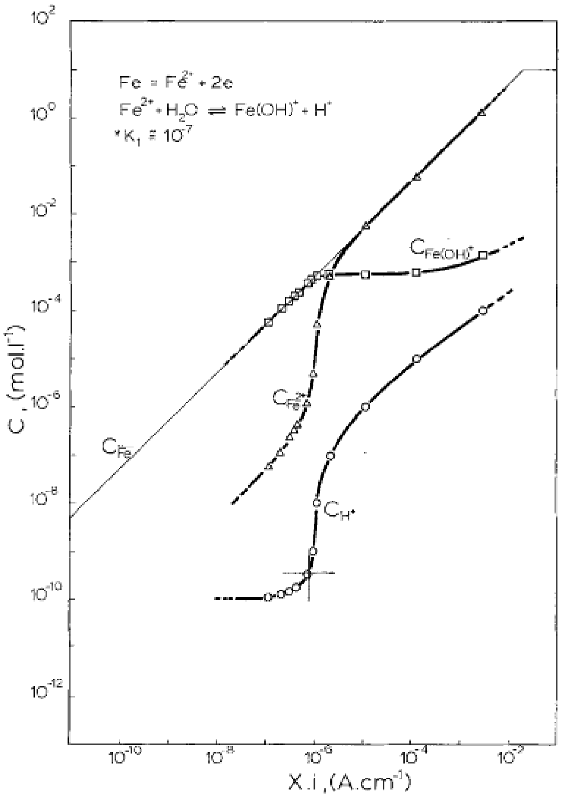

Figure 2-3- concentration of Fe^{2+}, $Fe(OH)^+$ and H^+ as a function of *x.i* product, for a unidirectional pit of Fe in a bulk solution of pH 10 [56]

Galvele's model also described the difference between E_{pit} and E_{rep}. Once a pit initiates at a critical *i.x* at E_{pit}, the current density only depends on the applied potential, ignoring the small changes in *IR* drop and salt film precipitation. Then, as the pit grows *x* increases and on the reverse scan less current is required to suffice $\mathrm{pH}_{\mathrm{crit}}$.

Based on the work of Galvele, stable pit growth necessitates continuation of high rate anodic dissolution within a corroding cavity to ensure higher concentration of aggressive anions and a low pH. The chemistry of the solution inside the pit and the anodic dissolution kinetics studied by various researchers are summarised in the next section.

2.2.3 Pit solution chemistry

Wilde and Williams [55] extracted the anolyte solution from the artificial pits in 304L and found that as the applied potential lowered from +500 to -200 mV (SCE) the pH values decreased from 3.6 to 0 with an increase in the ratio of concentration of Fe(II) to (FeIII) from 1.59 to 9.8. They proposed that hydrolysis of Fe(II) species is responsible for the decrease in pH.

The concentration of each individual species of the anolyte solution extracted from artificial pits of 304L and 316L was analysed by Suzuki *et al.* [54] using atomic absorption spectroscopy. The dissolved alloying elements in the pit solution were observed in the same approximate portion as in the alloy with the concentration of metal ions varying from 3.83 to 6.8 N. Chloride concentrations between 3.87 and 6.47 N and pH values of 0.8 to -0.18 were reported. The low pH values measured could not be predicted by thermodynamic calculations (Table 2-1). The formation of hydroxyl-chloro complexes of dissolved metal ions was given as the reason for the low measured pH value. Significant increase in the activity coefficient of H^+ due to the presence of concentrated chloride was given as an alternative reason.

Table 2-1- hydrolysis reactions and thermodynamically calculated equilibrium pH value of the metal ions found in anolyte [54]

Hydrolysis reaction	Equilibrium pH
$Fe^{2+} + 2H_2O \Leftrightarrow Fe(OH)_2 + 2H^+$	$pH = 6.64 - 1/2 \log [Fe^{2+}]$
$Cr^{3+} + 3H_2O \Leftrightarrow Cr(OH)_3 + 3H^+$	$pH = 1.53 - 1/3 \log [Cr^{3+}]$
$Ni^{2+} + 2H_2O \Leftrightarrow Fe(OH)_2 + 2H^+$	$pH = 6.09 - 1/2 \log [Ni^{2+}]$
$Mo^{3+} + 2H_2O \Leftrightarrow MoO_2 + 4H^+ + 2e$	$pH = (0.311 – 0.0591 \log [Mo^{3+}] – E_0)/0.236$
$Mn^{2+} + 2H_2O \Leftrightarrow Mn(OH)_2 + 2H^+$	$pH = 7.66 - 1/2 \log [Mn^{2+}]$

Mankowski and Smialowska [61] grew pits on an 18Cr-12Ni-2Mo-Ti in 0.5 NaCl solutions at +860 mV (NHE) and froze the contents of the pits with solid CO_2 before the end of the measurement. Colorimetrically analysis of the anolyte gave a chloride ion concentration of 12 N that gradually decreased during the pit development to 2 N depending on the "*tightness*" of the pit cover. They observed that the rate of pit development reduced with the accumulation of chloride ions inside the pit, indicating that pit growth is diffusion controlled. Then they measured pH values of made-up bulk solutions of $FeCl_2$ and $CrCl_3$ at concentrations of 1 to 6 N and observed a decrease in pH values as the chloride concentration increased. A pH of 0.06 consistent with the results of Suzuki *et al.* was observed for a solution similar to the composition of pit anolyte (8N Cl^-, 3 Fe: 1 Cr).

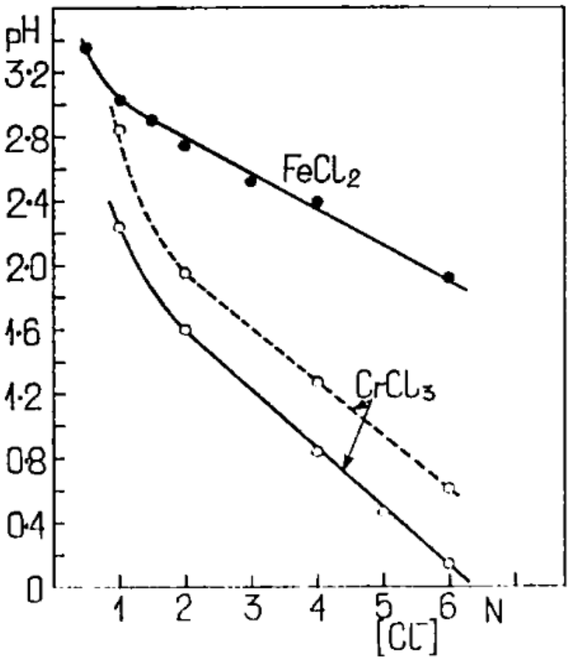

Figure 2-4- pH values as a function of chloride concentrations in $FeCl_2$ and $CrCl_3$ solutions [62]

Tsuru *et al.* [63] investigated the mass transport and chloride ion complexes from galvanostatic dissolution of 304 stainless steel in a specifically occluded cell. They observed hydrolysis reactions of Cr^{+3} ions and formation of $Cr(OH)_3$ consistent with their measured low pH values of 1 to 2. They also found an increase in the chloride concentration to ~ 6 N as the pit grew. However, the amount of free chloride remained constant at 2 N which was attributed to the formation of $CrCl_n^{3-n}$ complexes, which affect transport of chloride into the bulk solution which suppresses the transport of cations and results in aggressive solution inside the cell at the initial stage.

2.2.4 Pit shape and morphology

In 1964, Schwenk [53] discussed the physical shape of the pits growing on 18Cr-10Ni stainless steel at a wide range of applied potentials in 1 M NaCl. He found that pits in their initial stages are of hemispherical shape covered with a thin and perforated layer of metal. He reported the edge of the pits are often (not always) circular. *"Regularly etched pits, mostly squares and hexagons"* were reported to form at low applied potentials (with low current density at the pit bottom) with bounding planes at of type (111); the most compact plane in the case of austenitic stainless steel. At higher applied potentials, however, hemisphere and isotropic pits with polished or dull interiors were found to form. He believed that this transition was due to increasing local current density within the pits.

Consistent with the work of Schwenk [53], Pickering and Frankenthal [64, 65] reported crystallographic pits as the typical of initial stages of pitting in stainless steel (and iron). However, they observed a mixture of crystallographic etch and hemispherical pits at more noble applied potentials. They observed that small pits were not related with inclusions (Figure 2-5), whereas, the larger pits initiated at the boundary between the metal matrix and inclusions and propagated underneath the surface with a porous cover over the cavity resulting an often faceted interior.

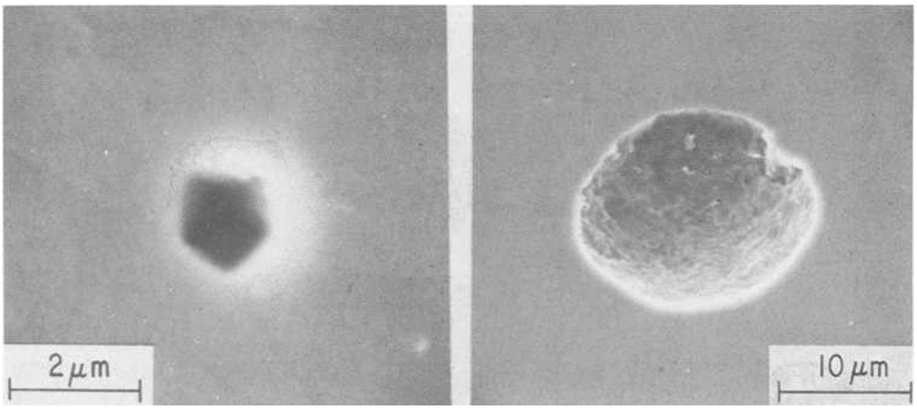

Figure 2-5- typical of small pits not associated with inclusions on stainless steel. (a) crystallographic pit at the initial stages of growth, (b) more advanced stage showing the vanishing of the crystallographic structure. Sample held at 1.0 V (SHE) in solution of 0.4 M $FeCl_2$ acidified with HCl to pH 0.9 [65]

Mankowski and Smialowska [61] also reported that pits initially propagated isotropically with a hemispherical shape, however, after a certain time their shape transform into a spherical cup with faster development in the lower part than in the upper one.

Initiation of corrosion micro-pits at inclusions on 304 stainless steel in 0.1 M NaCl solution was investigated by Ke and Alkire [43] and it was found that all pits initiated at inclusions, and grew with crystallographic hexagonal shape before forming to hemispherical geometries. No evidence of inclusions in larger pits was detected as they were dissolved during the pit growth.

Sato [66-69] extensively analysed the shape of pits in iron group metals at different potentials. He distinguished that at lower potentials etching pits with crystallographic structure formed. He believed that this type of dissolution occurred if a critical pH is reached within the solution of the pit cavity and metal is kept at the active state. At higher potentials (noble) polishing pits were formed with bright (polished) surfaces (Figure 2-6 (a)). He noticed that the transition from polishing to etching (active state) occurs at concentration close to the critical concentration required for stable pitting of stainless steel. He completed his work later [67] by showing that pits at potential above E_{pit} grew with hemispherical shape and polished interiors and if the potential is decayed (Figure 2-6 (b)), the pit either repassivate or propagate in active state with etching interior, deep and non-hemispherical geometries or crevice-like forms.

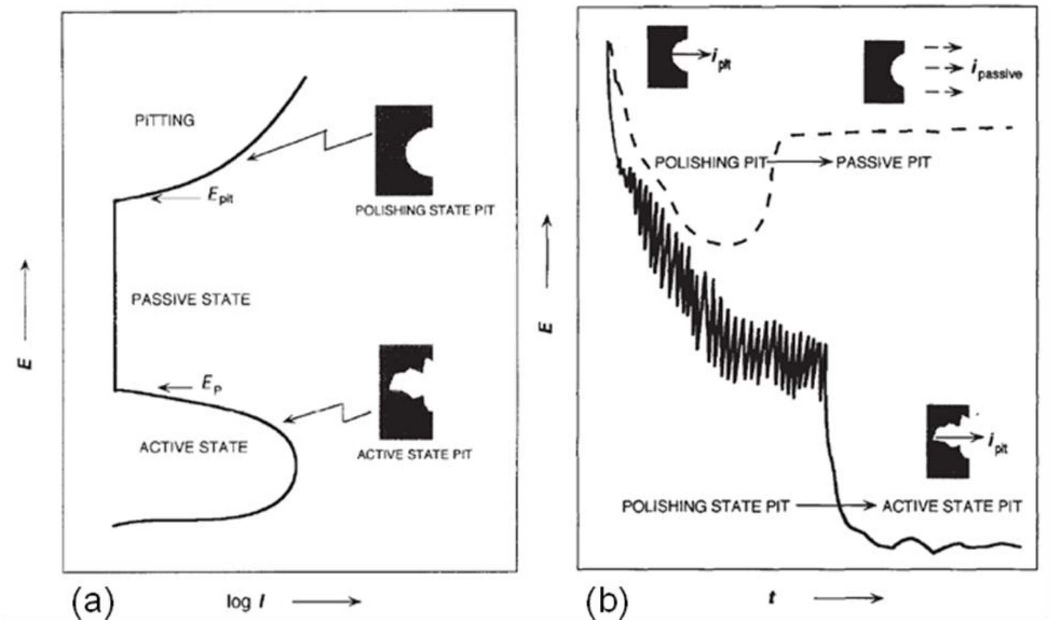

Figure 2-6- (a) anodic polarization curve of metal showing active and polishing state pit regions, (b) potential decay with time for a pit at polishing state showing either repassivation or transition to active state pit. E_p is the passivation-depassivation potential, E_{pit} is the pitting potential [67].

2.2.5 Pit covers

As mentioned above, Schwenk [53] noted that pits in stainless steel had a thin perforated cover of the original metal surface and it was difficult to observe them during growth. He examined the steel surface with a fine pin after the test to detect the pits. Rosenfeld and Danilov [70] found that pits galvanostatically grown at 2 μA in 0.1 N NaCl were mainly covered with a porous *"shielding"* layer. Therefore, they considered pitting as a *"peculiar"* type of crevice corrosion where the concentration gradient of corrosive medium was provided by the cover. Therefore, they found that destroying the shielding layer during the growth appeared to lead to direct repassivation (Figure 2-7).

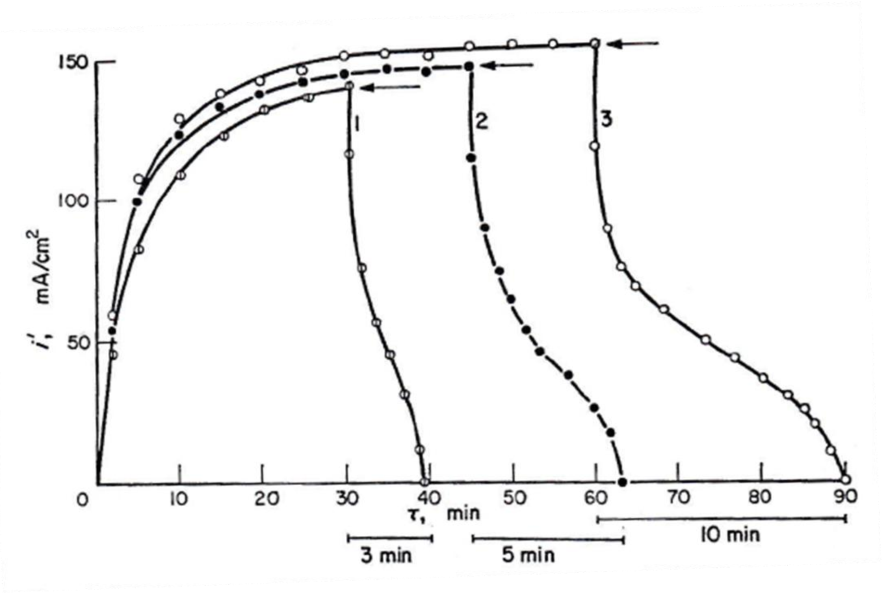

Figure 2-7- current density variation as a function of time of various growing pit and its decay once the protecting layer over the pit was destroyed [53].

Similarly, Isaacs and Kissel [71] also found that puncturing the cover over pits in 304 stainless steel resulted in repassivation except for very large pits which could survive the removal of their cover. They investigated the effect of surface oxide properties on the pit propagation by using different abraded and electropolished surfaces and thickened oxide films at high temperature. They observed that although the pit initiation might not depend on oxide layer properties, pit propagation was significantly affected by the oxide layer thickness. They concluded that thick oxide layers supplied a stronger cover for the pit propagation, whereas thinner oxide films were broke more easily leading to quick repassivation. Therefore, the number of actively growing pits was more associated with the oxide film properties rather than to the initiation factors.

As noted above, Mankowski and Smialowska [61] observed that pits propagated underneath surface layers that initially appeared slightly convex which made the pits clearly observable. As the pits grew, the convex layers became less evident. They attributed this effect to the osmotic pressure of the pit solutions moving outside the pit. In addition to the initial central hole in the cover, as the pit grew they also detected newly emerging holes in the cover through which, streams of coloured solution were escaping. This was in consistent with the observation of Pickering and Frankenthal [65] that had earlier detected porous cover and attributed the perforations in the cover to underneath attack by aggressive pit chemistry.

Further researchers [50, 72] also observed the remnants of the perforated passive layers and established the role of such a cover over the pit on stabilising the early stages of pit growth. It is now a well known idea that if a pit at its early stages (metastable stage) can remain active after its cover collapses or is removed, then it turns into a stable pit. The role of the cover during metastable growth is considered to be either an electrical resistive barrier [72] or a transport diffusion barrier [50] in order to protect the pit from passivation.

2.2.6 Local dissolution kinetics

Once the approximate chemical composition of the solution inside pit is known, it is possible to measure the kinetics of metal dissolution in a simulated bulk solution of the pit composition.

Mankowski and Smialowska [61] measured polarization curves of 18Cr-12Ni-2Mo-Ti stainless steel in 1 N HCl solutions with different amount of $FeCl_2$, as shown in Figure 2-8. At solutions with more than 4 N $FeCl_2$, the increase in potential resulted in salt film precipitation and accordingly a diffusion limited current density was reached. At lower concentrations of $FeCl_2$, active dissolution continued with passivation and then some localised dissolution.

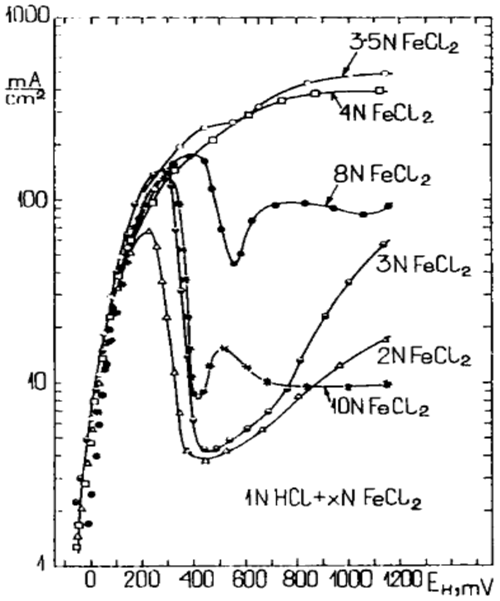

Figure 2-8- anodic polarization curves for stainless steel in 1 N HCl with indicated amount of $FeCl_2$ [61]

Hakkarainen [73, 74] dissolved 304 and 316 stainless steel in 10 M HCl solutions to produce simulated pit solutions with the same proportions of elements in the alloy.

He then measured the anodic dissolution behaviour of fresh samples of both steels in the resulting solutions of different degrees of saturation of metal cations. He reported strong dependence of anodic dissolution behaviour on the metal ion concentration in the solution; repassivation would occur if the degree of saturation of metal ions becomes less than ~80%. In more concentrated solutions, it was shown that active dissolution was controlled by diffusion and salt film precipitation and the current density decreased with an increase in the degree of saturation. At a given potential, there is a critical concentration of metal ions below which an abrupt change from dissolution to passivation occurs. This critical concentration increases with increase in potential and is higher for 316 stainless steel than for 304. It was shown that the polarization curve for 316 is displaced to higher potentials compared with that for 304. However, the polarization behaviour of both steels was exactly the same in solutions made by dissolution of either 304 or 316. This suggests that the dissolved Mo in the pit solution does not affect the dissolution process, and it is the presence of Mo in the alloy matrix that shifts the dissolution kinetics to higher potentials.

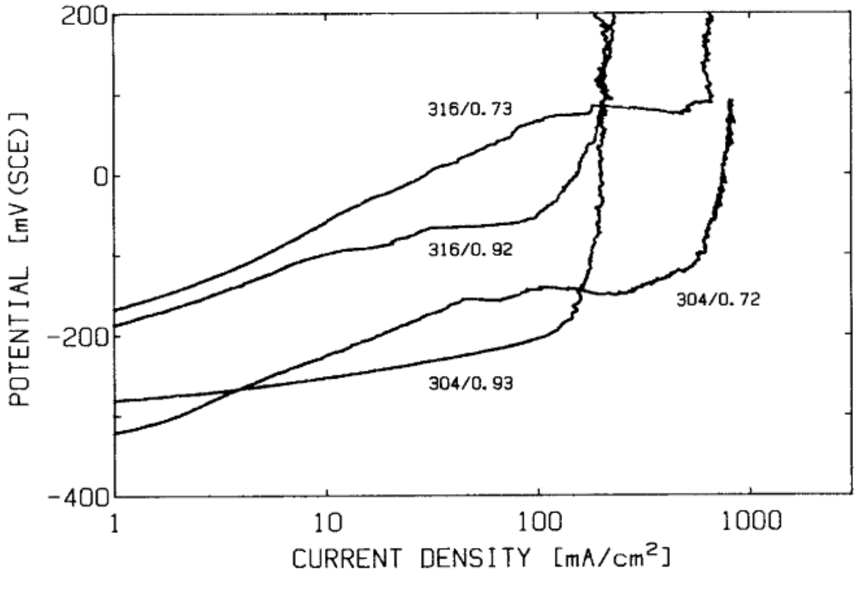

Figure 2-9- polarization curves of 304 and 316 stainless steel in solutions made by dissolving 304 stainless steel in 10 M HCl to the indicated degree of saturation [73, 74].

2.2.6.1 One dimensional artificial pits

An alternative method for studying dissolution kinetics under conditions that simulate those found inside pits is the use of artificial pit electrodes, which are also known as “lead-in-pencil” electrodes. These electrodes consist of a thin metal wire in an insulating mounting that dissolves uniformly and recedes into the mounting forming a one dimensional (1D) cavity in which the corrosion products accumulate, simulating the solution inside a real pit (Figure 2-10). This method has been extensively used to simulate the naturally formed local pit chemistry for study of dissolution kinetics, salt layer precipitation and mass transport within pits [75-82] .

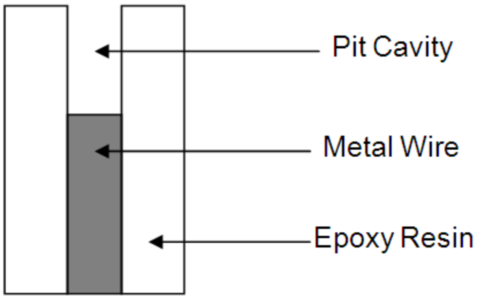

Figure 2-10- schematic diagram of an artificial pit

Isaacs [76], in 1973, used artificial pit electrodes and studied localised corrosion and resistive layers of stainless steel. He distinguished two stages of growth. At the initial stages (transient period) after stepping the potential from the open circuit potential (OCP) to 500 mV(SCE), micropits initiated and grew and caused a sharp increase in the current. As the micropits coalesced, the wire then dissolved uniformly. At this stage (quasi-steady state period) the current gradually decreased with time. Impedance measurements at this stage on the pit surface indicated the presence of a resistive layer. It was interpreted as a layer ~10 nm thick on the metal surface with a resistivity of 10^8 Ω.cm which was obeying Ohm’s law. It was observed that in a range of applied potential between 200 mV to 1 V, almost all of the potential is absorbed by the layer through regulating its thickness, indicating that the thickness is potential dependent. Based on the conservation of mass, it was assumed that the metal ion flux across the layer was equal to the current from metal and this should match with the diffusional flux outside the pit cavity. Once the potential is increased, the electric field across the layer is raised and metal ion flux to the film/solution interface is increased accordingly. As the diffusional flux does not depend on potential, the surplus metal ions cannot move into the saturated solution, thus the layer becomes thicker. As a result, the metal ion flux across the film decreases to equal the diffusional flux. Therefore, the process is assumed to be *self regulating*, i.e. the salt film regulates its thickness so that the current density remains constant regardless of applied potential. It was assumed that this layer consists of a solid metal chloride, and a saturation concentration of 6 M was calculated.

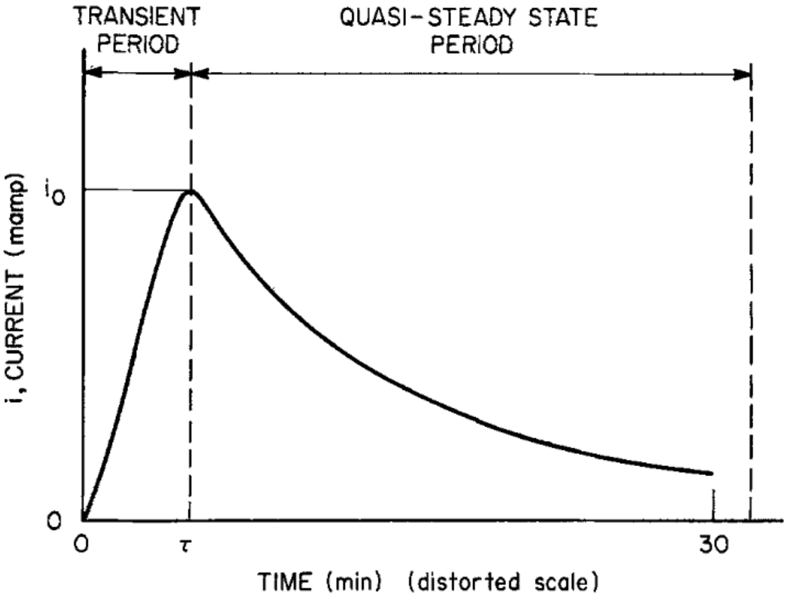

Figure 2-11- schematic diagram of current vs. time during anodic dissolution [83]

Based on the earlier work, Tester and Isaacs [83] extended the model by assuming that the pit cavity is at steady state. It was assumed that no anodic current was consumed in the process of salt film thickening and therefore the metal ions dissolved at the corroding surface of metal/salt interface are transported into the bulk solution. Ignoring the convection, they described the transport by the Nernst-Einstein equation

$$\frac{i}{zF} = -D\left(\frac{dC}{dx}\right) - \frac{zFDC}{RT}\left(\frac{d\phi}{dx}\right)$$ **Equation 2.4**

where i is the anodic current density, z is the transferred charge, F is the Faraday constant, R is the gas constant, T is the temperature and ϕ is the potential drop in solution with respect to reference electrode. It had been shown in Isaacs' earlier work [76] that the potential gradient in solution was unimportant (the potential drop was dropped across the salt film), only the diffusion part was considered. Therefore, the above equation was simplified to describe the diffusion-controlled current density, i_{lim}.

$$i_{\text{lim}} = zFD.\left(\frac{C_s - C_{bulk}}{l + \delta}\right)$$ **Equation 2.5**

Where l is the pit depth, δ is the boundary layer thickness, D is the metal ion diffusion coefficient, and C_s and C_{bulk} are the surface and bulk metal ion concentrations, respectively. They compared their model with results of measurements in solutions of 0.5 to 10 M made from chloride salt of metal electrode (such as $NiCl_2$, $FeCl_2$) in a range of applied potentials from 0.5 V to 1 V (SCE). Reasonable agreement was observed for chloride concentrations below 3 M. However, at concentrations above 5 M, the experimental limiting current density was lower. They believed that this was due to increased activity of chloride in the bulk solution that decreased the solubility of the metal ions.

Isaacs and Newman [81] grew pits at +200 mV(SCE) to a depth of 0.8 mm to establish a diffusion-controlled steady state. They then stepped the potential down to values between -200 mV and -400 mV and recorded the current. An initial increase in current was observed, followed by gradual decrease in the current as the salt film was dissolved. The decrease in current was believed to be caused by a split between active and passive areas. Using a diffusion model to calculate surface concentrations of metal ions as a function of time, they then generated a plot of current density against surface concentration of metal ions.

Gaudet *et al.* [84] carried out this type of experiment on 304 and 600 alloy stainless steel and compared experimentally generated plots of current density against surface concentration at different applied potentials with linear plots obtained from Fick's 1^{st} law of diffusion (Figure 2-12(a)). The crossing points of the two lines (I, H, and G) where the dissolution current matches the diffusion current are predicted to be steady states. Line $B'G$ corresponds to a lower potential than $BIHG$ and indicates that at a certain pit depth, a minimum potential is required for any steady state condition apart from G (passivity) to exist. Points I and G are stable under either potentiostatic or galvanostatic conditions whereas, H was only at steady state under galvanostatic conditions.

The results obtained at different pit depths and applied potentials were corrected for the IR drop and a family of isopotential curves of surface kinetics were generated (Figure 2-12(b)). From their work, it was concluded that active dissolution (salt film free) only occurs above a critical potential and in a critical surface concentration of metal ions above ~ 60 % of saturation (C_{crit}). At lower potentials or surface concentrations only passivation occurs. This was consistent with the work of Hakkarainen [73, 74] on the localised kinetics on the simulated pit solutions.

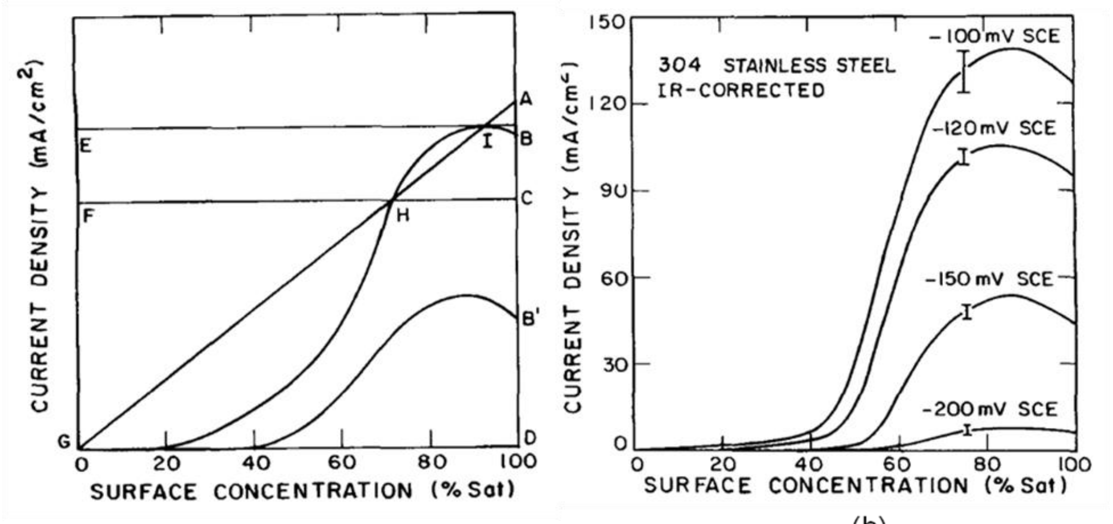

(a) (b)

Figure 2-12- (a) theoretical prediction of multiple steady state, the letters A-H represent different states of the surface as described in the text. (b) surface kinetics at different applied potentials for 304 stainless steel [84]

Building on the finding that active dissolution is possible within a metal ion solution concentration range of 60 to ~130% of metal ion saturation [81, 84], Isaacs and Newman [85] concluded that pitting in stainless steel occurs at both active (salt film free) or diffusion controlled (salt covered) state. This conclusion was in agreement with the difference between etched (salt film free) and polished (salt film-covered) pits proposed by Sato. Simultaneously, the possibility of pit growth under active (ohmic control) and diffusion control was also shown by Hunkeler and Bohni [86] for stainless steel and nickel.

Similar experiments to the work of Gaudet *et al.* [84] were followed by Steinsmo and Isaacs [75, 87] to study the effect of Cr content in Fe-Cr alloys. Qualitatively similar results to the austenitic stainless steels [81, 84] were obtained. However, active dissolution occurred at much lower surface concentrations of metal ions (~ 10 %). An increased C_{crit} (the critical concentration below which passivation takes place) with increasing Cr content was also observed.

More recently, Enerhaug *et al.* [88] have studied the dissolution and repassivation kinetics of super martensitic stainless steel following the approach of Gaudet *et al.* [84] and a critical concentration (C_{crit}) of ~30% of the saturation value required for continuation of growth in active state has been reported.

2.2.7 Salt films

As described above, the propagation of a pit requires development of a concentrated solution inside the pit cavity. At high potentials, it is likely that a salt layer of precipitated metal chloride will form on the bare metal surface, as shown by Isaacs [76].

Landolt and co-workers [89-94] studied the salt film properties and mass transport controlled dissolution for iron and its alloys. Kuo and Landolt [89] measured a saturation concentration of 4.25 ± 0.05 M for $FeCl_2$ in water using atomic absorption analysis. Then at the limiting current density, they measured the concentration of Fe^{2+} at the anode surface and found it to be 4.2 M. By taking an effective diffusion coefficient of $8.5\times10^{-6}cm^2s^{-1}$ for Fe^{2+}, they accounted for the effect of migration over a range of supporting electrolyte concentrations.

Grimm *et al*. [93] modelled a duplex film structure for salt film formed on iron in an $FeCl_2$ electrolyte using AC impedance. They believed the inner part to be a compact and anhydrous film, and the outer to be porous hydrated film. They suggested that duplex structure could describe the varying properties of the salt film with depth. The duplex model was then employed by West *et al*. [95] to analyse electrohydrodynamic impedance measurements which enabled them to calculate a porosity value between 0.2 and 0.9 % for the outer layer. Grimm and Landolt [92] continued the study on the salt films on Fe-Cr alloys in $FeCl_2$ and NaCl solutions and reported $FeCl_2$ as the precipitated salt film and limiting current densities being controlled by the transport of Fe^{2+} ions.

Beck [96] proposed that the precipitation of salt films (as a diffusion barrier) is crucial during the early stages of pit growth. In his conclusion he took the important fact from the work of Vermilyea [97] who had demonstrated that the pitting potential for various metals (such as Fe, Ni and Mg) was close to the standard potential of formation of the metal chloride. Therefore, he concluded that even crystallographic etched pits could grow with a very thin layer (~10 nm) of salt film whereas the thicker films that form at higher applied potentials result in hemispherical pits with electropolished interiors. Similar to the work of Tester [83], he then proposed that the diffusion limited current density, i_{lim}, for an open hemispherical pit, can be given by

$$i_{\mathrm{lim}} = z\,FDC_{\mathrm{sat}} / r \qquad \textbf{Equation 2.6}$$

in which *r* is the pit radius.

Laycock and Newman [82] carried out a detailed study on the localised dissolution kinetics of 302 and 316 stainless steel using different diameter of artificial pits. Two growth regimes were identified for the pit growth. At lower potentials, the pit growth was ohmic/charge transfer control and at higher potentials, growth was under mass transport control. It was shown that the salt film precipitation potential (or the transition potential between the two regimes), E_T, in artificial pits is indeed very close to the conventionally measured pitting potential at various chloride concentrations.

Thus, salt films are regarded as a stabilising factor in pit growth, either as a resistive barrier that provides a potential difference between active and passive areas, or as a diffusion barrier that prevents water access to the corroding surface of metal.

2.2.8 Metastable pits and pit stability

As noted earlier, corrosion pits on stainless steel exposed to chloride solution grow in two consecutive stages of metastable and stable. It is shown that metastable pits initiate and grow at potentials well below the pitting potential [82] and with the same mechanism as the early growth of stable pits but for a limited period before repassivation occurs [98]. It has been shown that the survival of a metastable pit depends on the maintenance of a perforated cover over the pit mouth either as an effective diffusion [50, 99] or a resistive [72] barrier.

Metastable pit growth depends on the original geometry. Pistorius and Burstein showed that narrower and more deeply recessed sites developed faster and may be active at lower potentials for a given chloride concentration [100].

Figure 2-13 shows a typical current transient from metastable pit growth showing a slow rise in current (dissolution) followed by a fast decay (repassivation).

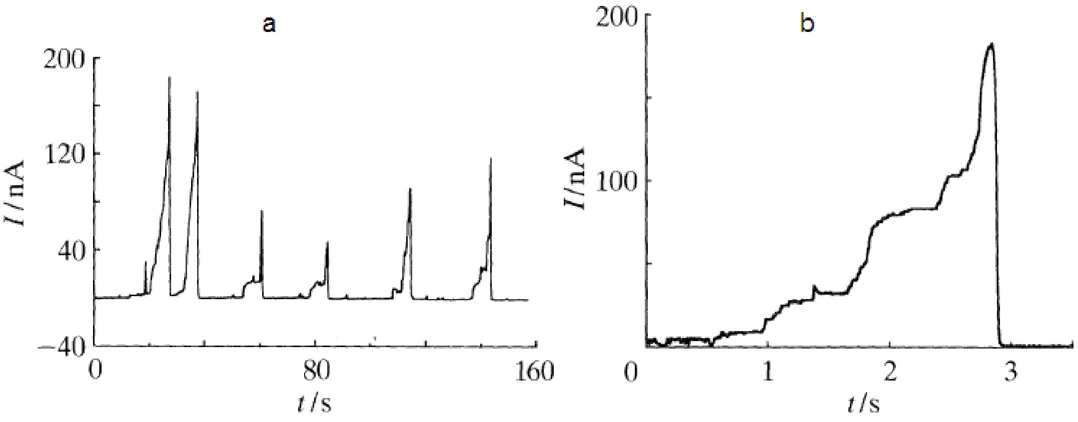

Figure 2-13- (a) Series of current transients from metastable pit growth on a 50 µm disc of type 304 stainless steel held at 100 mV in a solution of 1 M Cl$^-$, pH 0.7, (b) Single current transient from a metastable pit [50].

Boehni and colleagues extensively studied the metastable pitting of austenitic stainless steels [72, 101-103]. Similar to the Beck’s idea [96], they showed that below the salt film formation potential, E_{sf} (or as explained above, E_T), metastable pitting is not possible. Above E_{sf}, the salt film is stable. However, as salt film precipitation is a kinetically slow process, the early stages of pit growth are under ohmic/charge transfer control, until salt film precipitation establishes the diffusion-controlled regime. In their model, the pit cover was the key parameter in controlling pit stability. Frankel [72, 102] supported the idea that it was the porous pit cover that provides this high resistance at the early stages of pit growth and not a salt layer. This approach can be traced back to Vetter and Strehblow [104], who argued that a highly resistant layer was essential to maintain the potential gradient between the passive surface of the metal and the active pit surface,

Building up on the approach by Frankel *et al.* [72, 102], Pistorius and Burstein measured the diameter of micropits that initiated and grew below the pitting potential. By integrating the small associated current transient and assuming a hemispherical pit shape, they calculated the average anodic current density as a function of pit radius. They assumed that the minimum concentration of metal ions required for maintaining the pH required for continuation of dissolution was 3 M (~75% of saturation value of 4.2 M) and ignored the migration and convection effects. Then the concentration gradient from the pit bottom to the pit mouth was established for an open, hemispherical pit of radius, r, as

$$\Delta C = (2\pi / 3\, zFD)\, i.r \qquad \textbf{Equation 2.7}$$

Similar to the work of Galvele [56], *i.r* is the critical parameter which Pistorius and Burstein termed the *"pit stability product"*. Assuming a zero concentration of metal ions at the pit mouth, the minimum and maximum concentration of metal ions at the pit surface was taken as 3 and 6 M (assuming 150% saturation), the stability product was obtained as

$0.3 \text{ A/m} \leq i.r \leq 0.6 \text{ A/m}$

This was in agreement with the work of Frankel *et al*. [72] and Williams *et al*. [105] who reported values of 0.4 A/m and 0.6 A/m, respectively. However, they noticed that at the initial stages all metastable pits, even the ones that became stable, grew with pit stability products below 0.3 A/m. They argued that during metastable growth, the pit cover acts as a diffusion barrier enabling the concentrated local chemistry to be maintained above the critical value required. They observed that pits grew with an almost constant current density; therefore as the pit grew *i.r* increased and once the value of 0.3 A/m was met then the pit was able to grow indefinitely even if its cover was removed or collapsed.

In contrast with the idea of Frankel *et al*. [72], Pistorius and Burstein [50] showed that even metastable pit growth is controlled by mass transport and metastable pits are covered with a salt film, even before the cover collapse. They grew real single pits at 700 mV (SCE), swept the potential downwards at 1 V/s and observed the current decay as shown in Figure 2-14. This indicated that at least at high potentials, pits were under diffusion control until repassivation occurred. If that was not the case then the current density should be dependent on the potential.

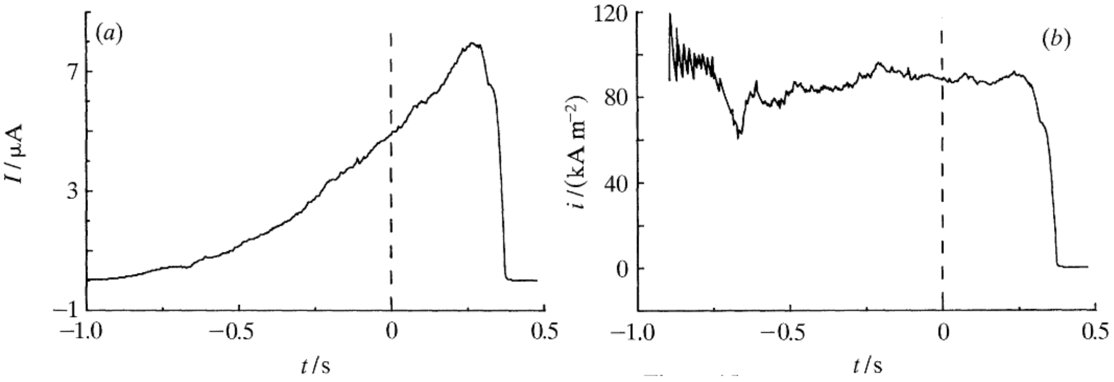

Figure 2-14- (a) Current transient for a metastable pit on 304 stainless steel initiated at 700 mV (SCE) in 0.8 M NaCl + 0.2 M HCl. The potential was scanned down at 1 V/s starting from t=0 (indicated by the dashed line). (b) Calculated pit current density of the pit shown in (a)

2.2.9 Two dimensional artificial pits

An edge-on foil technique has been used to view the development of two dimensional pits and lacy cover formation in stainless steels [106-109]. A thin foil is sandwiched between two glass slides using epoxy resin and one edge of the foil is exposed to solution. Pits growing from the foil edge are viewed by video microscopy allowing the study of real-time pit growth and shape. Using this technique, Ernst and Newman analysed the kinetics of pit growth in width and depth and suggesting a semi-quantitative model for pit propagation which explained the lacy pit cover formation during the pit growth. Comparing the pit depth variation by time obtained from 2D pits in foil with 1D artificial pits, it was observed that pit growth in depth is independent of potential and has a parabolic relation with time, whereas lateral pit growth is linear with time and potential. Figure 2-15 shows the stages of lacy pit cover formation proposed. The pit cover is partially a remnant of the passive film (shown as a thick line) and partially the metallic lacy top shown enlarged for clarity. In their model, they showed that as the pit starts to grow, metal ions inside the pit transport to the outside of the pit causing dilution of pit solution. Thus, near the pit mouth where C_M falls below C_{crit}, the surface locally repassivates. Closer to the pit bottom where $C_M > C_{crit}$ dissolution continues, and undercuts the metal (part d in figure), resulting in formation of a lobe that extends laterally and eventually perforates the passive metal surface and produces an opening on the metal edge. The new opening again causes dilution and local passivation close to the perforated area. This process repeats during the pit growth and generates a porous cover over the pit cavity. They also proposed that the effect of pit cover on the mass transport can be rationalised by comparing the growth kinetics of 2D pits with 1D pits and related the size of perforation in cover with the ratio of C_{crit}/C_{sat} obtained from 1D artificial pits.

In parallel with Ernst and Newman work, Laycock *et al.* [7, 110] developed a predictive model for pit propagation and formation of the perforated pit cover based on the critical concentration required for propagation in stainless steel in chloride solution. Their model will be discussed in details in Chapter 7.

Ryan *et al.* [111, 112] studied 2D pit growth in thin films of 304 and iron-chromium alloys prepared by sputter deposition. They reported that thin films were highly resistant to pit initiation due to the absence of inclusions in the thin film matrix. However, similar growth regimes were observed. At high potentials, the current density was independent of applied potential over a range of bulk chloride concentrations indicating a diffusion-controlled regime. At relatively low potentials, a linear relationship between current density and potential was seen, indicating mixed ohmic/activation control. The pit surface was seen to be polished and smooth in the diffusion-controlled regime with a transition to *"a more convoluted structure"* under the ohmic/activation controlled regime.

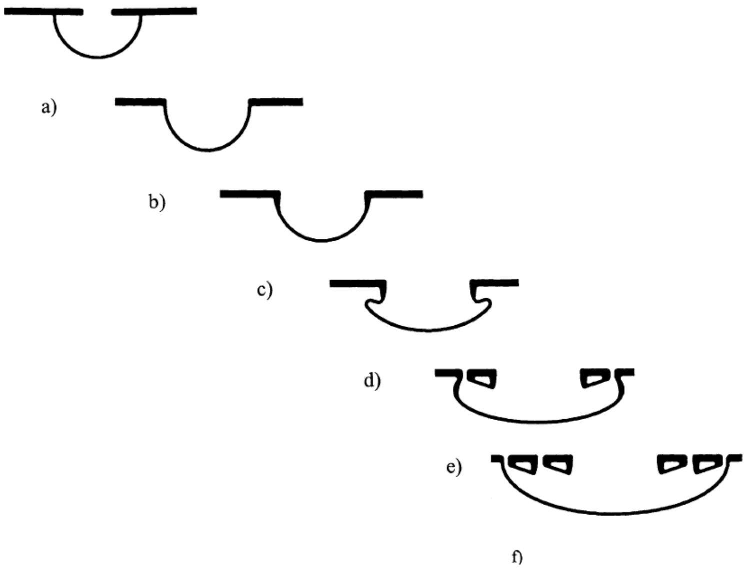

Figure 2-15- model proposed by Ernst and Newman [106] for pit shape and lacy cover formation based upon the variation of the metal cation concentration inside the pit. Thick lines in the drawing (a)–(f) represent passivated metal. The passive metal of the lacy cover is shown enlarged for clarity.

2.2.10 Critical pitting temperature

Pitting corrosion of stainless steel in chloride solutions has a critical pitting temperature (CPT), below which pitting does not occur (although metastable pitting is still observed). Above CPT, stable pitting occurs once the pitting potential is exceeded, [113]. A number of theories have been developed for the CPT phenomenon mainly assuming on the inability of metal to dissolve at a sufficient rate at below the CPT, even in the most aggressive local sites [80, 107, 113-118].

Salinas-Bravo and Newman [119] developed the idea of a critical current density for passivation, i_{crit}, in order to explain the CPT transition. Their approach also involved consideration of a limiting current density, i_{lim}, which can be calculated from Fick's 1st law, knowing the saturation concentration of metal ions, C_{sat}. They neglected any variation of the diffusivity and C_{sat} with temperature and concluded that the CPT is the temperature at which i_{crit} equals to i_{lim}. Therefore, at lower temperatures, the current density necessary to sustain the concentrated pit solution in an open pit is greater than the current density required for passivation and this the reason that a metastable pit repassivates.

Moayed *et al.* [114] confirmed the dependence of the CPT on surface finish, indicating that rougher surfaces create a longer diffusion length during pit stabilization. Also, Ernst and Newman have recently reported that the CPT falls at very high chloride concentration [120] while it does not in lower range up to 5 M [121].

2.3 Synchrotron X-Ray Facilities

Synchrotron radiation is usually made by injecting electrons (or positrons) into a “storage ring”, in which they circulate. The circular orbit is achieved by deflecting the electron beam with magnets. At each of these “bending magnets”, highly intense X-rays are generated tangentially to the electron beam down beamlines, where the experimental measurements are carried out. X-rays may also be generated by magnetic “insertion devices”, which are located in the straight sections of the storage ring (Figure 2-16). A primary benefit of synchrotron methods for studying process that take place in wet environments, such as the corrosion of metals, is that X-rays are used for excitation and detection and therefore vacuum conditions are not required [122, 123].

Figure 2-16-Schematic diagram of a synchrotron X-ray facility

2.3.1 X-Ray Tomography and Radiography

X-ray tomography is a non-destructive technique that enables three-dimensional (3D) analysis of microstructural interior of materials with a high spatial resolution. The basis of X-ray tomography is X-ray radiography, in which an X-ray beam is used to illuminate a sample and the transmitted beam attenuated by the object is recorded on a detector. For tomography, a series of radiographs are collected as the sample is rotated through 180°. This produces a set of projections that can be reconstructed to give the 3D structure of the object [124-126].

Hounsfield was the first who developed a commercial X-ray tomography system for medical imaging in 1972 with resolution capability of 300-1000 μm. However, most industrial applications were developed much later in the 1980s due to advancements in electronics and computer technology [39]. The current resolution of commercial laboratory-based instruments is ~2-5 μm, but the substantially lower intensity of laboratory-based sources means that it is not practical to carry out *in situ* time-dependent measurements since individual tomograms make take many hours to collect, whereas using synchrotron radiation, similar measurements can be taken in tens of minutes.

2.3.2 Principles of X-Ray Tomography

The contrast observed in an X-ray radiograph is associated with the material's local attenuation length, which is the distance at which the X-ray intensity is reduced to 37% of its original value. Attenuation lengths can differ by a factor of 100 between the lightest and the heaviest materials, and is roughly inversely proportional to the mass density of the material and increases with increasing X-ray energy.

2.3.2.1 X-Ray Source

Two types of X-ray source are mainly used to run tomography; a divergent beam produced by a micro-focus X-ray tube and a parallel beam of synchrotron radiation [125].

2.3.2.2 Focus Tube X-Ray Tomography

In this method, X-rays emitted from a metallic target are focused to a very small size in an X-ray tube, producing a polychromatic, conical X-ray beam with energy in the order of 10 to 100 keV, which traverses the object. A CCD camera typically 1024 x 1024 pixels records the transmitted X-rays, Figure 2-17 (a). Spatial resolution generally is between 3 and 500μm, although latest generation equipment now claims submicron resolution [127].

2.3.2.3 Synchrotron X-Ray Tomography

Synchrotron radiation produces a small-source size and very high flux which is at least 1000 times larger than focus X-ray tubes [125]. Either white X-ray beams or monochromatic beams can be used; the X-ray beam is parallel so that no magnification of the image is made on the detector, Figure 2-17 (b). This parallel, monochromatic beam provides an exact and quantitative reconstruction, free of geometrical and beam hardening artefacts [125]. Converting X-rays into visible light is mainly made with a scintillator and projecting them onto the CCD with typically 2048 × 2048 pixels via suitable microscopic optics. Resolution on the order of 0.3 to 0.7 μm can be achieved in this method [128].

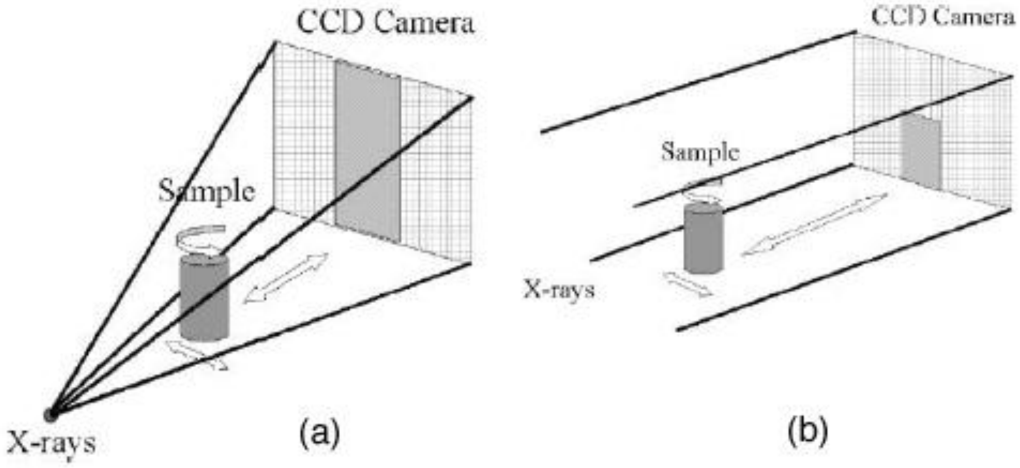

Figure 2-17- Cone-beam geometry: micro focus source with 2 D detector. (b) Parallel beam geometry: synchrotron source ensures parallel X-ray beam [38]

2.3.2.4 X-ray microtomography studies of corrosion

Synchrotron X-ray microtomography is a non-destructive technique for 3D analysis of microstructure with resolution on the micrometre length scale. The method is ideal for real time 3D monitoring of corrosion pit evolution in wet environments. X-ray tomography has been utilised in various materials research including observations of intergranular stress corrosion crack nucleation and growth in aluminium and stainless steel alloys [129-131]. Marrow *et al.* [129] performed *in situ* X-ray tomographic experiments to examine pitting, intergranular corrosion and cracking in aluminium alloy and cracking in sensitised type 302 stainless steel. Davenport *et al.* [132] correlated Y distribution in a Mg alloy with corrosion damage and Connolly *et al.* [133] studied localised corrosion morphology and transition to stress corrosion cracking of aluminium and steel specimens using X-ray microtomography. Localised corrosion of aluminium alloys has also been studied by Eckerman *et al*. [134-136], who first demonstrated the use of a capillary microcell for tomographic experiments [136]. Knight *et al.* [137] explored the development of intergranular corrosion occurred in Al alloys under droplets of sodium chloride.

2.4 Summary

The basic mechanism of the propagation of pits in stainless steels is well understood, and a range of methods have been used to measure relevant electrochemical parameters, which have been used to develop models to predict the pitting behaviour of stainless steels. However, in order to develop and validate these models, an improved understanding is required of the morphology of pit propagation and its relationship to the electrochemical kinetics of pit growth. Imaging methods using highly intense X-rays offer a new approach for *in situ* measurement of pit morphology, including the possibility of extracting kinetic data on pit propagation for refining pit propagation models. In this work, *in situ* methods for observing 2D and 3D pits using X-ray synchrotron radiation were used and pit propagation in stainless steel was studied in real time. A method was developed for obtaining localised dissolution kinetics from X-ray synchrotron radiographs taken from 2D pit, and these data were used to refine the model of Laycock *et al.* [7, 110, 138-143] for prediction of pit propagation.

3 Experimental procedures

3.1 Radiography sample preparation

AISI 304 and 316L stainless steel foils 20 and 25 μm (±15%) in thickness were supplied by Goodfellow Cambridge Ltd and Advent Materials, Oxford UK, respectively. The compositions of these steels are listed in Table 3-1. Foils were cut to ~ 0.7 mm wide ribbons parallel to the main rolling direction of the foil. Ribbons were then ultrasonically degreased with ethanol, immersed in nitric acid for a few seconds, rinsed with distilled water and dried with warm air. Cleaned and prepared ribbons were sandwiched between two glass cover slips 80-130 μm thick using Araldite® epoxy resin. The exposed edge of the embedded foil was polished to 4000 grit, rinsed with deionised water and dried. , These strip electrodes were attached to a 2.5×2.5 cm^2 square section PVC tube cell using Kapton® tape (RS Components) so that the cut edge faced upward as shown in Figure 3-1(a). The cell contained ~20 ml of electrolyte. An Ag/AgCl reference electrode and a platinum wire counter electrode were used for all measurements schematically shown in Figure 3-1(b). Electrolytes were 0.005, 0.01, 0.1 and 1 M NaCl prepared from laboratory-grade chemicals and deionised water supplied from an Elix water purification system. All tests were done at room temperature (21±3 ^{o}C) with the solution open to air. An Ivium (type CompactStat) potentiostat was used for all electrochemical tests.

Table 3-1- Composition of 304 and 316L stainless steel as determined by the supplier

Material	C(ppm)	S(ppm)	P(ppm)	Si(wt%)	Mn(wt%)	Ni(wt%)	Cr(wt%)	Mo(wt%)	Fe(wt%)
304	> 800	*	*	*	> 2	8-11	17-20	-	bal.
316L	> 300	> 300	450	> 1	> 2	10-14	16-18	2-3	bal.

* not known

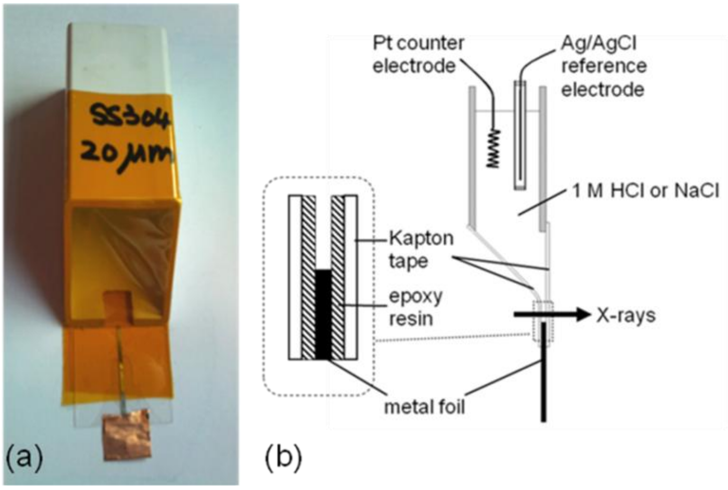

Figure 3-1- Electrochemical PVC tube Cell with Kapton® for X-Ray measurements b) Schematic diagram of the electrochemical cell for X-ray diffraction and radiography measurements

3.2 Synchrotron fast radiography experiments

Fast radiography experiments were performed at the TOMCAT beamline at the Swiss Light Source. High resolution high speed radiography was carried out at 15 keV. The TOMCAT detector used with a 20×objective and 1×1 binning covered a maximum field of view of 0.75 × 0.75 mm^2 providing the minimum pixel size of 0.37×0.37 μm^2. The TOMCAT detector was operated with a readout frequency of 36 Hz for the binned chip (the 20 × objectives with 2×2 binning provide a 700 nm pixel size). The corresponding readout time is 27 ms. Exposure times in the range of ~23-125 ms will give sampling rates in the range of 7-20 Hz. All radiographs were flat-field corrected before analysis.

3.3 Synchrotron tomography experiments

X-ray microtomography measurements were carried out at the tomography station of the Materials Science beamline (TOMCAT) at the Swiss Light Source (SLS) [144]. The experimental setup used was the capillary microcell developed by Suter for microtomography measurements on this beamline [136]. A photographic image and a schematic diagram of the cell and sample holder in front of beam are shown in Figure 3-2 and Figure 3-3. Electrochemical control was provided by a modified low-noise battery-operated potentiostat/galvanostat (Jaissle IMP= 83 PC T-BC) with an Ag/AgCl reference electrode and a platinum wire counter electrode mounted above the capillary

(Figure 3-3) [136]. The cell potentials quoted in this work are those applied relative to the Ag/AgCl reference electrode; the IR drop down the capillary is not taken into account. The solution was confined by a glass capillary 100 μm internal diameter sealed with a silicone seal at the interface with the pin tip as shown in the reconstructed x-ray image in Figure 3-4. Details of the capillary preparation method are given in reference [145]. The contact area of the electrolyte on the metal typically had a diameter of 100±5 μm (estimated from tomograms of the type shown in Figure 3-5). The solution used in all tomography experiments was 1 M NaCl.

Grades 304 and 303 stainless steel were used in measurements, which were aimed at developing a testing methodology. The 304 grade was used since its higher susceptibility to corrosion (relative to 316) made it easier to develop pits under electrochemical control on very small areas. The 303 type alloy was chosen to study the effect of its higher content of MnS inclusions (compared with 304) on pit propagation.

Tomographic measurements were made on the top surface of 0.5 mm machined pins of commercial 304 type stainless steel at 40 keV. Low resolution data were collected at 700 nm pixel size, 2×2 binning with 300-500 projections and 0.6 second counting time that took ~5 min per tomogram. Higher resolution data with 350 nm pixel size obtained at 1×1 binning with 1200 projections and 2 seconds exposure time giving data collection time of ~45 min per tomogram.

2D radiographs were reconstructed via a standard filtered back projection algorithm [146]. For image processing, ImageJ [147] software and Avizo$^{®}$ were used.

Good absorption contrast was obtained with the samples 1-2 cm from the detector. Some phase contrast images were obtained (to show the glass capillary and silicone seal on the metal) with the samples at ~9 cm from the detector.

Electrochemical experiments were conducted in galvanostatic mode or at constant cell potential. Imaging was carried out with the sample at the open-circuit potential in order to decrease the rate of corrosion propagation during the 5–45 min necessary to record the series of 2D radiographs required for each tomogram.

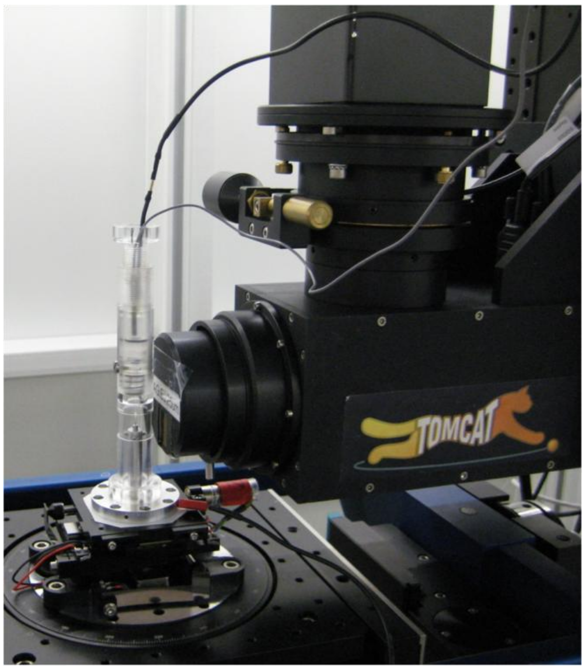

Figure 3-2- Electrochemical cell and sample holder in front of beam microscope

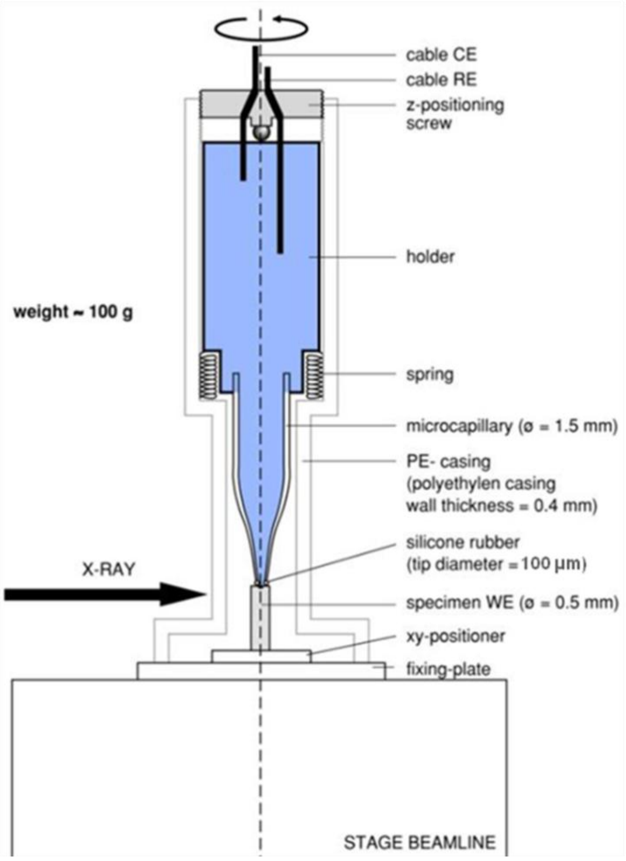

Figure 3-3- schematic diagram of capillary cell for tomography

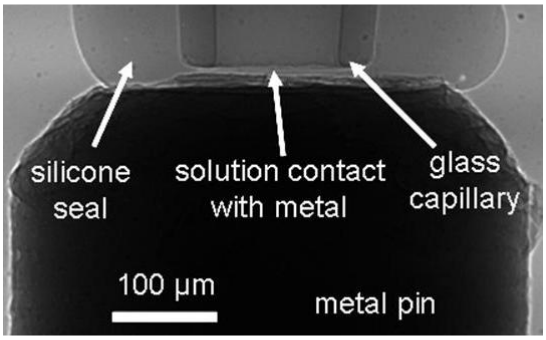

Figure 3-4- Glass Capillary in touch with tip of metal pin allowing electrochemical control at metal surface

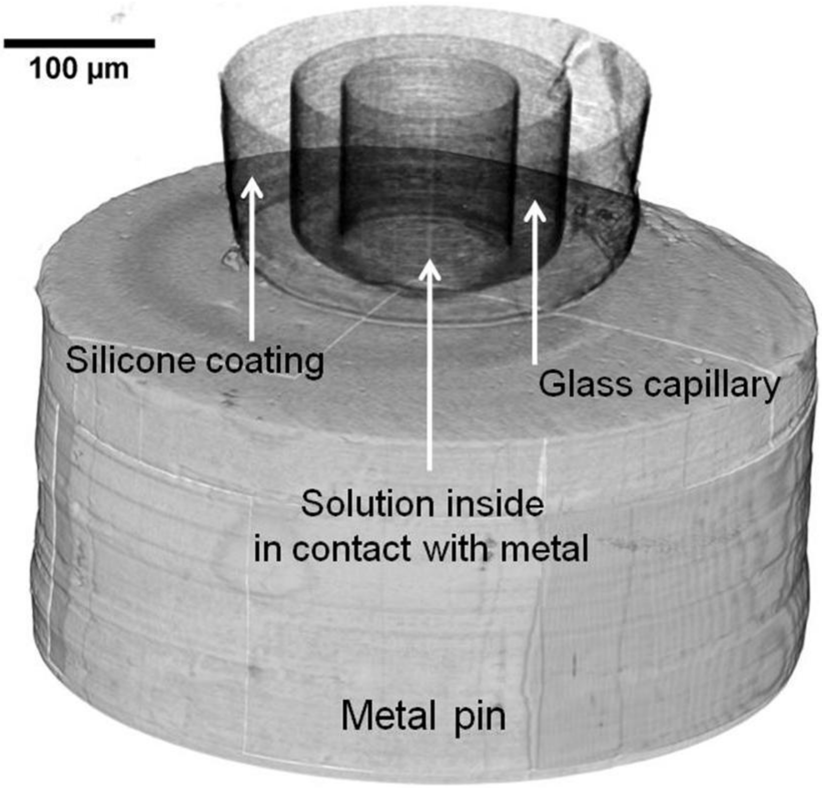

Figure 3-5- 3D reconstructed view of the electrochemical setup collected using phase contrast enhancement. The image shows the silicone-coated glass capillary on the top of metal pin.

4 Microtomography of pitting corrosion in stainless steel

4.1 Introduction

The aim of the present work is to demonstrate the feasibility of X-ray microtomography using a capillary microcell on the top of a stainless steel pin to show that the pit propagation morphology in 3D is similar to that observed in 2D experiments. With microelectrochemically-controlled microtomography, pioneered by Suter and co-workers [136], it is possible to monitor the growth of pits *in situ* and in real time, unlike conventional characterisation methods based on successive sectioning of *ex situ* samples. X-ray microtomography measurements were carried out at the tomography station of the Materials Science beamline (TOMCAT) at the Swiss Light Source (SLS) [144].

4.2 Results and discussion

4.2.1 Absorption contrast and phase contrast enhancement

Microtomography measurements were made using the microcell arrangement described in Chapter 3. With the detector placed as close as possible to the sample (~1 cm), imaging is achieved using absorption contrast. By placing the detector at some distance (~9 cm) from the sample, there is phase contrast enhancement of interfaces between phases of similar low densities. Figure 4-1 shows a 3D view of the tomography electrochemical setup. Although the images were obtained at 40 keV, phase contrast enhancement enables visualisation of the glass microcapillary with a silicone-modified tip that was used to drive pit growth electrochemically.

Phase contrast imaging also enhances detection of inclusions in the stainless steel pin. Figure 4-2 compares tomographs made in (a) absorption contrast and (b) phase contrast modes, in which inclusions in the type 303 stainless steel pin (dark vertical streaks marked by red arrows) and microcapillary are shown. This type of stainless steel contains a higher sulfur level, leading to an increased number of sulfide inclusions. These are elongated in the rolling direction of the steel, which is parallel to the axis of the pin.

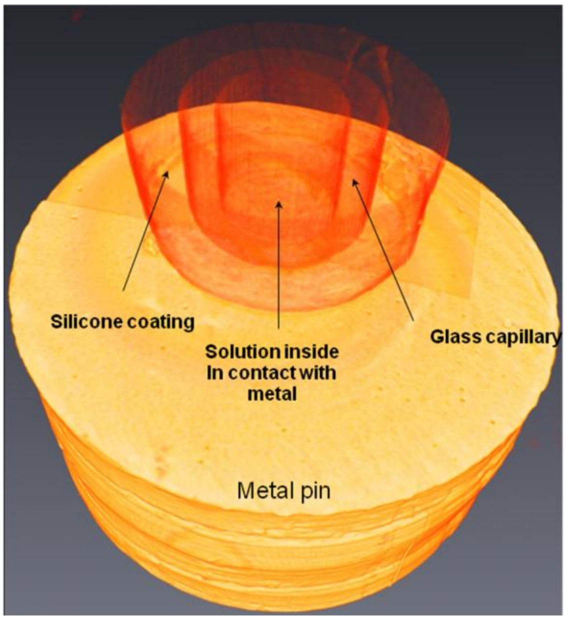

Figure 4-1- reconstructed 3D view of tomography electrochemical setup showing the tip of the silicone coated glass microcapillary on a 0.5 mm diameter 304 stainless steel pin (visualised with Avizo software).

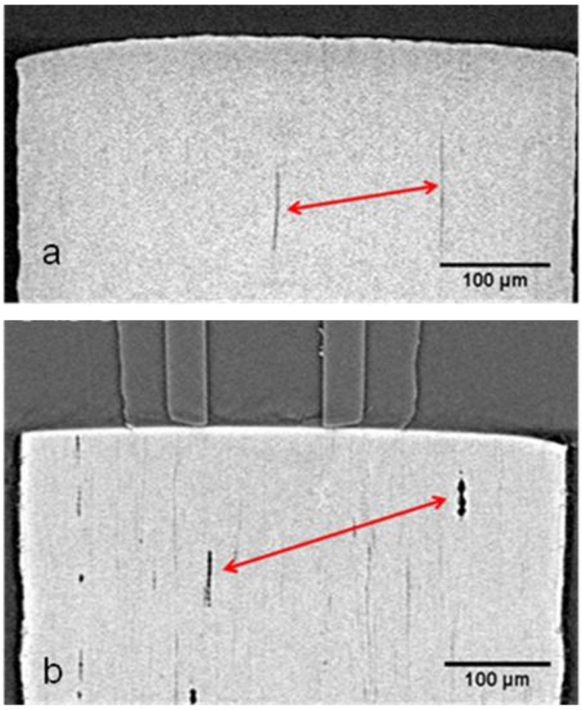

Figure 4-2- comparison of (a) absorption contrast and (b) phase contrast imaging showing the capillary and enhanced imaging of inclusions (indicated with red arrows) in a type 303 stainless steel pin. (TOMCAT beamline of the Swiss Light Source, 40 keV; the metal is bright)

4.2.2 Lacy covers on pits

As noted in the literature section, pits in stainless steel propagate by undermining the metal from within the cavity, perforating the surface from beneath and making holes into the bulk solution. This process repeats and gradually forms a porous cover over the pit.

Figure 4-3 shows a (a) 3D reconstructed image and (b) vertical section through the tomogram of a pit growing at the top of the 304 stainless steel pin. The pit was grown under galvanostatic control at 500 μA for 1 min in 1 M NaCl. The lacy cover can be observed. The cross section of the tomogram shows the pit morphology to be very similar in shape to that obtained by Ernst and Newman [106] and Laycock [140] for 2D pits measured at the edge of foils. An SEM image of the pin after 6 minutes of galvanostatic growth at 500 μA in 1 M NaCl is shown in (c), illustrating the partial collapse of the lacy cover during growth.

Figure 4-4 compares a vertical section of the pin following galvanostatic pit growth in a 304 SS pin by applying 500 μA for (a) 1 min and (b) 6 min after sitting at open circuit potential for 5 min during the preceding imaging measurement. It can be seen that pits are growing in a hemispherical shape. The smeared view at the bottom of the pit is an artefact resulting from pit growth during the measurement.

Figure 4-5 compares different pairs of vertical sections of the same pit after the two measurements shown in Figure 4-4. It can be seen that after 6 min, a number of corrosion fronts have propagated laterally and upwards and are approaching the metal surface where they are likely to perforate it, forming the lacy pit cover as illustrated in Figure 4-3 (a) and/or the eventual collapse of the cover as illustrated in Figure 4-3(c).

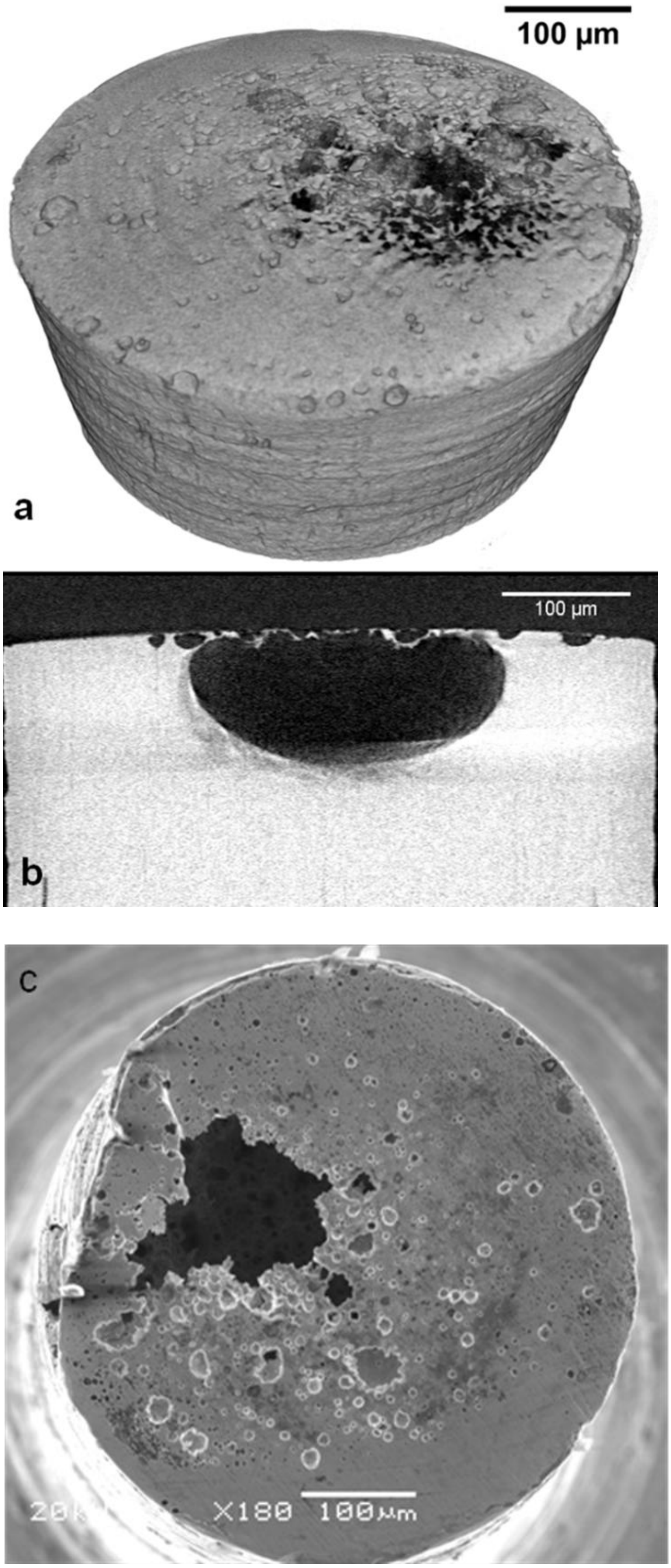

Figure 4-3- (a) 3D view and (b) cross section of reconstructed tomogram of a lacy top cover on a 304 type stainless steel pin galvanostatically grown at 500 µA for 1 min in 1 M NaCl. (TOMCAT beamline of the Swiss Light Source, 40 keV; metal is white)- (c) SEM image of the pin after 6 min growth at 500 µA in 1 M NaCl

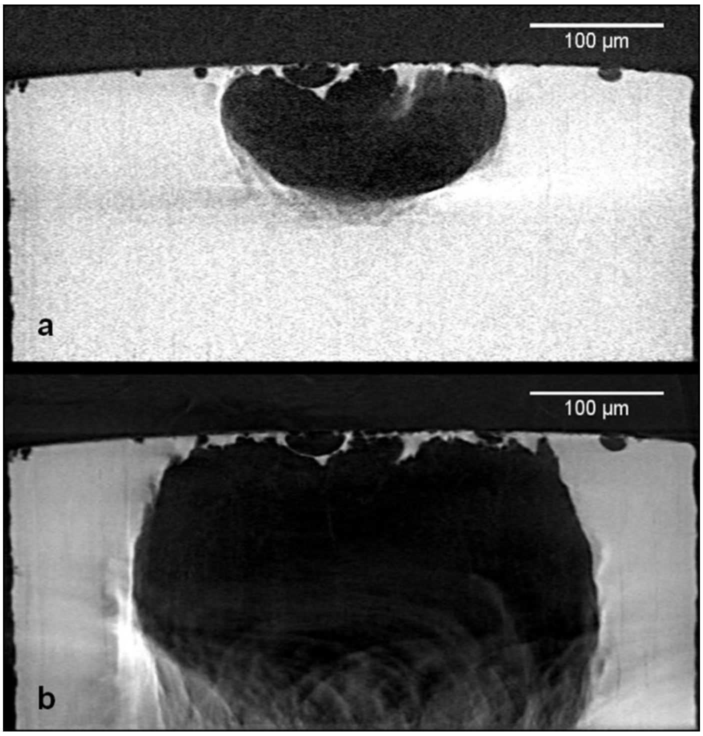

Figure 4-4- A vertical section of a 304 stainless steel pin through a pit grown galvanostatically in 1 M NaCl at 500 μA for (a) 1 min, and (b) 6 min (after exposure at OCP for ~5 min during the prior image collection). (TOMCAT beamline of the Swiss Light Source, 40 keV; metal is white and solution is black; measurements took (a) 5 and (b) 45 min to collect while the sample was at open circuit).

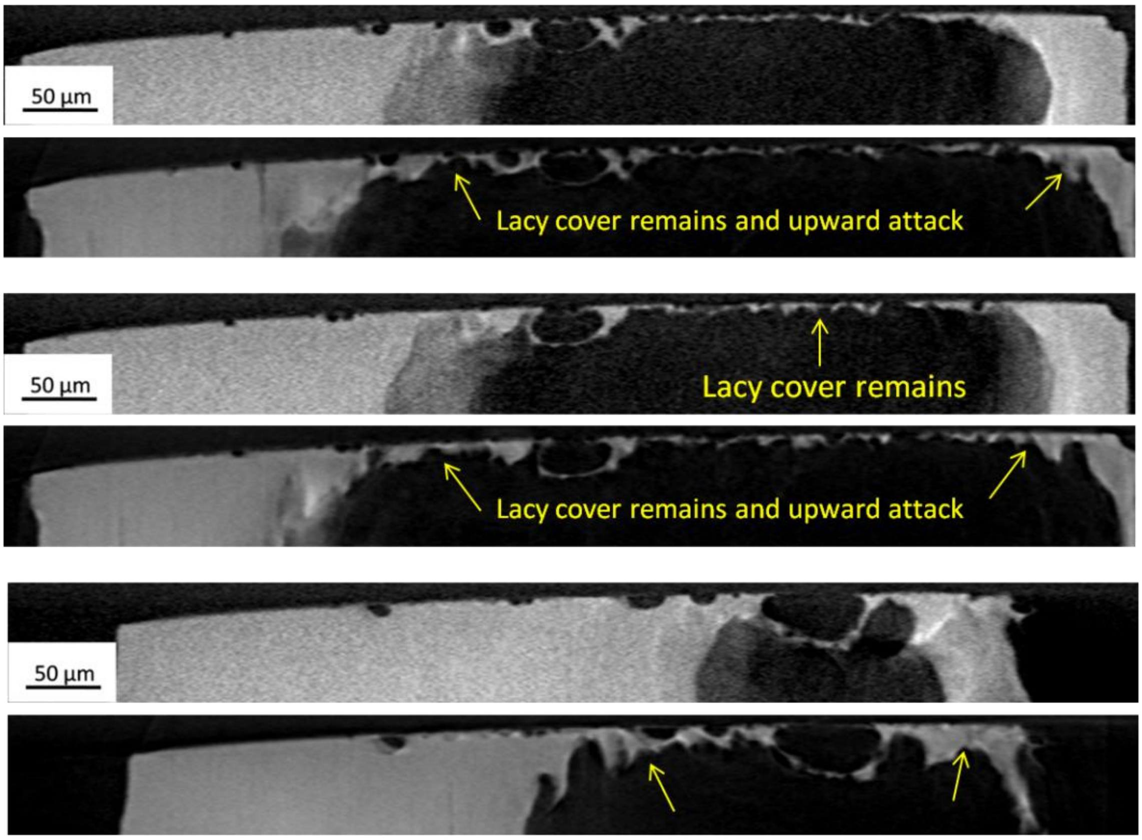

Figure 4-5- Several pairs of different vertical sections of the pit shown in Figure 4-4

Figure 4-6 shows pits that have formed in type 304 stainless steel under potentiostatic control. The same vertical slice is shown after (a) 2 min at 2.0 V followed by 5 min at 4.0 V and (b) 2 min at 5.0 V followed by 10 min at 8.0 V (vs. Ag/AgCl). It was commonly found that multiple pits grow under potentiostatic control, whereas under galvanostatic conditions, typically only one pit survives and continues to grow. This is consistent with the concept of "champion pits" introduced by the experimental observations of Suleiman and Newman [10] and computer simulations of Krouse *et al.* [138] and is in the line with 2D radiography observations in this work which will be discussed in the next chapters. It is notable that the pits often show protrusions at the bottom parallel to the rolling direction of the alloy. It is possible that these are related to manganese sulfide inclusions in stringers parallel to the rolling direction of the alloy.

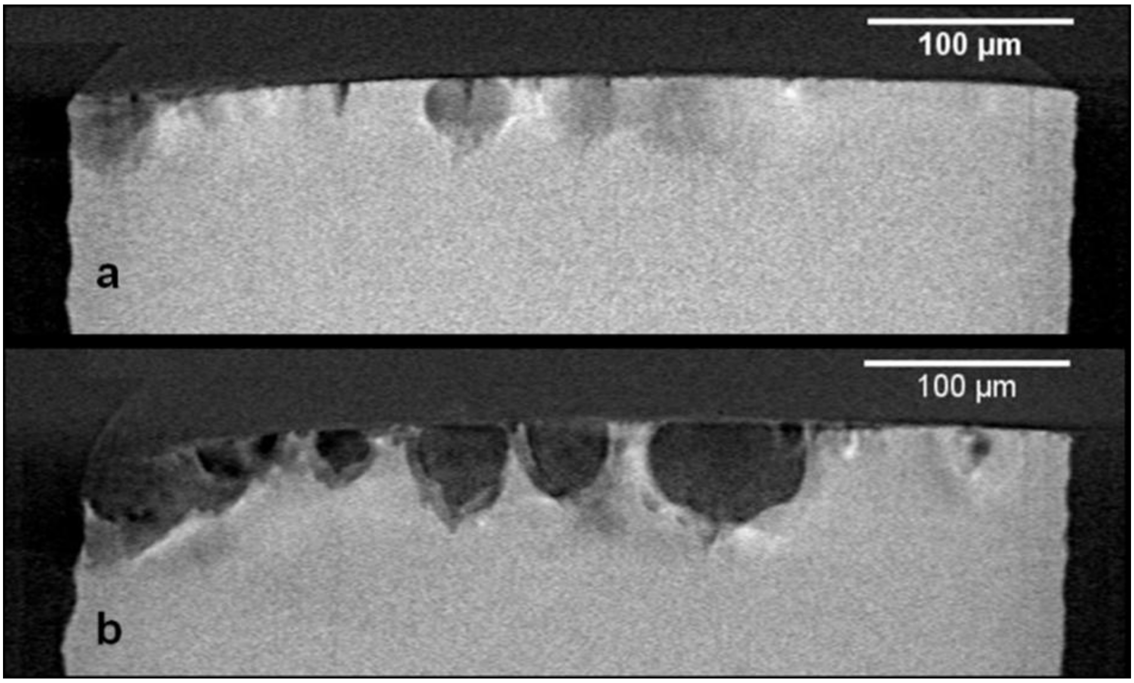

Figure 4-6- Vertical section of a 304 stainless steel pin following potentiostatic polarisation (vs. Ag/AgCl) in 1 M NaCl after (a) 2 min at 2 V followed by 5 min at 4.0 V and (b) 2 min at 5.0 followed by 10 min at 8.0 V. (TOMCAT beamline of the Swiss Light Source, 40 keV; metal is white, measurements took (a) ~5 and (b) ~17 min to collect while the sample was at open circuit)

Figure 4-7 shows SEM images of cross sections (a) parallel and (b) perpendicular to the axis of a 304 stainless steel pin used in the tomography measurements. The inclusions elongated in the rolling direction of the pin can be seen. A typical EDX analysis at the inclusion sites showing the presence of MnS is presented in Table 4-1.

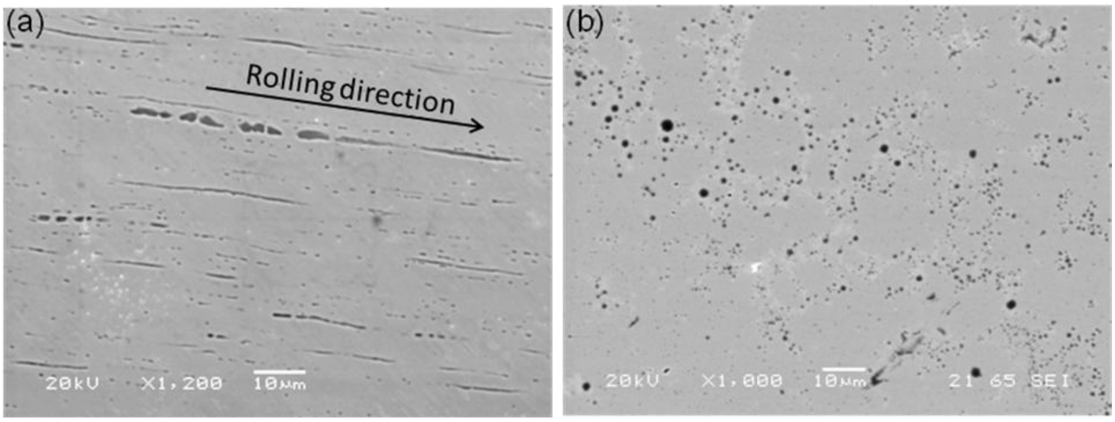

Figure 4-7- SEM image of the 304 pin used in tomography measurements (a) cross section parallel to the pin axis and rolling direction showing elongated inclusions (b) cross section perpendicular to the pin axis.

Table 4-1- a typical EDX analysis at the inclusion sites of the pin microstructure shown in Figure 4-7

Element	Weight%
Si K	0.17
S K	20.96
Cr K	13.26
Mn K	31.65
Fe K	30.58
Ni K	3.39
Totals	100.00

4.2.3 Role of inclusions in pit propagation

The effect elongated inclusions on the pit propagation shape is more pronounced for measurements made on type 303 stainless steel owing to the higher content of non-metallic inclusions in 303 compared with 304 [37]. Figure 4-8 shows a vertical slice of the pin when 100 μA was applied for 1 min. Then, the applied current was changed to 3 μA for 90 min to propagate narrow and deep pits along inclusions as shown in Figure 4-8 (b). It is noticeable that pits grow parallel to the pin axis (which is parallel to the rolling direction of the alloy) at a higher rate than they grow laterally.

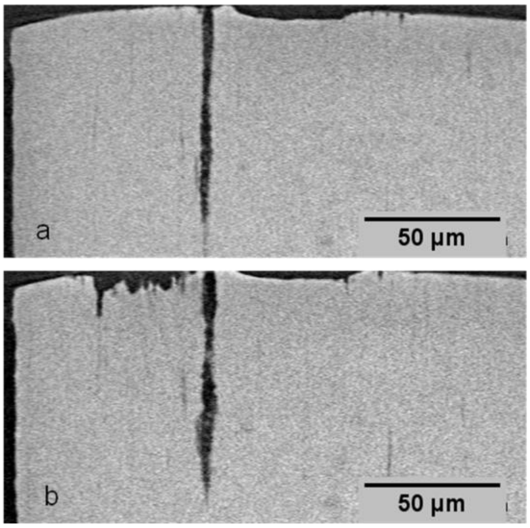

Figure 4-8- Vertical slices through the tomographic reconstruction of a pin of 303 stainless steel polarised in 1 M NaCl (a) after applying 100µA for 1 min (b) after applying 3 µA for 90 min.

These measurements demonstrate the feasibility of measuring the 3D evolution of pit shape *in situ* in real time in a capillary microcell under electrochemical control. The morphology of pit growth is similar to that observed [109, 143] and modelled [7, 106, 107, 140] for the growth of 2D pits, with the lateral and upwards growth of corrosion fronts that perforate the surface, leading to the classical "lacy top pits".

4.3 Conclusion

1. Real time *in situ* 3D pit growth at the tip of stainless steel pins under electrochemical control in a capillary microcell was observed by X-ray synchrotron microtomography with a pixel size of 350 nm.
2. The morphology of 3D pit growth involves upwards growth of lateral lobes leading to perforation of the metal surface forming a lacy cover. The observations confirm that experimental observations of 2D pit growth at the edge of metal foils and 2D models of pit growth are representative of 3D pit growth.
3. Propagation of corrosion pits in stainless steel is influenced by the presence of sulfide inclusions.

5 Propagation of 2D pits in stainless steel

Synchrotron radiography was used to study the propagation of 2D pits growing at the edge of stainless steel foils following the approach of Ernst and Newman [106, 107], who studied 2D pit growth with optical microscopy. Pits were grown at the edge of stainless steel foils under electrochemical control of either the applied potential or current using the electrochemical cell setup described in Section 3.1. Experiments were carried out for fairly short periods of several minutes in order to extract robust growth parameters to input into a predictive model which can simulate pit propagation. Under applied potential control and at high chloride concentrations, normally multiple pits quickly initiated after applying the potential and grew simultaneously together. In these cases, experiments were short and stopped after pits merged together. However, under applied current control or lower chloride concentrations, normally one or two pits initiated or continued to grow. It is also notable that in lower chloride concentrations, the *induction time* for pits to initiate was longer [18]. Therefore, these experiments were performed for longer periods.

The aim of the investigation in this chapter is to determine the effect of solution composition and electrochemical growth conditions on pit morphology.

5.1 Pit phenomenology

Figure 5-1 shows a typical radiograph of a growing pit. The grey body in the image is the stainless steel foil and the semi-circular shape within the foil is a growing pit with an actively-growing internal surface. The external metal surface that is in contact with bulk solution does not corrode and is protected by a passive oxide film.

Figure 5-2 illustrates the definitions used for the pit “depth”, “width” and “mouth”. The maximum distance from pit bottom up to foil interface with solution is defined as the pit “depth”, the maximum lateral extent of pit is defined as pit “width”, and the horizontal distance between the two points where pit boundary connects to the foil top surface is considered as pit “mouth” (or the distance between the junction points of pit internal perimeter with foil interface with solution). The pit boundary is detected by a customised filter plug-in implemented into the ImageJ software, which is described in Section 6.2.2.

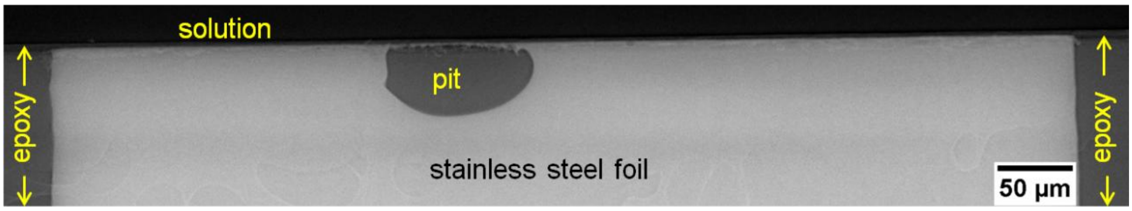

Figure 5-1- Typical radiograph of a stainless steel foil (grey region) embedded in epoxy resin and in contact with solution from the top. Pitting corrosion was initiated and grown by applying 600 mV vs. Ag/AgCl in 0.01 M NaCl.

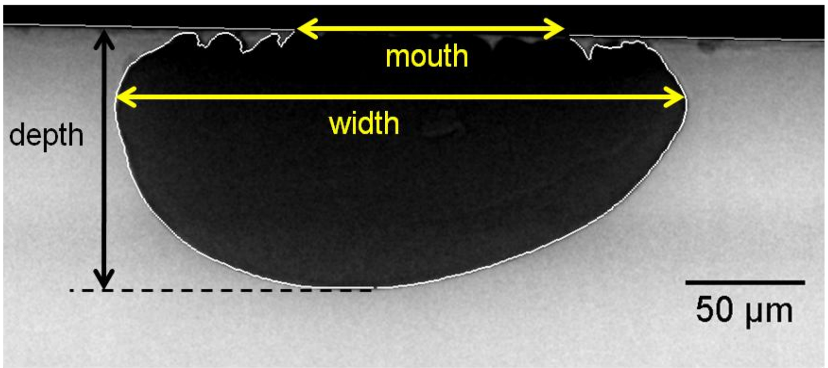

Figure 5-2- Pit grown in 304 stainless steel foil at 650 mV vs. Ag/AgCl in 0.005 M NaCl after 470 s. The arrows indicate the definitions used for the pit "mouth", "width" and "depth".

5.2 Pit growth morphology under potentiostatic conditions

Figure 5-3 shows the temporal development of a single pit growing in stainless steel foil in 0.005 M NaCl at 650 mV vs. Ag/AgCl (a video of this process is shown in Appendix A.5.1). At 75 s after the potential was increased to 650 mV, the pit is semi-circular in shape, and appears to be growing under a thin cover of un-dissolved metal. The current-time curve shown below the radiographs indicates continuous growth with an increasing current (owing to the increase in pit surface area). However, at 75 s, there is a sudden drop in current that is associated with repassivation of most of the pit. The current then starts to increase again. The radiograph at 81 s shows that this current increase is associated with growth of a new actively dissolving region, a "pit within a pit", which continues to undermine metal and propagate sideways, as can be seen from the radiograph at 90 s.

From 100 s onwards, the current signal is noisy as the pit continues to partially repassivate and grow by a series of lateral "lobes", which grow sideways and upwards, eventually perforating the metal surface, giving a "lacy" cover to the pit of metal foil with perforations. This continues until the end of the experiment at 600 s. The final shape of the pit is shown in Figure 5-4 together with an optical image of the perforated lacy cover, which also shows the location of lacquer on the top surface to prevent crevice corrosion at the edge of the foil, and an SEM image of the top surface following removal of the epoxy. Pit covers of this type have previously been observed for pits in stainless steels [50, 53, 61, 70-72, 148].

It is evident that, under these testing conditions, pit growth is zero close to the pit mouth (regions that have repassivated) and the pit grows laterally at a high rate in the lobes, and relatively slowly at the pit bottom. It is also notable that the pit surface is smooth. This is generally observed for pits growing under potentiostatic conditions.

One of characteristic features of potentiostatic control is simultaneous initiation and propagation of multiple pits, since there is no limit to the current that can be supplied to the system. Figure 5-5 shows multiple adjacent pits growing together at 650 mV vs. Ag/AgCl in 0.1 M NaCl. The pits grow with a similar size and shape until they merge.

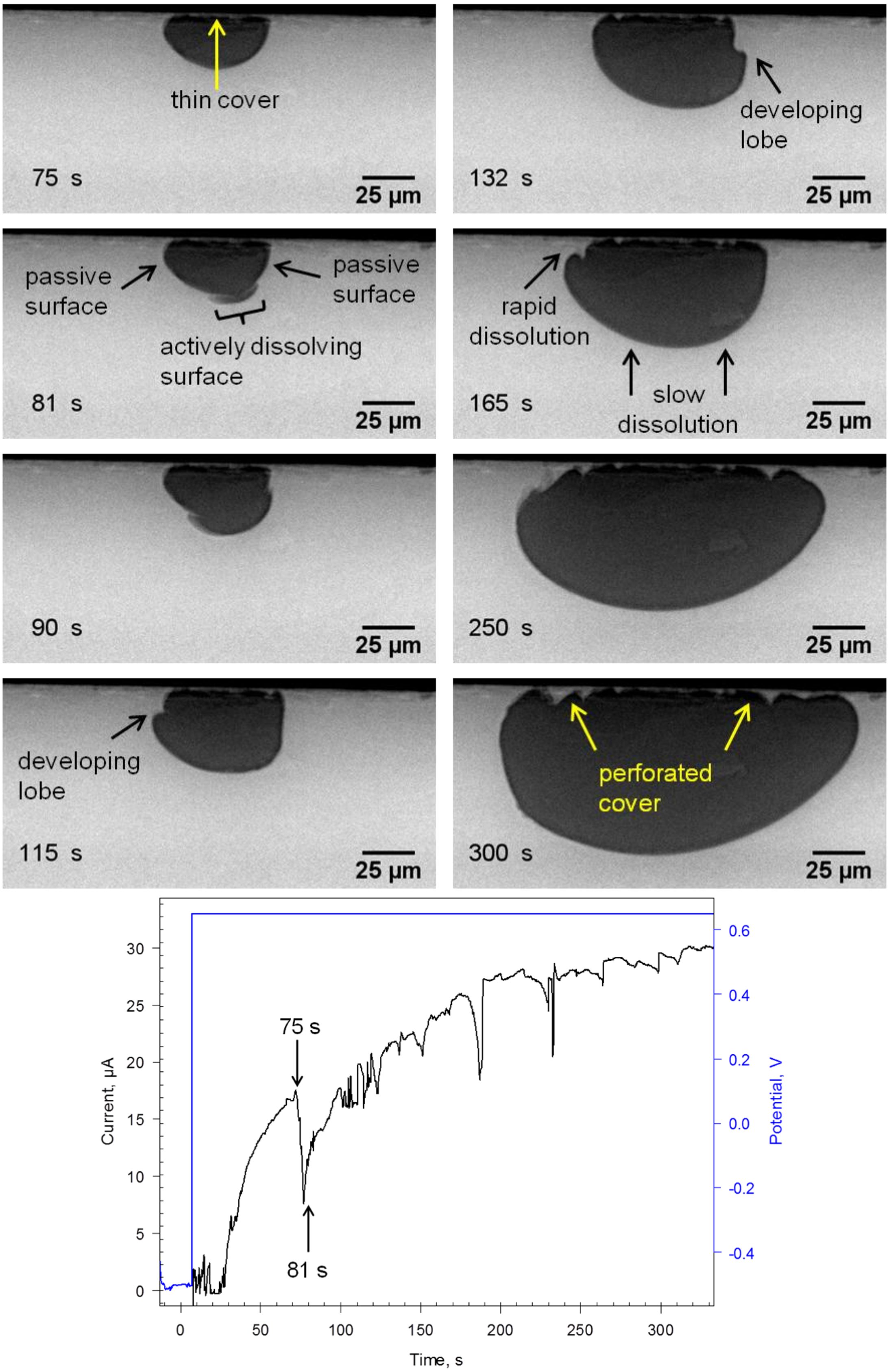

Figure 5-3- A series of radiographs of pit propagation in a 20 µm thick 304 stainless steel foil in 0.005 M NaCl at 650 mV vs. Ag/AgCl measured using X-ray radiography at the TOMCAT beamline at SLS with an X-ray energy of 15 keV; the time from pit initiation is shown, and regions where rapid dissolution is taking place are indicated. The current and potential plot shows the electrochemical behaviour of the pit during its growth.

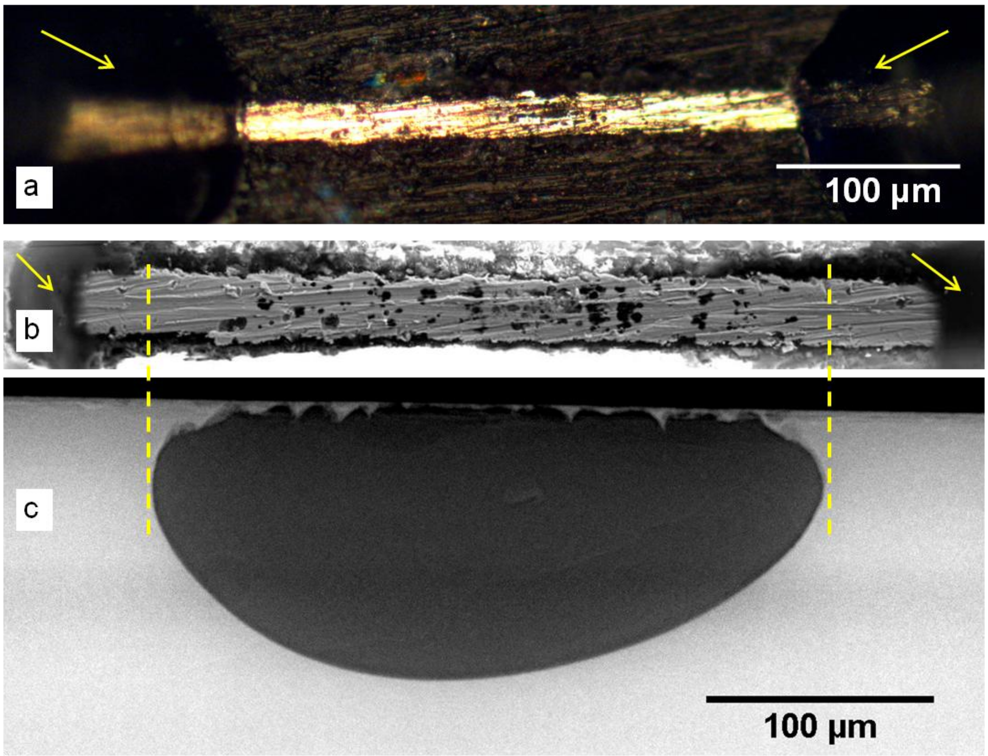

Figure 5-4- The pit shown in Figure 1-3 following growth for 600 s at 650 mV vs. Ag/AgCl in 0.005 M NaCl; (a) optical micrography of top surface of the foil, (b) SEM image of the top of the foil showing the perforated cover, (c) radiograph of the final shape of pit. The scale bar for (b) and (c) is identical. and the yellow dashed lines correlate the pit extent in (b) and (c). The dark regions at both edges of foil in (a) and (b), marked with arrows, are the lacquer/epoxy coating placed to protect edges of foil from pit/crevice intiation.

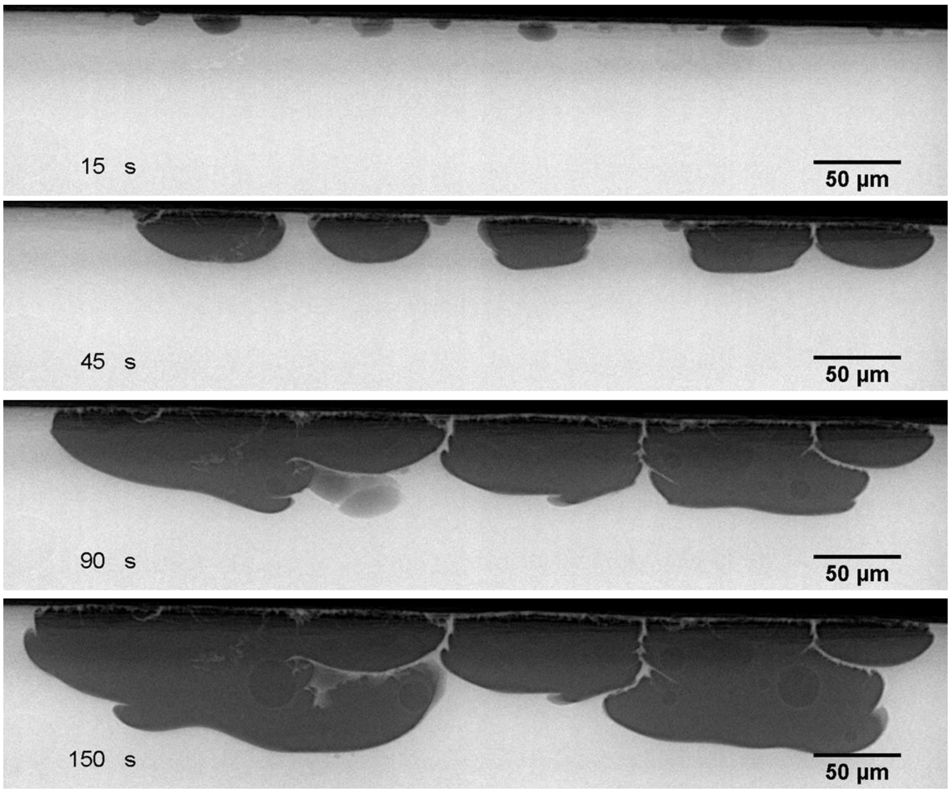

Figure 5-5- A series of radiographs of several 2D pits growing under potentiostatic control at the edge of a 20 µm foil of 304 stainless steel in 0.1 M NaCl at +650 mV vs. Ag/AgCl. The time at which each radiograph was taken is shown (the potential was applied at t=0).

5.3 Pit growth under galvanostatic conditions

It was difficult to initiate pits reproducibly under galvanostatic conditions since this often led to crevice corrosion at the edge of the foil, so galvanostatic measurements were generally preceded by a brief period under potentiostatic control to initiate the pits. Figure 5-6 shows the electrochemical behaviour and typical growth of a pit under galvanostatic conditions at a current of 10 μA following pit initiation under potentiostatic control at +650 mV for a period of 10 s. It is evident that a number of pits were initiated in the potentiostatic regime, but once the sample was switched to galvanostatic control, the smaller pits repassivated and only one pit survived and continued to grow. It was always the case in the galvanostatic measurements carried out in this way that only one or two pits survived after switching from potential control to current control. Pits initiated simultaneously in potential control mode normally grew with very similar size. Following switching to galvanostatic mode, if two pits survived, they usually grew with the same size (this will be shown in more detail below). Figure 5-7 illustrates a pairs of images for a series of samples showing pit survival following switching from potential control to current control in 0.1 M NaCl. In the first radiograph of each pair, pits are shown at the end of the period of potentiostatic growth and the later second image illustrates pit growth under the galvanostatic regime. For example in Figure 5-7(a-1), three pits have initiated and continued to grow for 30 s at 650 mV. However, the pit in the middle stops growing once the sample was switched to current control at 50 μA (a-2).

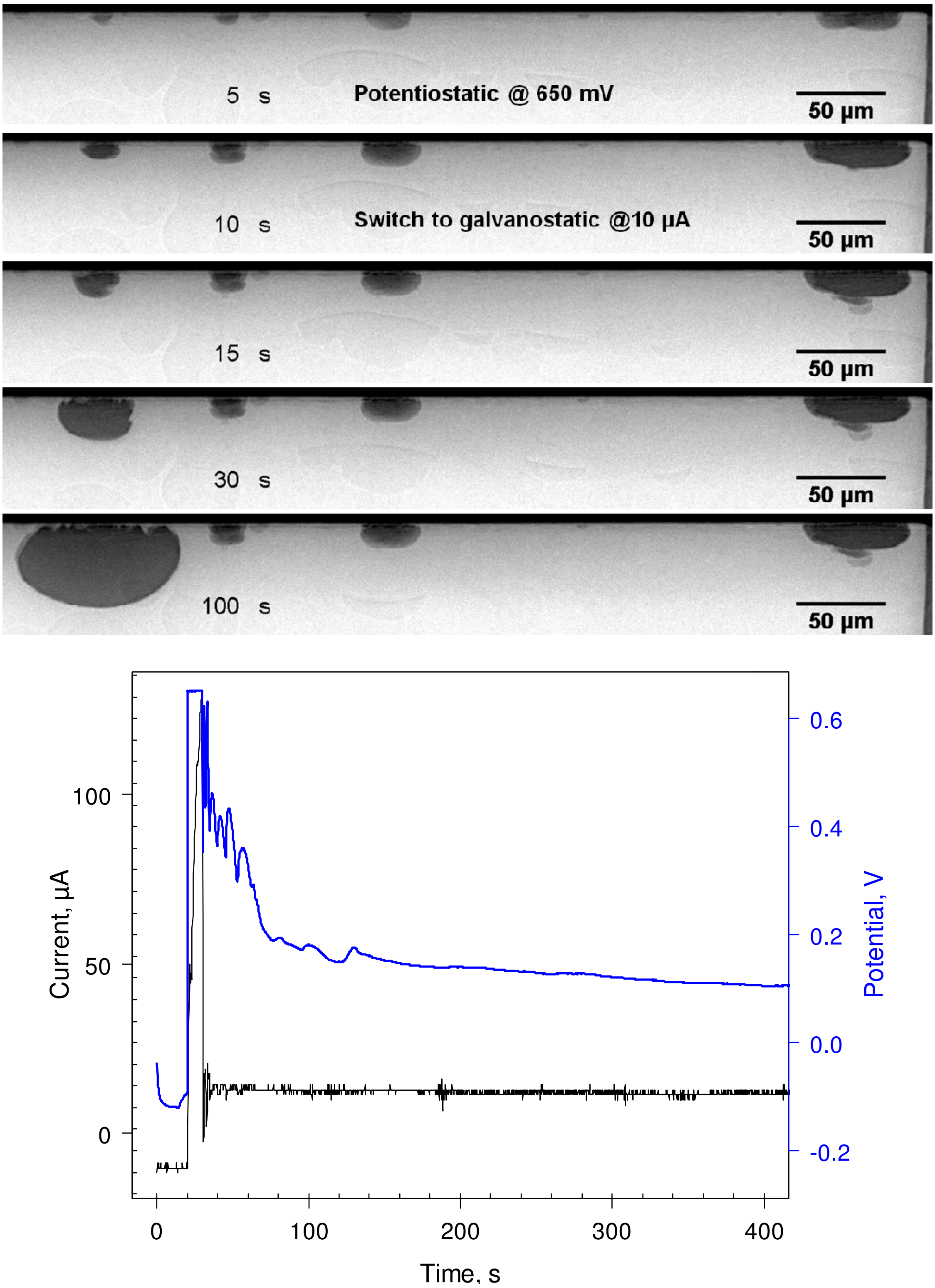

Figure 5-6- A series of radiographs of a 2D pit growing at the edge of 20 µm foil of 304 stainless steel that was initiated in 0.1 M NaCl at +650 mV for 10 s then propagated galvanostatically at 10 µA. The time at which each radiograph is taken is shown (+650 mV was applied at t=20). The current and potential plot shows the electrochemical behaviour of the pit during its growth.

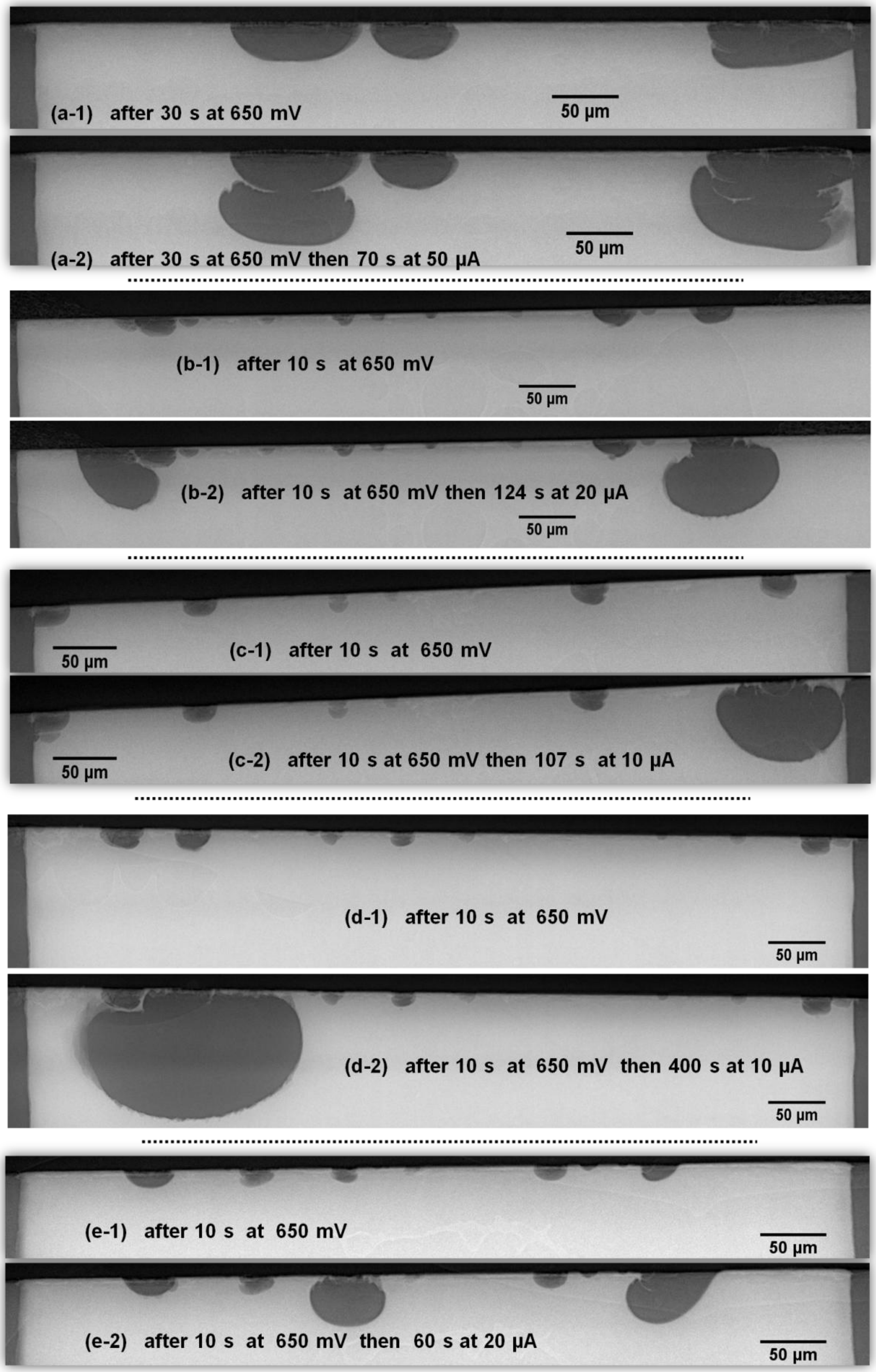

Figure 5-7- Selective pit growth after switching to galvanostatic control following initiation under potentiostatic control at 650 mV in 0.1 M NaCl. Two radiographs are shown for each sample a-e. The first radiograph of each pair is at the end of potential-controlled growth and the second one shows further growth after a period of current control. The applied potential, current and time are shown in each image.

A difference in morphology was frequently observed between two pits grown under applied potential and current control. Figure 5-8 compares the morphology of two pits grown potentiostatically and galvanostatically after a charge of ~2.6 mC have been passed. Figure 5-8(a) shows a pit grown potentiostatically at 650 mV in 0.01 M NaCl for 220 s; it is shallow and smooth with a clearly defined and polished perimeter. In contrast, the galvanostatically-grown pit at 10 μA for 300 s (after 10 s initiation at 650 mV) shown in Figure 5-8(b) is deeper with a rougher surface and an etched perimeter.

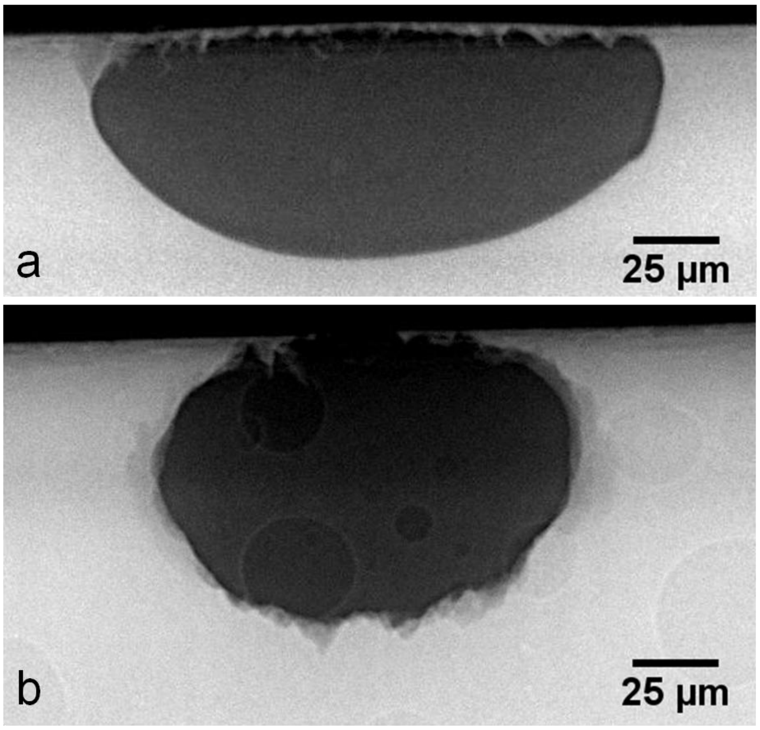

Figure 5-8- Radiographs of 2D pits grown at the edge of 20 μm foil of 304 stainless steel in 0.01 M NaCl until a charge of ~2.6 mC had been passed; (a) potentiostatic growth at 600 mV for 220 s, (b) galvanostatic growth at 10 μA for 300 s after 10 s initiation at 650 mV vs. Ag/AgCl.

5.4 Pit shape

5.4.1 Effect of cover on pit shape

As noted above, in order to prevent pit or crevice intiation at the foil edges, these were covered with lacquer or epoxy. This was also useful to increase the probability of growing a single pit in the foil. Figure 5-9 illustrate a selection of typical images of the lacquer covering the foil edges in different independent measurements (the lacquer is more visible in Figure 5-9(a) and (b)). As can be seen in Figure 5-3 and Figure 5-5, pits gradually develop their shape from almost semi-circular at the start to elongated dish-shape, which is believed to be due to successive perforation of the cover[62, 106]. Because of the undercutting process, the pit mouth is narrower than its width. However, in Figure 5-9(b), (c) and (d), asymmetric pits can be observed. On one side, the typical undercutting behaviour is observed and the maximum width is not at the pit mouth. However, on the other side, the pit width is greatest at the pit mouth. In all these cases, the pits are growing underneath a covering of lacquer. This is seen most clearly in (b) where a surface spreading pit is evident under a covering of lacquer. Although the lacquer or epoxy is not visible in (c) and (d), similar shapes of growth underneath a coating are seen on the right side.

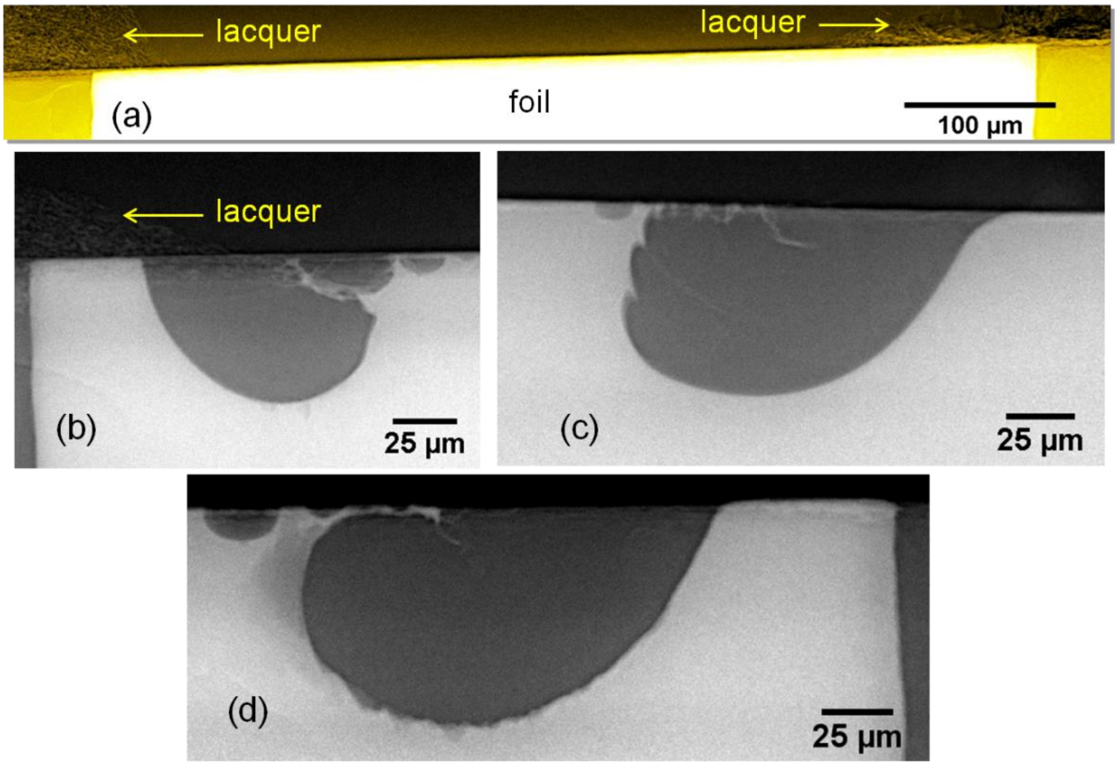

Figure 5-9- (a) and (b) lacquer covering the foil top interface with epoxy to prevent pit/crevice intiation at the edges. Semi-circular shape growth on the side which was covered with lacquer and undercutting events and perforated cover at the other side of pits, grown in 0.1 M NaCl at (b) 650 mV for 10 s then 183 s at 20 µA, (c) 650 mV for 10 s, 550, 450 and 350 mV each for 60 s, and (d) 650 mV for 10 s following 20 µA for 300 s.

5.4.2 Effect of chloride concentration and applied potential during potentiostatic growth

In an intermediate level of chloride concentration (0.1 M) under potentiostatic control, pits normally grow in a dish-shaped or semi-elliptical form (Figure 5-8a shows a typical pit grown in 0.01 M NaCl, which is similar in shape to those grown at 0.1 M). However, in more dilute solutions, pits are narrower and deeper. Figure 5-10 compares pits grown for *ca*. 60 s after initiation in (a) 0.005 and (b) 0.1 M NaCl.

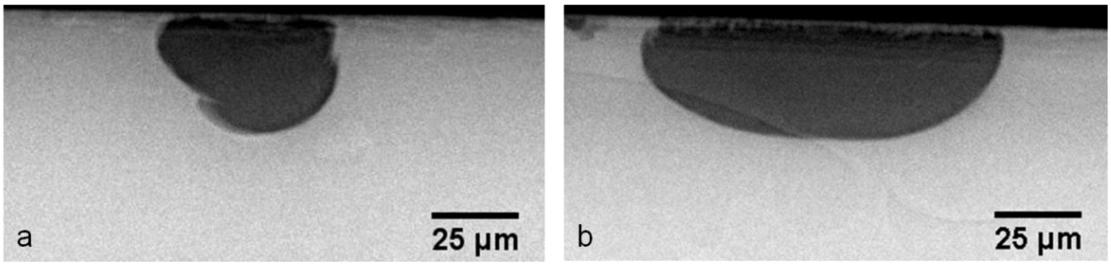

Figure 5-10- pits initiated and grown for ca. 60 s at 650 mV vs. Ag/AgCl reference electrode in (a) 0.005 M and (b) 0.1 M NaCl.

The pit depth and width as a function of time are shown in Figure 5-11 for pits grown in NaCl solutions of different concentration. Due to different induction time of pits (the period that took for pits to initiate after stepping the potential from an open circuit potential), the data have been time-corrected by subtracting the induction time of each pit. Measurements were made on three samples for 0.1 M, two for 0.005 M and one for 0.01 M, all at 650 mV. In all cases shown here, two or more pits initiated and grew (except for the single pit in 0.005 M NaCl) and depth and width data for the longest lasting pit (before merging into others) is shown in the figure. The number of growing pits in each measurement is indicated in the figure. The depth as a function of time shows considerable variation and there is no clear dependence on chloride concentration. However, since the pits compared are (mostly) not single pits, the dissolution process might be affected by adjacent growing pits [139, 149, 150].

In contrast to the pit depth, the pit width shows a trend in which it is greater for higher solution concentrations (Figure 5-11), with the exception of the short-lived pit grown in 0.005 M NaCl. The *(pit depth)*^{2} appears to increase linearly with time (Figure 5-12), while the width follows an approximately linear relation with time. The approximate parabolic behaviour of the pit depth with time is also confirmed by plotting *log(pit depth)* against *log(time)* as shown in Figure 5-13 in which the slopes (*n*) are estimated between 0.52 to 0.65.

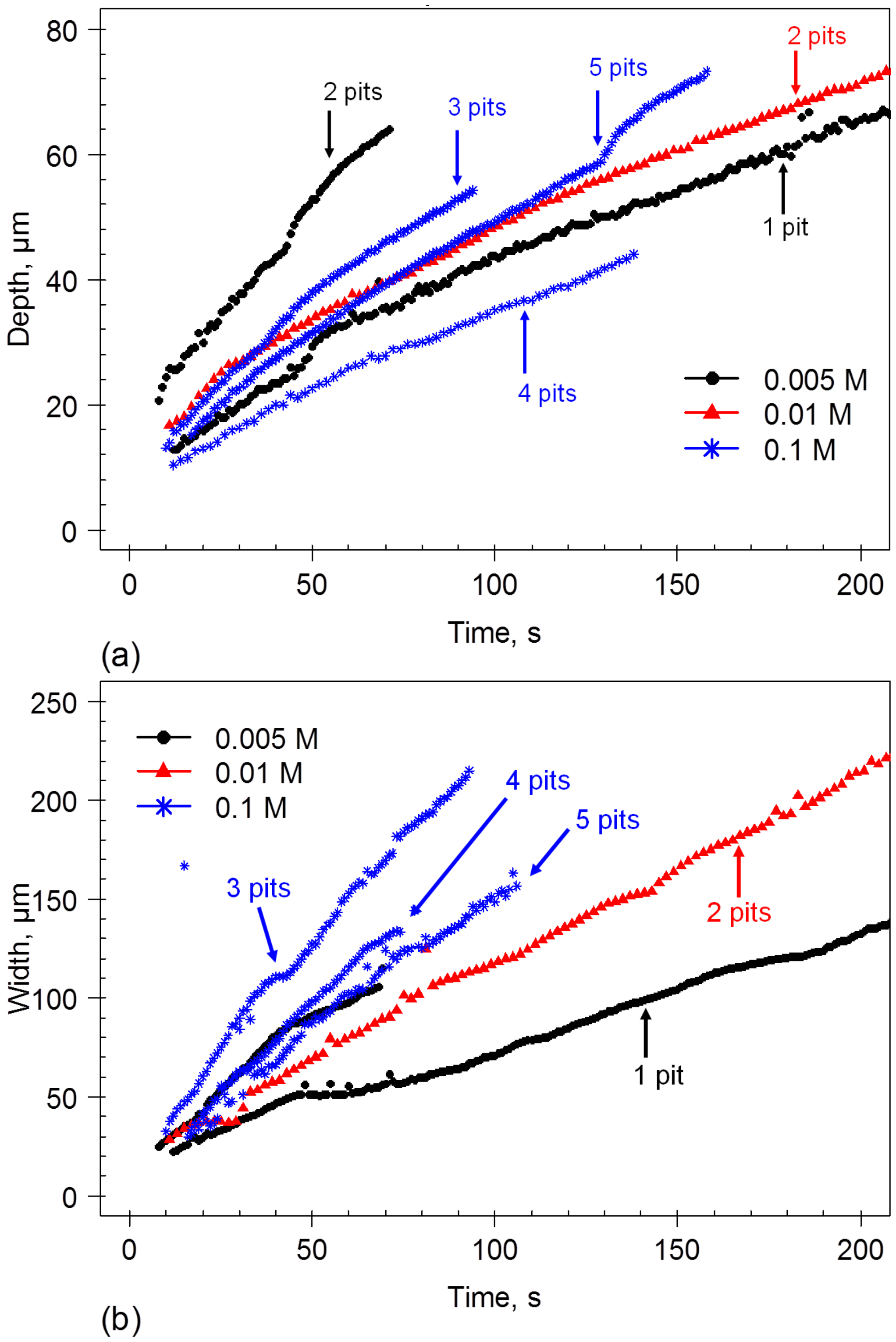

Figure 5-11- Pit depth (a) and width (b) as a function of time in NaCl solutions of the concentrations indicated. All pits were grown at 650 mV vs. Ag/AgCl. Each curve is associated with the longest lasting pit in an independent measurement from which the number of growing pits in the sample is indicated. The data have been time-corrected by subtracting the induction time of each pit. The values were extracted automatically from pit boundary coordinate data of the type shown in Figure 6-3 using the routine described in Section 6.2.2 and Appendix A.6.1. Scatter in data is associated with the errors in detecting the pit boundary by the customised filter in ImageJ.

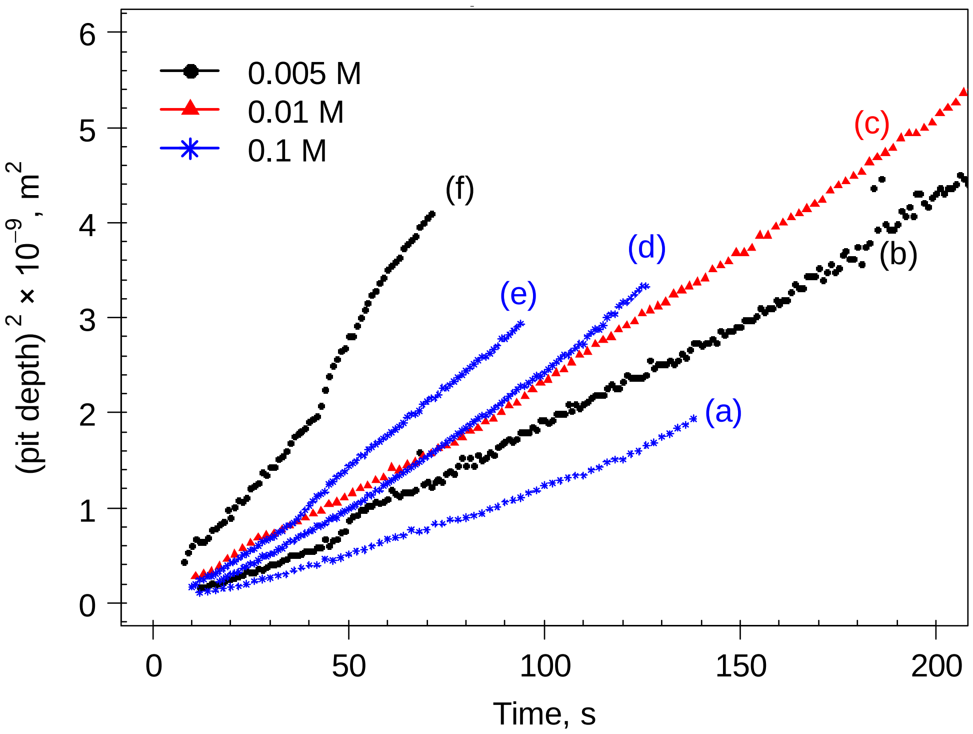

Figure 5-12- (Pit depth)^2 against time for the pits (labelled (a)-(f)) shown in Figure 5-11

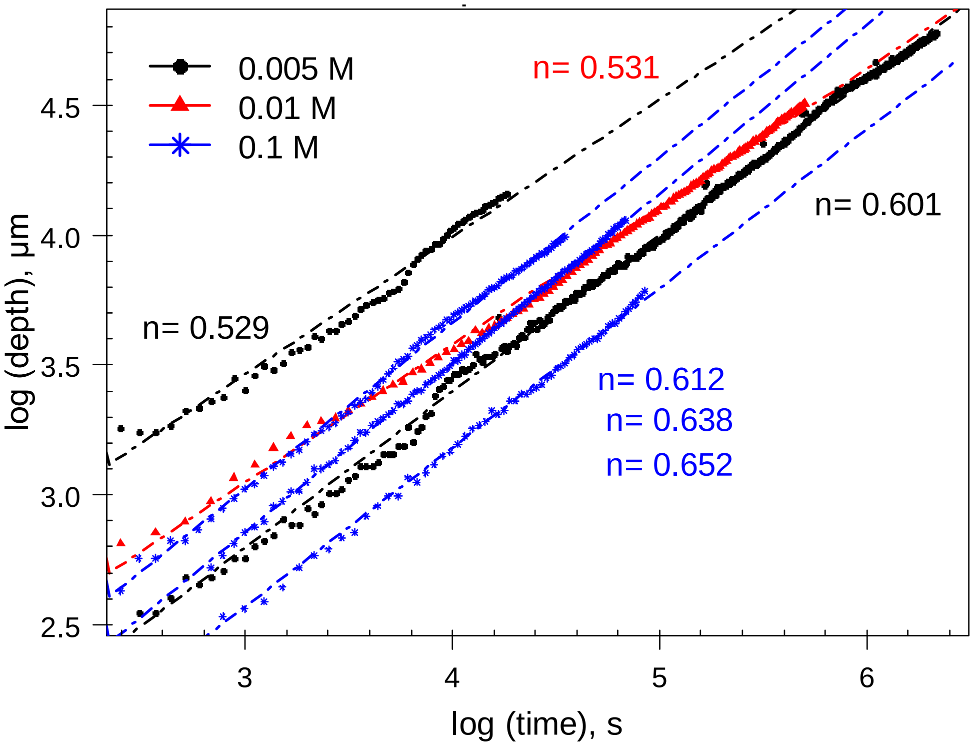

Figure 5-13- *log(pit depth)* against *log(time)* for the pits shown in Figure 5-11. The slope (n) of each line is indicated.

The ratio of pit width to pit depth in different chloride concentrations can be inferred from the slope of the plot shown in Figure 5-14. The slope of pit width vs. depth varies as the pit grows; however, it tends to follow a certain value during growth. The slope of width vs. depth plot increased with chloride concentration from *ca.* 2 in 0.005 M NaCl to *ca.* 4 in 0.1 M NaCl.

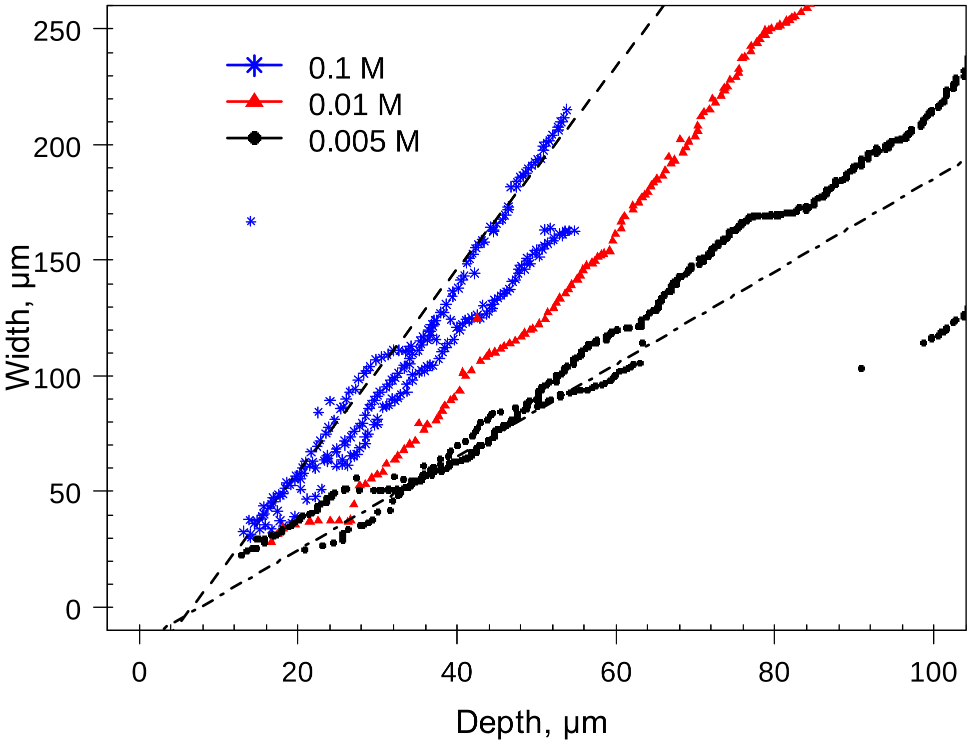

Figure 5-14- Pit width against pit depth of pits shown in Figure 5-11 grown at 650 mV vs. Ag/AgCl in NaCl solutions with the concentrations indicated. The values were extracted automatically from pit boundary coordinates data of the type shown in Figure 6-3 using the routine described in Section 6.2.2 and Appendix A.6.1. The scatter in data is associated with the errors in detecting pit boundary by the customised filter in ImageJ. The dashed lines are fits to pits with the highest and lowest slopes for reference.

Figure 5-15 shows pit depth and width in 0.01 M NaCl at 650, 600 and 550 mV vs. Ag/AgCl. For 0.01 M (one measurement was made at each potential). Again, an approximately linear relationship between the pit width with time is seen while the pit depth follows approximately parabolic behaviour with time as shown in Figure 5-16. It can be seen that the pit depth at a given time increases with applied potential. The pit width increases at a similar rate at 550 mV and 600 mV, but the rate is higher for the pit grown at 650 mV. However, since only one measurement was made at each potential, and given the scatter in the data at a fixed potential (Figure 5-11), the trends may not be statistically significant.

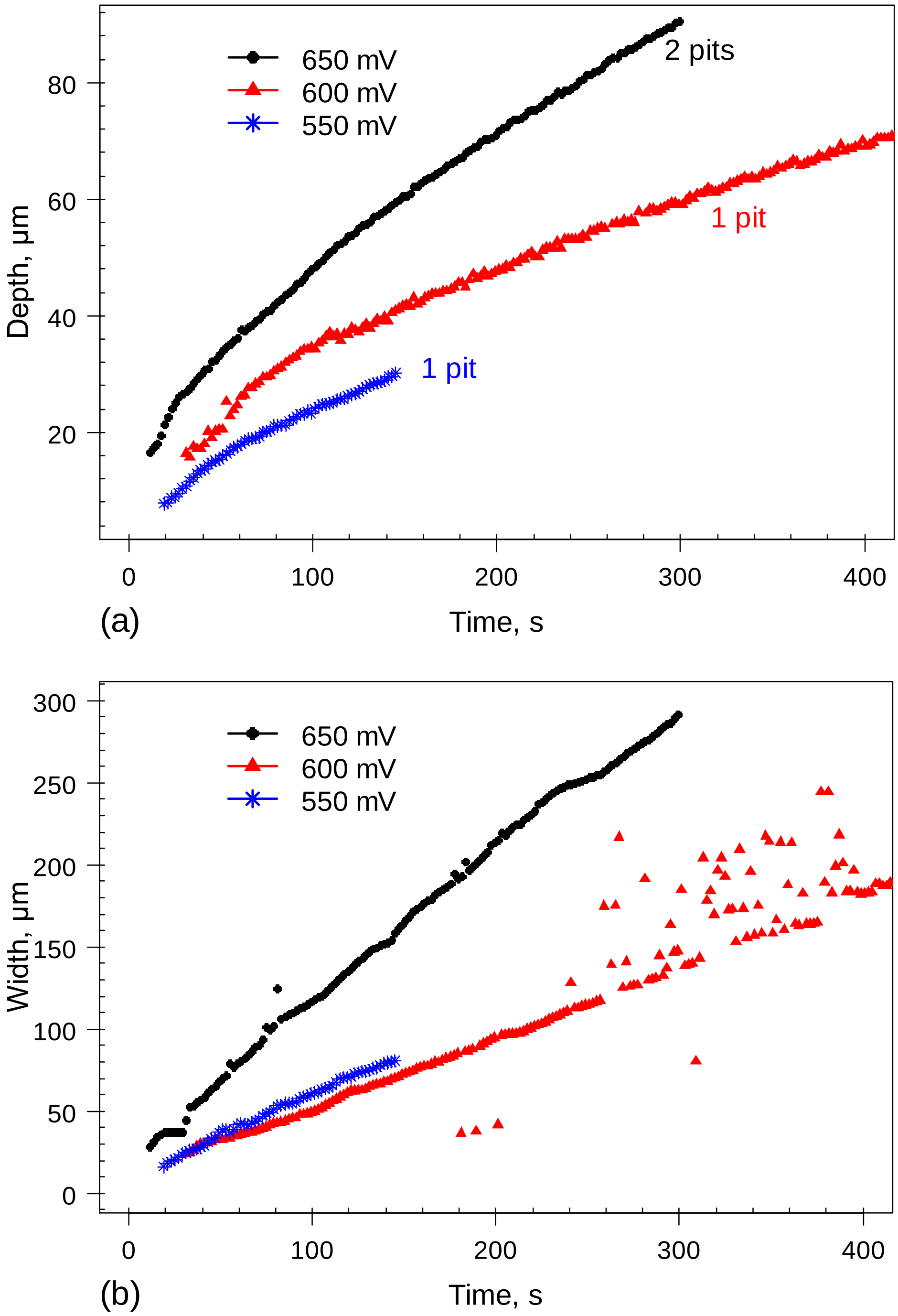

Figure 5-15- Pit depth (a) and width (b) as a function of time for pits grown in 304 stainless steel foil at different applied potentials (vs. Ag/AgCl) in 0.01 M NaCl. Each curve shows the data from the longest lasting pit in an independent measurement for which the number of growing pits is indicated. The data have been time-corrected by subtracting the induction time of each pit. The values were extracted automatically from pit boundary coordinates data of the type shown in Figure 6-3 using the routine described in Section 6.2.2 and Appendix A.6.1. The scatter in data is associated with the errors in detecting pit boundary by the customised filter in ImageJ.

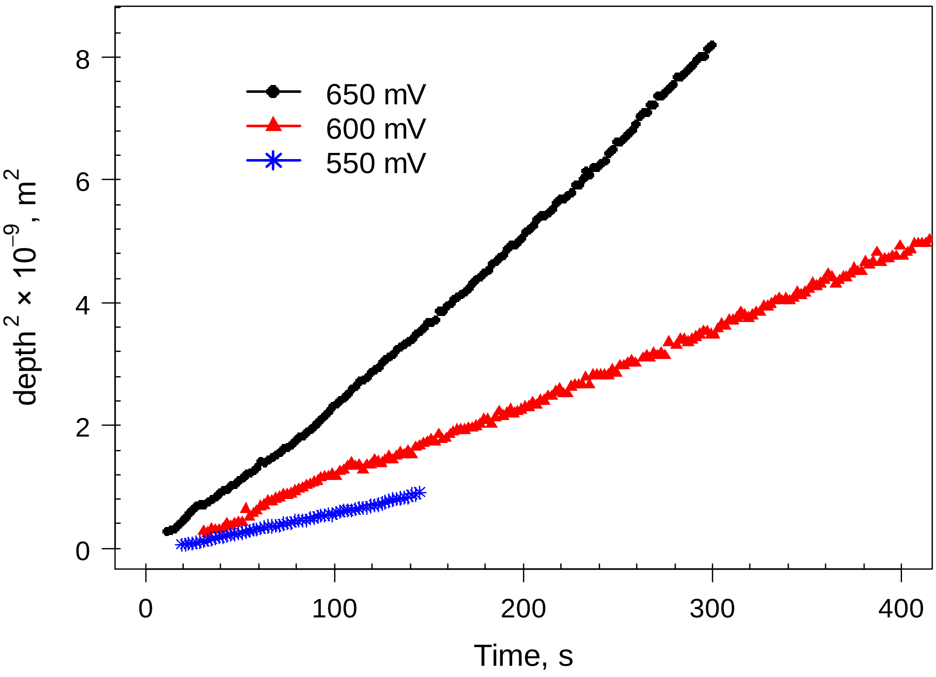

Figure 5-16- (Pit depth)^2 against time for the pits shown in Figure 5-15.

5.4.3 Effect of chloride concentration on galvanostatic growth

As mentioned above, pits grown under galvanostatic control are deeper and more round in shape compared with those grown under potentiostatic control. This is illustrated in Figure 5-17, which shows two pits growing concurrently for 400 s under galvanostatic control of 20 μA in 0.01 M NaCl following initiation at 650 mV for 10 s. This shows that growth in the initial stages (46 s) is similar to potentiostatic growth in terms of undercutting process via small lobes and the sharp pit boundary at the bottom. However, at longer times, the depths of pits increase as rapidly as their widths and a rough surface develops at the pit bottoms.

Figure 5-18 shows the data containing the evolution of pit depth and width as a function of time for pits grown galvanostatically for samples in 0.1 and 0.01 M NaCl. In measurements (1) and (2), single pits (shown in Figure 5-6 and Figure 5-7-d, respectively) grew with an applied current of 10 μA following initiation at 650 mV for 10 s. Thus, each pit is driven by the total applied current. For the pit reported in measurement (3), a current of 10 μA was applied in 0.01 M NaCl but another semi-pit grew under the covering lacquer (which could not be detected by an edge detecting filter that will be described in Section 6.2.2). Therefore, the pit in (3) certainly grew with current less than 10 µA. Pits (4) and (5) are the two adjacent grown pits shown in Figure 5-17. The applied current was 20 µA and considering the equal size of the pits; it was assumed that each one is driven by 10 µA.

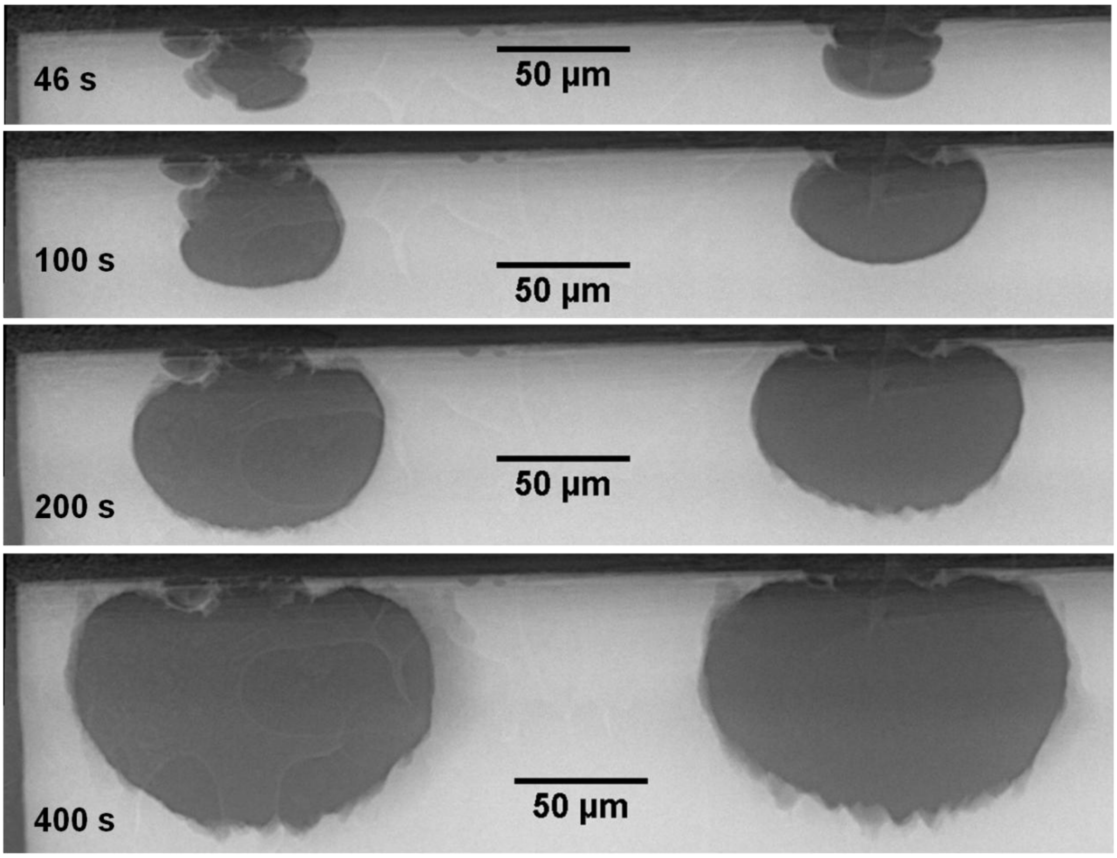

Figure 5-17-Radiographs of two pits growing simultaneously at the edge of 20 µm foil of 304 stainless steel in 0.01 M NaCl at 20 µA after initiation at 650 mV vs. Ag/AgCl for 10 s.

In contrast with potentiostatic growth, it is seen in Figure 5-18 and Figure 5-19 that both pit depth and pit width follow a parabolic trend with time. Lowering the chloride concentration does not change the rate of growth in depth, even for the pit in measurement (3), which grew with less current compared with the other pits shown. Similar to potentiostatic growth, wider pits are seen in 0.1 M NaCl solution compared to pits in 0.01 M. Also as shown in Figure 5-20, the slope of pit width to pit depth decreases from *ca.* 2 to 1.4 by lowering bulk chloride concentration from 0.1 to 0.01 M.

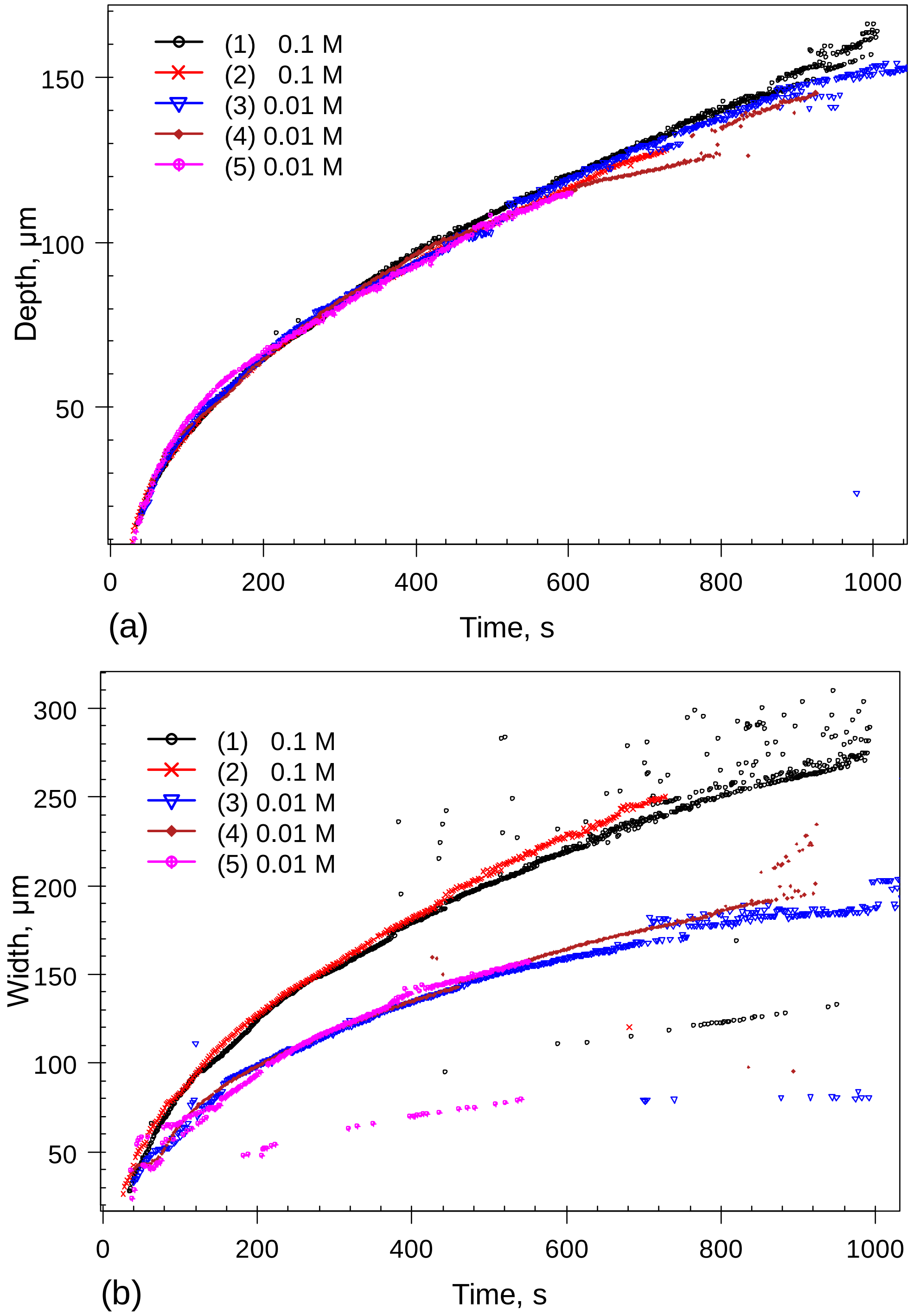

Figure 5-18- Pit depth (a) and width (b) as a function of time in indicated NaCl concentration and applied current. (1) and (2) are single pit each grown at 10 µA in independent measurement, (3) a pit grown at 10 µA adjacent to another smaller semi-pit, (4) and (5) are adjacent pits grown simultaneously together at 20 µA (it is assumed that each pit grew at ~10 µA). All pits started off at 650 mV vs. Ag/AgCl for 10 s then switched to current control. The data have been time-corrected by subtracting the induction time of each pit. The values were extracted automatically from pit boundary coordinates data of the type shown in Figure 6-3 using the routine described in Section 6.2.2 and Appendix A.6.1. The scatter in data is associated with the errors in detecting pit boundary by the customised filter in ImageJ.

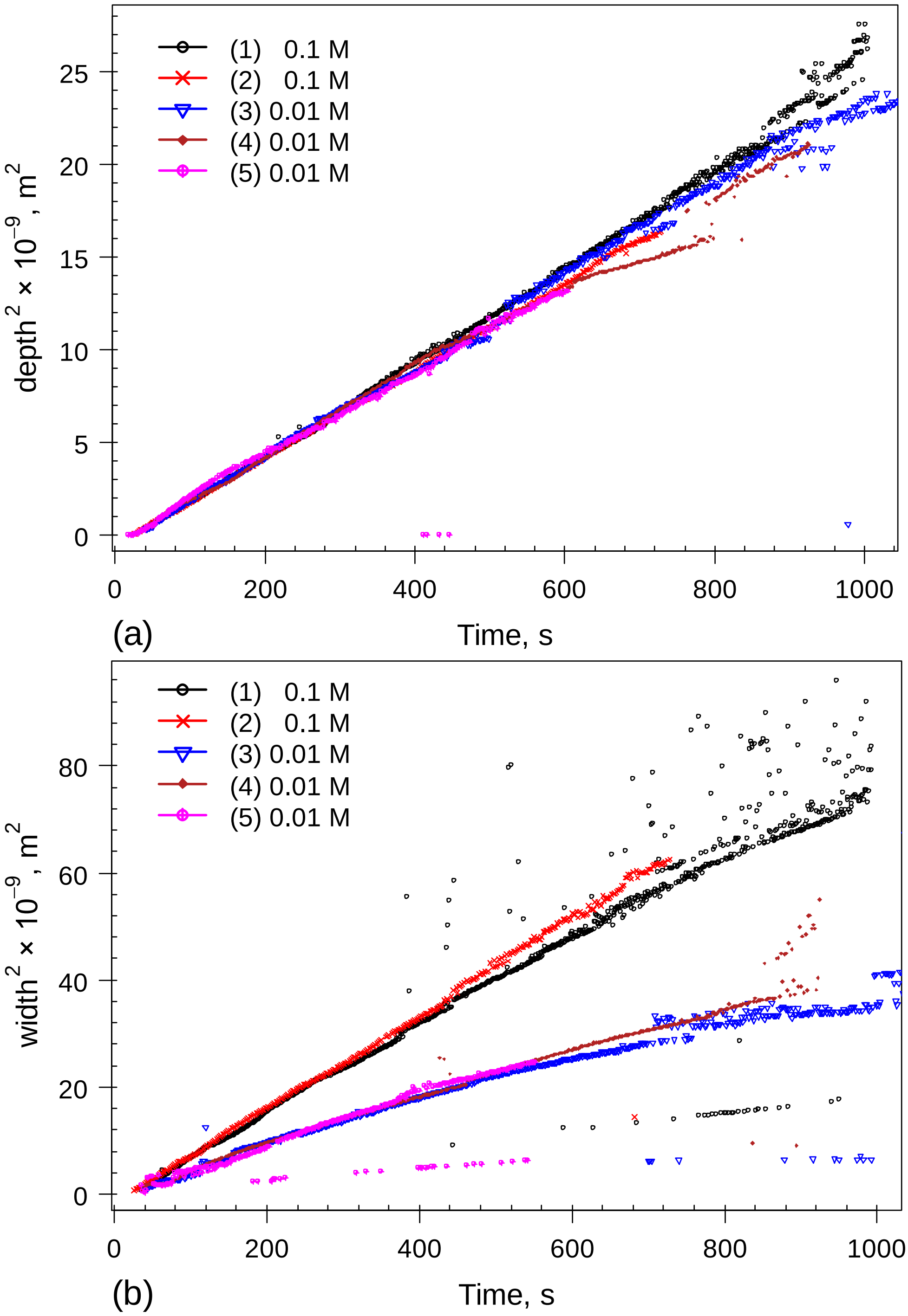

Figure 5-19- (a) (pit depth)^2 and (b) (pit width)^2 vs. time for the pits shown in Figure 5-18. The scatter in data is associated with the errors in detecting pit boundary by the customised filter in ImageJ described in 6.2.2.

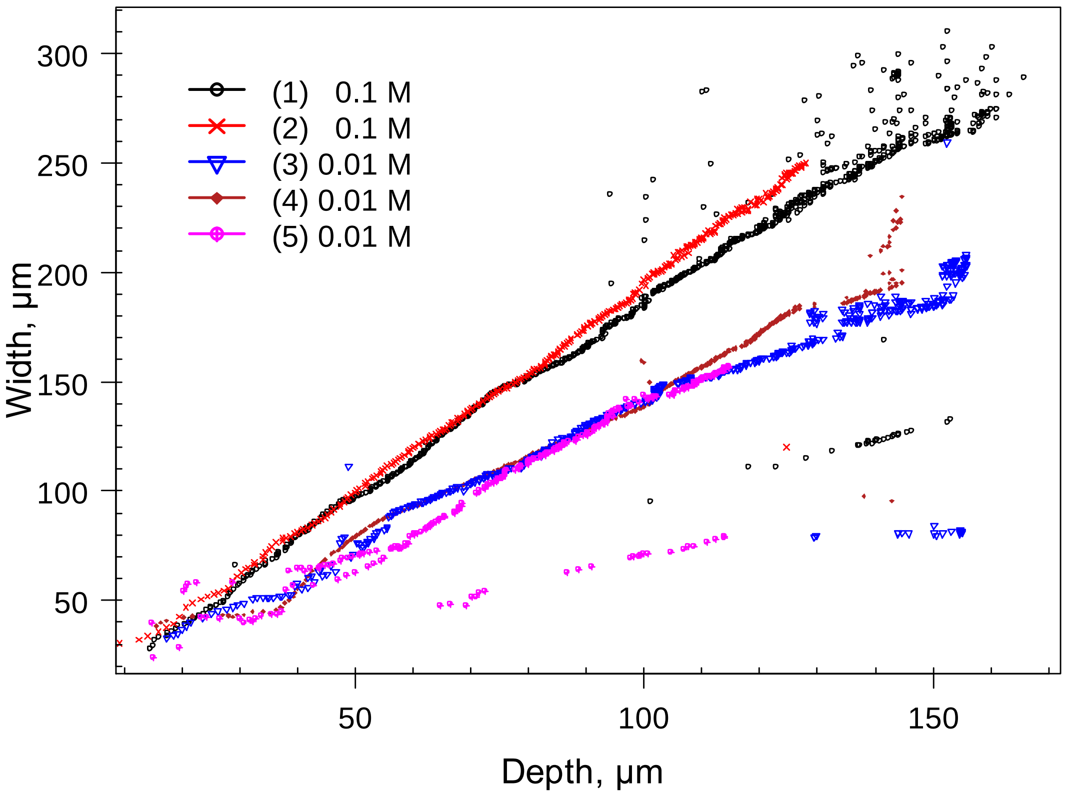

Figure 5-20- Pit width vs. pit depth changes by time for pits shown in Figure 5-18; The values were extracted automatically from data of the type shown in Figure 6-3 using the routine described in Section 6.2.2 and Appendix A.6.1. The scatter in data is associated with the errors in detecting pit boundary by the customised filter in ImageJ described in 6.2.2.

One pit was grown at 20 µA was for a short period. The higher applied current resulted in faster dissolution and a deeper pit as shown in Figure 5-21. However, no systematic change is seen in the pit width. As only a single measurement was made, it is not possible to make any assessment of the effect of current on the pit shape.

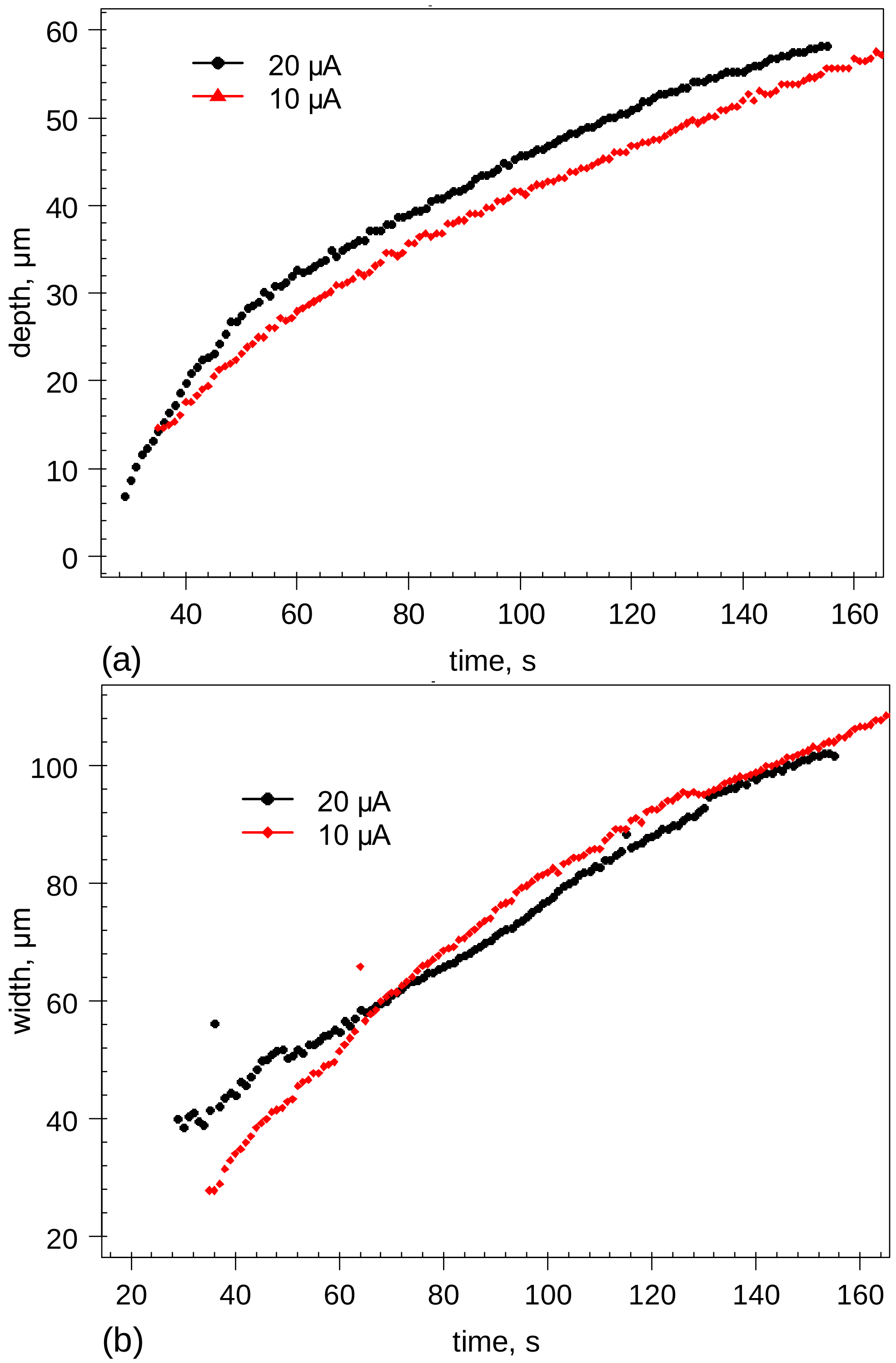

Figure 5-21- Pit depth (a) and width (b) as a function of time for pits in 0.1 M NaCl at applied current of 10 and 20 µA. The values were extracted automatically from pit boundary coordinates data of the type shown in Figure 6-3 using the routine described in Section 6.2.2 and Appendix A.6.1.

5.5 Discussion

5.5.1 Potentiostatic growth and porous cover formation

Under potential control, pits propagate by undermining the metal from within the cavity. Pits undercut the surface at the edge of cavity and eventually perforate the surface from beneath and make a new hole into the bulk solution. As the pit grows, the supplied current increases owing to the increase in pit surface area. However, fluctuations are seen in the current (Figure 5-3) due to perforation in the cover and local repassivation (decrease in current) and undercutting and further growth (increase in current).

Pits at their initial stages are hemispherical/semi-circular as shown in Figure 5-3 (75 s). This is similar to the shape reported by Mankowski and Szklarska-Smialowska [62]. The solution inside the cavity is highly acidic [54, 55] and concentrated in metal cations [54, 61, 63]. Close to the pit mouth, the pit solution is considerably more dilute owing to escaping metal ions [151]. Where the concentration drops below the critical value (~60% of saturation [84]) required for continuation of propagation, the metal does not dissolve at a high enough rate to counter-balance the cation diffusion rate and therefore, that region of the pit wall repassivates. The dissolution only continues at the portions of surface that still are in contact with a sufficiently concentrated solution. The passive and active portions of pit surface are shown at 81 s in Figure 5-3. The active area propagates with a rapid dissolution rate (~1 μm/s) forming a lobe-shape at the moving front and undercuts the repassivated surface (90 and 115 s in Figure 5-3). The developing lobe extends upward and eventually punctures the top passive metal surface and produces a hole onto the top edge. The new hole causes metal ions to diffuse away more quickly into the bulk solution due to a steep concentration gradient. The perforation dilutes the cations concentration of solution close to pit mouth leading to repassivation of the pit surface at a point where concentration falls below the critical value. Then at the interface between active and passive regions, undercutting recurs (115, 132 and 165 s in Figure 5-3). This process repeats constantly and eventually a porous cover known as a *lacy* cover forms by successive development of lobes from both sides of the pit cavity as shown in Figure 5-4(a) and (b) and schematically shown by Ernst and Newman [106] (described in Section 2.2.9).

For pits grown under potentiostatic control, the pit perimeter looks sharp and well-defined during the whole growth period (see e.g. Figure 5-10), and this is consistent with observations of Sato [66] that pits grown at higher potentials have polished and bright internal surfaces compared with etched surfaces of pits grown at less noble (lower) potentials. This is consistent with the characteristics of electropolishing dissolution beneath salt films reported by a number of researchers [50, 51, 53, 141]. This suggests that pits growing at higher potentials are covered by salt film over the majority of their internal surface. Evidence for the presence of a crystalline salt film at the bottom of pits has also been observed in X-ray diffraction measurements of 2D pits of the type shown in the present work [152].

5.5.2 Galvanostatic growth

Pits growing under galvanostatic conditions (following initiation under potentiostatic control) initially propagate in a similar shape to potentiostatically grown pits; small lobes from both sides of the pit undercut metal and perforate the cover with a sharp pit perimeter. As the pit grows, its area increases, so the average current density decreases. This means that a lower potential is required to support the lower current density, so the potential gradually decreases (as can be seen in electrochemical plot shown in Figure 5-6), and the pit perimeter at the bottom transforms to a rough and etched surface. This transition agrees with Sato's idea [66, 67] and the observations of Ryan *et al.* [111] that pits initiated at high potential often grow with a polished surface but if the potential is decreased, pits either repassivate or propagate in a salt film-free active state with convoluted structure. It should be noted that in the present work, the potentiostatic measurements used a relatively high potential (+550 - +750 mV vs. Ag/AgCl) whereas the galvanostatically grown pits develop at lower potentials (typically ranging from +600 down to <100 mV vs. Ag/AgCl) during the growth of a pit)

The difference in pit shape between galvanostatic and potentiostatic pits can be characterised through the difference in slope of pit width vs. pit depth, which is *ca.* 2-4 in the potentiostatically-grown pits and *ca.* 1.4-2 in the galvanostatically-grown pits, suggesting that pits grown under potentiostatic control tend to be less penetrating (more dish-shaped) than those grown under galvanostatic control (This may be related to the different potentials involved). The reason for the pit shape difference is that under current control, the pit adjusts its shape to accommodate the limited applied current with the lowest electrical resistance; therefore, it maximizes the corroding surface area resulting in a relatively uniform dissolution rate in all directions, thereby approaching an approximately circular shape.

5.5.3 Pit depth

There is considerable variation in the pit depth behaviour for pits grown under potentiostatic conditions, with no clear trend for pits grown in different chloride concentrations as shown in Figure 5-11a. This implies that the dissolution rate at the pit bottom is not significantly affected by the bulk chloride concentration. The lack of dependence of pit depth on chloride and potential is also reported by Tester and Isaacs for 1D pits [83] and by Ernst and Newman for 2D pits [106] (under potentiostatic control). It is inferred that there is a salt film on the bottom of pits grown at high potentials [76, 78] (an observation also confirmed by independent X-ray diffraction measurements [152]), which regulates interfacial potential under the salt film by changing its thickness, so that the metal dissolution (growth) rate in depth is controlled by the diffusion of metal ions dissolving from the salt film.

It can be seen in Figure 5-15 that a higher potential resulted in a higher rate of increase of depth with time (i.e. current density). As discussed above, the rate of increase in pit depth in intermediate chloride concentrations is diffusion-controlled and should therefore be independent of applied potential [106] owing to presence of a saturated metal chloride salt layer on the metal surface along pit bottom [76]. However, in dilute bulk solutions (in this case 0.01 M NaCl), the growth behaviour is probably also affected by ion electromigration due to the increased potential gradient caused by a lower conductivity. Ion transport in the electrolyte is therefore facilitated by the potential gradient, which results in thinning of the salt film and accordingly more dissolution of metal to thicken the salt film. Therefore, a higher metal dissolution rate at the bottom of pits is seen at higher applied potentials in less concentrated solution of 0.01 M NaCl.

During galvanostatic growth, the rate of increase in pit depth also shows no dependence on bulk chloride concentration as shown in Figure 5-18a. Although the pit bottom is not covered by a salt film (as described above), the linear correlation between the (pit depth)^2 and time indicates that diffusion of ions from the metal surface controls the growth in depth in these conditions as well.

Using Fick's 1st law (Equation 5-1) [83, 153] in conjunction with Faraday's 2nd law (Equation 5-2), the relation between (pit depth)^2 and time can be established as Equation 5-3:

Equation 5-1 $$i_{\lim} = \frac{zFD(C_b - C_m)}{x}$$

Equation 5-2 $$idt = \frac{zF\rho dx}{M}$$

Equation 5-3 $$x^2 = \frac{M}{\rho} D(C_b - C_m)t$$

where $i_{\lim}$ is the diffusion-controlled anodic current density, z is the transferred charge, F is the Faraday constant, ρ is the metal density, D is the diffusion coefficient, C_b is the concentration at the pit bottom, C_m is the concentration at the pit mouth, x is the pit depth and M is the atomic mass. Therefore, $D(C_b\text{-}C_m)$ can be estimated from the slope of the square of the pit depth against time. Taking M=57.6 g.mol^{-1} and ρ=7.82 g.cm^{-3}, the $D(C_b\text{-}C_m)$ in galvanostatic pits (of 0.1 M solution) shown in Figure 5-19 is *ca.* 1.5±0.2×10^{-6} (mol.m^{-1}s^{-1}). Taking a typical value of 2.2×10^{-6} (mol.m^{-1}s^{-1}) for potentiostatic pits (of 0.1 M) of curve (d) and (e) from Figure 5-12, then the $D(C_b\text{-}C_m)$ in galvanostatic pits is ~65 % of the value for pits under potential control. Considering the existence of salt film at the bottom of potentiostatic pits (as discussed above), concentration at the bottom of these pits should be saturation concentration. Assuming identical metal ion diffusivity, therefore, the concentration at the bottom of galvanostatic pits is ~65 % of saturation concentration, which is consistent with the critical concentration, C_{crit}, required for pit propagation. If $C<C_{crit}$, pit will not propagate; this happens towards the mouth of pit. While this is a reasonable interpretation and is consistent with the idea of possibility of active dissolution (salt film free) within chemistries between 60 % and 130 % of saturation concentration [81, 84], however, as will be considered in detail in the next chapter, this may not be correct because the perforated cover introduces a diffusion barrier.

In potentiostatic pits, the pit bottom is normally covered by a salt film, so the concentration of metal ions at the bottom of the pit is likely to be the saturation concentration C_{sat}.

In contrast, in galvanostatic mode, as the pit grows and its area increases, the average current density, and therefore the interfacial potential, decreases. As the local current density decreases, it may be insufficient to maintain the critical concentration of metal ions in solution required to prevent passivation. In these areas (close to the pit mouth), the surface of the pit repassivates, decreasing the total active area, while the pit remains active at the bottom, where the diffusion length is longest and critical concentration is maintained. The typical concentration in the active region is therefore likely to be the critical value required to maintain active dissolution, C_{crit}.

5.5.4 Pit width

As shown in Figure 5-11b, Figure 5-15b and Figure 5-18b, the pit width increases with chloride concentration and potential. These changes are consistent with the results of Ernst and Newman [106].

The likely reason for the changes in width with chloride concentration is that lowering the bulk concentration leads to an increase in IR drop in the solution and therefore, a decrease in the interfacial potential and dissolution rate at the laterally developing fronts, which grow under activation/ohmic-drop control. However, at the pit bottom, dissolution is diffusion-limited as described above, so that changes in the pit depth with time are independent of salt concentration. Also, there are larger concentration gradients and higher rate of diffusion close to the pit mouth for a pit in a dilute solution. Hence, repassivation occurs and undermining events take place deeper within the pit and the pit gets deeper with a lower horizontal dissolution rate compared with pits grown in higher chloride solution. The same explanation can be applied to results seen in galvanostatically grown pits.

Thus, the growth of the pit width is controlled by IR drop in solution in pit growth under both potentiostatic and galvanostatic conditions.

5.6 Conclusions

1. Pits grown under potentiostatic control develop via an undercutting process that perforates the metal surface and gradually changes the pit shape from semi-circular at the start to dish-shaped as growth occurs. The pit perimeter is polished with a salt film covering the pit bottom.

2. In the initial stages under galvanostatic control, pits propagate by lobes undercutting the metal in a similar way to potentiostatic growth with sharp and well defined perimeters which is consistent with dissolution underneath a salt film. As the pits propagate, they tend to grow with the maximum possible corroding area and approach a circular shape with a rough etched surface at the bottom, which is likely to grow without a salt film close to the critical concentration required for propagation.

3. For both potentiostatically- and galvanostatically-grown pits, a linear relation exists between the square of the pit depth and growth time, which suggests that growth is under diffusion control. This is supported by the observation that the pit depth growth rate is independent of the bulk chloride concentration and applied potential except in dilute solutions where electromigration may accelerate the diffusion process and thus the dissolution rate at the pit bottom.

4. Lateral growth of pits is controlled by the conductivity (and therefore potential drop) of solution for both potential and current controlled regimes.

6 Extraction of stainless steel pit growth parameters from *in situ* real time 2D radiography

6.1 Introduction

The synchrotron X-ray radiographs of the evolution of pits *in situ* in real time, as shown in the previous chapter, can be used for qualitative and quantitative comparison with numerical simulations based on 2D finite element modelling of pit propagation. For quantitative comparison and refinement of the model, the key growth parameters need to be extracted from experimental observations. The key dissolution parameters are local anodic current density, metal ion concentration and interfacial potential at the pit surface.

There have been relatively few attempts to extract dissolution kinetics parameters from video images taken of growing 2D pits. Frankel presented a method to directly measure the average anodic current density from the growing pit boundary velocity in Al [154], an Al alloy [155] and Ni-Fe [156] thin films. Subsequently, Ryan *et al.* [111, 112] determined the anodic current density in pits propagating as 2D disks in stainless steel thin films by measuring the pit edge movement velocity. Ernst and Newman [106-108] studied stability of pit growth in details and measured the kinetics of pit propagation in depth and width and compared the results with kinetics in 1D pencil electrode. However, they did not measure current density and concentration within the pit. More recently, Tang and Davenport [157] tracked the pit boundary movement and computed the instantaneous but average current density in Fe-Co thin films.

In our experiments, pits grow as 2D semicircles during propagation. Therefore, it is possible to calculate the local anodic current density from the pit boundary velocities determined from radiographs, irrespective of any other cathodic and anodic reactions occurring on the pit surface. Hence, radiographs of 2D pits can be processed to provide data for calibrating and validating a finite element model (FEM) for pit growth. In this chapter, a method for extracting the key kinetic parameters from sequences of synchrotron X-ray radiograph images is described. In the next chapter, these parameters are compared with those which are currently used in the Laycock/White/Krouse model [7, 110, 138-143] for pit propagation in stainless steel and the experimentally derived parameters are used to refine their model.

6.2 Pit perimeter image processing with ImageJ

The first step in analysing the radiographs is to segment the image into the relevant domains: metal and solution. A number of alternative methods have been investigated and results using public domain software are presented here.

6.2.1 Image segmentation using standard commands in ImageJ

Standard techniques employ some form of thresholding (i.e. defining a point in the grey scale that represents the boundary between the metal and solution) but the results are sensitive to the quality of the image. The image has to be decreased from 16-bit to 8-bit to enable its conversion into binary format. The image is then converted into binary format based on an automatically determined universal threshold value for the whole image. Finally, outlines within the image are detected. Figure 6-1 shows the result using the commands in the publically-available software ImageJ [147]: *"Image/Type/8-bit"+"Process/ Binary/ Make Binary"+"Process/ Binary/Outline"*. A manually-determined straight line is added into the image to represent the original interface. A significant amount of noise is seen along the edges and interface between metal and solution. Artefacts and loss of key features are both associated with poorer quality images which make it impractical to feed the data points into a finite element package for further processing.

6.2.2 Pit edge detection through implementing a customised filter in ImageJ

To obtain a segmented image suitable for finite element modelling, a smoothing edge detector was developed that takes into account known landmark features in the image. The method has been implemented as a customised plug-in filter using Java scripts, "Pit" into ImageJ software [147]. The "Pit" filter script is attached in Appendix A.6.1. The initial step in applying the filter involves manual input of approximate values for the horizontal centre of the pit and the foil interface with solution on both sides of the pit. A smoothing filter is applied to the image to reduce any possible noise. Then a line is fitted to the input values to generate the interface. Based on the contrast differentiation of metal and solution, the filter starts tracking the edges along the interface from the left side of the pit towards the approximate horizontal centre input. The same tracking is done from the right side until it reaches the defined approximate centre of the pit. The filter differentiates and moves forwards based on an edge detection algorithm within an arbitrarily resolution of 5×5 pixel. The window size of contrast differentiation can be optimised depending on the extent of edge sharpness along pit boundary. A radiograph frame showing the segmented pit boundary is shown in Figure 6-2.

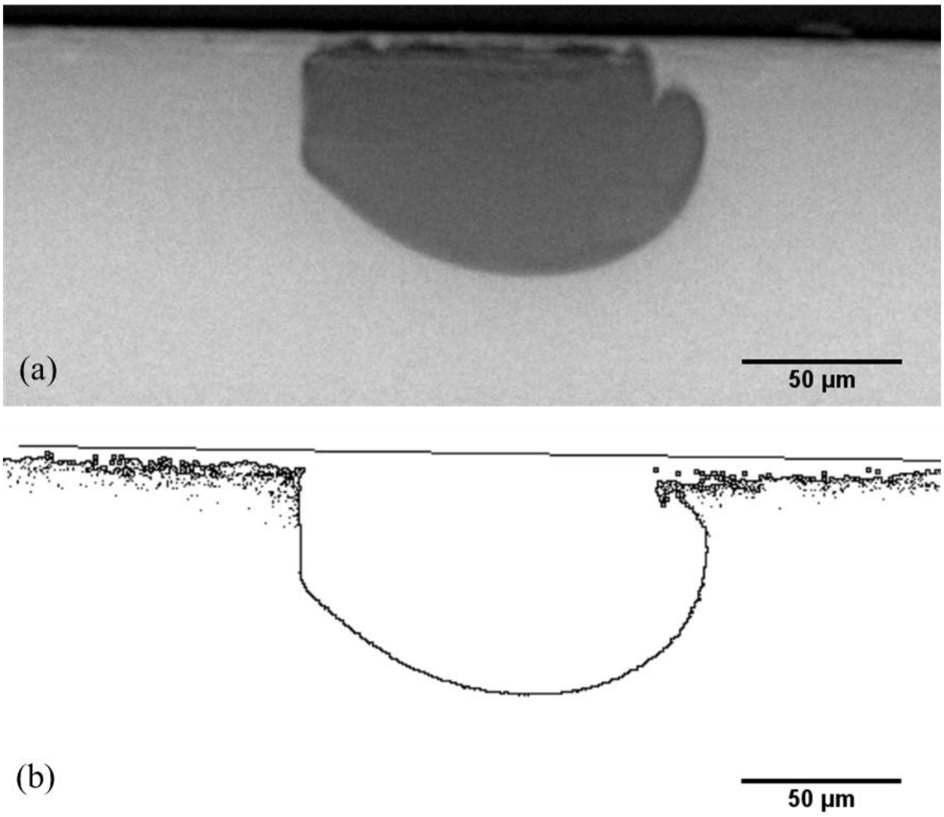

Figure 6-1- Radiograph of a typical pit (a) raw image (b) automatically detected outline by converting the image into binary format via the standard techniques in ImageJ software [147] along with a manually determined straight-line interface for comparison with the original interface.

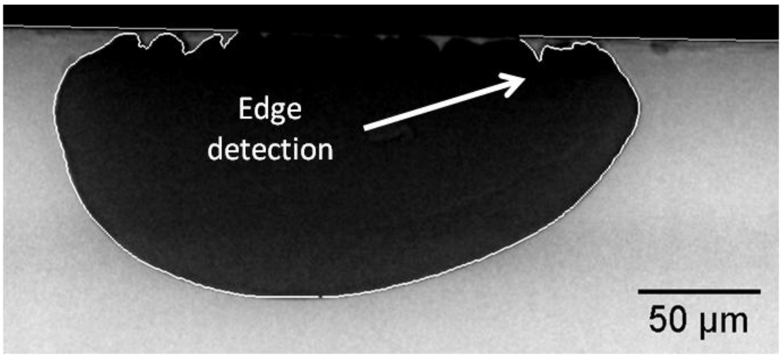

Figure 6-2- Radiograph frame showing segmentation generated by the customised "Pit" filter (attached in Appendix A.6.1) implemented in ImageJ software using Java scripts which segments the image into pit boundary and metal-solution interface.

The *x* and *y* coordinates of the pit boundary for each video frame (Figure 6-3) are written to a text file to be used in generating the perimeter of pit cavity in a finite element method package.

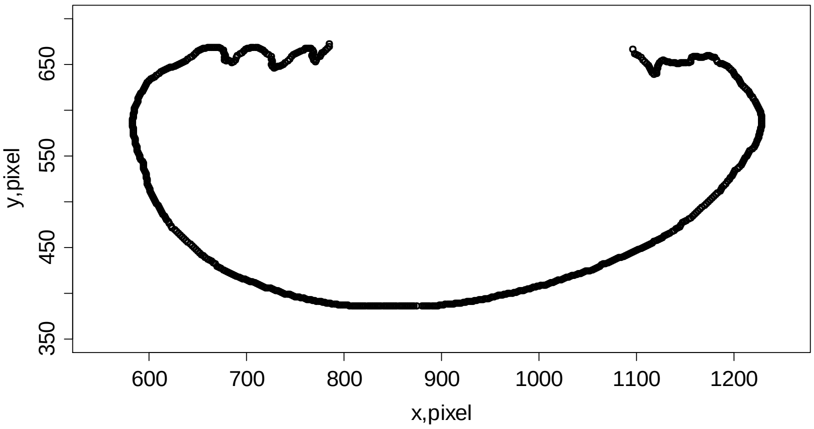

Figure 6-3- Coordinates of perimeter of the pit cavity shown in Figure 6-2 determined and recorded by the customised "Pit" filter attached in Appendix A.6.1.

Pit detection by the filter is limited by the number of pixels required for contrast differentiation which in turn leads to difficulties in detecting pits during their initial growth stages. The smallest pit that was successfully detected by filter was ca. 8 µm deep.

6.3 Local current density at the pit boundary

6.3.1 Pit perimeter displacement perpendicular to the pit boundary

Once the pit boundary has been segmented for several successive radiograph frames of a growing pit, then the local current densities at the pit boundary can be calculated from the boundary velocity. Figure 6-4 shows the position of the pit boundary 20 s later than the position (yellow boundary) shown in Figure 6-2.

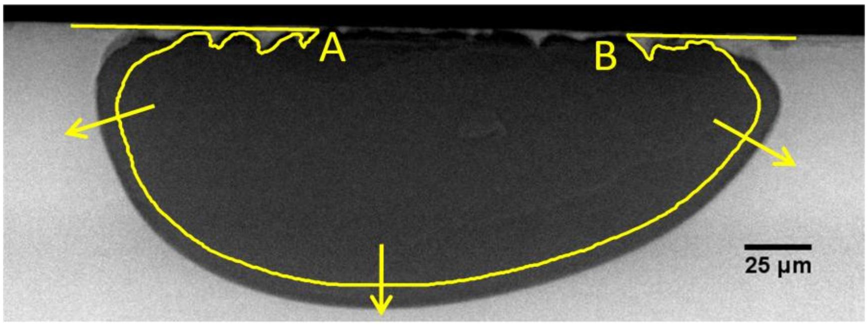

Figure 6-4- Movement of the pit boundary after 20 s compared with its earlier position (yellow boundary) as shown in Figure 6-2

The velocity of the pit boundary can be calculated at each point by the displacement along the local normal from one frame to a subsequent one at a later time *dt*. The displacement is measured by the normal distance from the centre of two adjacent points in the boundary at time *t* with respect to the boundary at time *t+dt*. Figure 6-5 shows the local normal distance (at part of the pit boundary) measured between two subsequent frames with 10 second time step along the pit boundary. The velocity is the displacement *dx* divided by *dt* (the time interval between frames), which is then converted using Faraday's 2nd law into a local current density:

Equation 6-1

$$i = \frac{dx}{dt}\frac{zF\rho}{M}$$

where i is the local current density, dx/dt is the local measured pit boundary velocity, F is the Faraday constant, M is the molar mass of the material (57.6 g/mol), ρ is metal density (7.8 g/cm^3) and z is the number of transferred electrons (2.2).

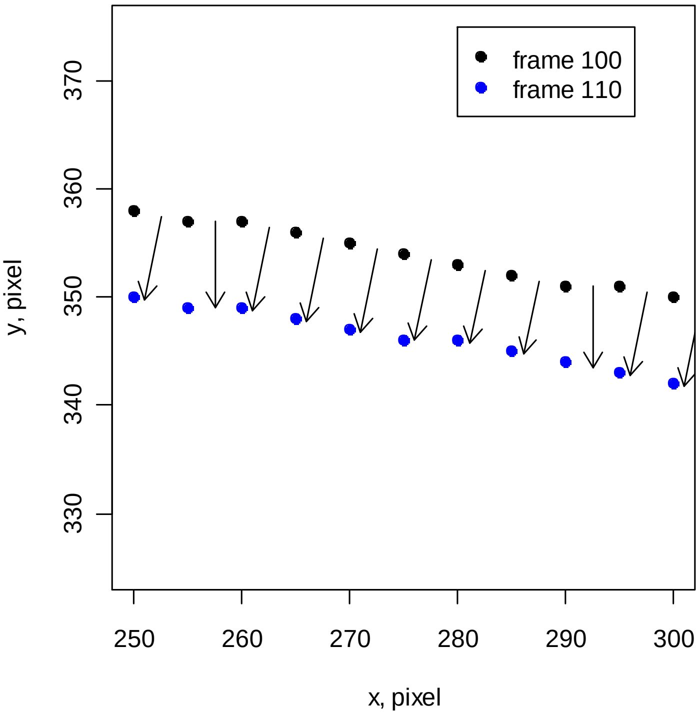

Figure 6-5- Typical local normal distance (indicated by the arrows at part of the pit boundary) measured between two subsequent frames with 10 s time step along pit boundary. Points were detected and recorded by the edge detection algorithm described above. The blue points represent the boundary position 10 s after the black points. The arrows represent the normal direction from the centre of two adjacent points of the pit boundary with respect to the pit boundary at 10 s later.

Figure 6-6 shows a growing pit with a plot of local current density along the pit boundary measured from the velocity of boundary movement by considering frames that are (b) 2, (c) 5 and (d) 10 s apart. The pixel size for the radiograph images is

0.37 μm × 0.37 μm. The detected boundaries are slightly noisy at this resolution, particularly when small time steps are used. By choosing a larger time step, smoother results are obtained. In Figure 6-6, noisy results are seen if a time step of 2 s is used whereas smoother results are observed for a time step of 10 s, but the value of the maximum current density is suppressed. In order to minimise noise but maintain a reasonably high resolution of the peak current density, data were mainly analysed with a 5 s time step. The finite element script that reads pit boundary coordinates and calculates the local current density is attached in Appendix A.6.2.

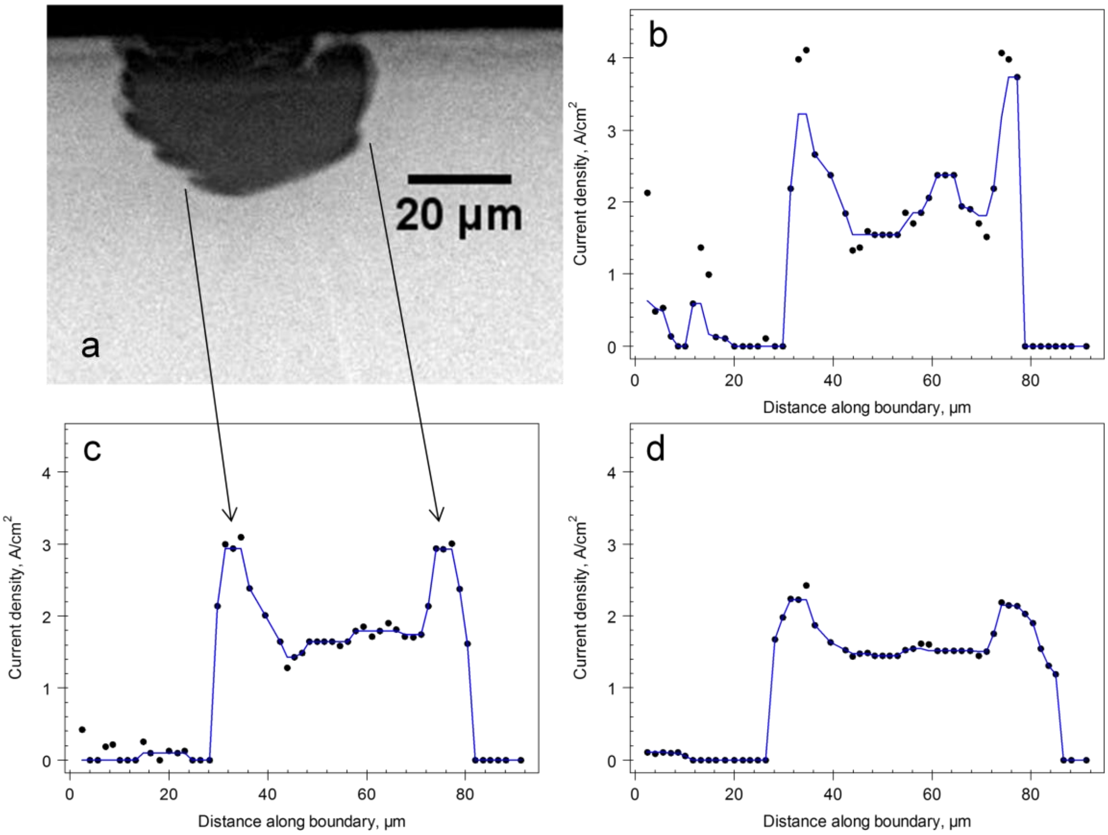

Figure 6-6- Radiograph of a growing pit and its current density along pit boundary measured by considering movement of the pit boundary over a period of (b) 2, (c) 5 and (d) 10 s. The distance along the pit boundary is calculated starting from the left corner of the pit mouth. The blue line is a smooth function through the data points.

6.3.2 Current verification

For each frame in the pit growth sequence, the integrated area under the plot of current density vs. pit boundary position is the total instantaneous anodic current. It is therefore possible to compare the integrated current densities as a function of time with the current applied by the potentiostat.

An alternative method for determining the current passed as a function of time is to determine the rate at which pixels of metal are lost using the following equation:

Equation 6-2
$$I = \frac{z.F.\rho.s.dA}{Mdt}$$

where dA is the area of metal lost between subsequent frames (which is the product of the number of pixels lost and the pixel area), s is the metal foil thickness (20 µm) and dt is the time interval between frames. Figure 6-7 compares the current supplied by the potentiostat with the current determined by integrating the current densities along the pit perimeter and the current determined by the loss of metal pixels from frame to frame. A good correlation is observed between current supplied by the potentiostat and the values measured from the radiographs. However, some pixelation noise is observed for the latter.

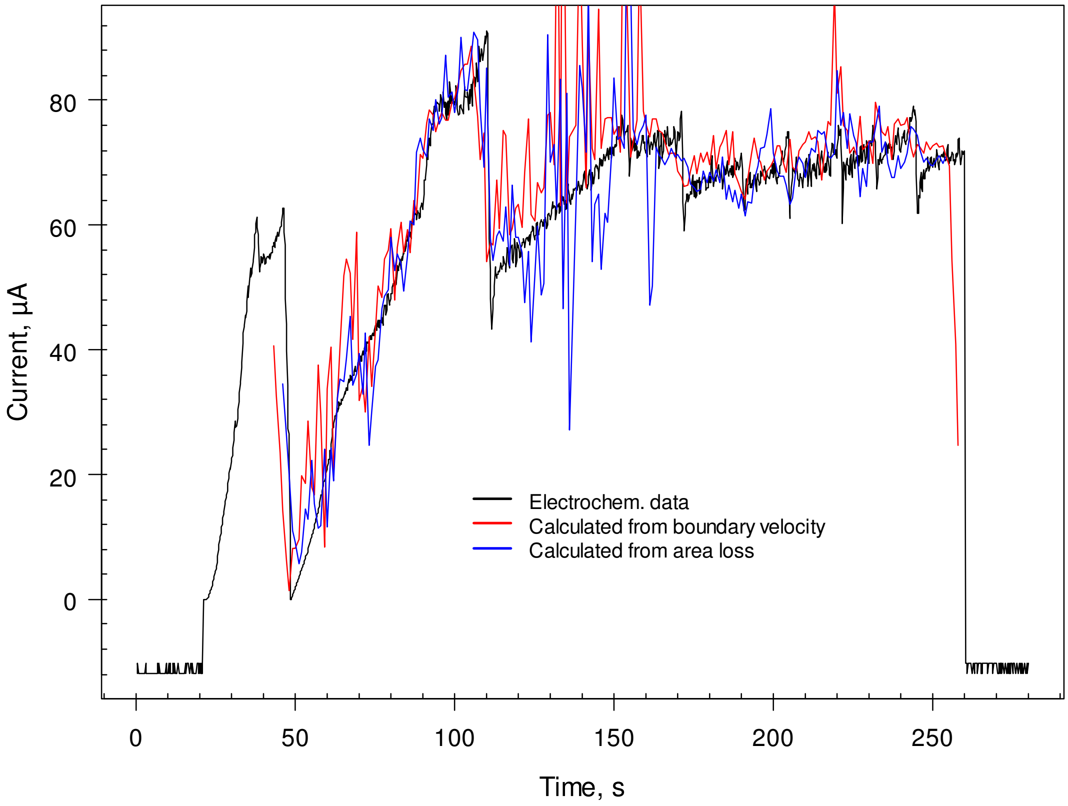

Figure 6-7- Comparison of the current determined by integrating the current densities along the pit perimeter (red line), the current determined by the loss of metal pixels from frame to frame (blue line) and the current supplied by the potentiostat (black line) for a pit grown on 316L stainless steel in 1 M NaCl at 750 mV vs. Ag/AgCl.

6.4 Local current density results

The local anodic current density, i_a, along perimeter of pits grown under potentiostatic control for a series of increasing electrolyte concentrations are shown in Figure 6-8 to 6-11. The pit perimeter is defined as the internal region between the pit mouth extents (points A and B in Figure 6-4) at both sides of the pit with the surrounding metal. The pit rims are automatically detected by the filter based on the extent of perforation of the cover. All pits reported in this section are single unless indicated otherwise.

The current density of the pit grown in 304 stainless steel foil in 0.005 M NaCl at 650 mV vs. Ag/AgCl after (a) 82 and (b) 121 s is shown in Figure 6-8. The black arrows show the relationship between the pit boundary in the radiograph and the current density along the pit perimeter. At 82 s, the current density (i_a) within the pit close to the pit mouth on both sides of the pit cavity is almost zero, i.e. the surface is passive and no dissolution occurs. Immediately next to the passive region, i_a jumps to its highest value, ~3 Acm^{-2} at the actively corroding lobe on the left side of the pit. Further down towards the pit bottom, i_a gradually decreases and stays almost constant with a lower dissolution rate of ~1 Acm^{-2} until it slowly goes up forming another peak (~2 Acm^{-2}) and immediately afterwards drops down to nearly zero. Similar behaviour is seen at 121 s, although the passive region is smaller as the lobes have spread further up the side of the pit.

Figure 6-9 shows i_a around the pit boundary for a pit grown in 304 stainless steel foil in 0.01 M NaCl at 600 mV vs. Ag/AgCl. Again the pit wall is passive with zero current density for the initial ~30 μm on the left side of the pit. Immediately adjacent to the passive region, a peak current density of *ca.* 4 A/cm^2 can be observed. Then i_a drops to a stable region with almost constant dissolution rate of ~1.5 Acm^{-2}. As the pit grows (Figure 6-9 b-d), a narrower passive region is seen as the lobes grow laterally, and both the maximum values of i_a (corresponding to the developing lobs) and the current densities at the bottom of the pit gradually decrease.

Figure 6-10 shows current density along the pit boundary for a pit grown in 304 stainless steel foil in 0.1 M at 650 mV vs. Ag/AgCl. In this measurement three pits were growing simultaneously and the one in the middle of foil is reported. The behaviour of i_a is similar to that observed for pits shown in Figure 6-8 and Figure 6-9.

However, in this case the current densities at the pit bottom are slightly higher as the pit is at an earlier stage of growth and possibly because of the more aggressive electrolyte (higher bulk chloride concentration) in which the pit cover is less occluded and less of a barrier [72].

Figure 6-11 shows i_a along the perimeter of the pit grown in 316L stainless steel in 1 M NaCl at 750 mV vs. Ag/AgCl after (a) 40 s and (b) 107 s. The majority of the pit wall on both sides is passive at 40 s with active corrosion occurring only in a “pit within pit” ~20 µm long. At 107 s, it can be seen that the pit has developed a rapidly dissolving lobe on the left side close to the pit bottom while the right side is smoothly growing (general dissolution up to the foil edge) with a steady current density, most likely due to the epoxy cover partially placed on the foil edges to prevent pit/crevice intiation at the foil edges (as described in 5.4.1).

The final pit in this sequence, Figure 6-12, shows the current density for a galvanostatically grown pit in 0.1 M NaCl at 10 µA after (a) 29 s and (b) 135 s following initiation at 650 mV vs. Ag/AgCl for 10 s. At 29 s, current density peaks (~2.5-3 Acm^{-2}) corresponding to the developing lobes are seen at both sides of the pit with a stable region of growth at the central bottom of pit governed with a lower and almost constant current density (~1.5 Acm^{-2}). At 135 s, the majority of the pit wall grows with a dissolution rate less than 1 Acm^{-2}, while small regions at both sides of the pits are passive.

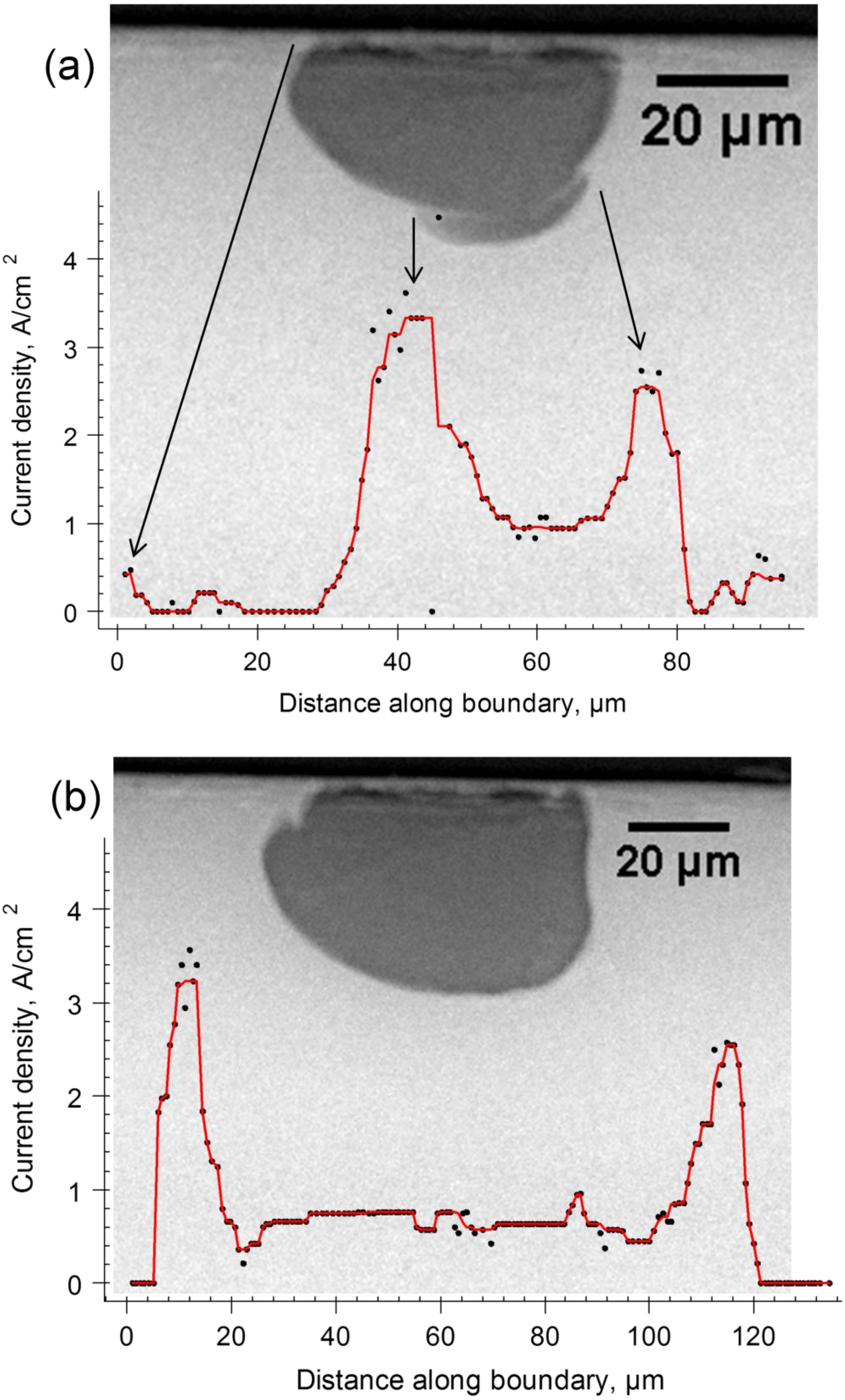

Figure 6-8- Local current density along the perimeter of the pit grown on 304 stainless steel foil in 0.005 M NaCl at 650 mV vs. Ag/AgCl for (a) 82 and (b) 121 s. The red line is a smoothing function. The distance along the pit boundary is calculated starting from the left corner of the pit mouth. The black arrows show the relationship between the radiograph and the local current density along the pit perimeter.

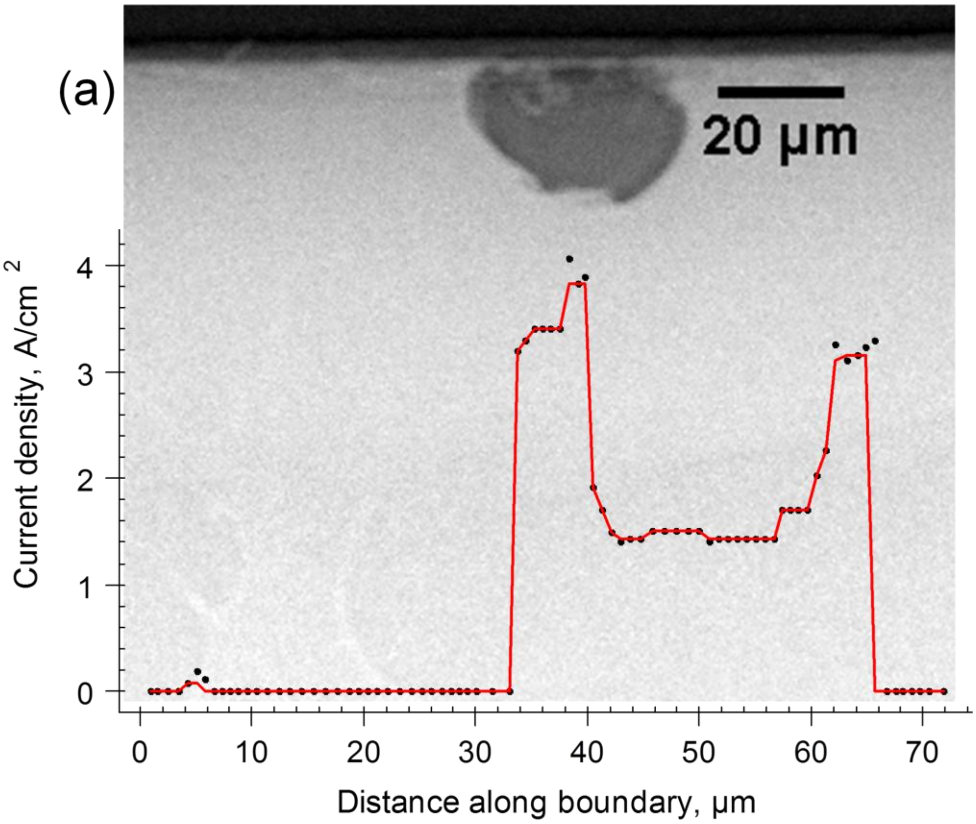

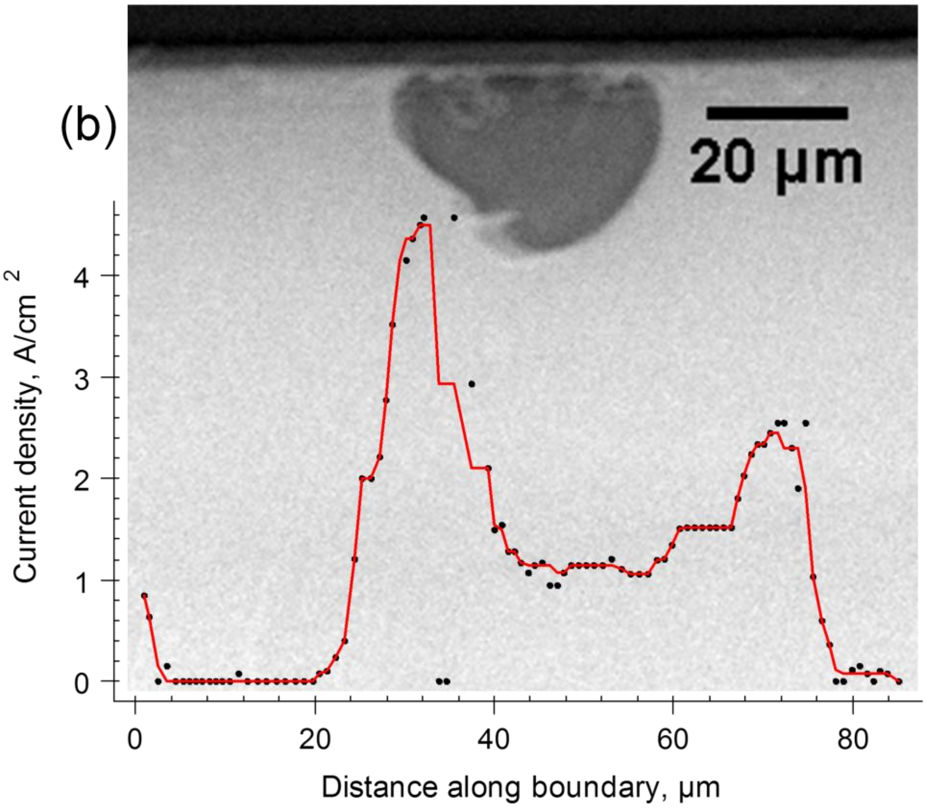

Figure 6-9- Local current density along the perimeter of the pit grown on 304 stainless steel foil in 0.01 M NaCl at 600 mV vs. Ag/AgCl for (a) 62 and (b) 67 s. The red line is a smoothing function.

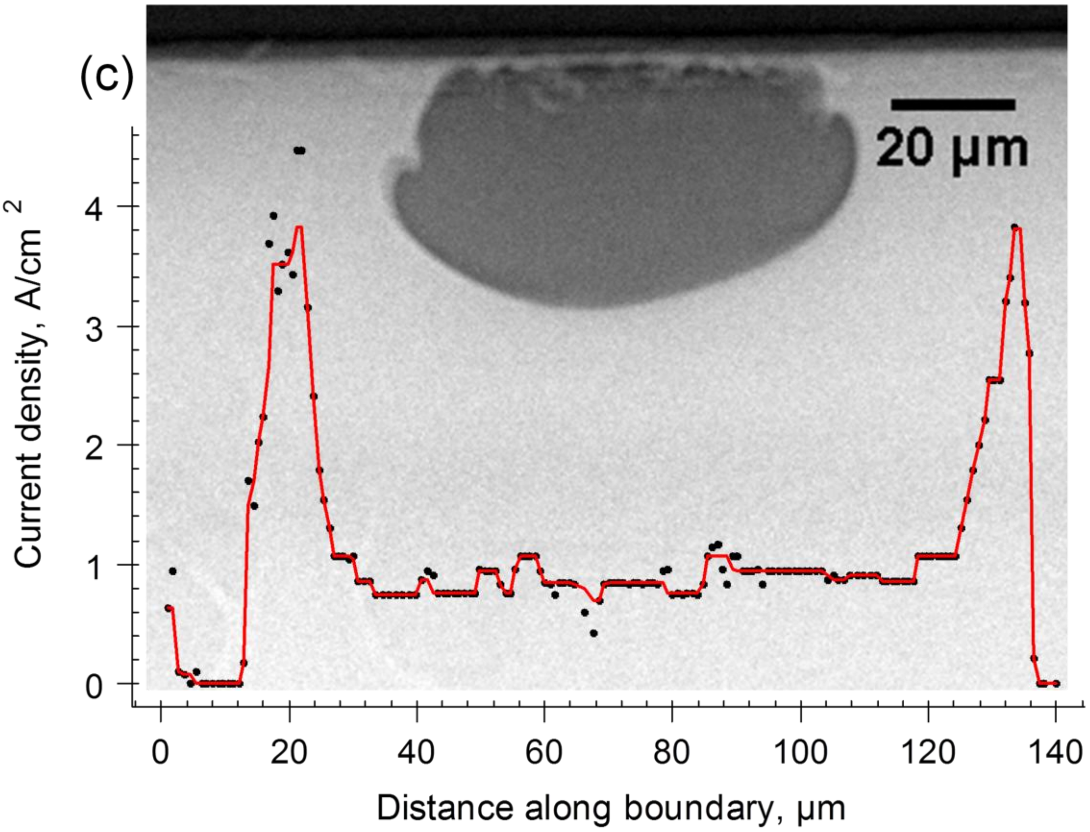

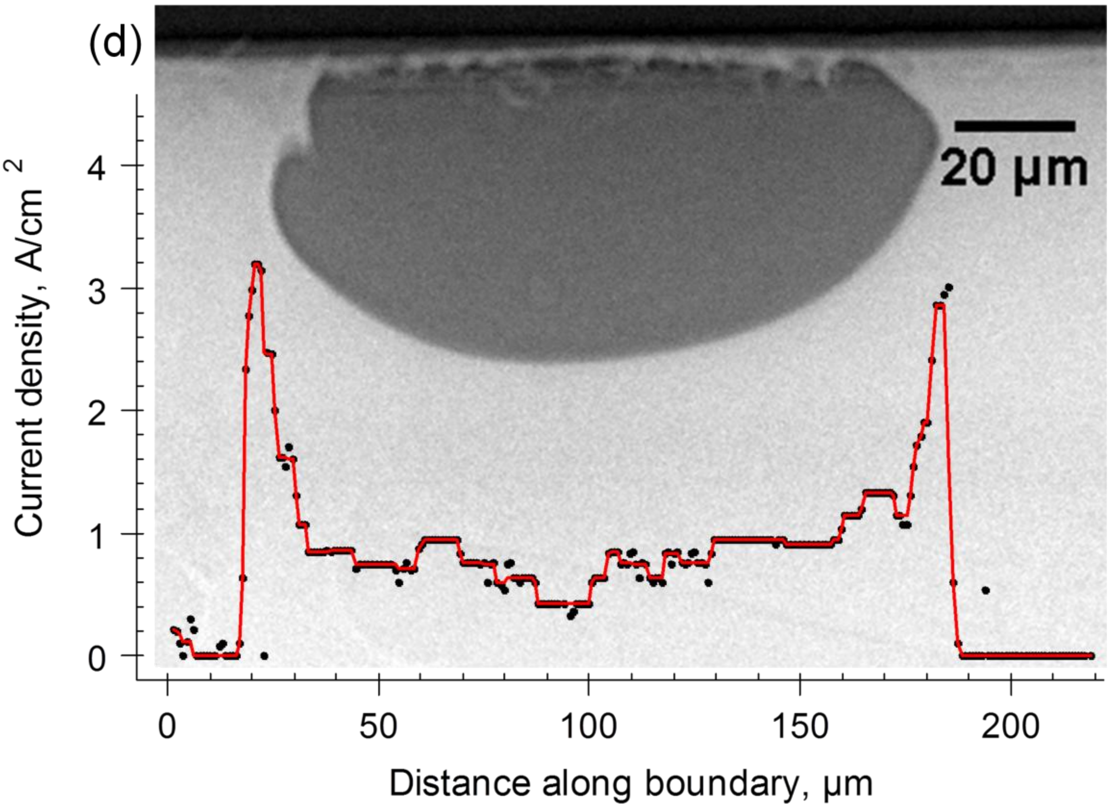

Figure 6-9-continued Local current density along the perimeter of the pit grown on 304 stainless steel foil in 0.01 M NaCl at 600 mV vs. Ag/AgCl for (c) 110 and (d) 152 s. The red line is the smooth function applied.

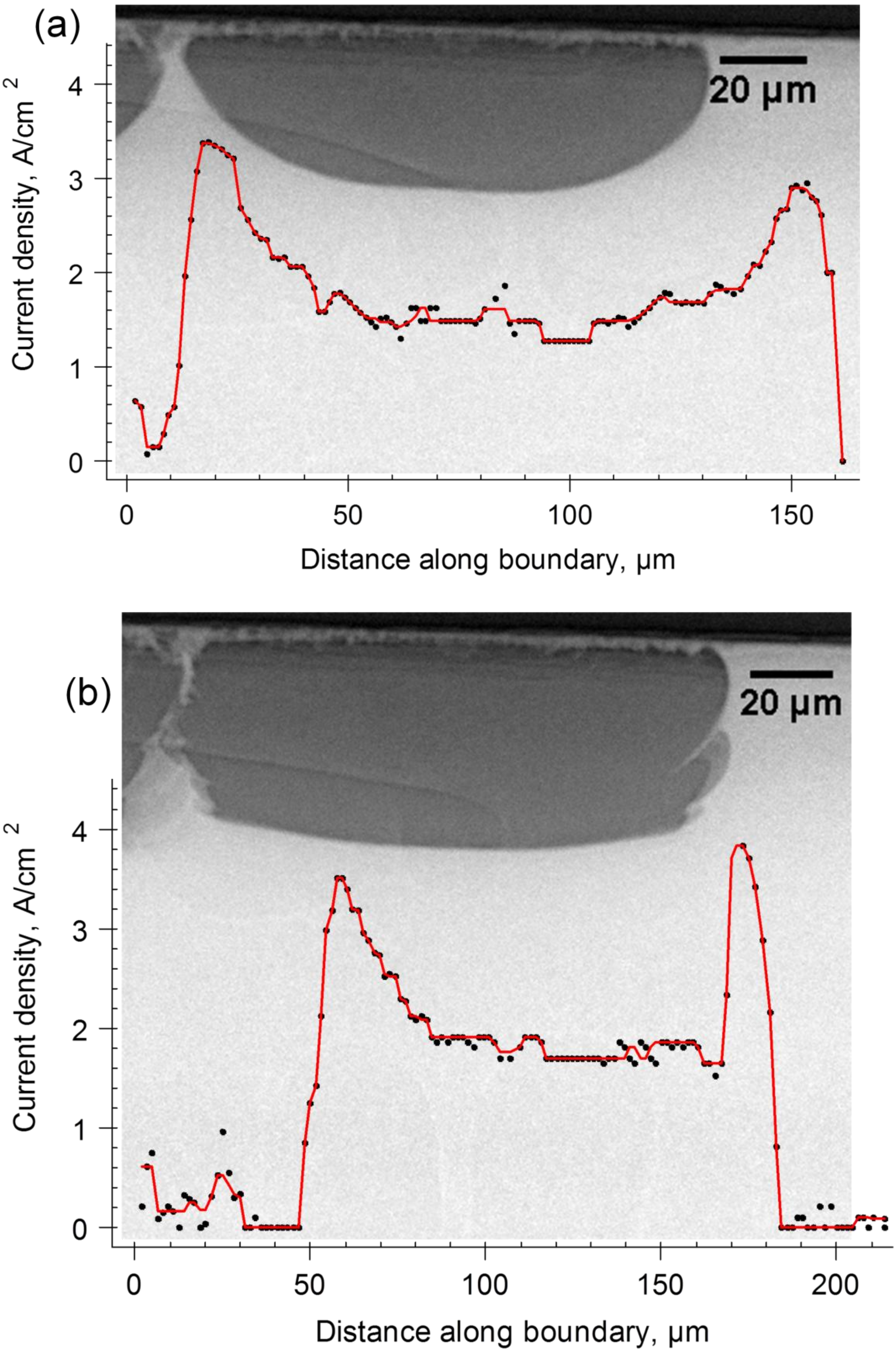

Figure 6-10- Local current density along the perimeter of the pit grown on 304 stainless steel foil in 0.1 M NaCl at 650 mV vs. Ag/AgCl for (a) 70 and (b) 94 s. The red line is a smoothing function.

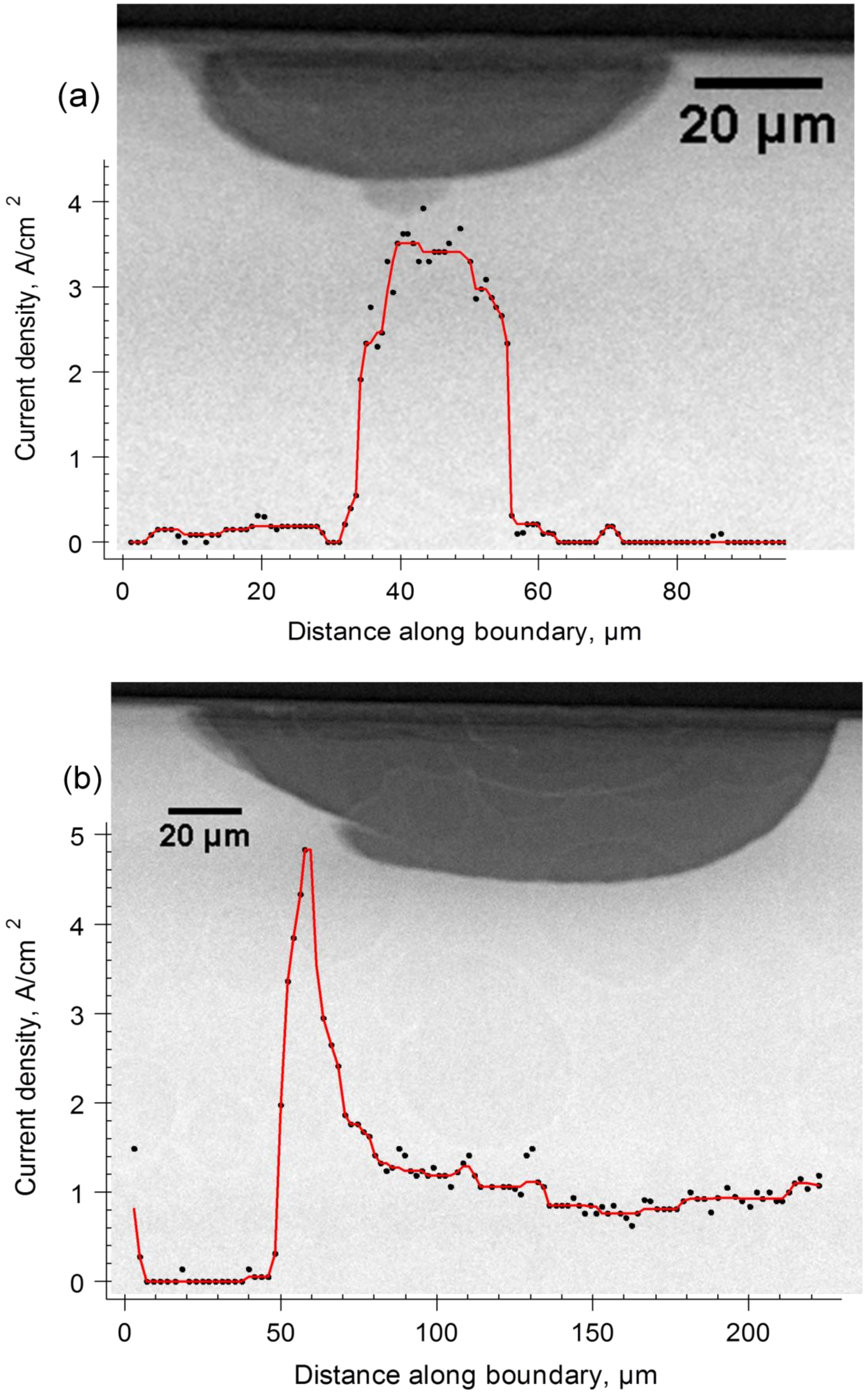

Figure 6-11- Local current density along the perimeter of the pit grown on 316L stainless steel foil in 1 M NaCl at 750 mV vs. Ag/AgCl for (a) 40 s and (b) 107 s. The red line is a smoothing function.

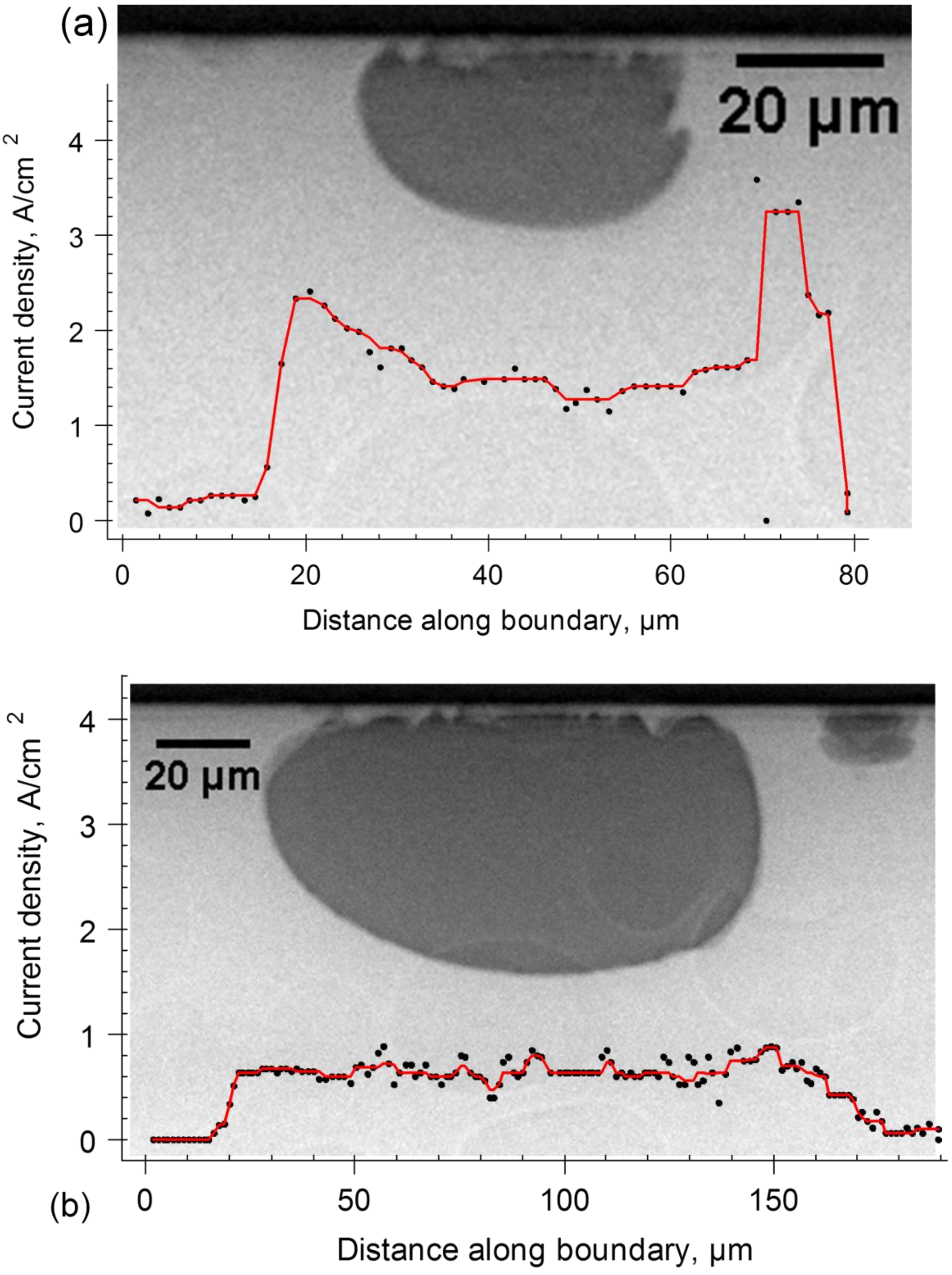

Figure 6-12- Local current density along the perimeter of the pit grown on 304 stainless steel foil in 0.1 M NaCl at 10 µA for (a) 29 and (b) 135 s following initiation at 600 mV vs. Ag/AgCl for 10 s. The red line is a smoothing function.

Figure 6-13 to Figure 6-17 show the time-dependence of local current densities within the pits shown in Figure 6-8 to Figure 6-12. For each frame during the pit growth radiograph sequence, three current density parameters were extracted. The first is the maximum value around the pit perimeter, the second is the average (mean) current density, which was determined by adding up all the current densities along the pit perimeter and then dividing by the number of points and the third is the current density in the mid-point of the pit perimeter (in order to give an indication of the current density at the pit bottom, if the symmetry of the pit cavity is retained during growth).

The maximum current density shows considerable fluctuation, particularly for pits growing in 304 stainless steel foils in more dilute NaCl solutions. Figure 6-13 shows a pit potentiostatically grown in 0.005 M NaCl at 650 mV vs. Ag/AgCl and Figure 6-14 shows a pit potentiostatically grown in 0.01 M NaCl at 600 mV vs. Ag/AgCl. In both cases, the maximum current density shows fluctuations mainly in the range of 2-4 A/cm^2, with increasing numbers of excursions to higher values as high as 8 A/cm^2 at longer times (~300 s). The current density at the pit bottom (both the average and mid-point values) shows a gradual decay from ~1.5 to 1 A/cm^2.

Figure 6-15 shows a pit growing potentiostatically for a shorter time (up to 120 s) in 0.1 M NaCl at 650 mV vs. Ag/AgCl. The maximum current density shows similar behaviour to that found for lower concentrations at similar time scales (Figure 6-13 and Figure 6-14) but the average and mid-point values are slightly higher (2 A/cm^2).

Pit growth (potentiostatic) in 316L stainless steel foil in 1 M NaCl at 750 mV (Figure 6-16) shows similar behaviour: the maximum current density shows a small decrease but mostly fluctuates around 2 to 4 A/cm^2. The current density at bottom of potentiostatically grown pits fluctuates between 1 to 2 A/cm^2.

The maximum current density in the single galvanostatically grown pits at 10 μA, shown in Figure 6-17 and Figure 6-18 (radiograph of the pits are shown in Figure 5-6 and 5-7d, respectively), decreases from ~3 A/cm^2 at the initial times to less than 1 A/cm^2 at the later stages of growth, but there are significant excursions up to substantially higher values. The average and current densities at the pit bottom follow very similar trend as to the maximum current density. The difference between the maximum current density and that at the pit bottom for galvanostatic growth is smaller than for potentiostatic pits, which indicates more uniform current density distribution and dissolution during galvanostatic growth.

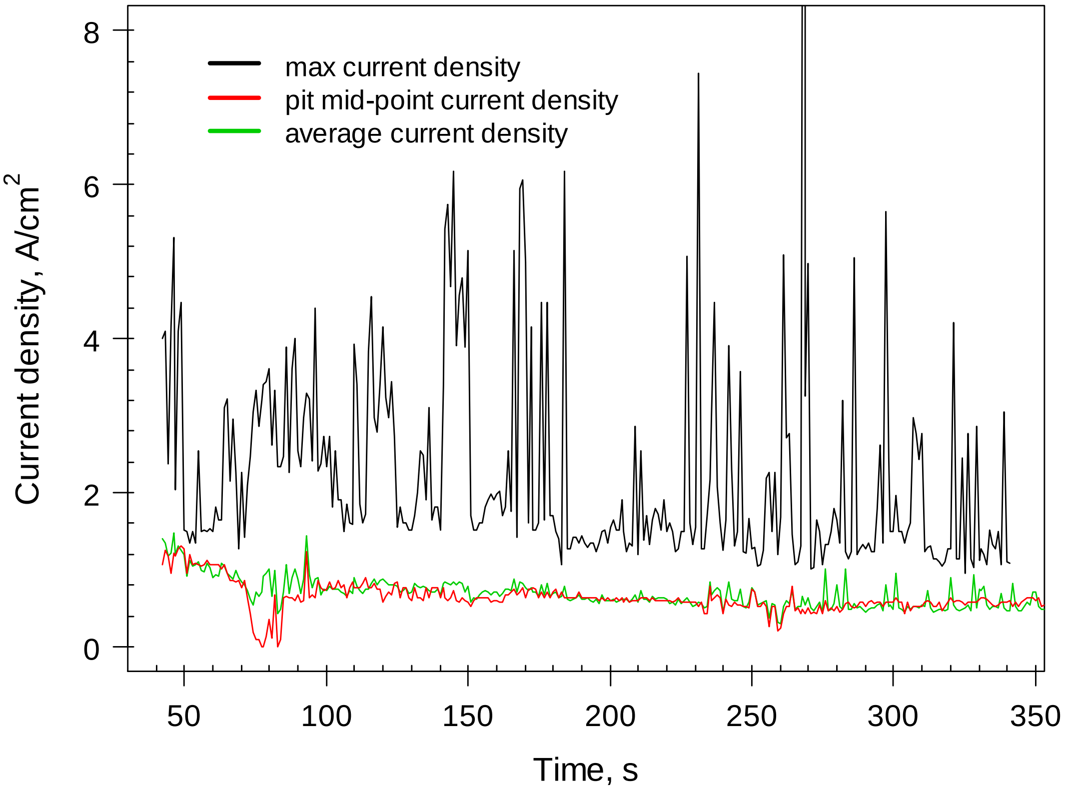

Figure 6-13- Maximum, average and pit mid-point current density along pit boundary as a function of time during growth of the pit grown on 304 stainless steel foil in 0.005 M NaCl at 650 mV vs. Ag/AgCl.

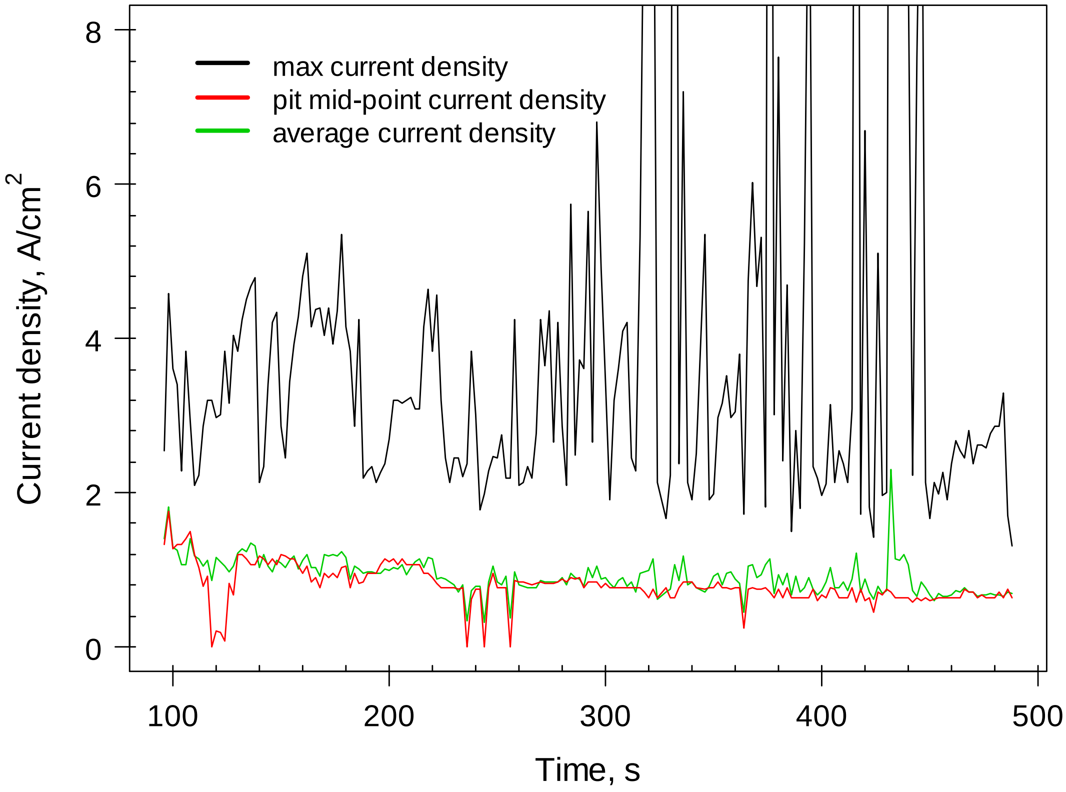

Figure 6-14- Maximum, average and pit mid-point current density along pit boundary as a function of time during growth of the pit grown on 304 stainless steel foil in 0.01 M NaCl at 600 mV vs. Ag/AgCl.

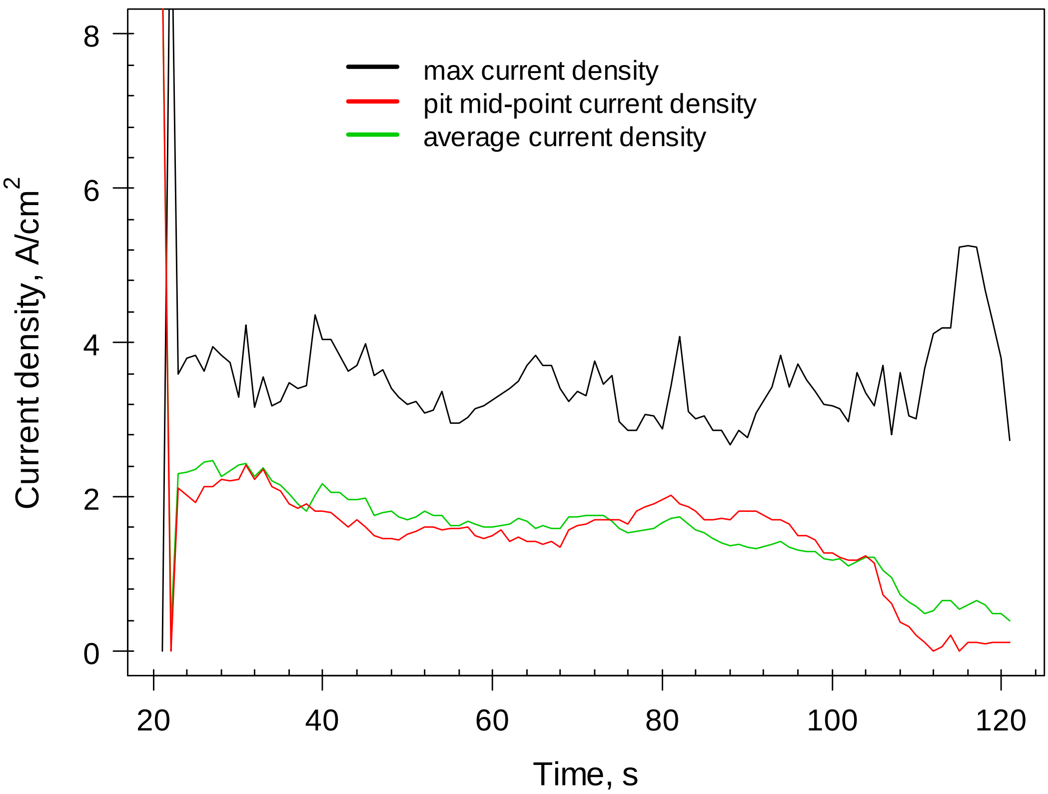

Figure 6-15- Maximum, average and pit mid-point current density along pit boundary as a function of time during growth of the pit grown on 304 stainless steel foil in 0.1 M NaCl at 650 mV vs. Ag/AgCl.

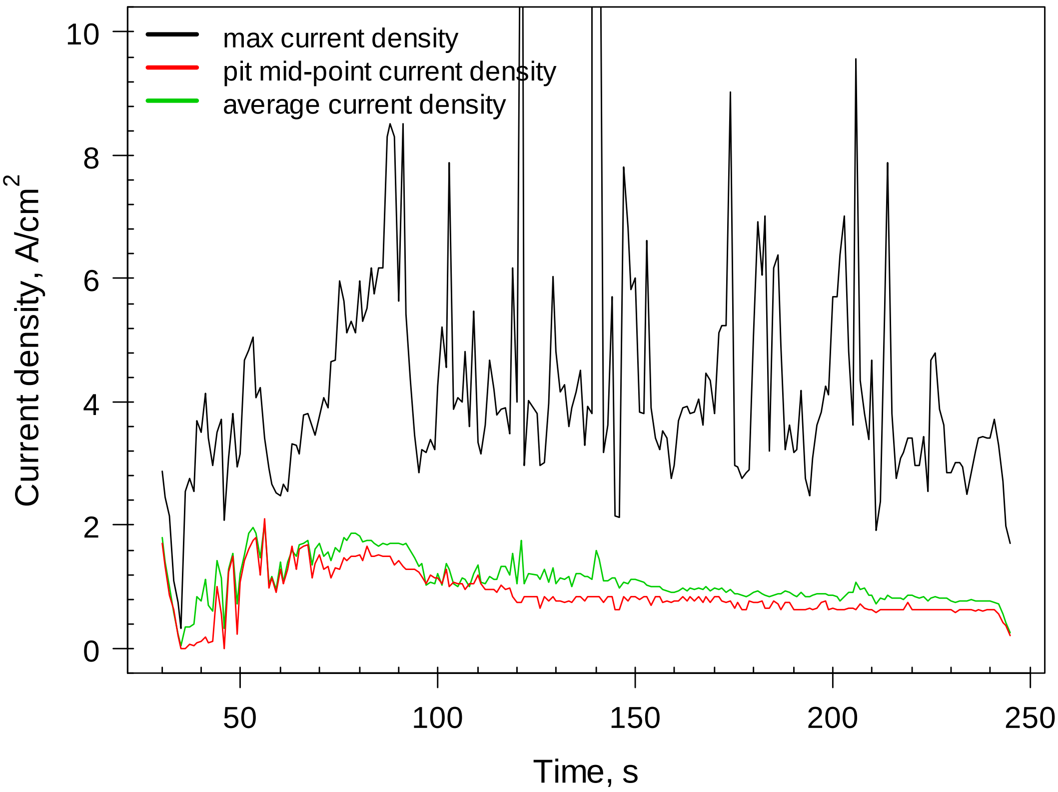

Figure 6-16- Maximum, average and pit mid-point current density along pit boundary as a function of time during growth of the pit grown on 316L stainless steel foil in 1 M NaCl at 750 mV vs. Ag/AgCl.

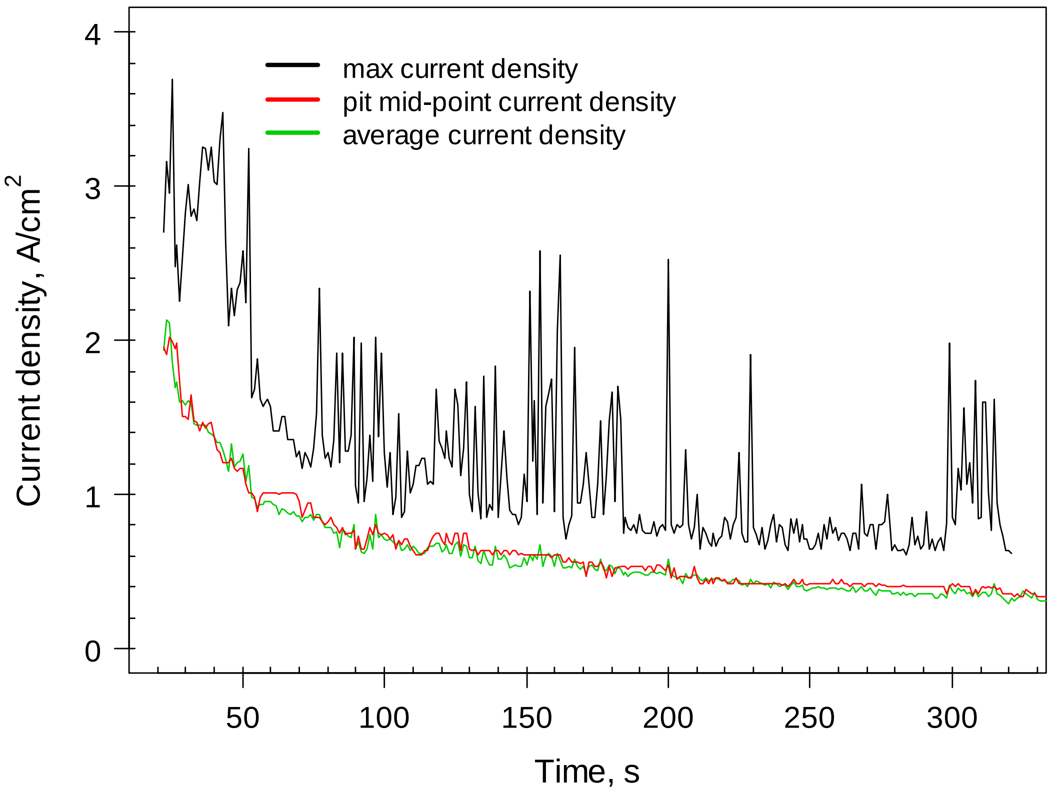

Figure 6-17- Maximum, average and pit mid-point current density along pit boundary as a function of time during growth of the pit grown on 304 stainless steel foil in 0.1 M NaCl at 10 µA following initiation at 650 mV (vs. Ag/AgCl) for 10 s.

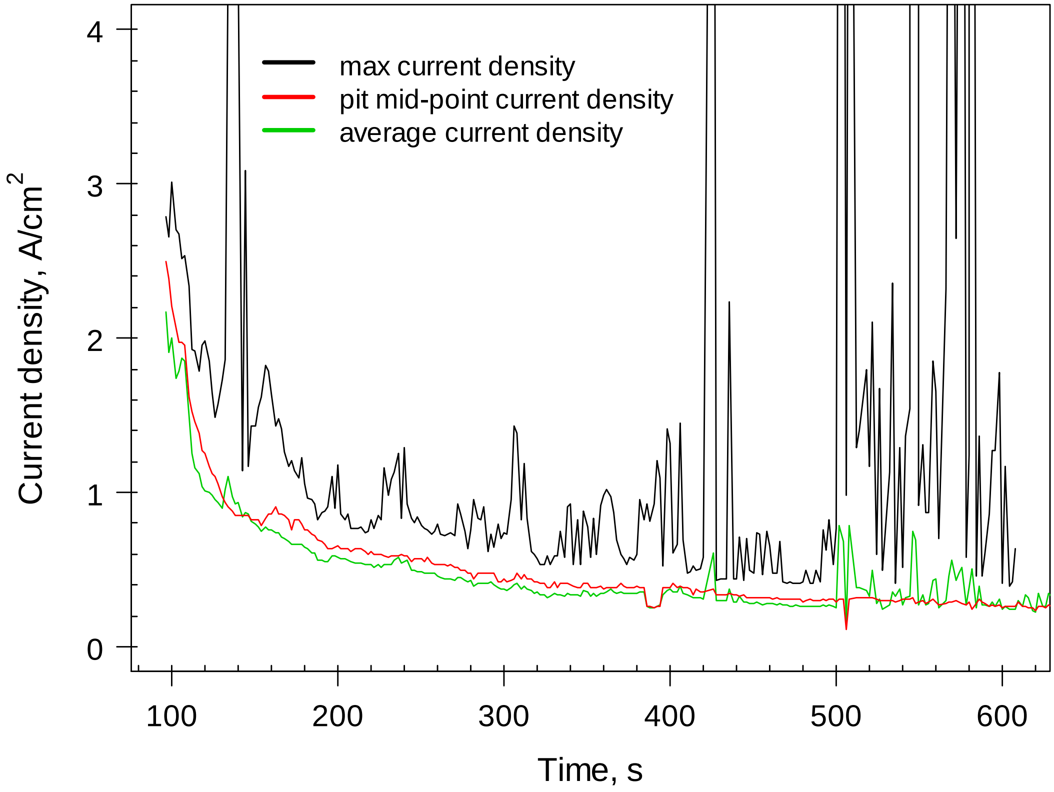

Figure 6-18- Maximum, average and pit mid-point current density along pit boundary as a function of time during growth of the pit grown on 304 stainless steel foil in 0.1 M NaCl at 10 µA following initiation at 650 mV (vs. Ag/AgCl) for 10 s.

6.5 Estimation of effective diffusion coefficient

Once a pit boundary has been segmented, the pit depth profile as a function of time can be obtained. In Chapter 5, the time-dependence of the pit depth was shown to be limited by diffusion of metal ions from the salt film to the bulk solution. In this chapter, the pit growth rate in depth will be used to estimate the diffusivity of metal ions. An effective diffusion coefficient can be estimated from relationship between (pit depth)^2 and time using Faraday's second law in conjunction with Fick's first law for diffusion. Fick's first law can be written as [83, 94, 153]:

Equation 6-3

$$i_{\lim} = zFD\frac{(C_b - C_m)}{x}$$

where $i_{\lim}$ is the diffusion controlled current density, z is the transferred charge (2.2 [82, 111]), F is the Faraday constant (96485 C/mol), D is diffusion coefficient, C_b and C_m are the concentration of metal ions at the pit bottom (or pit surface) and mouth (or bulk solution), respectively, and x is the pit depth. Taking (C_b-C_m) as ΔC and combining with Faraday's 2nd law (Equation 6-2), therefore the relationship between (pit depth)^2 and time is:

Equation 6-4

$$x^2 = \frac{M}{\rho} D.\Delta C.t$$

where, ρ is the metal density, M is the atomic weight and t is time. The value of $D\Delta C$ can be extracted from the slope in the plot of (pit depth)^2 versus growth time, assuming that growth is diffusion-controlled. This approach is investigated in this section for one and two-dimensional growing pits.

6.5.1 1D pit

As explained in Section 2.2.6.1 of literature, extensive work has been done on studying pit electrochemistry and dissolution kinetics using artificial pit electrodes [83, 84, 87, 89]. These electrodes are usually pseudo-one-dimensional cavities with small corroding surface area containing concentrated solutions of metal ions similar to a real pit. In 2D pit (foil electrode) experiments, it is observed that when several simultaneously growing pits reach each other, depending on the corrosivity of the applied conditions, they usually merge and form an almost uniform 1D corroding area which is similar to 1D artificial pit electrodes but with significantly larger corroding area. This concept has been used for comparison of the results obtained from 1D growth in foil electrodes with artificial pit electrodes.

Figure 6-19 shows the process of coalescence of multiple micropits initiated on a 304 stainless steel foil at 1 M NaCl at 650 mV vs. Ag/AgCl. Numerous shallow 2D micropits initiated all along the foil simultaneously (still at second 5) reached each other quickly and coalesced (still at second 10). Further growth continued via general 1D dissolution can be seen in still at second 300. At the resolution of the radiograph, no cover is visible at the original interface of the foil and solution. As the micropits have grown rapidly without the sideways growth of lobes that are necessary for the formation of a porous cover, it is reasonable to assume that such a cover is not present to a sufficient extent to change transport properties.

Figure 6-20(a) shows the pit depth data as a function of time for the pit shown in Figure 6-19. The values are taken from the deepest part of the pit up to the pit mouth (original interface between foil and solution). Accordingly, a graph of pit depth squared against time can be plotted as shown in Figure 6-20(b) where it can be seen that the plot is linear to a good level of approximation. Taking into account Equation 6-4 and considering M=57.6 g.mol^{-1} and ρ=7.82 g.cm^{-3}, therefore from the gradient of the plot, the value of $D\Delta C$ is estimated as 4.36×10^{-8} mol.cm^{-1}s^{-1}. In order to estimate the value of effective diffusivity, it is necessary to estimate values of C_b and C_m. The presence of salt films on the corroding surface of pits growing at relatively high potentials (>200 mV SCE) has been shown [76, 78, 83, 89, 92, 93, 95, 152] and the concentration of metal ions at the pit bottom is likely to be at the saturation concentration, C_{sat} [158]. The concentration of metal ions at the mouth (C_m at x=0) of 1D artificial pits in the literature has been commonly assumed as zero [56, 75, 76, 81, 83-88, 159]. Although C_m may not be exactly zero in the configuration of artificial pits of this work, given that $C_b \gg C_m$ and considering that C_m is decreasing as the pit deepens, therefore C_b-C_m is not very sensitive to the actual values of C_m and it is reasonable assumption to consider $C_b-C_m \approx C_b$.

A saturation concentration of *ca.* 4.2 M as reported by Kuo and Landolt [89] is commonly used in the literature [50, 82, 84, 86, 88]. Assuming this value for C_b, the diffusivity will be 1.03×10^{-5} (cm^2.s^{-1}). However, the diffusivity with C_{sat}=5.1 M as measured by Isaacs [160] will yield D=0.85×10^{-5} cm^2.s^{-1}, which is reasonably close to measured values in literature [82, 84, 89].

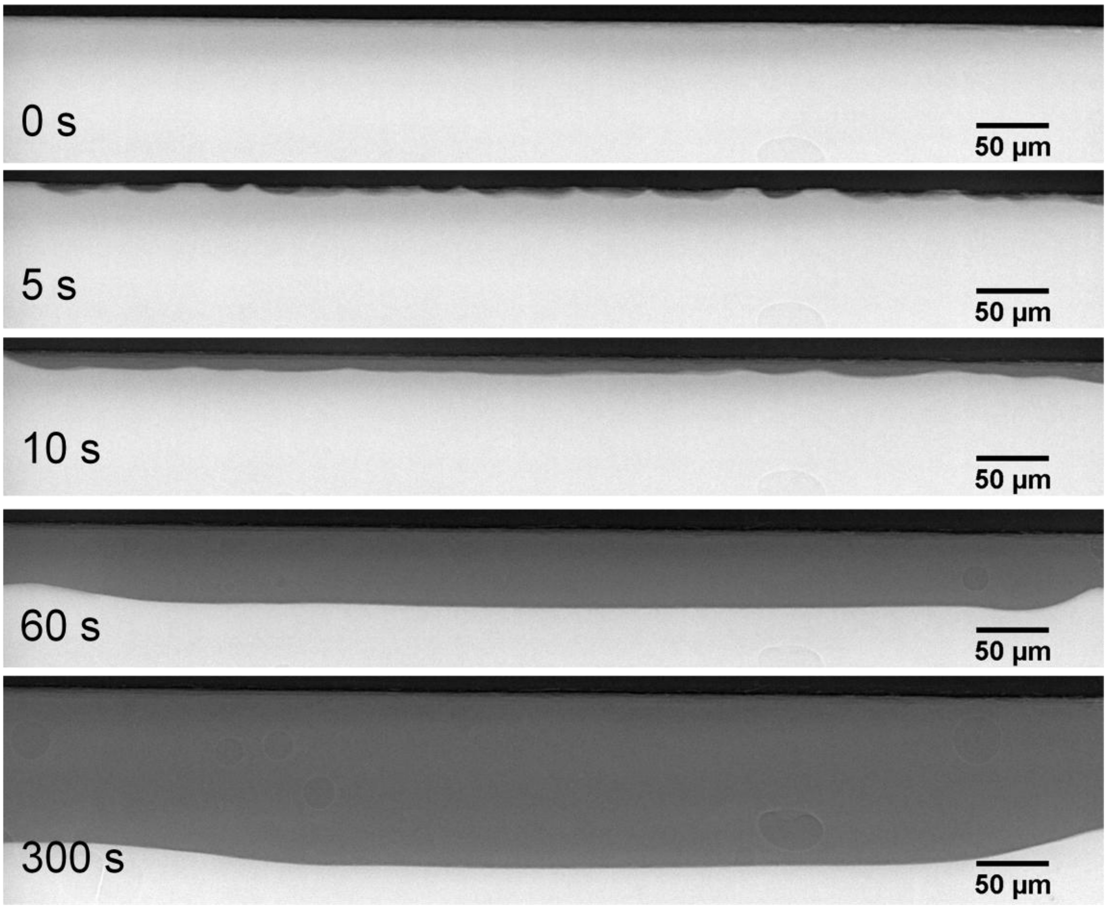

Figure 6-19- pit growth stages on a 304 stainless steel foil at 650 mV vs. Ag/AgCl in 1 M NaCl; shallow dish-shaped micropits initiate all along the surface (still at 5 s) and merge together immediately after (still at 10 s) and general dissolution continues for the rest of experiment. The maximum vertical distance from the pit bottom up to the mouth (original interface between foil and sol) is considered as the pit depth.

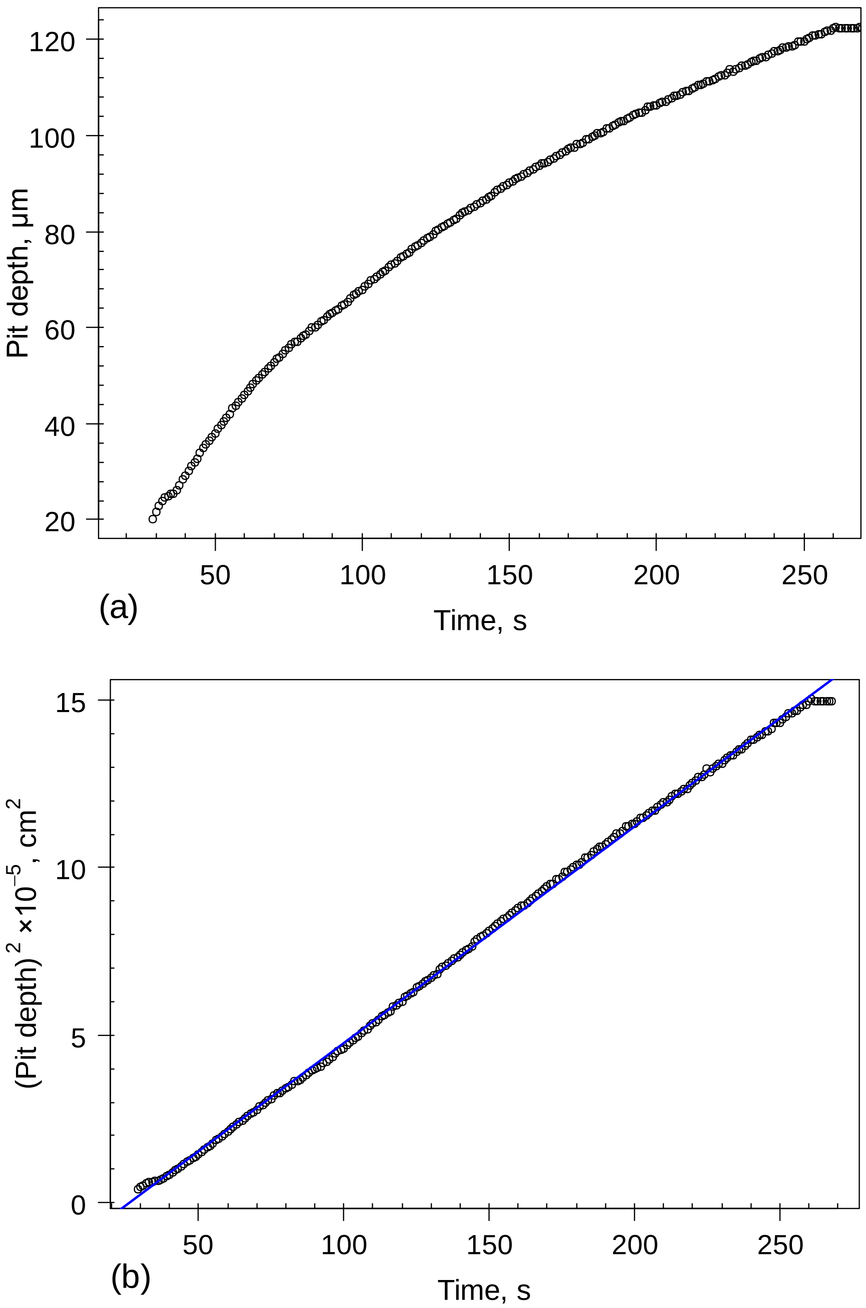

Figure 6-20- (a) pit depth and (b) pit depth squared as a function of time for the pit shown in Figure 6-19 in which generalised dissolution occurs after multiple pits have coalesced on a 304 stainless steel foil at 650 mV in 1 M NaCl. The pit depth values are taken from the deepest part of the pit.

6.5.2 2D pit

The same approach used in the previous section for a 1D pit will be applied to 2D pit propagation: it will be assumed that if the resulting plot of (pit depth)^2 against time is linear, then the diffusion length is equal to the pit depth and furthermore that dissolution is diffusion controlled. Figure 6-21 shows the pit growth stages on a 316L stainless steel foil in 1 M NaCl at 750 mV vs. Ag/AgCl electrode. Whilst experiments were mainly carried out on 304 stainless steel foils some attempts were also made on pitting on the more corrosion resistant alloy 316L stainless steel. It was difficult and not reproducible to initiate pits on 316L type at room temperature (~23 °C) in relatively low chloride concentration. Also, given the higher conventionally measured pitting potential for 316L type [73, 74], a higher potential was applied. The pit propagates in 2D and the maximum vertical distance from the pit mouth is considered to be the depth. Pit depth and pit depth squared as a function of time are shown in Figure 6-22 from which the value of $D\Delta C$ is estimated to be 2.5×10^{-8} mol.cm^{-1}.s^{-1}.

In 2D pits, the metal ions concentration at the pit mouth is affected by the diffusion of metal ions away from the pit mouth into the bulk solution and also the diffusion barrier provided by the lacy metal cover. It is worth noting that although 1D artificial pit experiments are usually carried out on deeper pits (with longer diffusion length) than those shown here, the effect of a perforated cover at the pit mouth as a diffusion barrier should still be considered in the transport of ions towards the bulk solution. Considering the suppressing effect of cover as a barrier in metal ions transport for a 2D pit and again taking into account that $C_b \gg C_m$ as noted above, C_m is taken as zero in the effective diffusion calculation for 2D pits. Therefore , the effective diffusivity values of 0.597×10^{-5} and 0.492×10^{-5} cm^2.s^{-1} are obtained assuming that C_{sat} = 4.2 and 5.1 M, respectively, which are less than the literature values discussed above.

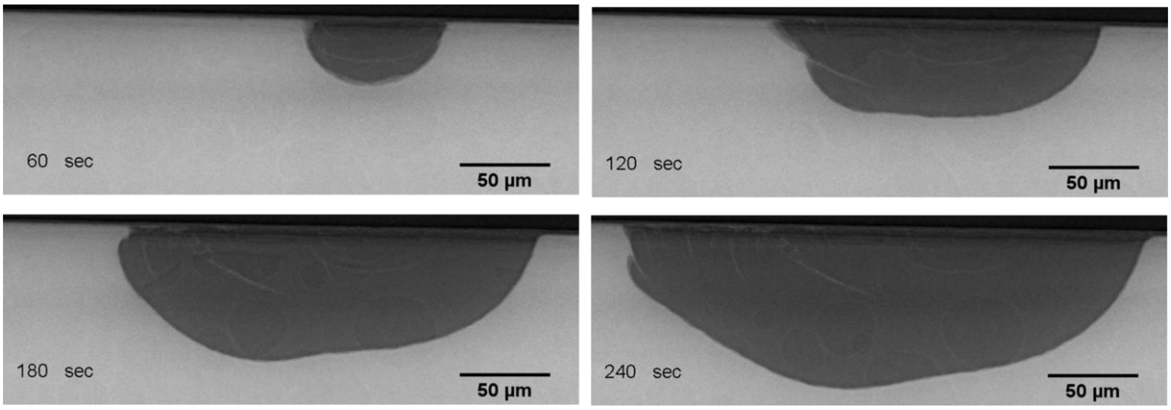

Figure 6-21- Stages of pit growth in a 316L stainless steel foil at 750 mV vs. Ag/AgCl in 1 M NaCl

Figure 6-23 shows multiple pits growing simultaneously on a 304 stainless steel foil after 45 s in 0.1 M NaCl at 650 mV vs. Ag/AgCl reference electrode. The pit depth squared relation with time for each pit and the associated $D\Delta C$ values obtained are shown in Figure 6-24. Apart from one pit where $D\Delta C$ is 1.65×10^{-5} cm^2.s^{-1}, the others show reasonably close values to each other.

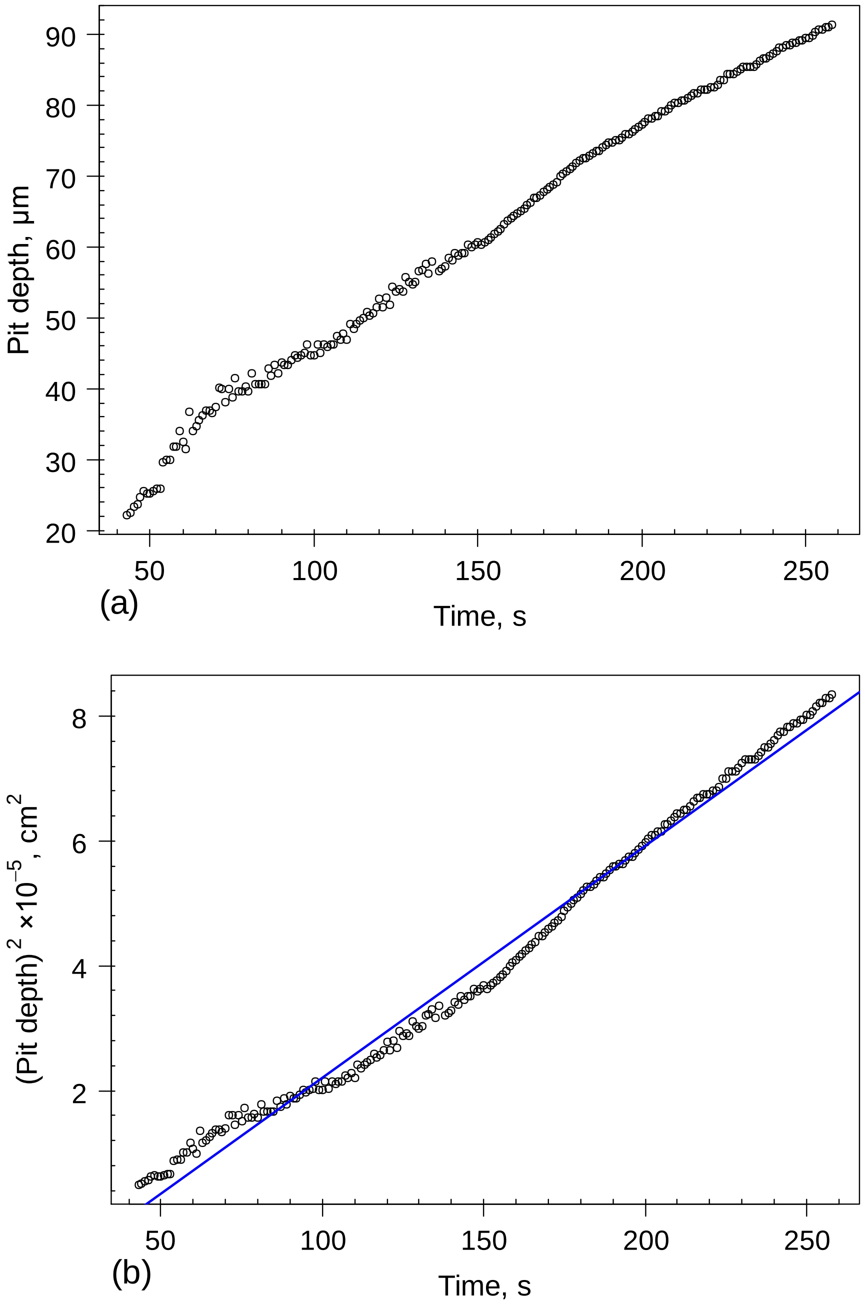

Figure 6-22- (a) Pit depth and (b) (pit depth)^2 as a function of time for a 2D pit in 1 M NaCl at 750 mV vs. Ag/AgCl shown in Figure 6-21

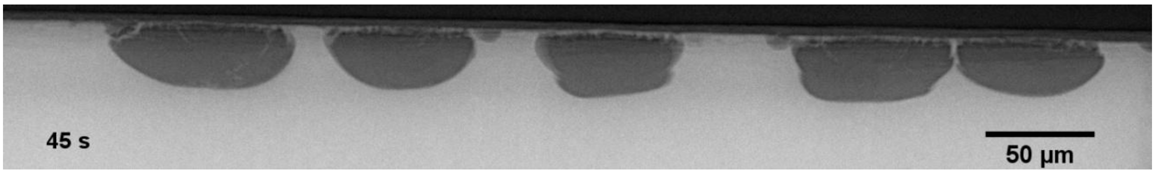

Figure 6-23- Multiple growing pits simultaneously together on 304 stainless steel foil at 650 mV vs. Ag/AgCl in 0.1 M NaCl after 45 s.

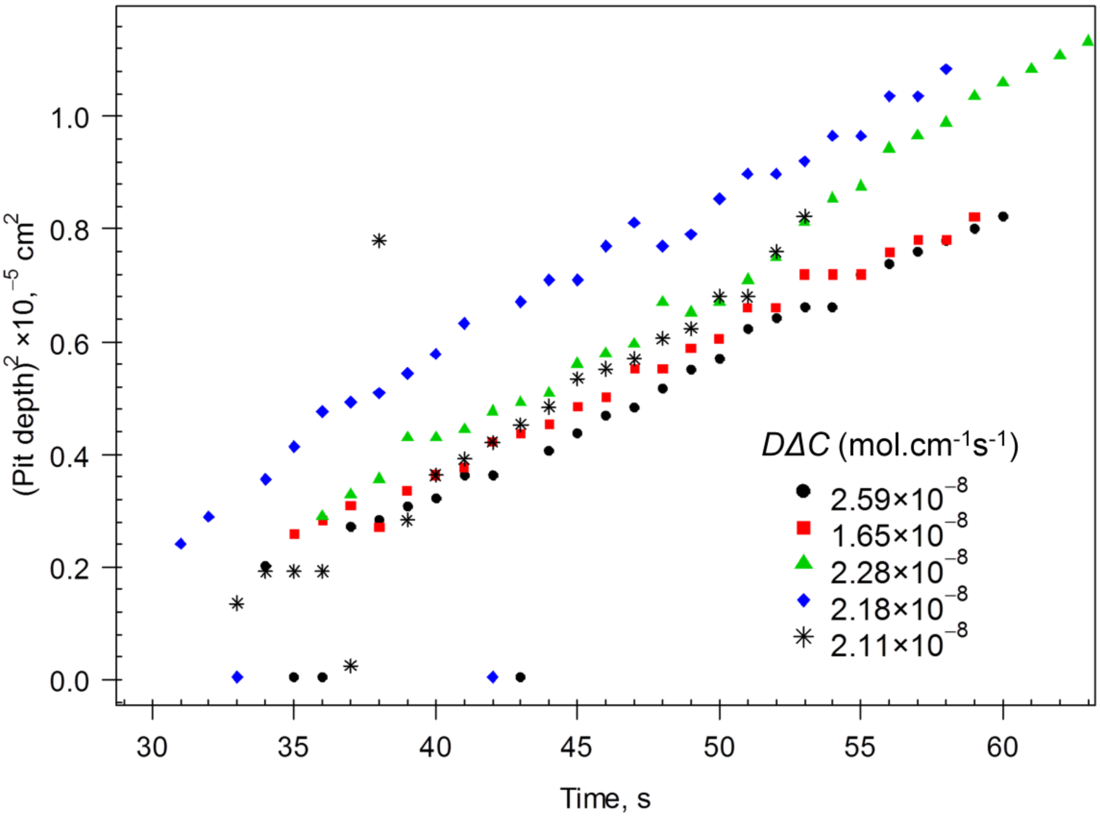

Figure 6-24- (pit depth)^2 vs. time for multiple pits growing together shown in Figure 6-23. The values of *DΔC* are estimated from the slope. The zero values are given from errors in pit boundary detection and were not included in slope estimation.

Figure 6-25(a) and (b) show the pit depth and (pit depth)^2, respectively as a function of time for a single pit growing on a 304 stainless steel foil in 0.1 M NaCl at 10 µA after 10 s initiation at 650 mV vs. Ag/AgCl. The *DΔC* value is estimated 1.59×10^{-8} mol.cm^{-1}.s^{-1} from the slope of plot in Figure 6-25(b).

For pits under galvanostatic control, it is shown that the surface concentration of metal ions gradually decreases from the saturation value at the initial stages of growth to the critical concentration required for propagation, C_{crit} [141] and then pit is able to continue the growth under steady state at C_{crit}. However, for simplicity in this calculation, and as the slope of the plot shows no variation, the concentration at the pit bottom is assumed to be C_{sat} and 4.2 M, and an effective diffusivity of 0.37×10^{-5} $cm^2.s^{-1}$ is obtained.

Table 6-1 summarised the $D\Delta C$ and effective diffusion coefficient values obtained for pits on different conditions assuming $C_{sat} = 4.2$ M. It may be seen that the diffusivity values obtained for 2D pits are all lower than the value measured in 1D growth shown in Figure 6-20 and the literature values for 1D pit. Slight variation around ~ 0.4 is seen in potentiostatic pits grown in 0.1 M (pits No. 3 to 18) whilst wide variation is seen for the diffusivity values of pits grown in lower chloride concentrations of 0.01 and 0.005 M (pits No. 19 to 23). This variation is smaller in galvanostatically grown pits (No. 24 to 30).

Using this approach, an average value of effective diffusion coefficient over the range of concentration within the 2D pit is estimated. It would be expected that it may change to some extent with the pit geometry but in fact the most likely cause of the variation in the measured effective diffusivity is from the variation in the cover perforation. In the 1D pit, where it is likely that no cover exists (similar to the common 1D artificial pits in the literature), the maximum effective diffusivity is observed, which is in agreement with the values reported in the literature. However, the decrease in effective diffusivity obtained for 2D pits can be attributed to the effect of the pit cover. It may be assumed that scatter reflects variable degrees of coveredness over a pit. The effective diffusion coefficient obtained with this method will be considered together with the transport processes and calculation of metal ion concentration in the next section.

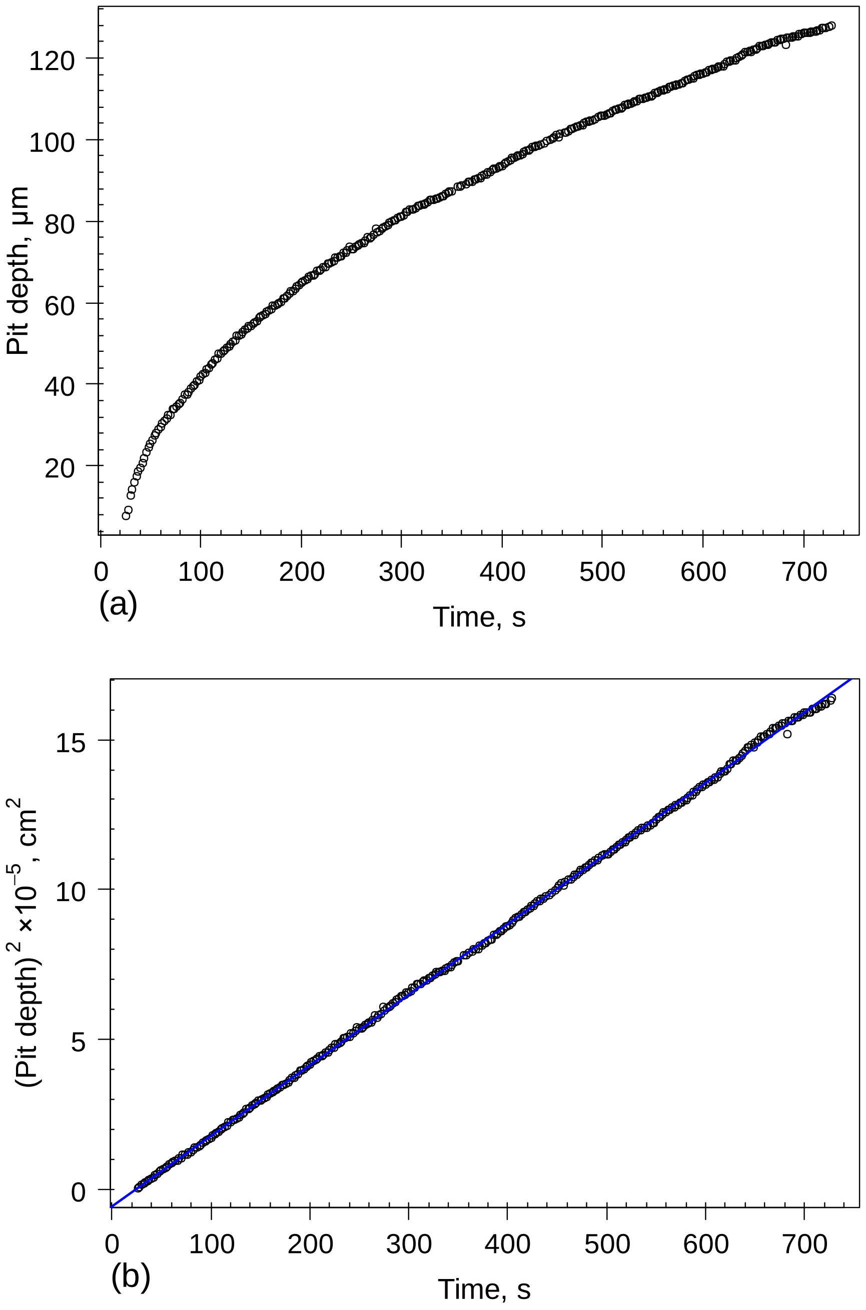

Figure 6-25- (a) Pit depth and (b) (pit depth)^2 as a function of time for a pit grown in 0.1 M NaCl at 10 µA current after 10 s at 650 mV vs. Ag/AgCl.

Table 6-1- *DΔC* and the effective diffusion coefficient calculated for pits grown in different conditions indicated assuming C_{sat}=4.2 [89]. The pit reported in the 1st row is a 1D general dissolution in 304 stainless steel foil, while other pits all grow as 2D. All pits were grown in 304 foil, unless otherwise stated.

No.	[NaCl] (M)	E (mV)*	I (µA) †	$D\Delta C \times 10^8$ (mol.cm^{-1}.s^{-1})	$D \times 10^5$ (cm^2.s^{-1})	Notes
1	1	650		4.360	1.035	1D pit
2	1	750		2.509	0.597	316L SS, single pit
3	0.1	650		2.074	0.494	**3,4,5
4	0.1	650		1.919	0.457	
5	0.1	650		2.296	0.547	
6	0.1	650		2.023	0.482	
7	0.1	650		2.058	0.490	
8	0.1	650		1.874	0.446	
9	0.1	650		1.052	0.250	
10	0.1	650		1.799	0.428	
11	0.1	650		1.986	0.473	
12	0.1	650		2.288	0.545	
13	0.1	650		2.661	0.634	
14	0.1	650		1.684	0.401	
15	0.1	650		1.655	0.394	
16	0.1	650		2.282	0.543	
17	0.1	650		2.182	0.519	
18	0.1	650		2.116	0.504	
19	0.01	650		3.749	0.893	One of two pits (other under resin)
20	0.01	550		3.555	0.846	One of two pits (other under resin)
21	0.01	600		0.832	0.198	single pit
22	0.005	650		1.790	0.426	single pit
23	0.005	650		4.110	0.979	**
24	0.1		50µA	2.296	0.547	One of two pits (other under resin)
25	0.1		10µA	1.590	0.379	single pit
26	0.1		10µA	1.775	0.423	single pit
27	0.1		20µA	1.600	0.381	One of two pits (other under resin)
28	0.01		10µA	1.534	0.365	One of two pits (other under resin)
29	0.01		20µA	1.499	0.357	One of two pits (other pit No. 30)
30	0.01		20µA	1.512	0.360	One of two pits (other pit No. 29)

* Potentiostatic mode: E (mV vs. Ag/AgCl)

**multiple pits from same experiment (other pits in same experiment listed)

† Galvanostatic mode: pit initiated under potentiostatic conditions at 650 mV (Ag/AgCl) for 10 s and then grown at the current indicated I (µA).

6.6 Back-calculation of local metal ion concentration and potential drop in solution

6.6.1 Method description

Having measured the local current density inside the pit, it is then possible to back-calculate the local metal ions concentration and potential drop in solution. As described earlier in Section 2.2.2, an aggressive solution inside a pit cavity is required to sustain active dissolution. The aggressive chemistry is provided by metal cations, which generate a low pH by metal hydrolysis as per Equation 2.1 and 2.2, and a correspondingly high chloride concentration for charge balance. The chemistry inside a pit is controlled by the balance between the rate at which metal cations are dissolved into the solution and the rate at which ions diffuse away from metal surface and are transported towards the outside of the pit.

Within the pit cavity, the fluid can be assumed to be entirely stagnant and mass transport is therefore only due to concentration and potential gradients. The electrochemical transport equation applicable to infinitely dilute solutions is the Nernst-Einstein equation, which has been used in calculating concentration within pits [56, 84] and is currently used for modelling localised corrosion in stainless steel [7].

6.6.2 Transport equations

In this work, transport equations are solved for two-dimensional (within the pit) and three-dimensional (within the cell) systems. As noted above, the transport equations used here were developed for infinitely dilute solutions, but are applied here to highly concentrated solutions. Furthermore, a single value of diffusivity is used for all of the species in the system.

The transport equations are used here to back-calculate the distribution of metal ions in the pit, providing the concentration of metal ions adjacent to the dissolving metal, and the potential gradients within the solution, providing the interfacial potential across the dissolving interface. This enables determination of a key input parameter to the pit prediction model: the current density as a function of metal ion concentration and interfacial potential. This parameter can be extracted from the measured current density at each point along the pit perimeter at each time step and the back-calculated values of metal ion concentration and interfacial potential difference at each point.

Based on conservation of mass, the transport equations are solved considering the boundary conditions defined below. The transport equations for charged species are [7, 56]:

Equation 6-5
$$N_i = -D_i \nabla C_i - \frac{z_i F D_i}{RT} C_i \nabla \phi$$

Equation 6-6
$$\frac{\partial C_i}{\partial t} = -\nabla N_i$$

where N_i is the molar flux of metal ions into solution, C_i is the concentration and D_i is the diffusion coefficient of the species, ϕ is the electrical potential, t is the time, T is the temperature and R is the gas constant. The first term in Equation 6-5 considers the effect of diffusion and the second term takes into account the effect of electrical gradient force (migration) in ions transport. Ohm's law gives the current in solution as:

Equation 6-7
$$-\sigma \nabla \phi = i$$

where σ is conductivity and based on the dilute solution theory given by:

Equation 6-8
$$\sigma = \frac{F^2}{RT} \sum_i D_i z_i^2 C_i$$

The solution is assumed electrically neutral based on the conservation of charge. Therefore, electroneutrality reduces Equation 6-7:

Equation 6-9
$$\nabla \cdot i = 0$$

Boundary conditions are set for the pit cavity as below:

At the pit bottom:

Equation 6-10
$$N_i = -\frac{i_a}{zF}$$

At the pit mouth and outside pit C_M =0 and at the counter electrode ϕ =0.

The D_i in Equation 6-5 is taken as the effective diffusion coefficient estimated from the (pit depth)^2 relationship with growth time in Section 6.5 to consider the effect of pit cover barrier in the ions transport from inside the pit towards the bulk solution. A single diffusion coefficient of 1×10^{-5}cm^2/s [7, 50] is assumed for all diffusion species in the calculation of conductivity in Equation 6-8.

6.6.3 Back-calculation process

The *x* and *y* coordinates of pit (normally from the first frame in which the ImageJ "pit filter" is able to detect a pit) are read by FreeFEM++ software [161] and a triangular mesh of the pit cavity and its surrounding area (Figure 6-26) is produced. This is carried out for each frame in the pit growth video. At each time step, the mesh then is used in calculating the pit boundary movement, the local current density and solving transport equations and determining the potential distribution within the pit.

The basis of the back-calculation procedure is to calculate the metal ions concentration and potential distribution given the current density on the pit boundary and the concentration calculated from the previous time step. Therefore, to start the process at time *t*, the concentration at time *t-dt* is required. The concentration at the first time step is given by solving the diffusion equations (Equation 6-11) with $C_M=C_{sat}$ on the pit boundary, $C_M=0$ at the pit mouth, assuming that $i=0$ on the pit boundary and that the pit is at steady state:

Equation 6-11

$$\nabla\cdot D_i\nabla C_M = 0$$

where D_i is the diffusion coefficient of metal ions. Having known the concentration at any point within the pit at the previous time step, then the concentration of metal ions and the potential distribution within the pit at present time as a result of the anodic current density of i_a on the pit surface is calculated by solving the Equation 6-6 and Equation 6-7. The analysing steps at time *t* are as follows:

1. Initialise the starting condition of C_M and ϕ at time t
2. The *x* and *y* coordinates for the pit at *t* and *t+dt* are read. The latter pit coordinates are used to calculate the boundary velocity and hence the current density and molar flux on the pit boundary at time *t*.
3. Calculate i_a from the pit boundary velocity.
4. Calculate metal ion flux, N_i, at the pit boundary.

5. Calculate new distribution of C_M and ϕ (iterative process as C_M is required for conductivity and ϕ is required for electrolytic migration).
6. Move the pit boundary to $xy(t+dt)$ and interpolate C_M and ϕ for the new positions.
7. Define $t+dt$ as t, go to 1.

The finite element running scripts are attached in Appendix A.6.3 and A.6.4.

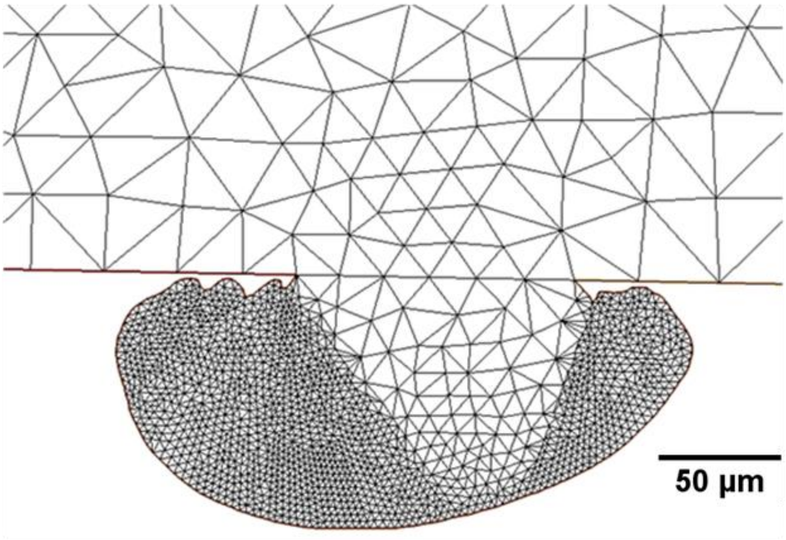

Figure 6-26- Triangular mesh of the pit cavity and its surrounding area shown in Figure 6-2

6.6.4 Electrochemical cell resistance

In order to calculate the potential drop in the back-calculation process, it is necessary to know the resistance of each component of the electrochemical system. The resistance of a single growing pit comprises the resistance of solution inside the cavity, the perforated cover interfacing pit with bulk solution, and the resistance of external bulk solution. Frankel [102] has shown the dependence of pit resistance upon the number and radius of pores in a pit cover in stainless steel. It is not possible to observe and detect accurately the pores within radiographs; however, it is possible to measure the pit mouth size (the perforation extent) during pit growth.

In a galvanostatic case where the applied current is constant, the potential changes directly with fluctuations in the resistance. The solution inside the pit has a high conductivity. If it is assumed that the resistance in the bulk solution (outside the pit) does not change significantly during growth, it is possible to relate changes in potential (or IR drop) with the development of perforations in the pit cover and changes in the geometry of the pit mouth, and accordingly the resistance component of the perforated cover. Figure 6-27 shows typical growth of a galvanostatic pit at a current of 10 μA (following initiation at 650 mV vs. Ag/AgCl for 10 s. Figure 6-28 and Figure 6-30 show the pit mouth width as a function of time for two single-pits of the type shown in Figure 6-27 and grown under the same condition in two independent measurements. The pit mouth width changes stepwise with time; it initially increases linearly with time due to high number of perforations of the cover at early stages, and then as the pit enlarges it remains unchanged for the period required for a developing lobe to perforate the top metal surface producing a jump in the plot of mouth width vs. time.

The potential is shown as a function of the reciprocal of pit mouth width (from Figure 6-28 and Figure 6-30) in Figure 6-29 and Figure 6-31. At the initial stages of pit growth, the potential is unstable and gradually decreases at the pit mouth width increases owing to the increasing number of perforations in the cover. It is notable that as the pit grows, corroding surface area increases and hence resistance should reduce. However, the drops in applied potential do correlate with new perforations (the step in mouth plot) in the cover. Once the pit grows large enough, propagation occurs with larger lobes and perforation is less effective in decreasing the cover resistance. Therefore, the potential fluctuates less and decreases more smoothly with enlargement of the corroding surface and mouth.

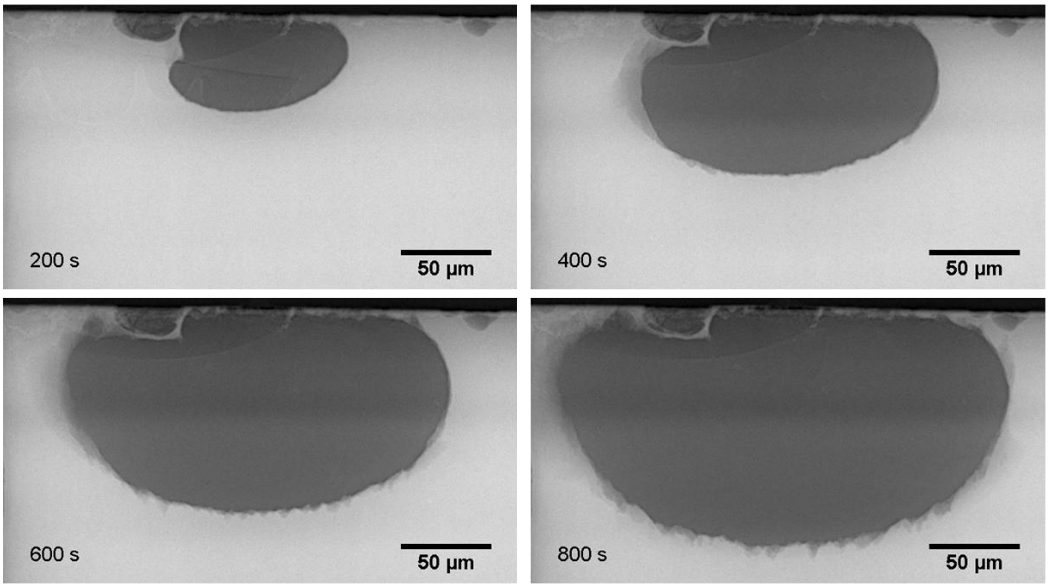

Figure 6-27- Radiographs of the growing pit in 0.1 M NaCl at 10 μA current applied after 10 s initiation at 650 mV vs. Ag/AgCl.

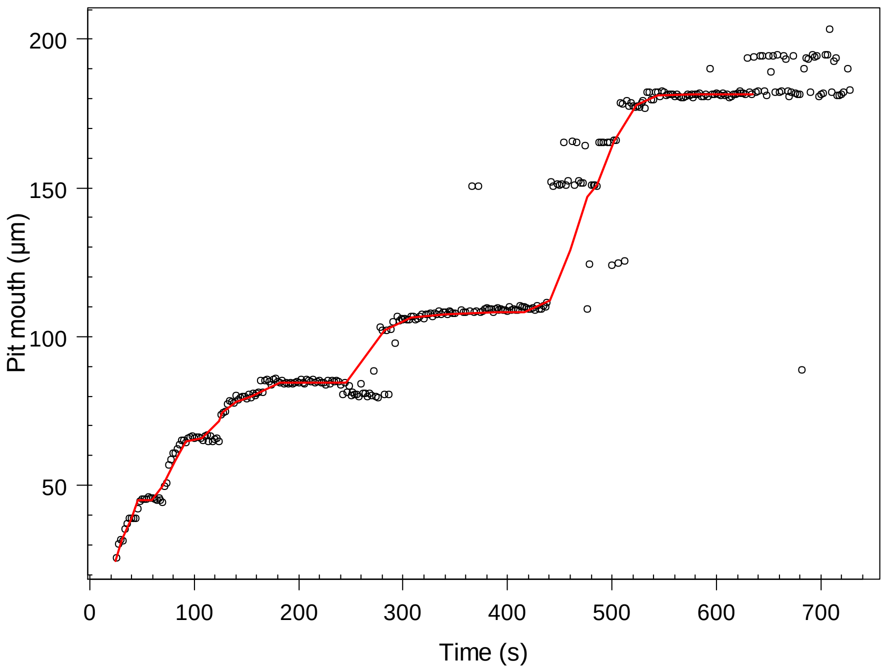

Figure 6-28- Pit mouth size as a function of time for a single pit growing in 0.1 M NaCl at 10 µA current after initiation at 650 mV vs. Ag/AgCl for 10 s. The red line is the result of applying a smoothing function to the data. The scattered points are errors in detecting edge boundary. The values were extracted automatically from pit boundary coordinates data of the type shown in Figure 6-3 using the routine described in Section 6.2.2 and Appendix A.6.1. The scatter in data is associated with the errors in detecting pit boundary by the customised filter in ImageJ.

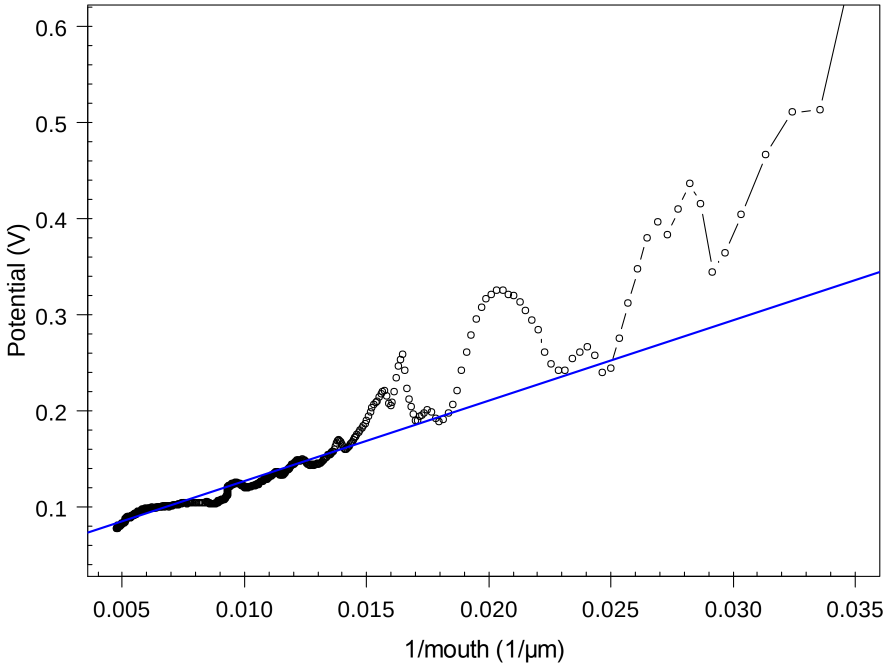

Figure 6-29- Applied potential fluctuations as a function of the reciprocal of pit mouth width for the single pit described in Figure 6-28. The potential is plotted against the smoothed values of mouth size shown in red in above figure. Blue line shows the slope.

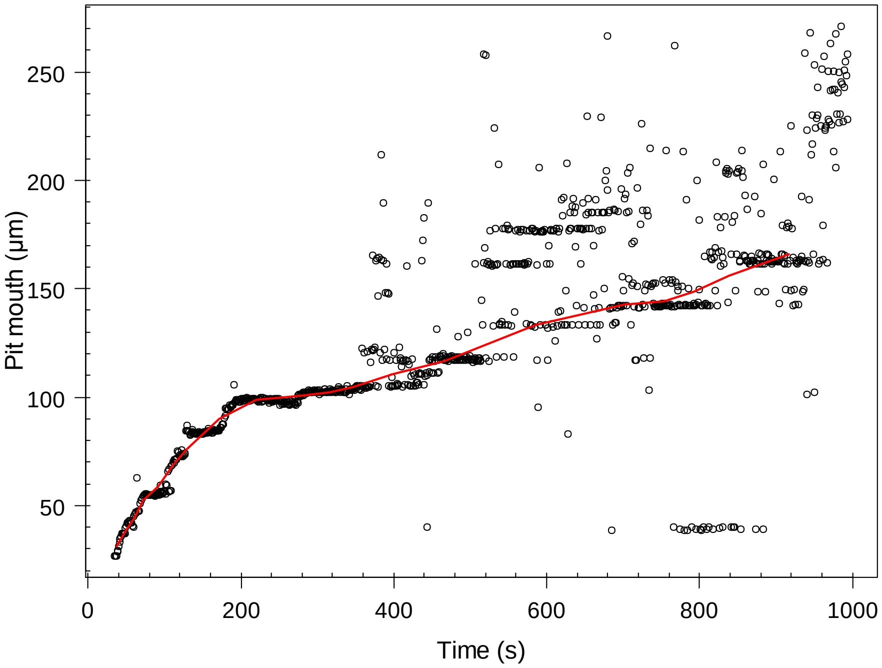

Figure 6-30- Pit mouth size as a function of time for a single pit growing in 0.1 M NaCl at 10 µA current after initiation at 650 mV vs. Ag/AgCl for 10 s. The red line is the result of applying a smoothing function to the data. The scattered points are errors in detecting edge boundary. The values were extracted automatically from pit boundary coordinates data of the type shown in Figure 6-3 using the routine described in Section 6.2.2 and Appendix A.6.1. The scatter in data is associated with the errors in detecting pit boundary by the customised filter in ImageJ.

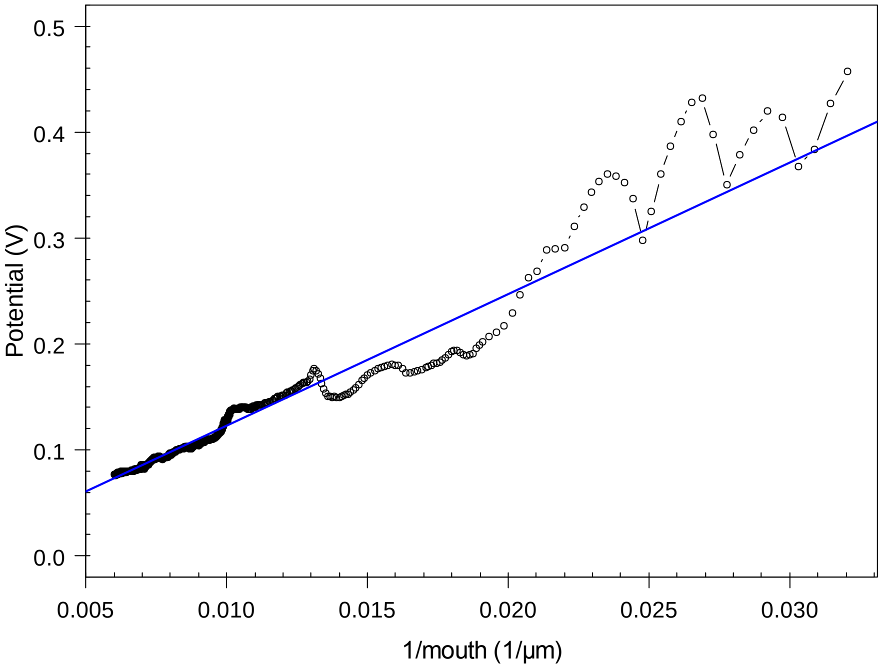

Figure 6-31- Applied potential fluctuations as a function of pit mouth size for the single pit described in Figure 6-30. The potential is plotted against the smoothed values of mouth size shown in red in the above figure. Blue line shows the slope.

6.6.5 Estimation of external solution resistance

A finite element method is developed for estimating the cell resistance of the setup shown in Figure 3-1. Assuming constant solution conductivity, σ, the potential satisfies Laplace's equation in solution. Therefore:

$$\nabla^2\phi = 0 \qquad \textbf{Equation 6-12}$$

the boundary condition at the working electrode (WE) is

$$\sigma\frac{\partial\phi}{\partial n} = i \qquad \textbf{Equation 6-13}$$

where n is the normal direction to the pit surface boundary. At the counter electrode (CE) $\phi = 0$, thus the solution resistance is

$$R = \frac{\gamma}{\sigma} \qquad \textbf{Equation 6-14}$$

where γ is the 'geometrical factor':

$$\gamma = \frac{\max\phi}{\int\frac{\partial\phi}{\partial n}dA} \qquad \textbf{Equation 6-15}$$

Finite element analysis can be used to solve for the potential in solution by using a suitable tetrahedral mesh as shown in Figure 6-32. Results are summarised in Figure 6-33, which gives 1/ γ as a function of the pit mouth size, w. The linear regression line gives the approximate relationship:

$$\frac{1}{\gamma} = 0.025 + 0.21w \qquad \textbf{Equation 6-16}$$

from which electrical resistance for the solution in the cell can be given by:

$$R(\Omega) = \frac{1000}{0.025 + 0.21w(\mathrm{mm})}\frac{1}{\sigma(\mathrm{S/m})} \qquad \textbf{Equation 6-17}$$

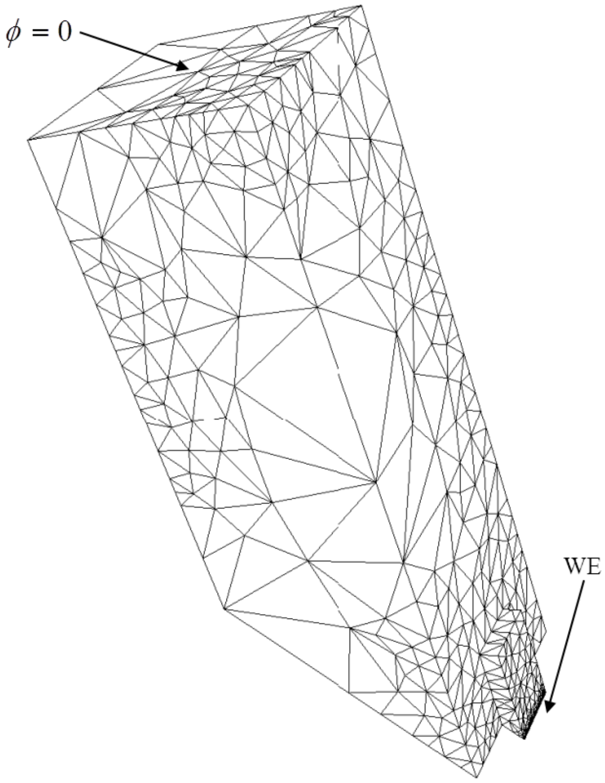

Figure 6-32- Finite element mesh of the electrochemical cell shown in Figure 3-1

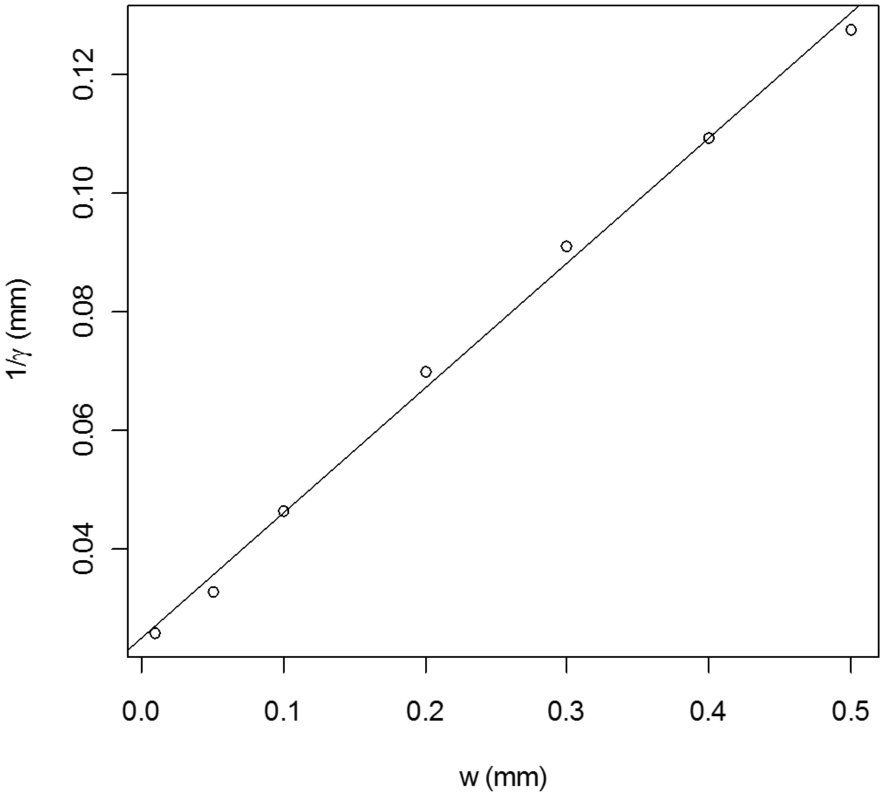

Figure 6-33- Finite element analysis results of the geometrical factor (1/ γ) in resistance as a function of the pit mouth size

In reality the solution conductivity close to the pit mouth is not constant when the pit is growing. Chloride enters the pit creating a local increase in conductivity at the pit mouth. Because of the cell geometry, which has its narrowest restriction at the cell mouth, the resistance to the pit drops significantly. A high bulk concentration of chloride (or a deep pit) is required to mitigate this effect.

6.6.6 Calculation of the external IR drop

Having estimated the resistance in bulk solution within the cell during pit growth, the IR drop in solution can be calculated with the current generated from anodic dissolution from pit cavity. Figure 6-34 shows the calculated external IR drop comparison with the applied potential for a pit grown in 0.1 M NaCl at 10 μA as shown in Figure 6-27. The conductivity of bulk solution is taken as 1.07 S/m [82]. It can be seen that fluctuation in calculated IR corresponds to potential changes with time confirming the dependence of resistance upon the size of the pit mouth and extent of perforation in the cover.

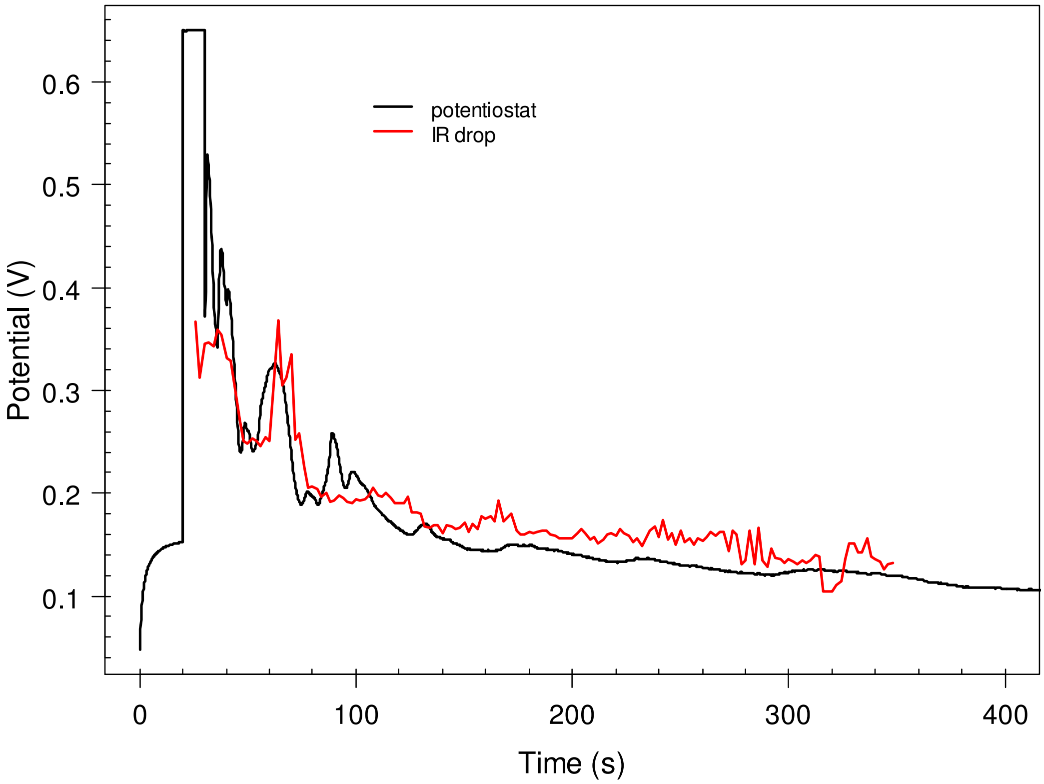

Figure 6-34- Comparison of the calculated IR drop within the bulk solution with applied potential for the single pit shown in Figure 6-27.

6.7 Back-calculated metal ion concentrations

The metal ion concentrations within the pit can be calculated by determining the amount of ions injected into the solution by local dissolution and then solving transport equations via finite element methods as described in Section 6.6. The back-calculated metal ions concentrations within the 2D pits grown under different conditions are presented in this section.

The concentration of metal ions inside pits under potentiostatic control at different chloride concentration of bulk solutions are shown in Figure 6-35 to Figure 6-37. Figure 6-35 shows the radiograph and concentration of metal ions within a pit grown in 0.1 M NaCl at 650 mV vs. Ag/AgCl after (a) 25 and (b) 94 s. The conductivity of bulk and pit solution are considered as 1.07 S/m and 20 S/m [82]. An effective diffusion coefficient of 0.54×10^{-5} cm^2s^{-1} (from pit No. 5 in Table 6-1, estimated based on the method described in Section 6.5) is applied in calculation to consider the effect of pit cover barrier in ions transport. The highest metal ion concentration is seen along the pit boundary and it gradually decreases within the solution towards the pit mouth. On the pit surface, the concentration is close to zero near the pit rim, and it gradually increases down to the pit bottom. As the pit grows, shown in Figure 6-35(b), the metal ion concentration on the pit surface increases.

The radiographs and the metal ion concentration inside the pit grown in 0.01 M NaCl at 600 mV vs. Ag/AgCl after (a) 124 and (b) 316 s are shown in Figure 6-36. The bulk solution conductivity is taken as 0.118 S/m [82] and an effective diffusion coefficient of 0.198×10^{-5} cm^2s^{-1} from pit No. 21 in Table 6-1 is considered in calculation. A highly concentrated solution of ~5.7 M is seen in the lower right developing lobe of the pit at 124 s (Figure 6-36(a)) while the rest of the pit surface is repassivated and the concentration decreases towards the pit mouth. At 316 s, the majority of the pit surface is stably growing with the concentrations higher than ~ 2.5 M.

Figure 6-37 shows the radiograph and the metal ion concentration gradient within the pit grown in 0.005 M NaCl at 650 mV vs. Ag/AgCl after (a) 81 and (b) 274 s. The conductivity of the bulk solution is considered as 0.06 S/m [162]and the effective diffusion coefficient is taken as 0.426×10^{-5} cm^2s^{-1} from pit No. 22 in Table 6-1. The highest concentration of metal ions is seen over the region of small pit within the pit where it is actively growing and the other part of the pit is repassivated. The concentration gradient decreases along the pit surface toward the pit rim. At 274 s after pit initiation, the pit is stably growing with the maximum concentration at the pit bottom and at its developing lateral lobes.

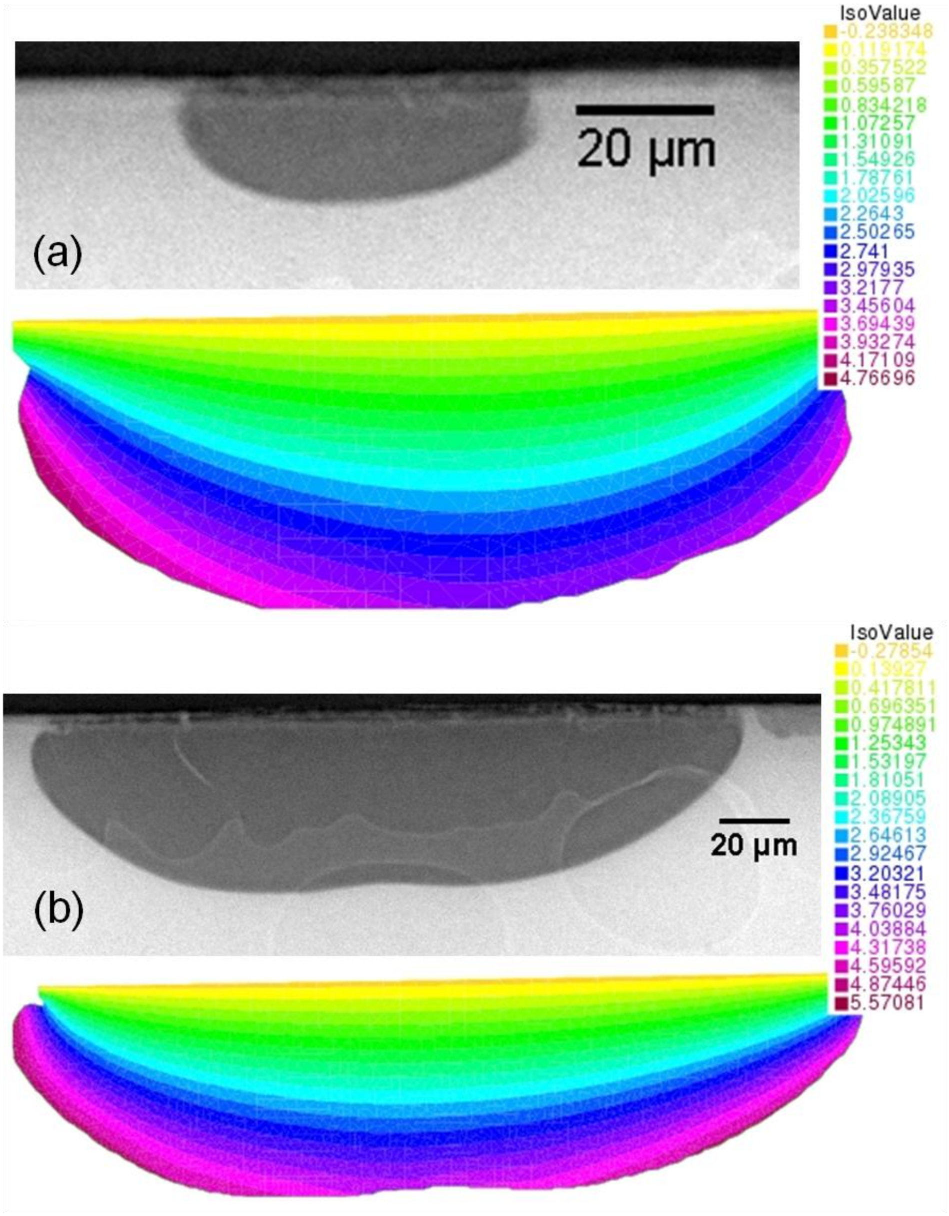

Figure 6-35- Radiograph and concentration gradient inside the pit grown on 304 stainless steel foil in 0.1 M NaCl at 650 mV vs. Ag/AgCl for (a) 25 and (b) 94 s. The iso plots show the concentration gradient (M).

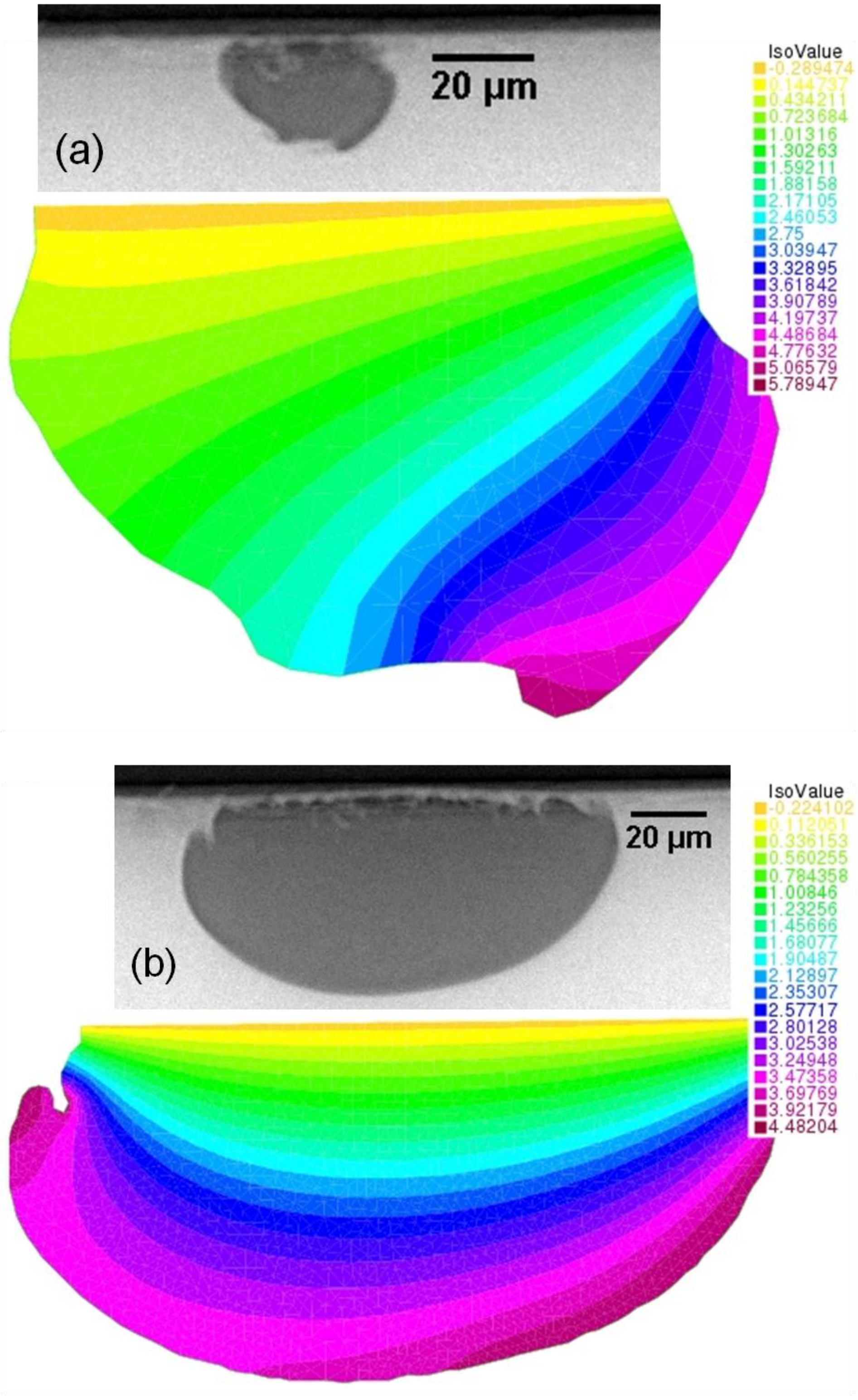

Figure 6-36- Radiograph and concentration gradient inside the pit grown on 304 stainless steel foil in 0.01 M NaCl at 600 mV vs. Ag/AgCl for (a) 124 and (b) 316 s. The iso plots show the concentration gradient (M).

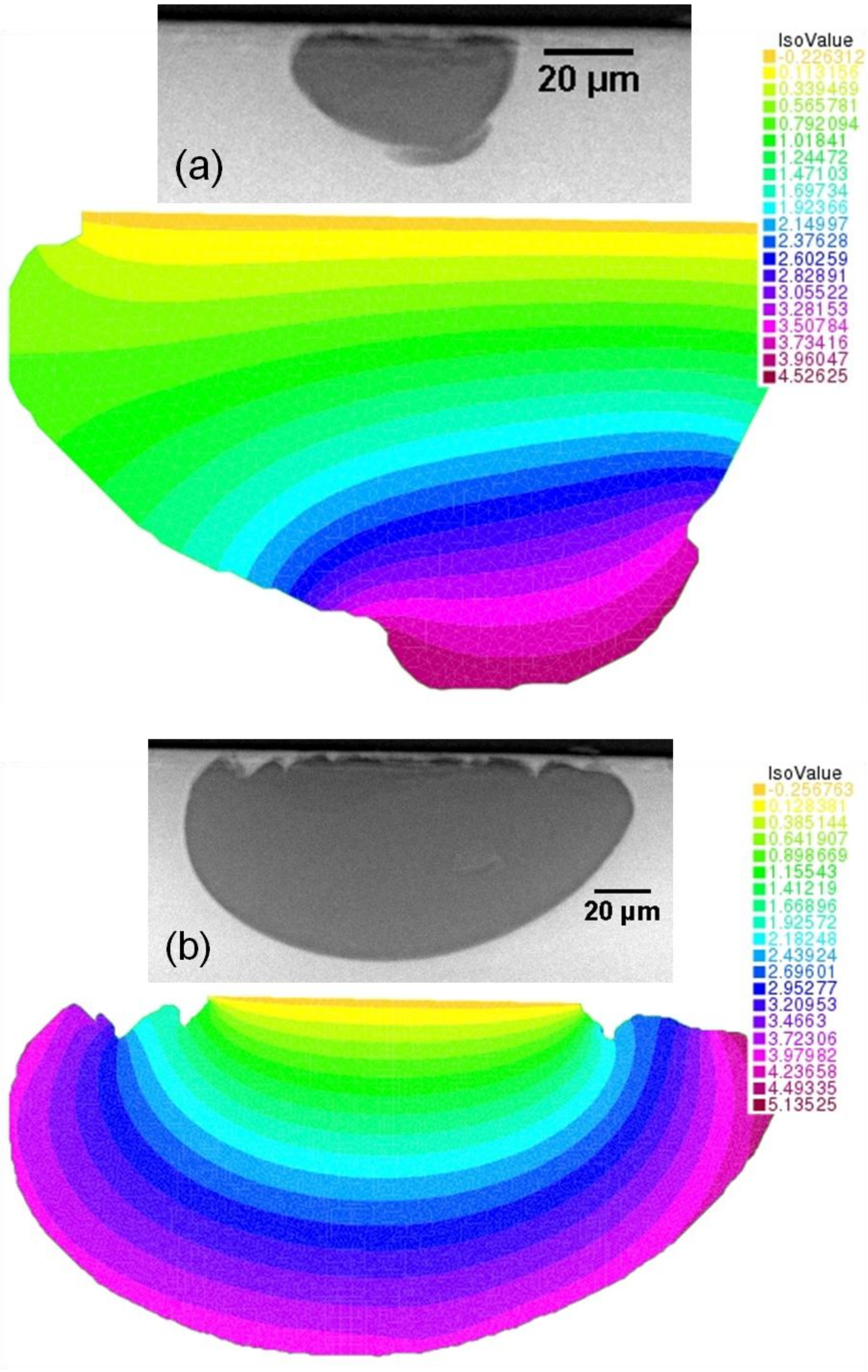

Figure 6-37- Radiograph and concentration gradient inside the pit grown on 304 stainless steel foil in 0.005 M NaCl at 650 mV vs. Ag/AgCl for (a) 81 and (b) 274 s. The iso plots show the concentration gradient (M).

Figure 6-38 shows the radiograph and metal ion concentration inside the pit galvanostatically grown in 0.1 M NaCl at 10 µA after (a) 39 and (b) 145 s preceded by 10 s initiation at 650 mV vs. Ag/AgCl. An effective diffusion coefficient of 0.423×10^{-5} cm^2s^{-1} from pit No. 26 in Table 6-1 is taken in calculation. After 39 s, the most concentrated solution is seen over the right side developing lobe while the concentration gradually decreases towards the pit mouth. At 145 s, the concentration at the pit bottom has decreased to 3.8 M.

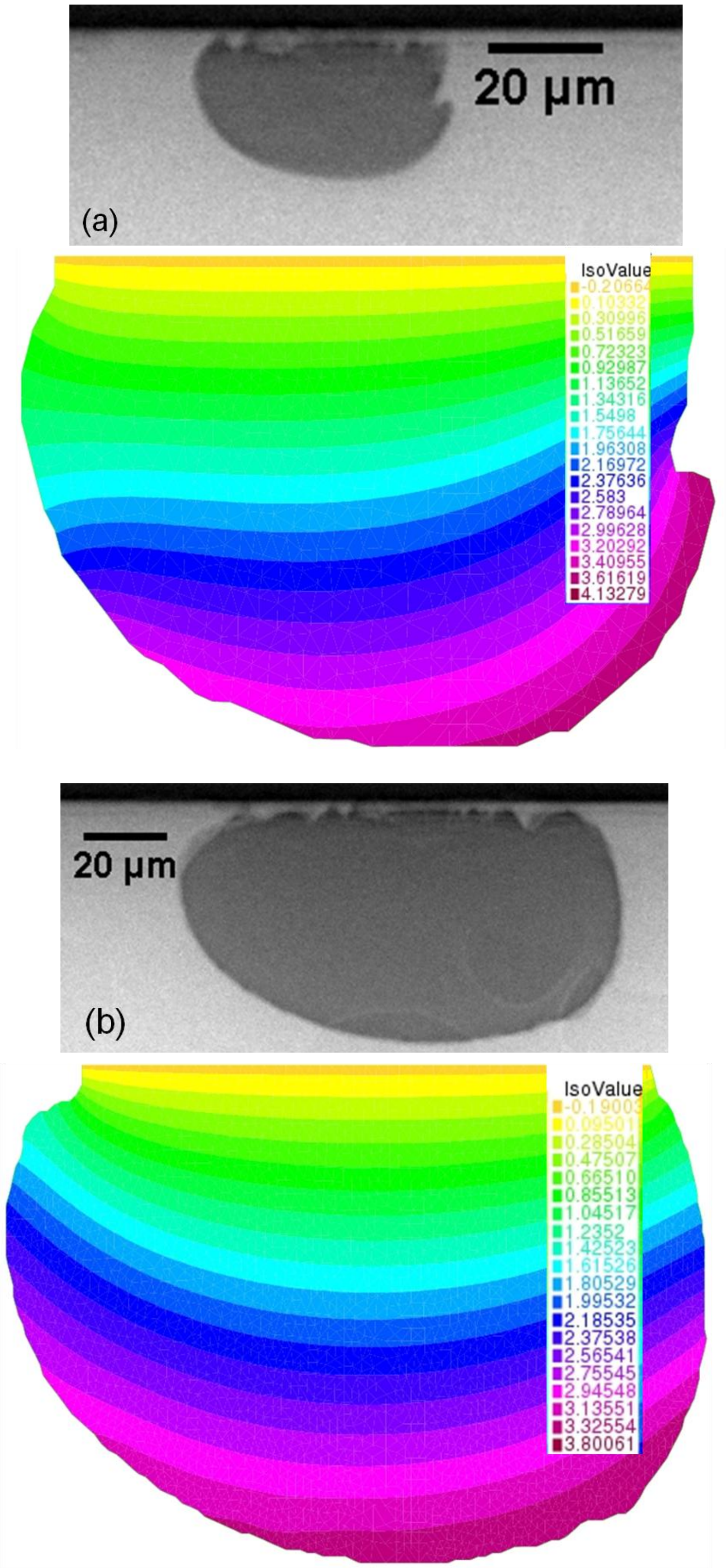

Figure 6-38- Radiograph and concentration gradient inside the pit grown on 304 stainless steel foil in 0.1 M NaCl after 10 s at 650 mV vs. Ag/AgCl then at 10 μA for (a) 39 and (b) 145 s. The iso plots show the concentration gradient (M).

The time dependence of local metal ions concentration within the pits is shown in Figure 6-39 to Figure 6-42. For each radiograph frame during the pit growth sequence, the maximum C_M value around the pit perimeter, the average (mean) C_M value (determined by adding up all the C_M values along the pit perimeter and then dividing by the number of points) and the C_M at the mid-point of the pit perimeter (in order to give an estimation of the metal ions concentration at the pit bottom, if the symmetry of the pit cavity is retained during growth) are extracted. Figure 6-39 shows the maximum, average and mid-point concentration of metal ions within the pit as a function of time for the pit grown in 0.1 M NaCl at 650 mV vs. Ag/AgCl. An increase in the maximum concentration values is seen at the initial stages of growth from ~3.5 M to ~5 M in which the concentration remains almost constant for the rest of growth. This was seen in all potentiostatic measurements but not in the galvanostatic ones. The concentration at the pit mid-point (which represents the concentration at the pit bottom, assuming symmetrical pit geometry) shows less fluctuation which may indicate a uniform dish-shape growth within the pit.

The maximum, average and pit mid-point concentration of metal ions as a function of time for the pits shown in Figure 6-36 and Figure 6-37 are illustrated in Figure 6-40 and Figure 6-41, respectively. An initial increase followed by stabilisation in the concentration values is also seen in these figures. The peak in the maximum and drop in the pit mid-point concentrations at ~120 s (in Figure 6-40) and ~80 s (in Figure 6-41) correspond to undercutting events (“pit within a pit”) and passivation of the majority portions of the pit surface as shown in Figure 6-36(a) and Figure 6-37(a).

Figure 6-42 shows the maximum, average and pit mid-point concentration of metal ions within the pit as a function of time for the pit shown in Figure 6-38, which was grown galvanostatically. The concentration values show no significant changes with time, while the maximum concentration tends to fluctuate between 3 and 4 M in contrast to the potentiostatically-grown pits shown in Figure 6-39, where the metal ion concentration varies between ~3.5 and 5 M. Assuming that the saturation concentration of metal ions is 4.2 M [89], this suggests that the potentiostatically-grown pits shown in Figure 6-35 to Figure 6-37 have a salt film on the dissolving interface whereas that grown under galvanostatic conditions (Figure 6-38) does not.

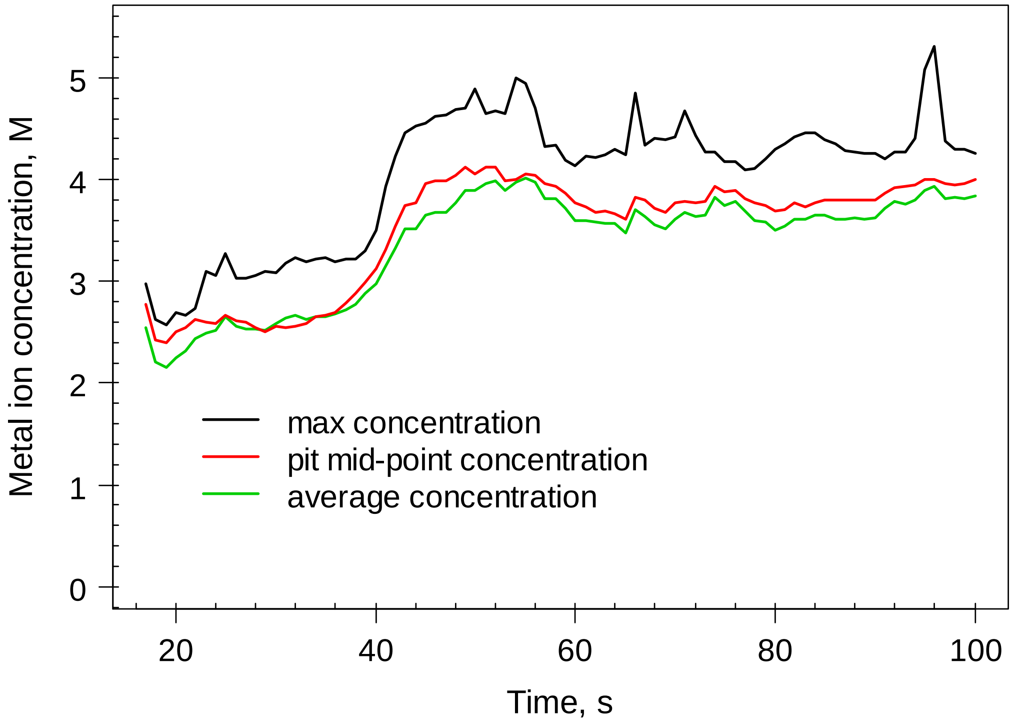

Figure 6-39- Maximum, average and pit mid-point concentration of metal ions along the pit boundary as a function of time during growth of the pit grown on 304 stainless steel foil in 0.1 M NaCl at 650 mV vs. Ag/AgCl.

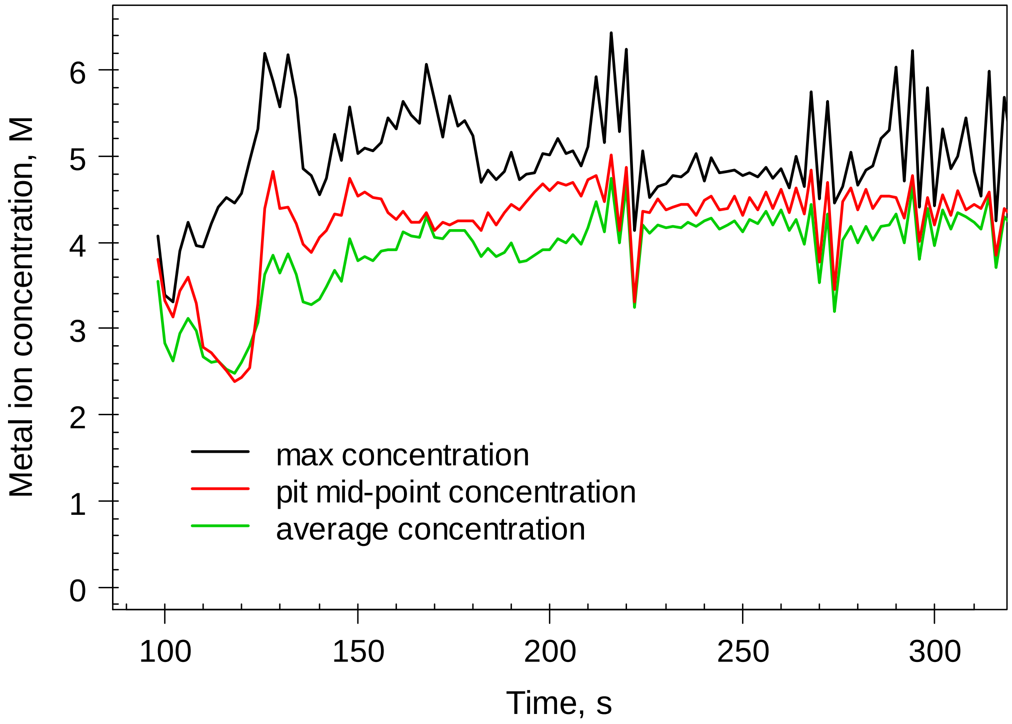

Figure 6-40- Maximum, average and pit mid-point concentration of metal ions along the pit boundary as a function of time during growth of the pit grown on 304 stainless steel foil in 0.01 M NaCl at 600 mV vs. Ag/AgCl.

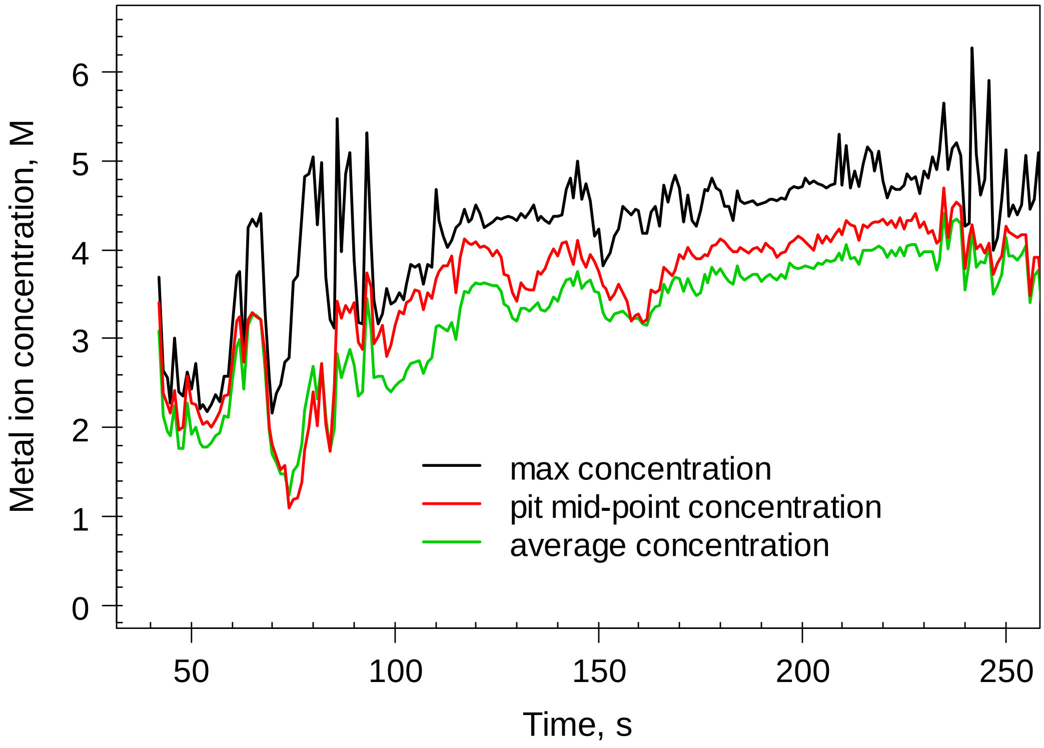

Figure 6-41- Maximum, average and pit mid-point concentration of metal ions along the pit boundary as a function of time during growth of the pit grown on 304 stainless steel foil in 0.005 M NaCl at 650 mV vs. Ag/AgCl.

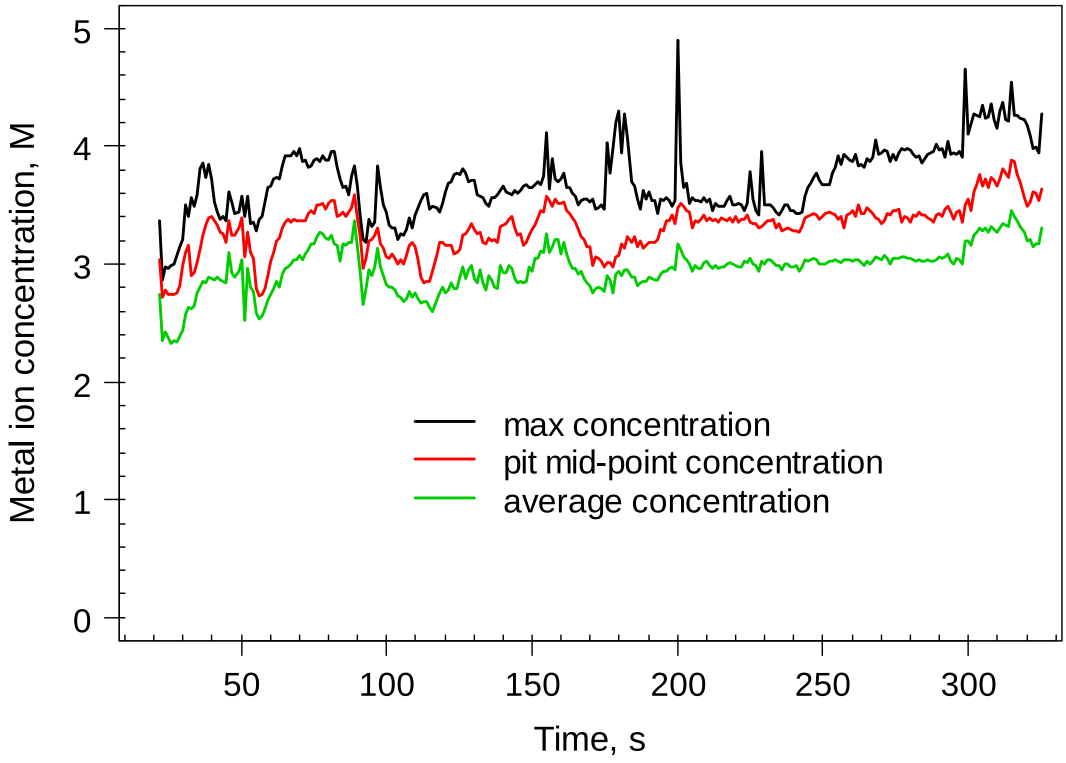

Figure 6-42- Maximum, average and pit mid-point concentration of metal ions along the pit boundary as a function of time for the pit grown on 304 stainless steel foil in 0.1 M NaCl at 10 µA following 10 s initiation at 650 mV vs. Ag/AgCl.

6.8 Anodic Tafel slope measurement

The relationship among the applied potential, activation and ohmic overpotential and the dissolution kinetics of a growing pit can be quantified by [7, 82, 96]:

Equation 6-18

$$E_{app} = E_{corr} + b_a \log\left(\frac{i_a}{i_{corr}}\right) + \phi_s + \phi_{sf}$$

where E_{app} is the applied or measured potential, E_{corr} and i_{corr} are the open-circuit corrosion potential and current density, b_{a} is the anodic Tafel slope, ϕ_{s} is the potential drop in solution, and ϕ_{sf} is the potential drop across the salt film. For the galvanostatically-grown pit in Figure 6-42, the maximum metal ion concentration mostly fluctuates below the saturation concentration value required for salt film precipitation and the surface is mostly salt film free ($\phi_{\mathrm{sf}}=0$). Therefore, a galvanostatic growth with almost constant *IR*-drop during the later stages of growth (see Figure 6-34) provides the opportunity to estimate the anodic Tafel slope from the anodic dissolution current density and the *IR*-corrected potential. Figure 6-43 and Figure 6-44 show the *IR*-corrected applied potential as a function of the average current density (the total applied current divided by the pit surface) within the single pits (for two different measurements; radiographs of the pits are shown in Figure 5-6 and 5-7d) grown in 0.1 M NaCl 10 μA current after initiation at 650 mV vs. Ag/AgCl for 10 s. The potential drop within the pit cavity (~15 mV) is less than 10% of the drop in the bulk solution during the period of growth and it is neglected. The *IR*-corrected potential fluctuates significantly at the high values of current density which correlates with the initial stages of growth, however, it gradually decreases as the pit grows and the average current density is reduced. The method of iteratively reweighted least squares is used to fit the slope and b_{a} values of 103 and 102 mV are extracted.

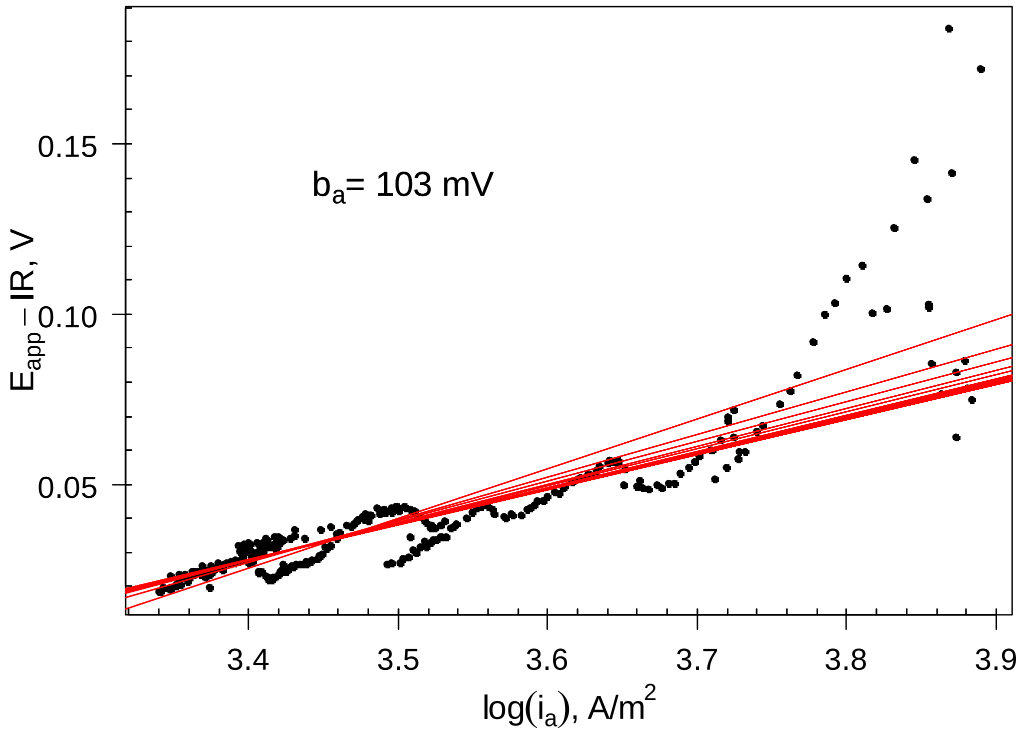

Figure 6-43- IR corrected applied potential as a function of the average current density of the pit grown in 0.1 M NaCl at 10 µA following initiation at 650 mV vs. Ag/AgCl for 10 s. The IR drop in solution is subtracted from the applied potential. Red lines are fitted by the method of iteratively reweighted least squares to find the slope.

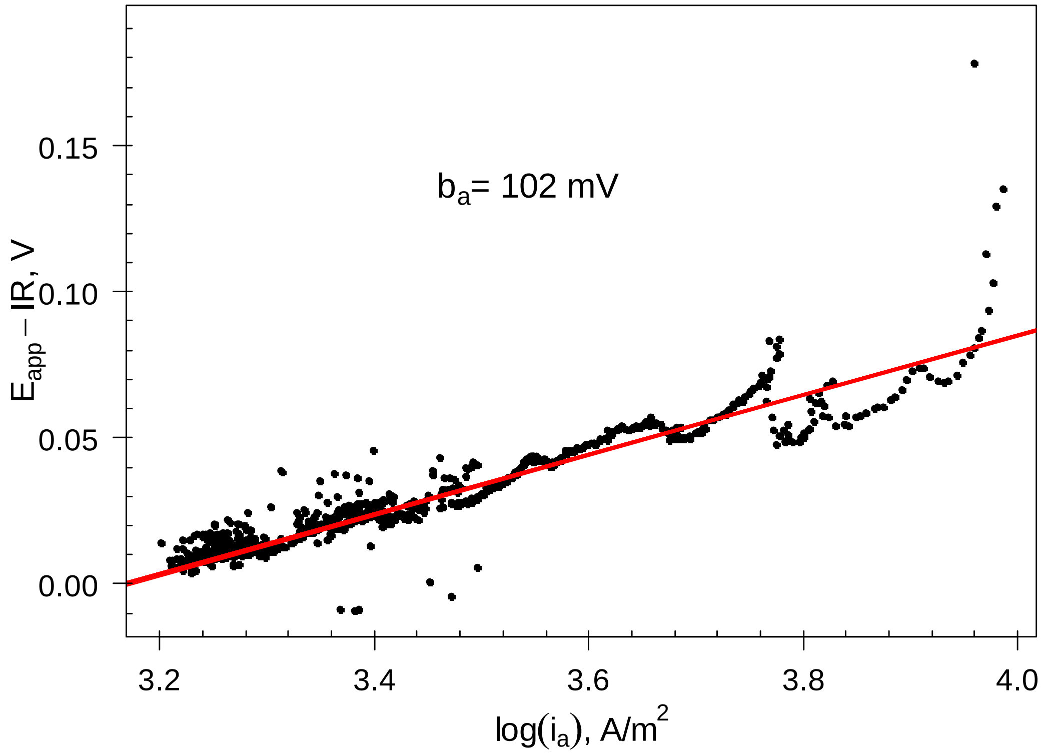

Figure 6-44- Interfacial potential as a function of the average current density of the pit grown in 0.1 M NaCl at 10 µA following initiation at 650 mV vs. Ag/AgCl for 10 s. The IR drop in solution is subtracted from the applied potential. Red lines are fitted by the method of iteratively reweighted least squares to find the slope.

6.9 Surface kinetics plots within 2D pit

Having an estimation of the potential drop in the bulk solution and within the pit, and taking into account the solution resistance effects, the "actual" kinetics on the pit surface can be deduced from the *IR*-corrected local current density as a function of the metal ions concentration and interfacial potential.

Previous work investigating the relationship between current density, potential and solution concentration within pits has used a current density that has been adjusted to take account of the *IR*-drop by using the Tafel equation [7, 82, 88, 109]:

Equation 6-19

$$i_a \times 10^{\frac{\phi_s}{b_a}} = i_{corr} \times 10^{\frac{E_{app}-E_{corr}}{b_a}}$$

where, E_{app} is the applied potential (the measured potential in the case of galvanostatic measurements), E_{corr} and i_{corr} are the open-circuit corrosion potential and current density in the pit solution, respectively, b_{a} is the anodic Tafel slope and ϕ_{s} is the potential drop in solution. The b_{a} is taken ~100 mV/decade as determined in the previous section.

Figure 6-45 shows the distribution of local anodic current density (a), metal ion concentration (b) and total potential drop (c) along the pit boundary for a pit grown galvanostatically at 10 μA 148 s after initiation. The potential drop in bulk solution is 118 mV (Ag/AgCl) which can be seen at the left hand side of the pit mouth (0 μm) in Figure 6-45 (c). Further down along the pit boundary, the potential drop slightly increases to ~130 mV (Ag/AgCl) at the pit bottom.

Figure 6-46 shows the *IR*-corrected local current density as a function of local metal ion concentration of the above described pit. The measured potential (from potentiostat) is 176 mV vs. SCE, and the current density at each surface point has been corrected by Equation 6-19 such that the *IR*-corrected local current density is the value that would flow if the interfacial potential at all points was equal to the measured potential recorded at that time. The red line in the figure joins data points from adjacent locations along the perimeter of the pit. The symmetry of the pit can be seen in Figure 6-46 since the lines from the left and right hand sides of the pit coincide. Near the mouth of the pit on both sides, the current density is almost zero for metal ion concentrations of 0 to ~2.5 M and then increases sharply as the concentration increases towards the bottom of the pit. At the bottom of the pit, where the concentration reaches the saturation concentration of 4.2 M [89], the current starts to decrease again.

Taking the results of the same pit in different times (and/or from several different experiments), can generate a family of current density plots against concentration at different applied potentials as shown in Figure 6-47.

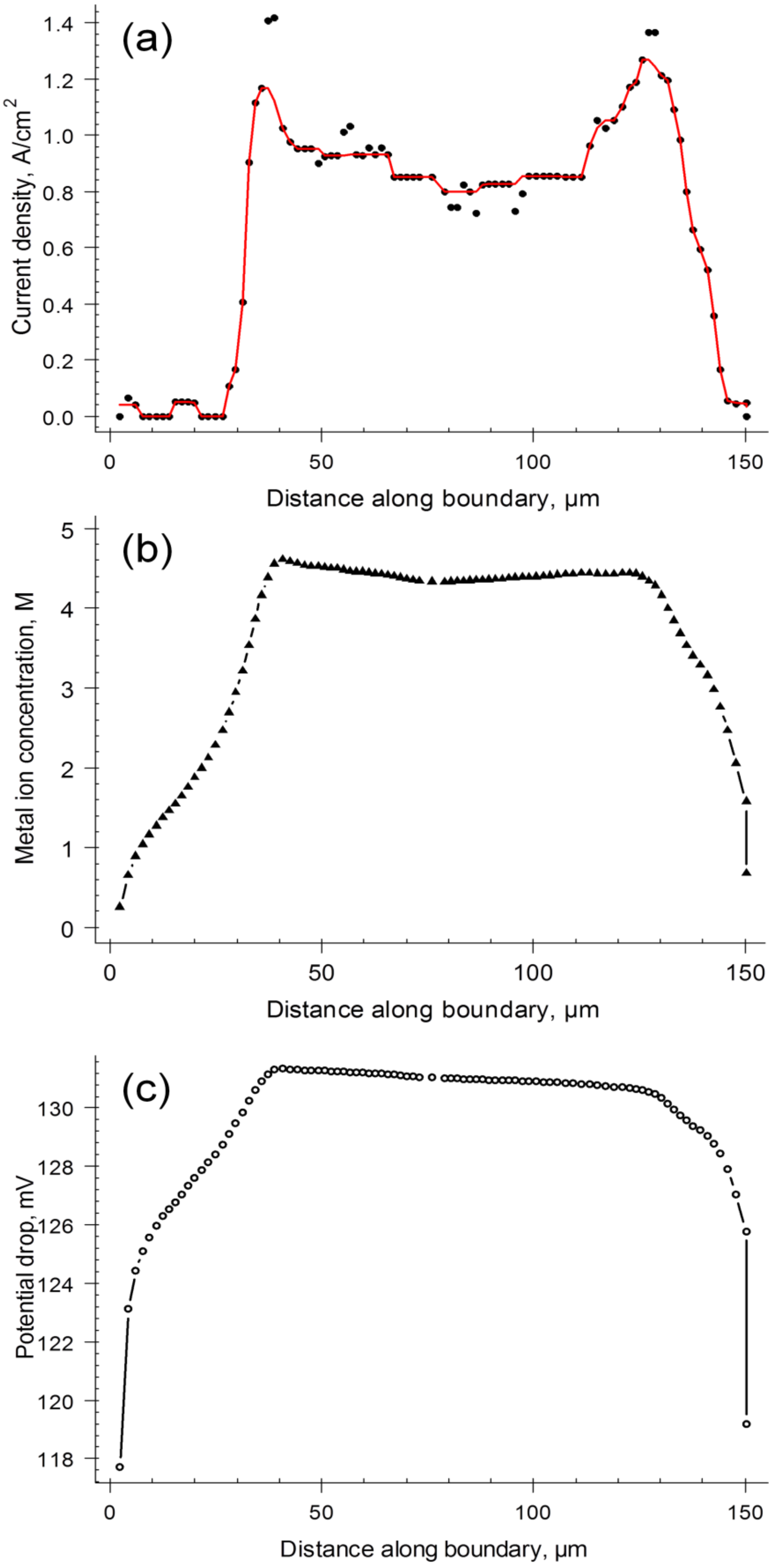

Figure 6-45- Distribution of the local current density, metal ions concentration and total potential drop along the boundary of a pit grown on 304 stainless steel foil in 0.1 M NaCl at 10 µA. The data were extracted from the frame at 148 s after initiation at 650 mV vs. Ag/AgCl for 10 s.

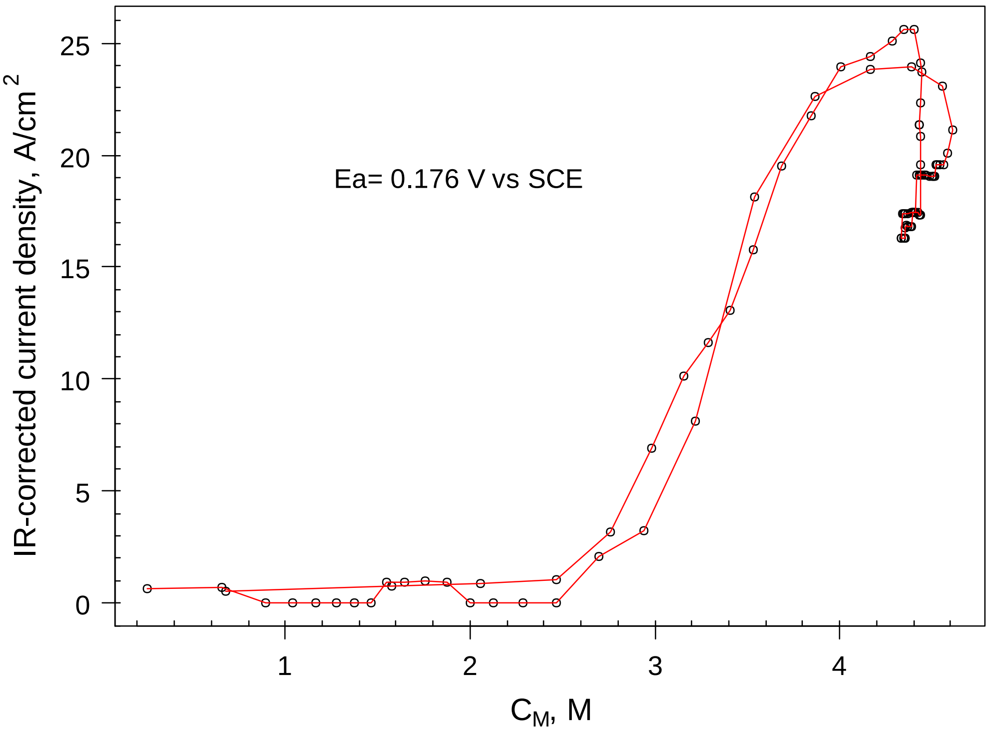

Figure 6-46- *IR* corrected local current density as a function of local metal ion concentration within a pit grown on 304 stainless steel foil in 0.1 M NaCl at 10 µA. The data were extracted from the frame at 148 s after initiation at 650 mV vs. Ag/AgCl for 10 s. The measured potential was 176 mV vs. SCE. The red line joins data points from adjacent locations along the perimeter of the pit.

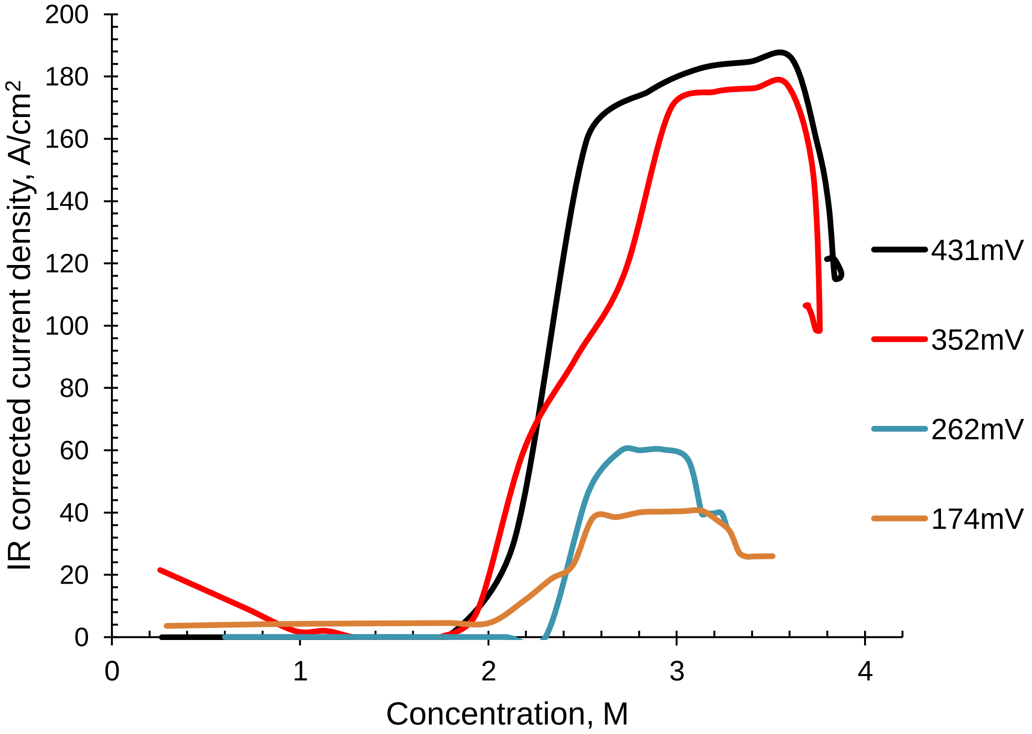

Figure 6-47- IR corrected anodic current density as a function of dissolved metal ion concentration at different times (and measured potentials) for the pit shown in Figure 6-46. For clarity, the data from only one side of the pit is shown at each potential.

6.10 Pit stability product

Previous work has defined a pit stability product, $i \times x$, the product of the pit current density and pit depth, such that a pit will repassivate if the product falls below a critical value at which the rate of metal ion production is lower than the rate of metal ion loss through diffusion[56]. For stainless steels, the stability criterion is calculated as 0.4 A/m [72], 0.6 A/m [105] and 0.3 A/m [50]. From the pit radiography data, a value for the pit stability product can be calculated from the product of the local current density (i_a) and the local depth at each point along the pit surface. It is assumed that the local depth may be defined as the vertical distance from the pit surface up to the pit rim as shown in Figure 6-48. Figure 6-49 shows the stability product along the boundary of the pit grown in 0.1 M NaCl at 10 μA for (a) 22, (b) 47 and (c) 437 s following initiation at 650 mV vs. Ag/AgCl for 10 s. At the initial stages (a) the stability product is less than 0.25 A/m all along the pit boundary. As the pit grows, (b) and (c), the stability product exceeds 0.3 A/m (stability criterion value) only at the pit bottom areas and fluctuates around this value during the rest of growth time.

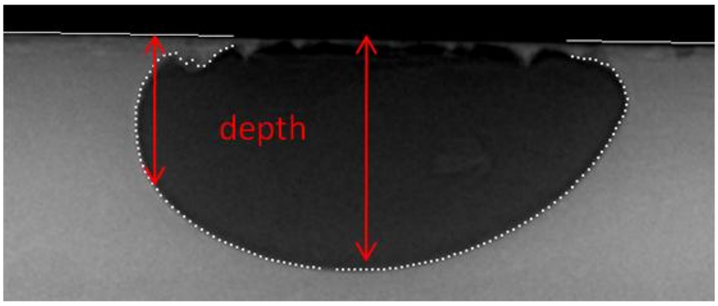

Figure 6-48- Local pit depth considered in pit stability calculation.

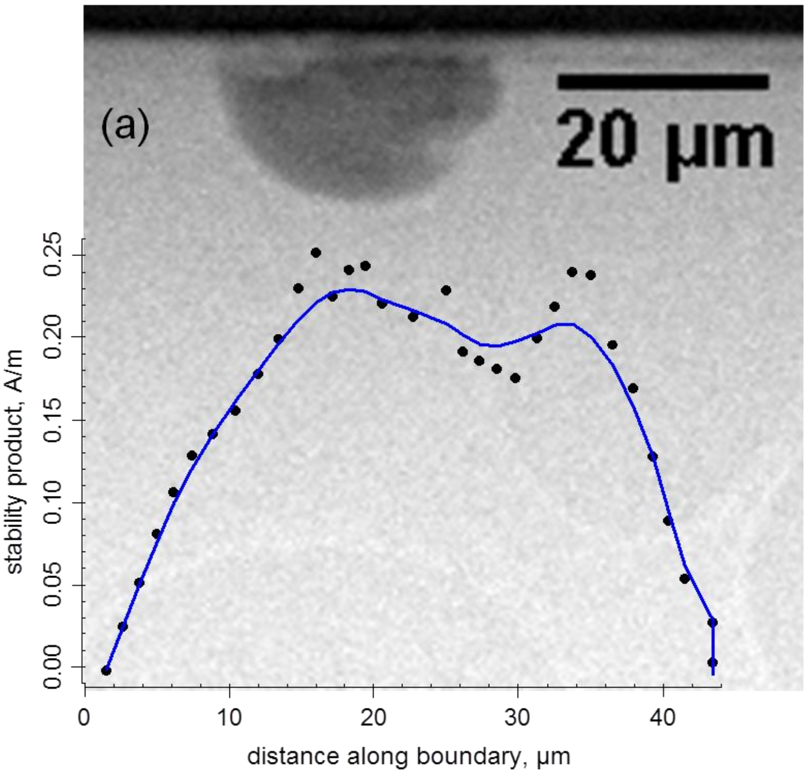

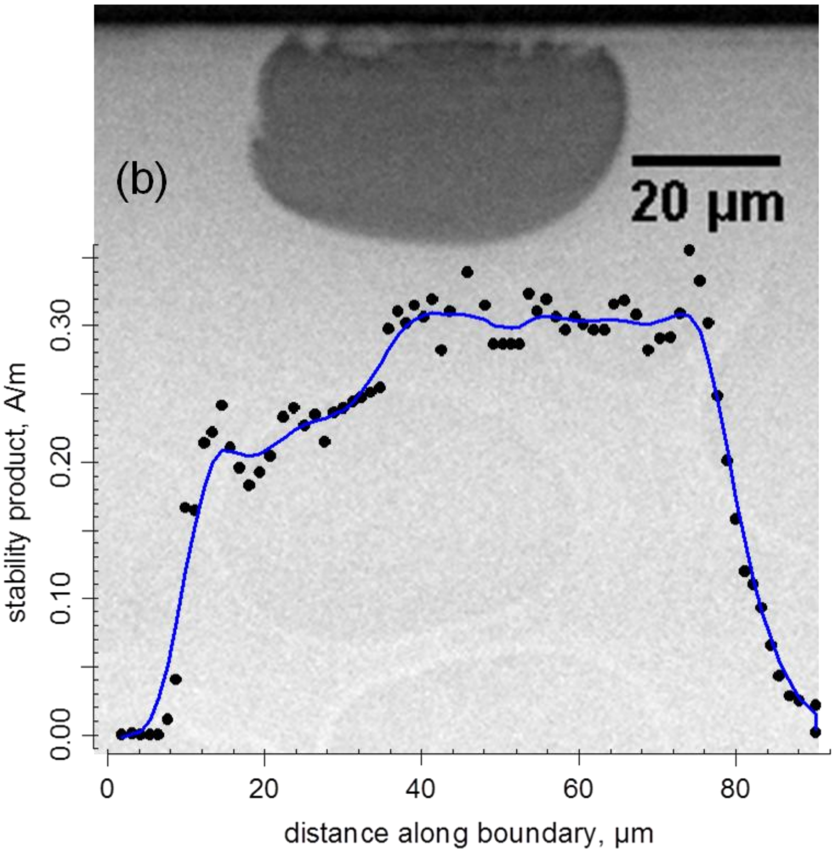

Figure 6-49- Radiograph and local stability product along the perimeter of the pit grown on 304 stainless steel foil in 0.1 M NaCl at 10 µA for (a) 22 and (b) 47 s following initiation at 650 mV vs. Ag/AgCl for 10 s.

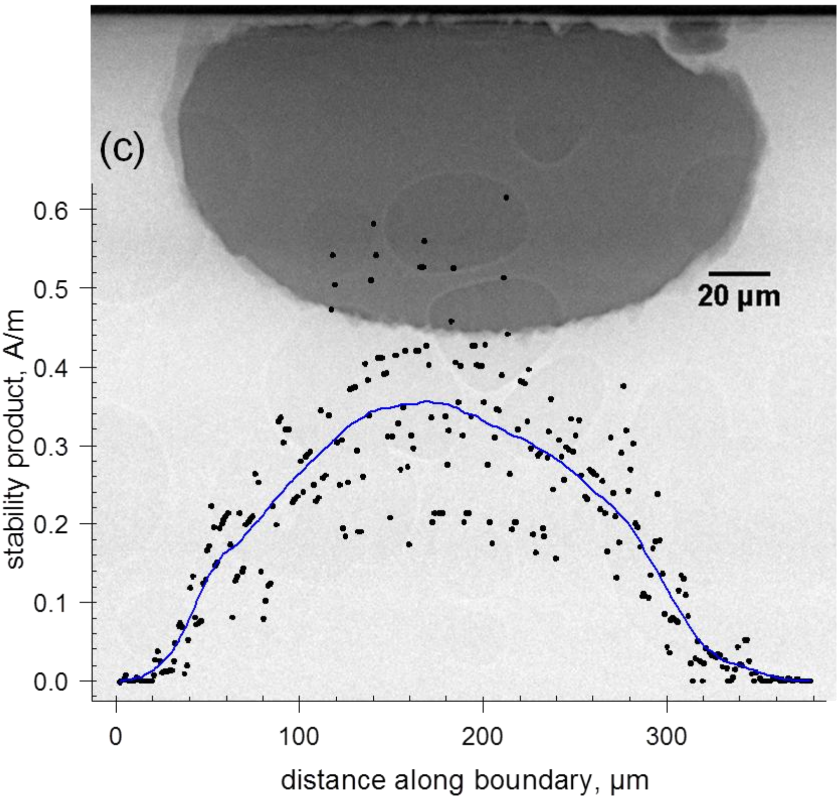

Continued Figure 6-49- Radiograph and local stability product along the perimeter of the pit grown on 304 stainless steel foil in 0.1 M NaCl at 10 μA for (c) 437 s following initiation at 650 mV vs. Ag/AgCl for 10 s.

Figure 6-50 to Figure 6-52 show the maximum stability product as a function of time for galvanostatically-grown pits at 10 μA in 0.1 and 0.01 M NaCl solutions. The stability products tend to fluctuate between 0.3 to 0.4 A/m with some sudden increases to higher values.

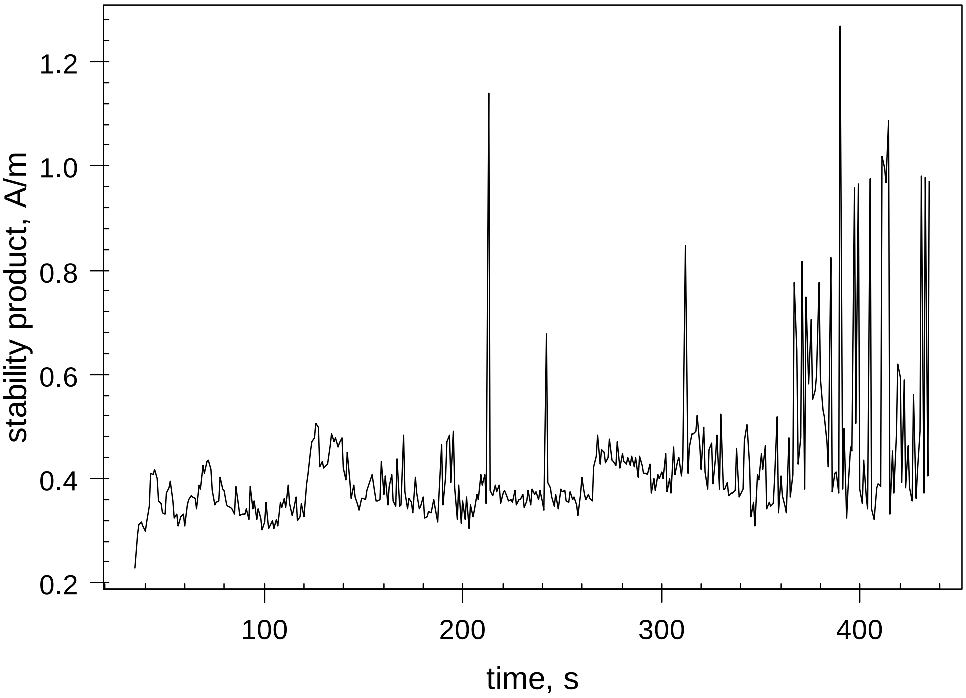

Figure 6-50- The maximum pit stability product as a function of time for pit grown on 304 stainless steel foil in 0.1 M NaCl at 10 µA following initiation at 650 mV vs. Ag/AgCl for 10 s.

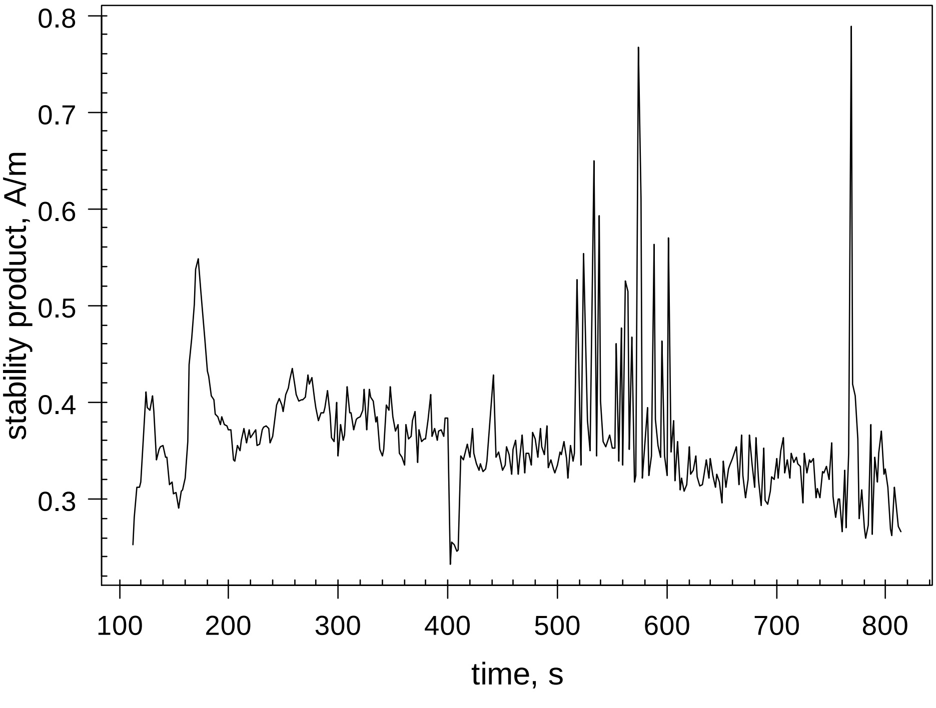

Figure 6-51- The maximum pit stability product as a function of time for pit grown on 304 stainless steel foil in 0.1 M NaCl at 10 µA following initiation at 650 mV vs. Ag/AgCl for 10 s.

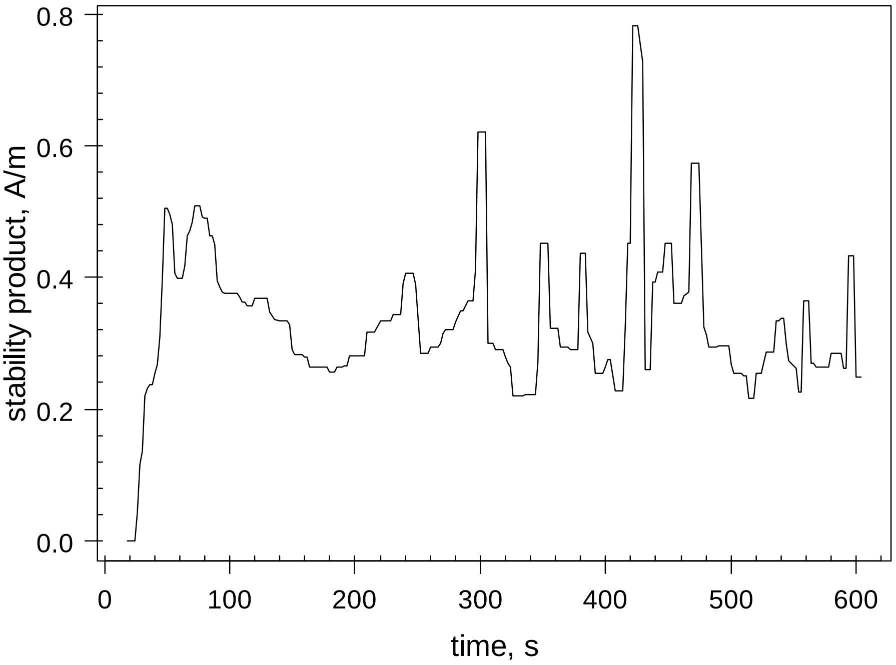

Figure 6-52- Smoothed data of the maximum pit stability product as a function of time for pit grown on 304 stainless steel foil in 0.01 M NaCl at 10 µA following initiation at 650 mV vs. Ag/AgCl for 10 s.

Figure 6-53 to Figure 6-56 show the maximum stability product of pits grown potentiostatically in 0.1, 0.01 and 0.005 M NaCl. Higher and continuous increase in stability product is seen in 0.1 M NaCl pits (shown in Figure 6-53 and Figure 6-54). However, more fluctuations with slight increase are seen in pits grown in dilute solutions of 0.01 and 0.005 M NaCl (Figure 6-55 and Figure 6-56). In all cases, the pit stability products are at or above 0.3-0.4 A/m

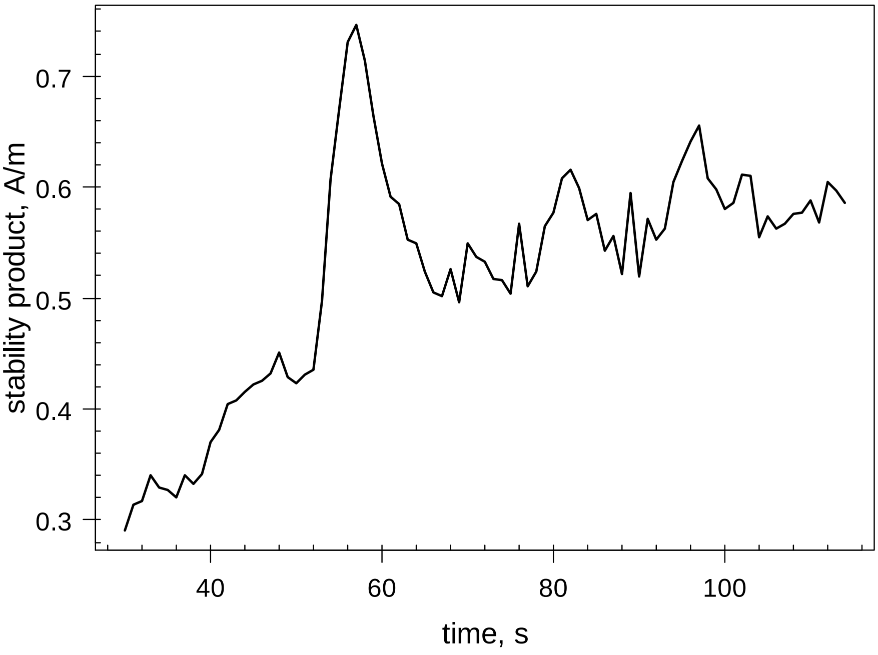

Figure 6-53- Smoothed data of the maximum pit stability product as a function of time for pit grown on 304 stainless steel foil in 0.1 M NaCl at 650 mV vs. Ag/AgCl.

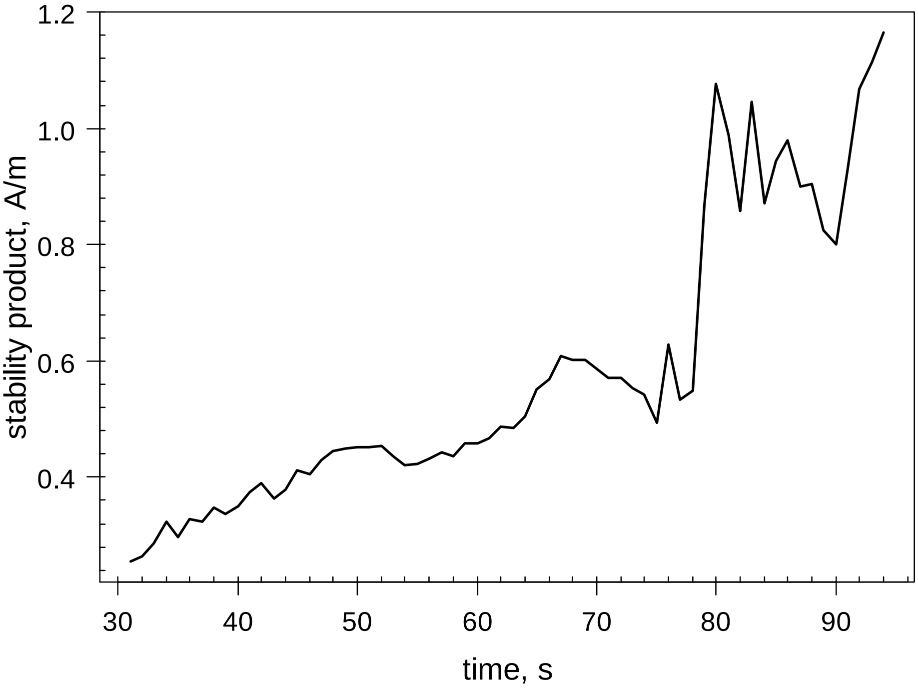

Figure 6-54- Smoothed data of the maximum pit stability product as a function of time for pit grown on 304 stainless steel foil in 0.1 M NaCl at 650 mV vs. Ag/AgCl.

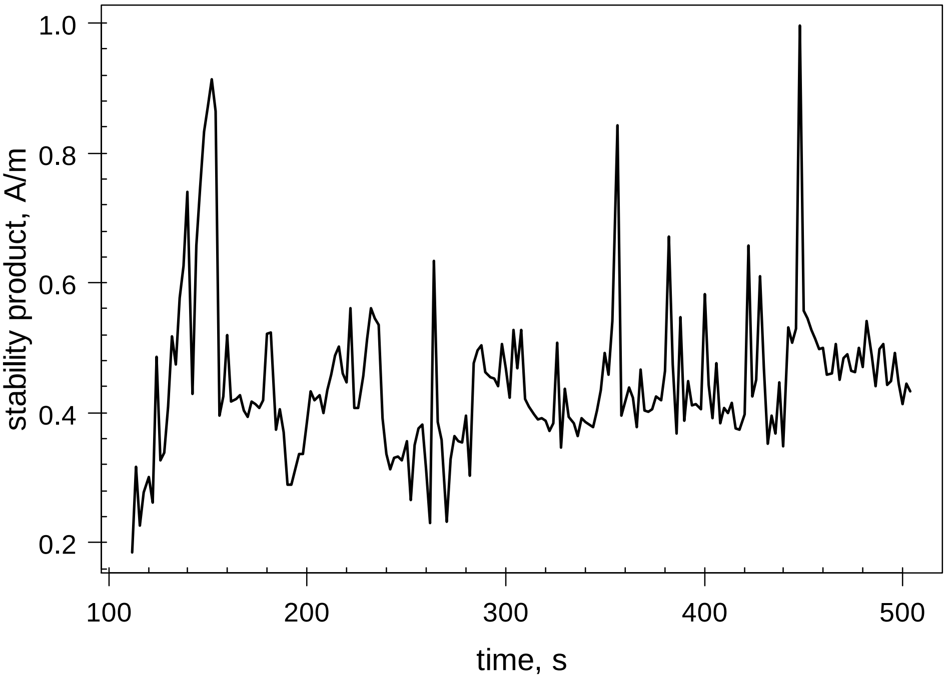

Figure 6-55- Smoothed data of the maximum pit stability product as a function of time for pit grown on 304 stainless steel foil in 0.01 M NaCl at 600 mV vs. Ag/AgCl.

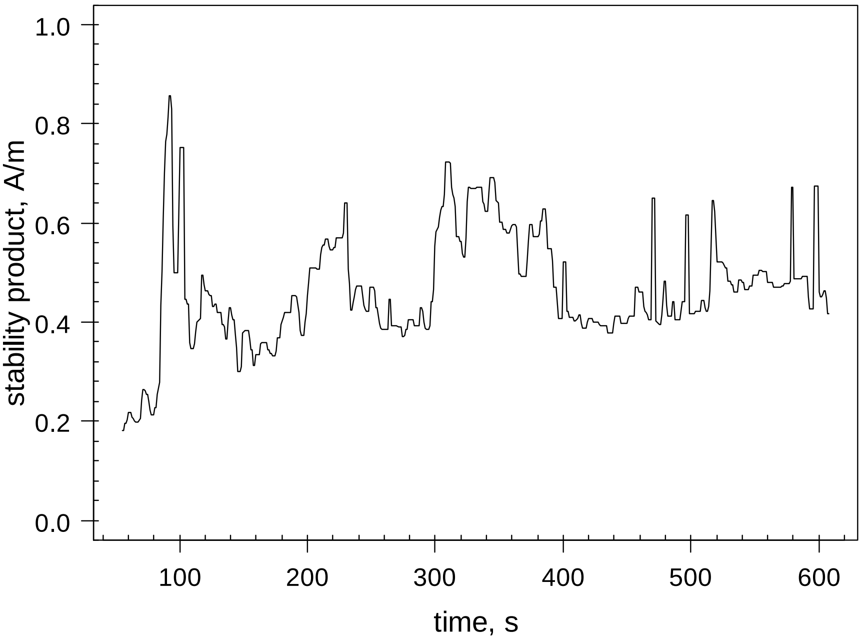

Figure 6-56- Smoothed data of the maximum pit stability product as a function of time for pit grown on 304 stainless steel foil in 0.005 M NaCl at 650 mV vs. Ag/AgCl.

Figure 6-57 to Figure 6-59 show the stability for the pit with ~150 μm long boundary grown in 0.1, 0.01 and 0.005 M NaCl solutions. The stability product along majority of the pit bottom in Figure 6-57 (0.1 M NaCl) has exceeded 0.3 A/m, whereas in lower chloride concentrations (Figure 6-58 and Figure 6-59), a small portion of the pit boundary at the very bottom has reached the stability of 0.3 A/m.

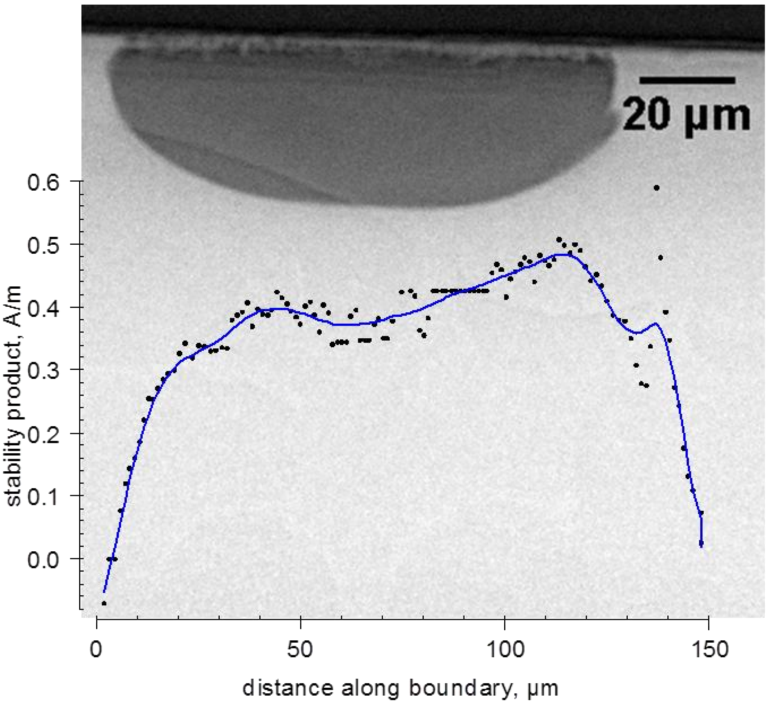

Figure 6-57- Radiograph and local stability product along the perimeter of the pit grown on 304 stainless steel foil in 0.1 M NaCl at 650 mV vs. Ag/AgCl for 63 s.

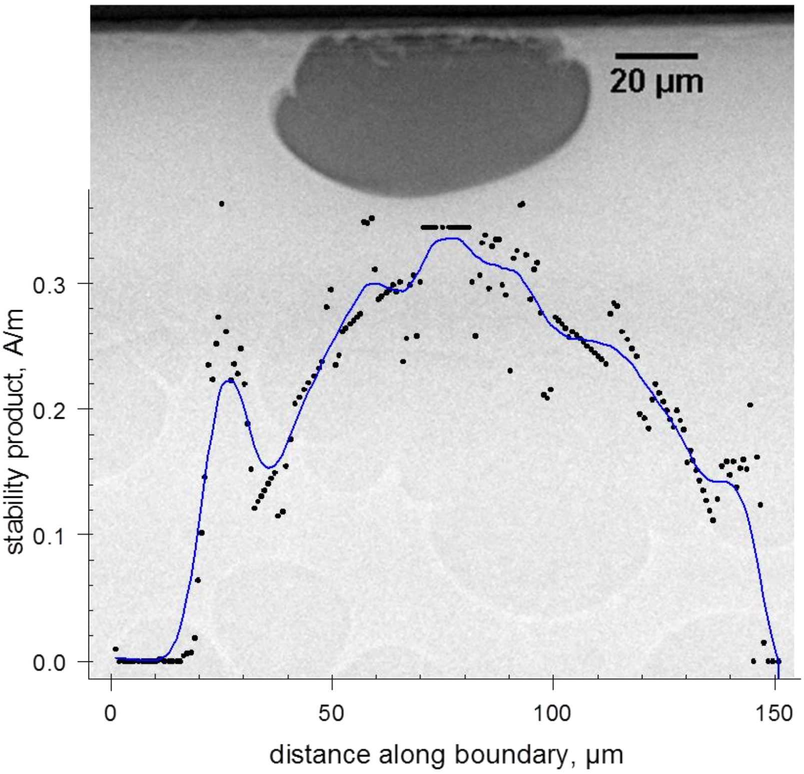

Figure 6-58- Radiograph and local stability product along the perimeter of the pit grown on 304 stainless steel foil in 0.01 M NaCl at 600 mV vs. Ag/AgCl for 224 s.

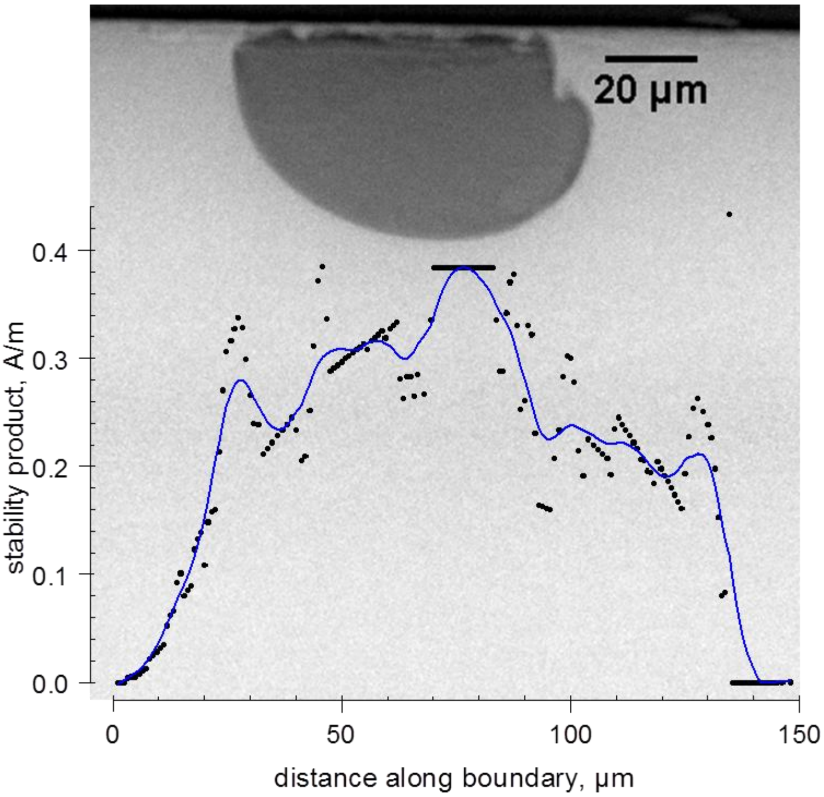

Figure 6-59- Radiograph and local stability product along the perimeter of the pit grown on 304 stainless steel foil in 0.005 M NaCl at 650 mV vs. Ag/AgCl for 137 s.

6.11 Discussion

6.11.1 Local current density in pits

Anodic current densities within the range of 0.1-10 A/cm^2 have been reported for metastable pits [50, 72, 163] and stable pits [51, 64]. In these measurements, an average current density was obtained from the total applied current divided by an estimation of the corroding surface area. For example, Alkire and Wong [51] reported current densities of ~1-5 A/cm^2 for single pits in 304 stainless steel grown in 1 N H_2SO_4 and 0.1 N NaCl at 0.6 V (SCE).

In a similar approach, i_a was obtained from the propagation rate of corroding edge over a time interval in Al [154], an Al alloy [155], a Ni-Fe alloy [156], iron-chromium [112] and 304 stainless steel thin films[111]. In these studies, an average value from points around the pit perimeter was taken and therefore, a constant current density was assumed over the time interval of each measurement. The range of current density Ryan *et al.* [111] observed in 1.3 M LiCl varies from ~ 4.5 to 12 A/cm^2 at 300 to 650 mV (Ag/AgCl), respectively. Ernst and Newman reported a local anodic current density of ~7.5 A/cm^2 within a 2D pit grown in 304 stainless steel foil under potential control [107].

Although the same approach of tracking the boundary of growing pit was applied by Frankel *et al.* [154-156] and Ryan *et al.* [111, 112], they assumed an average current density for the whole pit perimeter. However, the method presented in this work can yield accurate values of current densities at any point on the pit surface. Figure 6-8 to Figure 6-12 indicate that the distribution of current density along the pit boundary is not uniform. This is consistent with the hypothesis of Mankowski and Smialowska [62] that a non-uniform current density is responsible for the pit shape change from hemispherical to dish/cup like.

The anodic current density close to the pit rim is almost zero which means that dissolution does not occur and the surface is passive. This indicates an insufficient local dissolution rate to counterbalance the fast diffusion of metal ions as a result of shorter diffusion length. Immediately next to the passive region, a peak in current density is seen which correlates to the laterally developing lobe as marked with arrows in Figure 6-8 (a). Therefore it is seen that for the transition from the passive to active region, a maximum current density must be reached, where beyond this peak, the current density within the active region gradually decreases as the diffusion length and metal ion concentration increases (in the previous chapter it has been shown that pits grow under diffusion control). The observed peak indicates that at that local concentration, the anodic current density must exceed a critical value in order to provide sufficient dissolution rate to prevent passivation. It is suggested, therefore, that the maximum current density is the critical passivation current density which was introduced by Salinas-Bravo and Newman [119] and has been recently further developed [80, 113-115]. It has been proposed that passivation can occur at a “finite critical current density”, i_{crit}, even for very aggressive chemistry inside the pit below the critical pitting temperature (CPT). Below the CPT, therefore, the critical high rate dissolution cannot occur at the active/passive junction point [120]. Assuming this hypothesis, over the passive surface, anodic current density, i_a, to support propagation is higher that the critical current density required for passivation at that chemistry, therefore, i_{crit} is reached and surface passivates. At any metal ion concentration for which i_a is less than i_{crit} dissolution continues. Further down to the pit bottom, i_a gradually decreases mainly because of the longer diffusion length resulting in more concentration and also due to slightly higher *IR* drop in solution resulting in lower interfacial potential. Finally in the region of the pit bottom, concentration increases leading to supersaturation and salt film precipitation. At this point, i_a equals to dissolution current density underneath the salt film which is the diffusion limited current density, i_{lim} [84, 96].

The current density trends in all potentiostatically grown pits shown in Figure 6-13 to Figure 6-16 show that the maximum i_a fluctuates around a certain value which slightly decreases as the pits grow. Less fluctuation is seen in mid-point current density which can be considered as the current density at the pit bottom (assuming symmetrical pit shape) and there is a smooth decrease during pit growth.

Comparing the maximum i_a shown in Figure 6-13 to Figure 6-15 shows that increase in chloride concentration of the bulk solution results in slightly higher current density. This indicates the dependence of the growth at laterally developing lobes on bulk chloride concentration and its associated *IR* drop. In fact, it shows that growth at developing lobes (where i_a is at its maximum) depends on the interfacial potential. Therefore, an increase in chloride causes a smaller *IR* drop and thus a higher interfacial potential which leads to higher dissolution rate and i_a. The dependence of lateral growth on potential confirms that the lateral corroding surface is not covered with a salt film which is consistent with the observations of Ryan *et al.* [111, 112] and Ernst and Newman [106] but against the argument made by Beck and Alkire [153] and Strehblow and Ives [164] who believed that metal/electrode surfaces at this high current density might not be under activation/ohmic control.

The current density profiles shown in Figure 6-17 to Figure 6-18 illustrate a clear decrease with growth time which is a characteristic of galvanostatic growth in which as the pit propagates and corroding surface increases, the local current density reduces due to the limited applied current. Also, the more uniform distribution of current within the pit can be deduced from the smaller difference between the maximum and pit mid-point current density. The decrease in current density trends with time agrees with the results of Alkire and Wong [51] who showed that the average current density of individual natural pits decreases with time, although no relation of current density with square root of time is seen as they reported.

6.11.2 Effective diffusion coefficient

The effective diffusion coefficient for metal ions in solution, D, is an important parameter for modelling pit growth. It is normally calculated from the relationship between the diffusion limited current density and the pit depth according to the Fick's first law.

From the radiography data it is possible to extract a number of values of $D\Delta C$ – shown in Table 1. The values of $D\Delta C$ come from the (pit depth)^2 vs. time. In order to extract values of D, it is necessary to define the value of ΔC, which is the difference between the solution concentration at the dissolving interface and that at the pit mouth. For pits that are grown at high potentials (in the present work these are the potentiostatic measurements) where the presence of salt films is likely, the metal ion concentration at the pit bottom is likely to be the saturation concentration C_{sat} [76, 78, 83, 89, 92, 93, 95, 152]. However, for pits grown at lower potentials (the galvanostatic measurements in this work), the metal ions concentration at the pit bottom decreases during the growth from C_{sat} to the critical concentration for propagation, C_{crit} (as shown experimentally [84] and by simulation [141]). The metal ion concentration at the pit mouth is affected by the diffusion of metal ions away from the pit mouth into the bulk solution and the diffusion barrier provided by the lacy metal cover. In the literature, the concentration of metal ions at the mouth of 1D artificial pits has been generally assumed as zero [56, 75, 76, 81, 83-88, 159]. In order to compare the results with literature values, the concentrations of metal ions at the pit bottom and pit mouth are considered to be C_{sat} and 0, respectively.

From the plot of pit depth squared vs. time in Figure 6-20, an effective diffusion coefficient of metal ions can be obtained for a 1D growing pit. The DC_{sat} value extracted from the slope in plot is 4.36×10^{-8} mol.cm^{-1}.s^{-1}. Assuming C_{sat}=4.2 M as measured by Kuo and Landolt, then the diffusion coefficient is 1.03×10^{-5} cm^{-1}.s^{-1} which is slightly higher than 0.85×10^{-5} cm^{-1}.s^{-1} quoted by Kuo and Landolt and 0.824×10^{-5} cm^{-1}s^{-1} fitted by Gaudet *et al*. The discrepancy can come from the C_{sat} value, as assuming saturation concentration of 5.1 M calculated by Isaacs [76] yields the diffusivity to be 0.85×10^{-5} cm^{-1}s^{-1}. The disagreement may also be resulted in by the difference in calculation method from the literature work where diffusion limited current densities, i_{lim}, were directly used to calculate diffusivity.

The diffusivity values for 2D pits shown in Table 6-1 are all lower than the above obtained value and literature values for 1D pit. Less variation around ~0.4 is seen in potentiostatic pits grown in 0.1 M (No. 3 to 18 in Table 1) while broader variation is seen within the values obtained for pits grown in 0.01 and 0.005 M (No. 19 to 23 in Table 1). This variation is smaller in galvanostatically grown pits (No. 24 to 30). However, Ernst and Newman [107] reported very small change between DC_{sat} values of 1D pits in different chloride concentrations from 0.005 to 1 M. As there is a fundamental difference between the geometry of 1D pit (pencil electrode or general dissolution shown in Figure 6-19) and the 2D pit growing with a visible lacy cover, the decrease in DC_{sat} values seen in 2D pits may indicate the existence of a diffusion barrier in the metal ions transport form the pit bottom to the bulk solution imposed by the pit lacy cover. The role of the cover as either a resistive barrier [72] or a diffusion barrier [50] protecting metastable pits and even stable pits [70, 71] from repassivation has been reported. Therefore, based on the deviation of the DC_{sat} values obtained in 2D pits from the DC_{sat} values in 1D pits, a *"coveredness factor"* can be introduced to quantify the effect of perforated cover on metal ions transport from inside pit towards the bulk solution. This factor was applied in solving transport equations and concentration computation in Section 6.7.

6.11.3 Metal ions concentration in pits

The calculated concentration of metal ions within the pit shown in Figure 6-35(a) indicates a highly concentrated solution along the majority of the pit surface. The maximum concentration of 4.76 M is seen on the lateral developing fronts which slightly decreases as towards the pit bottom. Close to the pit rim, the concentration is around zero (as assumed in boundary conditions) and gradually increases towards the pit bottom. At the junction between the passive and active regions (lateral corroding front), concentrations of 2.5 to 2.9 M (dark blue areas in the concentration gradient) can be observed which is very close to the critical concentration required for propagation reported by various researchers [66, 67, 73, 74, 81, 84].

The range of the maximum concentrations shown in Figure 6-35(b) is in agreement with measured value of pit chemistry of 3.83-6.8 N by Suzuki *et al.*[54] and the saturation concentration of 5.1 M by Isaacs [160].

It can be seen that in potentiostatic growth the maximum concentration of metal ions (Figure 6-39 to Figure 6-41) gradually increases during the initial stages which is due to the increase in diffusion length for ion transport as the pit gets bigger. Then it stabilised and fluctuates around values >4 M for the rest of growth time. In galvanostatic growth (Figure 6-42), however, the maximum concentration (which is over the pit bottom in this case) fluctuates between 3 and 4 M and is in the range of >60% saturation concentration known as critical concentration for propagation. This is consistent with Laycock *et al.* prediction of concentration at pit bottom in the simulation of galvanostatic growth [141].

6.11.4 Anodic Tafel slope measurements

Figure 6-43 and Figure 6-44 show plots of *IR*-corrected potential against the average current density of single pit of two independent experiments. In both cases, at log (i_a, A/m^2) > 3.7, high variation of potential with current density is seen. This area correlates with the initial stages of pit growth as the applied potential fluctuates (shown in Figure 5-6) due to small lobes perforating the cover and decreasing the electrical resistance of the pit cover. However, in later stages as the pit enlarges via uniform distribution of the current density, the potential tends to follow a certain slope with current density. It was shown in Figure 6-42, for this specific type of measurement (galvanostatic at 10 μA), that the concentration of metal ions within the pit remained below the saturation value of 4.2 M [89] and thus the pit surface was not salted. Therefore, at the applied potential of E_{app}, the local current density anywhere within the pit surface, i_{a}, can be given by [7, 109, 143]:

$$E_{\mathrm{app}} = E_{\mathrm{corr}} + b_{\mathrm{a}} \log\left(\frac{i_{\mathrm{a}}}{i_{\mathrm{corr}}}\right) + IR$$

where, E_{corr} and i_{corr} are the open-circuit corrosion potential and current density in the pit solution, respectively, b_{a} is the anodic Tafel slope and IR is the total current drop.

In these conditions, b_{a} value can be obtained from the IR-corrected potential against current density plots shown in Figure 6-43 and Figure 6-44. The b_{a} values obtained are 103 and 102 mV/decade which are consistent with the results by Laycock and Newman [82, 118] which showed a value of ~110 mV/decade from the relation of the transition potential (E_{T}) and the diffusion limited current density (i_{lim}) for 302 SS artificial pits in 1 M NaCl.

For an Fe-19Cr-10Ni alloy, however, Newman and Isaacs [81] reported a value of 75 mV/decade at potentials below -300 mV with a shift to 60 mV at potentials between -300 and -250 mV. They also measured a Tafel slope of 60 mV/decade for 304L SS at potentials above -250 mV. Later, Gaudet *et al.*[84] measured a value of 54 mV/decade for 304 SS at potentials between -200 to -120 mV. The reason for this discrepancy may be that in these experiments the slope is extracted from a higher potential and current density range of 0 to ~50 mV and 0.1 to 1 A/cm^2, respectively, which are very close to the range of potential and current density reported by Laycock and Newman[82, 118]. Therefore, this may support the idea of increased Tafel slope in higher potentials/current densities.

Also, due to the dependence of b_{a} on the concentration of H^+ and Cl^- [91, 165, 166], it is notable that the surface concentration within the pit is approximately saturated which would result in slightly lower dissolution rate in the concentration range of 85-100% compared to lower degree of saturation [84]. It is worth to point out that b_{a} values of ~100 mV [165], ~110 mV [91] for dissolution of iron in high chloride concentration are reported in the literature.

6.11.5 Surface kinetics in pits

Having determined the local surface concentration and potential along a pit perimeter, it is possible to correlate surface current density, concentration and potential to generate plots similar to what has been made from 1D artificial pit [75, 84, 87, 88]. The one-dimensional "Gaudet" [84] type analysis can be applied to 2D pits with the advantage that an entire "Gaudet" curve can be generated from a single pit at one time.

Along the perimeter of a 2D pit, there are various dominating electrochemical regimes on the surface. Close to the pit rim towards the pit bottom, the surface is repassivated; this correlates with the areas where current density is zero in Figure 6-46 until the local concentration exceeds ~2.5 M which is the critical concentration required for propagation, C_{crit}, reported previously by various researchers [66, 67, 73, 74, 81, 84].

The C_{crit} value decreases with potential increase as can be seen in Figure 6-47 and is in agreement with the literature [84]. Deep in the pit bottom, concentration increases due to longer diffusion length and therefore, it may exceed saturation concentration of metal salt resulting in salt film precipitation.

Qualitative agreement of the results with the work of Gaudet *et al.*[84] is seen, however, as their measurements were done at potentials below -100 mV (SCE) and a b_a value of 54 mV/decade was taken in the calculation of *IR*-drop correction, it may not be fully correct to quantitatively compare the results.

6.11.6 Pit stability

Figure 6-49(a) shows that the pit at the initial stages grows below the stability product of $i \times x = 0.25$ A/m. This is in agreement with the work of Pistorius and Burstein [50] which showed metastable and even stable pits initially grew with the stability products value below 0.3 A/m. This is clearly due to the diffusion barrier provided by the pit cover, as is visible in Figure 6-49, maintaining the concentrated solution inside pit cavity. Figure 6-49(b) and (c) show the slight increase in the stability product as the pit enlarges. The stability products as a function of time for galvanostatically grown pits, shown in Figure 6-50 to Figure 6-52, illustrate an initial increase, but tend to fluctuate between 0.3 to 0.4 A/m for the rest of growth time. Whereas, the stability products of potentiostatic pits shown in Figure 6-53 to Figure

6-56 show slight increase from ~0.2 A/m in the initial stages to values higher than 0.4 A/m. This indicates that in potentiostatic growth, pits can survive and continue to grow if their cover is collapsed, while, galvanostatic pits require their cover for continuation of propagation.

It is also seen that pits initially grow below the stability product with the support of their cover. Even after that, only at the pit bottom does the stability product exceed 0.3 A/m; the rest of boundary grows under conditions below the stability value because of diffusion barrier provided by cover. This emphasises the importance of the lacy cover for transport of metal ions from the pit bottom into the bulk solution and supports the proposed *'coveredness factor'* applied to calculation of concentration within the pit.

The comparison of stability for a certain pit size (~150 μm boundary length) shown in Figure 6-57 to Figure 6-59 illustrates a higher stability product values in higher chloride concentration of bulk solution. The slightly higher stability product seen in pits grown in higher chloride concentrations may indicate a less occluded cover over the pit, which is consistent with the observation of Ernst and Newman[107] and Frankel *et al*. [72].

6.12 Conclusions

1. The feasibility of X-ray synchrotron radiography imaging to study pit propagation *in situ* in real time has been demonstrated. The key dissolution kinetics parameters of pit growth have been extracted from radiographs of 2D pits growing in stainless steel foils in sodium chloride solutions. The relationship between the local anodic current density, metal ions concentration and interfacial potential at the pit surface has been established, from which an anodic Tafel slope and surface kinetic plots have been obtained.

2. The local current density along pit perimeter can be directly measured from the movement of the pit boundary. The active local current density inside a pit varies between ~ 1 and 5 A/cm^2. The maximum current density is seen at the transition point from the passive to active region of the pit wall and is between ~3 and 5 A/cm^2. It is suggested that this is the critical passivation current density, i_{crit}. The i_{crit} values increase slightly with increase in the bulk chloride concentration and indicate that the lateral growth is potential dependent. The lowest active current density is seen at the pit bottom, and is the diffusion-limited current density. The current density within a pit under potential control remains almost constant during growth, whereas it shows significant decrease during galvanostatic pit growth.

3. Both galvanostatic and potentiostatic pits show diffusion controlled pit depth and an effective diffusion coefficient can be extracted from (pit depth)^2 vs. time. The value obtained for 2D pits is less than 1D pit and the discrepancy can be attributed to the lacy cover which acts as a diffusion barrier. A *"coveredness factor"* can be introduced to take into account of the lacy cover in metal ions transport.

4. The concentration of metal ions inside the pit cavity can be calculated by solving the transport equations knowing the local current density within the pit. The critical concentration required for continuation of pit propagation can be distinguished at the transition point between corroding and passive regions. In potentiostatic growth, as the pit grows, the surface concentration of metal ions increases owing to an increase in diffusion length. This leads to super-saturation and salt film precipitation. However, in galvanostatic growth, the surface

concentration fluctuates around the critical concentration for continued dissolution.

5. An anodic Tafel slope of ~100 mV is obtained from the long term relationship between the average interfacial potential and the average current density of a galvanostatically growing pit.

6. The relationship between local anodic current density, concentration and interfacial potential can be extracted from a 2D growing pit in order to generate surface kinetics plots of iso-potential current density as a function of metal ions concentration.

7. The stability product decreases with decrease in bulk chloride concentration implying more occluded pit cover. In potentiostatic growth, stability increases as the current density is almost constant while the pit depth increase and the pit can survive its complete loss of the cover. But, in galvanostatic growth, pit stability remains constant or slightly decrease as the current density decreases and pit will repassivate if the cover collapses. The discrepancy between the empirical stability product measured from 2D pits and the theoretical stability criterion can be correlated with the pit cover supporting the *“coveredness”* factor applied in the calculation of concentration of metal ions.

7 Pit propagation predictive model

7.1 Introduction and background

A number researchers have developed predictive models for the pitting corrosion of stainless steel including stochastic models [149, 167-172], deterministic model based on damage function analysis [173, 174] and models for pit propagation [8, 175]. However, to date, only the model of Laycock and co-workers [7, 110, 138-143] is able to simulate the ‘lacy cover’ that develops during pit growth. Such a cover plays a crucial role in the early stages of growth by maintaining the critical local chemistry required for metal dissolution within the pit.

In this chapter, the model developed by Laycock and co-workers is described, including its assumptions and input parameters. The sensitivity of the model to various key growth parameters is evaluated and a modified version of the model incorporating experimental data described in Chapter 6 is proposed and compared with the original version.

7.2 Model Basis and Assumption

The model was originally developed for propagation of a single pit in 300 series stainless steels in chloride solutions under potentiostatic and galvanostatic control [7, 141]. It has been recently developed to consider the interaction between multiple pits [138, 176]. The model covers stable and metastable pit growth and is based on the requirement for near saturated local chemistry for active dissolution. Salt film precipitation, transport phenomena including electromigration and diffusion, and lacy cover effect on ions transport are explicitly considered.

The model (Fortran) has a 3D geometry through the use of cylindrical (r,θ) co-ordinates. This is in contrast to the C++ routines used for extraction of experimental pit growth data shown in Chapter 6 in which 2D geometry is used in the pit (foil), extended to 3D in the cell above the pit.

The main components and basic assumptions of the model are as follows:

1. *Pit initiation* is not considered in the model mechanistically and only the initial condition for a pit cavity of a certain size is defined.

2. *Local chemistry*: pit propagation requires a critical chemistry inside the pit cavity for active dissolution. The concentration of expected species in the solution is calculated as a function of the total metal ion concentration. Salt film precipitation is also taken into account.

3. *Dissolution kinetics* are a function of the local chemistry and interfacial potential.

4. *Pit propagation* is simulated with a finite element method using cylindrical co-ordinates as described below (with the input from *dissolution kinetics* results).

These components, and the values used for input parameters and constants are described in the following sections.

7.3 Description

7.3.1 Initiation

For the purpose of modelling, the pitting process is interpreted into two steps; nucleation and propagation. The transition between these steps is considered as pit initiation. In the model, it is assumed that a nucleation event has occurred at a point on the surface. The stability of pit propagation from the nucleation is then tested, and if propagation is possible at that site, the pit will "initiate". It is assumed that nucleation has occurred at an inclusion on the metal surface. The results of a nucleation event occurred at an inclusion site are considered and simplified as the basis for propagation as follows:

1. Nucleation has occurred via dissolution at an inclusion site. The nature of any dissolution products from the inclusion are ignored in the pit solution chemistry.
2. The cavity geometry is dependent of the original size and shape of the inclusion.
3. Inclusions are considered to be spherical and the original geometry of a pit cavity, as shown in Figure 7-1, is "that of a truncated sphere".
4. Once an inclusion dissolves, it produces active metal surface (oxide free) and saturated chemistry within the cavity. The ability of the pit cavity to propagate from this point onward is the stability test that the model now deals with.

The stability test is based on a comparison between the anodic dissolution current density (generated by applying a given potential or current) and the theoretical current density required for pit propagation for the specific local chemistry at each point of the pit cavity. This will be discussed in detail in the next sections.

Figure 7-1 shows a cavity generated by dissolution of a model inclusion. This is considered to be the starting point for pit propagation. The original geometry of the cavity is defined by the pit radius (r_{pit}) and the angle that the centre of cavity makes with the pit mouth ($\theta<90$), which corresponds to the extent of the cavity's initial "openness". Therefore, varying r_{pit} and θ represents different possible geometries of a pit cavity. A cylindrical coordinate system is used to describe the pit geometry and growth. The *z* and *r* axes are considered to be perpendicular and horizontal, respectively, with respect to the metal surface. The pit is hemispherical in shape and symmetrical about the *z* axis. Figure 7-1 also shows the "infinity boundary", which is defined as 40 times the pit radius.

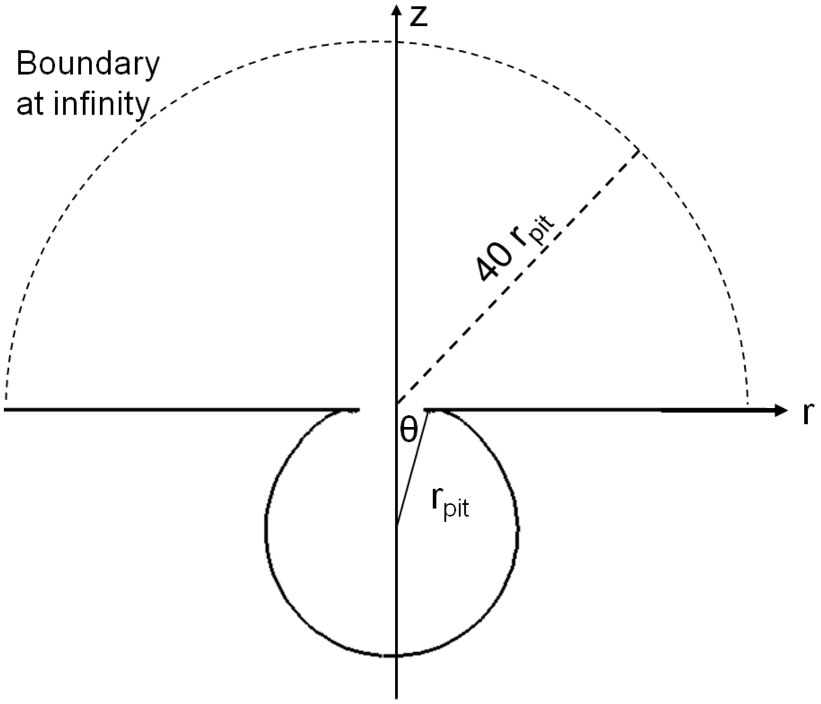

Figure 7-1- initial cavity geometry and its infinity boundary with variable r_{pit} and θ (after [7])

7.3.2 Local chemistry inside pit

The solution inside pit is assumed to be concentrated in metal and chloride ions. The metal ions, M^{z+}, are generated by the anodic dissolution, and undergo further hydrolysis reactions e.g.:

$$M^{z+} + yH_2O \quad \rightarrow \quad [M(OH)_y]^{(z-y)+} + yH^+$$

Thus the metal ion concentration and the extent of hydrolysis control the local pH inside the pit. Also it is assumed that the migration of anions from the bulk solution into the pit maintains electroneutrality with the pit solution. Considering stoichiometric dissolution of a typical composition of stainless steel (Fe-18Cr-10Ni), the pit solution chemistry can be calculated as a function of total metal ion concentration, C_M, based on the method proposed by Sharland [177]. The effect of any minor elements in the alloy, such as Mo, is considered as negligible for the purpose of calculating local solution chemistry. Thus, this approach to the calculation of metal ion concentrations is taken to be applicable to all 300 series stainless steels. Figure 7-2 shows the concentration of each species in the pit solution as a function of the total metal ion concentration.

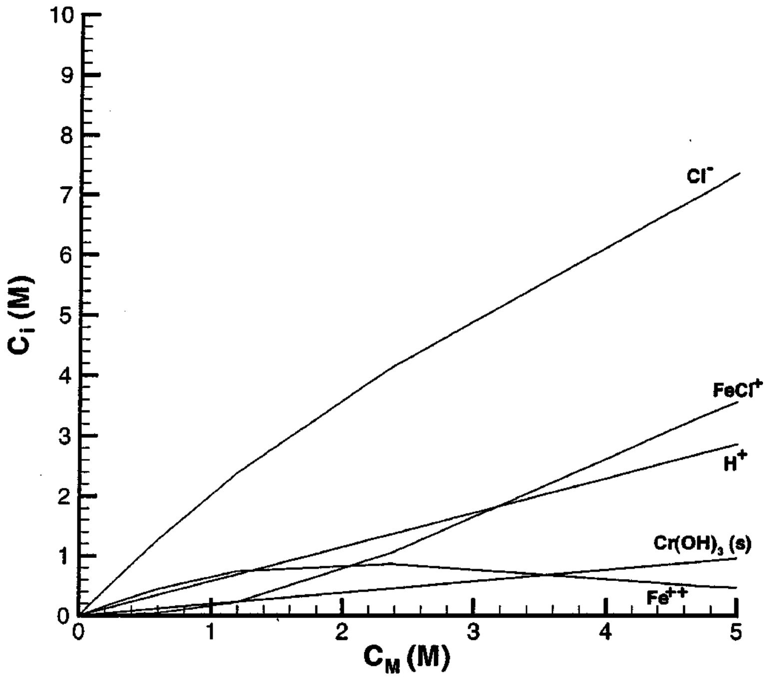

Figure 7-2- Concentration of metal ions in solution (C_i) as a function of the total metal ion concentration, C_M, calculated based on the method described by Sharland [177]. Figure is taken from reference [7].

7.3.2.1 Salt film

Once the metal chloride concentration exceeds the saturation value, a salt film may precipitate on the corroding metal surface [76, 78]. In this model, precipitation of a salt film is assumed to occur on the interior surface of a pit or on the existing salt film. Therefore, on the existing salt layer, a supersaturated solution [90] is expected in this model, consistent with the observation of 130% of saturated concentration before salt film precipitation by Isaacs and Newman [178]. The salt precipitation rate at the surface is defined by:

Equation 7-1

$$\frac{dC_{\mathrm{M}}}{dt} = \alpha(C_{\mathrm{M}} - C_{\mathrm{sat}})$$

where C_{sat} is the saturation concentration of metal ions in solution and α is a value chosen to maintain the supersaturation below 110%. The C_{sat} value is an input parameter and can be taken as the reported values of 5 M [160] or 4.2 M [89]. The salt film is assumed to be porous ferrous chloride and an Ohmic conductor with a density, ρ_{salt}, of 1.9 g.cm^{-3} [78, 89, 160] and the conductivity, σ_{salt}, of 20 µS.cm^{-1}[78].

7.3.3 Dissolution kinetics

7.3.3.1 Cathodic reaction:

As the model is designed to simulate pit growth under conditions where the cathodic reaction is remote from the pit, hydrogen evolution is the only cathodic reaction within the pit that is considered in this model:

$H^+ + e^- \rightarrow \frac{1}{2} H_2$

It is assumed that the cathodic reaction kinetics follow Tafel's law and depend on the concentration of individual species:

Equation 7-2

$$-b_{\mathrm{c}} \log(i_{\mathrm{c}}) = E - E_{\mathrm{c}} - \sum_{i} b_{\mathrm{c}} n_{\mathrm{c,i}} \log C_{\mathrm{i}}$$

where b_{c} is the cathodic Tafel slope, i_{c} is the cathodic current density, E is the electrode (interfacial) potential, E_{c} is a constant, $n_{\mathrm{c,i}}$ is the reaction order with respect to species, i. As shown in Figure 7-2, for any metal ion concentration, the concentration of H^+ can be calculated. In this model, the cathodic reaction is assumed to be only dependent on the concentration of $[H^+]$. Based on the work of Darwish *et al.* [165] for the evolution of hydrogen on pure iron, a reaction order of 1 with respect to H^+, and a cathodic Tafel slope of 120 mV is assumed in the model.

7.3.3.2 Anodic reaction:

The anodic passive current density is considered to be negligible and the only significant anodic reaction is metal dissolution within the pit. The dissolving metals are assumed to be Fe^{2+}, Ni^{2+} and Cr^{3+} [179]. The average charge on the dissolved metal ions is assumed to be 2.2, considering a stoichiometry of Fe-18Cr-10Ni (in wt %). The anodic reaction obeys Tafel's law and depends on species concentration, C_i:

Equation 7-3
$$-b_\mathrm{a}\log(i_\mathrm{a}) = E - E_\mathrm{A} - \sum_i b_\mathrm{a} n_\mathrm{a,i} \log C_\mathrm{i}$$

where b_a is the anodic Tafel slope, i_a is the anodic current density, E_A is a constant and $n_\mathrm{a,i}$ is the reaction order with respect to species i. A b_a value of 54 mV was reported for Fe-17Cr alloy stainless steel by Gaudet *et al*. [84]. However, similar experiments by Laycock and Newman [82, 118] showed a value of 120 mV for 304 stainless steel. In this model, a constant anodic Tafel slope of 100 mV is taken in the calculation. It is also assumed that the anodic reaction depends only on the concentration of H^+. A range of anodic reaction orders reported in the literature [91, 165, 166] have been used in the simulation and a $n_\mathrm{a,i}$ value of 0 has been optimised through the comparison of simulation and experimental results. The effect of different values of b_a and $n_\mathrm{a,i}$ on the model results will be discussed later in this chapter.

7.3.3.3 Applied potential

In this model, identical dissolution kinetics are assumed for bare and salt-film covered surfaces. However, a salt film creates a potential barrier on the surface, and the potential drop across the salt layer must be included in the potential distribution model. Therefore, from the work of Beck[96] and others[82, 143], the relation between anodic current density and applied potential can be written as:

Equation 7-4
$$E_\mathrm{app} = E_\mathrm{corr} + b_\mathrm{a}\log\left(\frac{i_\mathrm{a}}{i_\mathrm{corr}}\right) + \phi_\mathrm{s} + \phi_\mathrm{sf}$$

where E_app is the applied potential, E_corr and i_corr are the open-circuit corrosion potential and current density, ϕ_s is the ohmic potential drop in solution between the bare or salt film covered surfaces and the reference electrode, and ϕ_sf is the potential difference across the salt film. Hence, the current density at any point on the pit surface can be given by Equation 7-4 which is valid for all metal ion concentrations at which active corrosion takes place. However, E_corr and i_corr are a function of the concentration of metal ions, and this effect must be calculated for any C_M. For 304 and 316 stainless steel, E_corr and i_corr for the C_M value of 95% of the saturated metal ion concentration are taken from the work of Hakkarainen [74] as shown in Table 7-1. By solving Equation 7-2 and Equation 7-3 for the given concentration, E_A and E_C are derived. This enables calculation of E_{corr} and i_{corr} at any C_M. As described above, the anodic and cathodic currents are assumed to be dependent only on the H^+ concentration, therefore it can be written:

Equation 7-5
$$-b_c \log(i_c) = E - E_C - b_c n_c \log(C_{H^+})$$

Equation 7-6
$$b_a \log(i_a) = E - E_A + b_a n_a \log(C_{H^+})$$

Assuming $E = E_{corr}$ and $i_{corr} = i_a = i_c$, then

Equation 7-7
$$E_{corr} = -\left(\frac{b_a E_C + b_c E_A + (n_c b_a b_c - n_a b_a b_c)\log(C_{H^+})}{b_a + b_c}\right)$$

Equation 7-8
$$\log(i_{corr}) = \left(\frac{E_C - E_A + (b_a n_a + b_c n_c)\log(C_{H^+})}{b_a + b_c}\right)$$

Taking $C_{H+} \approx 0.574 \times C_M$ from Figure 7-2 and assuming the values of E_{corr} and i_{corr} for 316 stainless steel at 95% saturated C_M, the constant values of E_A and E_C can be derived as -0.35 and -0.402 mV, respectively. From these values E_{corr} and i_{corr} may be calculated for all metal ion concentrations between zero and the saturation value, C_M. Figure 7-3 shows the variation in E_{corr} and i_{corr} as a function of surface saturation of the total metal ion concentration in solution for 316 stainless steel.

In this model, the electrochemical behaviour of 300 series stainless steel are assumed similar and the difference between e.g. 304 and 316 stainless steel is accounted for by making changes in the E_{corr} and i_{corr} values as input into the model [7].

Table 7-1 Values of E_{corr} and i_{corr} assumed in the pit propagation model for 304 and 316 stainless steels in 95% saturated solutions of metal ions [7, 74]

Alloy	E_{corr} (mV, SCE)	i_{corr} (mAcm^{-2})
304	-400	1
316	-350	0.1

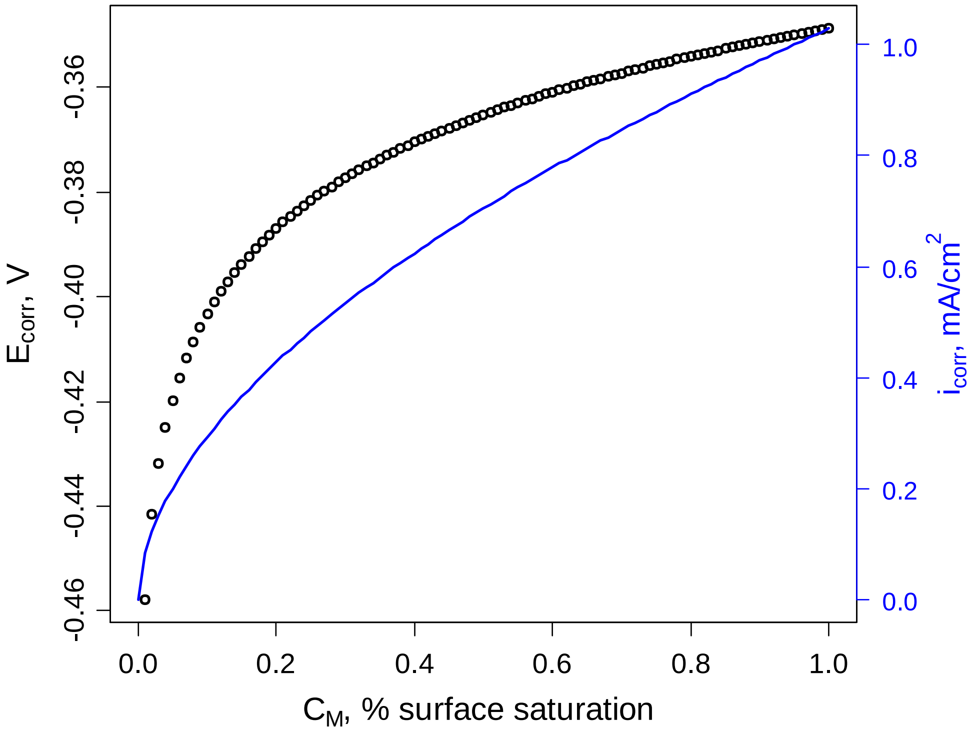

Figure 7-3- E_{corr} and i_{corr} as a function of the surface metal ion concentration C_M (plotted as C_M/C_{sat}) for 316 stainless steel assuming b_a=100 mV, n_{a,H^+} =0, b_c=120 mV and n_c=1.

7.3.3.4 Passivation

In order for the model to identify the active and passive region, a criterion for the transition between these two regions must be introduced. Salinas-Bravo and Newman [119] proposed the existence of a critical passivation current density, i_{crit}, above which the metal will passivate, to explain the critical pitting temperature (CPT). It was shown that below the CPT, the critical current density for passivation, i_{crit}, is less than the anodic dissolution current density required to maintain the critical chemistry necessary for the pit stability and consequently the pit repassivates. Therefore, it was proposed that the CPT is the temperature where the current density required for active dissolution is less than i_{crit}. It was also shown that i_{crit} increases with temperature. This suggestion has been adapted in this model to differentiate the dissolution kinetics at the junction between active and regions of the pit surface. At high values of C_M (higher than the critical concentration required for propagation) the active anodic current density, i_a, is less than i_{crit} and dissolution continues. However, at lower values of C_M, the required current density for dissolution (calculated value of i_a) exceeds i_{crit} and as a result surface repassivates. Therefore, it was assumed that the point at which i_a reaches i_{crit} corresponds to the critical dissolution concentration, C_{crit}. Although there was no evidence in the literature for the variation of i_{crit} within the pit, based on the dependence of i_{crit} on H^+ and Cl^- reported in the literature for stainless steel [180, 181], it was assumed in the model that i_{crit} increases with the concentration of dissolved metal ions, C_{M}. Therefore, an empirical function was adapted for the model to correlate i_{crit} with C_{M}

Equation 7-9

$$i_{crit} = x.10^{y(C_M / C_{Sat})}$$

where x and y are constant numbers chosen so that C_{crit} is between 50 to 80% of saturation. Therefore, the surface current density is modelled by the following step function algorithm:

$$\text{if} \quad \begin{cases} i_{\mathrm{a}} < i_{\mathrm{crit}} & \text{then} \quad i_{\mathrm{a}} = i_{\mathrm{corr}} 10^{\left(E_{\mathrm{app}} - \phi_{\mathrm{s}} - \phi_{\mathrm{sf}} - E_{\mathrm{corr}}\right) / b_{\mathrm{a}}} \\ i_{\mathrm{a}} > i_{\mathrm{crit}} & \text{then} \quad i_{\mathrm{a}} = 0 \end{cases}$$

7.3.4 Pit propagation

In this section, a method is introduced for numerical simulation of pit propagation in a NaCl electrolyte (of C_{sol} concentration) from the starting point described in the pit initiation section. The general procedure is that at time *t,* the local anodic current density is calculated on the pit surface, the resulting anodic flux is injected into the solution over a period of Δt and the boundary is moved to new location due to metal dissolution, the new concentration at time $t + \Delta t$ is calculated and then this sequence is repeated. In this process, the assumptions and initial conditions are taken as follows:

i. The symmetry of the initial cavity is retained during the growth process.
ii. M^{z+} is the only dissolution product i.e. the complicated solution chemistry displayed in Figure 7-2 is ignored.
iii. The solution is assumed electrically neutral in all points, therefore the equation for electrical potential is given by:

Equation 7-10

$$\nabla.(\sigma.\nabla\phi) = 0$$

where ϕ is the ohmic potential drop (with respect to a reference electrode located at infinity) and σ is the solution conductivity which is calculated by

$$\sigma = \frac{F^2}{RT}\sum_i C_i D_i z_i^2$$

Equation 7-11

where F is the Faraday constant, R is gas constant, T is the temperature and D_i is the diffusion coefficient, which is taken to be 1×10^{-5} cm^2/s for all species. All simulations are performed at ambient temperature (23 °C).

It is assumed that electroneutrality is maintained within the pit environments via the transport of cationic dissolution products from the pit cavity into the bulk solution and transport of anions from the bulk into the pit. Therefore, the transport of ions can be quantified by

Equation 7-12

$$\frac{\partial C_i}{\partial t} = -\nabla N_i$$

$$N_i = \frac{-D_i C_i}{RT}\nabla(\mathrm{z}_i F\phi) - D_i \nabla C_i$$

where N_i is the molar flux of ions. The above transport equations are solved subject to the following initial conditions set for the initial cavity described in the pit initiation section.

$C_\mathrm{M} = C_\mathrm{sat}$	everywhere inside the pit
$C_\mathrm{M} = 0$	elsewhere
$\phi = 0$	everywhere

The boundary conditions are described as below; where $\partial/\partial n$ is a partial derivative in a perpendicular direction to the pit surface (n is the local normal direction).

$C_M = 0$ and	$\phi = 0$	at infinity (which is assumed to be 40 r_pit)
$J_M = 0$		on metal surface outside the pit
$\frac{\partial \phi}{\partial n} = 0$		on metal surface outside the pit
$J_M = \frac{i_a}{zF}$		on the rounded surface of the pit
$\sigma \frac{\partial \phi}{\partial n} = i_a$		on the rounded surface of the pit

A hemispherical surface over the metal surface with a radius of ~40 r_pit is considered as the boundary condition at infinity.

During the growth simulations, and in order to identify the surface kinetics at each point on the pit surface, the model compares the i_a calculated from the Equation 6-4 with the i_{crit} values obtained from Equation 6-9. If $i_a > i_{crit}$, the surface is passive and the local flux is set to zero, otherwise material is removed from the surface with a velocity ν that is given by Faraday's 2nd law

Equation 7-13

$$\nu = \frac{Mi_a}{zF\rho}$$

where M is the molar mass of the material (56 g), z is the number of transferred electrons (+2.2), F is the Faraday constant (96485 C/mol) and ρ is metal density (8 g/cm^3).

7.3.5 Simulation process

The growth of a single pit, with the initial and boundary conditions defined above, is now simulated through the following algorithm.

1. The boundary location for the initial cavity is initialized, and C_M in the pit is set at C_{sat}, and outside the pit at 0, ϕ is set at 0 everywhere and t=0.
2. A Delaunay triangulation of the domain defined by the pit boundary, the metal surface and the hemisphere at infinity is generated using the program triangle.
3. The concentration onto the grid just defined is interpolated either from the initial conditions or from the calculated concentrations at the previous time step.
4. For the values of C_M at each boundary node, E_{corr}, i_{corr} and i_{crit} are calculated.
5. i_a is calculated over the pit using ϕ and salt film thickness at time t through Equation 7-4.
6. The new concentration (C_M) and potential drop (ϕ), as a result of the ion flux injection into the solution, are calculated at time $t+\delta t$ (step forward in time using the Crack-Nicholson algorithm) using a finite element approximation of Equation 7-10 and Equation 7-12. Salt film precipitation is accounted based on Equation 7-1. The equations are not linear and are solved by an iterative Newton's method.

7. The boundary is moved as a result of metal dissolution and a new position for each boundary node is calculated using Equation 7-13. The direction is obtained by bisecting the angle between the two boundary lines that meet at the node.
8. Repeat from 2.

7.3.6 Simulation results

Figure 7-4 shows the cross sections at different stages of growth lifetime for a pit simulation for 1 M NaCl at 180 mV vs. SCE. The initial pit cavity has a 3 μm radius with θ=15°. The white region in the cross section is the metal. The metal ion concentration counters are indicated in colour and vary from 4.2 M (red) at the pit surface to ~ 0.2 (dark blue) in the bulk solution and 0 in the infinity. Qualitatively, the pit cover formation and the pit shape development are reproduced by the simulation. As the pit starts to grow, metal ions inside the pit transport to the outside of the pit under the concentration gradient between the pit interior and the bulk solution, leading to dilution of pit solution. As a result, near the pit rim where C_M falls below C_{crit}, the surface locally repassivates. However, further down near the pit bottom (immediately next to the passive area) where $C_M > C_{crit}$ dissolution continues. This causes undercutting of the metal at the passive/active junction, resulting in formation of a lobe that extends laterally or upward until it eventually punctures the passive metal surface and produces a hole on the top edge. The new hole again causes dilution of the highly concentrated pit solution into the bulk electrolyte and local passivation close to the perforated area. This process repeats during the pit growth and generates a porous cover over the pit cavity.

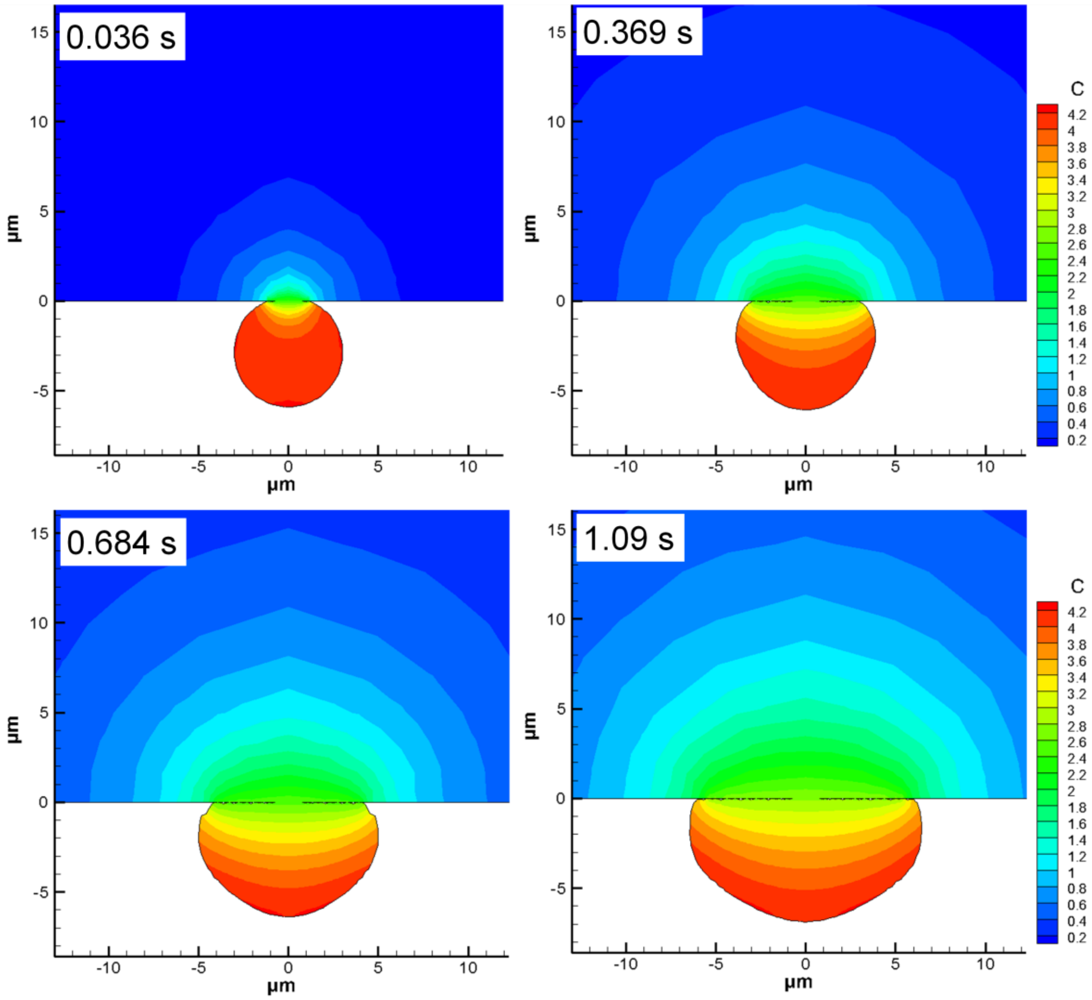

Figure 7-4- A series of cross sections through a simulated pit at different stages of lifetime (time of propagation from initial cavity) for a pit modelled in 316 stainless steel at 180 mV vs. SCE in 1 M NaCl. The initial pit cavity has a 3 µm radius with 15° subtended angle by the pit mouth.

Figure 7-5 illustrates the distribution of i_a, i_{crit}, C_M and the electrical potential drop in solution and across the salt film after (a) 0.036 and (b) 0.369 s of growth for the simulated pit described above (Figure 7-4). The distance along the pit boundary ranges from the left rim of the pit (excluding the porous pit cover) to the middle of the pit bottom. The anodic current density close to the pit mouth is zero. This is the area where $i_a > i_{crit}$ and therefore, the surface passivates and the model sets i_a to zero. i_{crit} (shown in red in plot) at each point is given by Equation 7-9. The junction of passive and active region is the point where i_a equals to i_{crit}. With increasing the pit depth, i_a decreases gradually as C_M increases while the potential drop in this region is only within the solution and almost constant. Increase in the metal ion concentration eventually leads to the salt film precipitation which results in further decrease in i_a down to i_{lim}. In this region, the majority of the potential drop is across the precipitated salt film. It is notable that that the increase in current density and potential drop at the middle of the pit bottom (right hand side of graph) is an error of unknown origin that sometimes occurs/disappears at the pit grows.

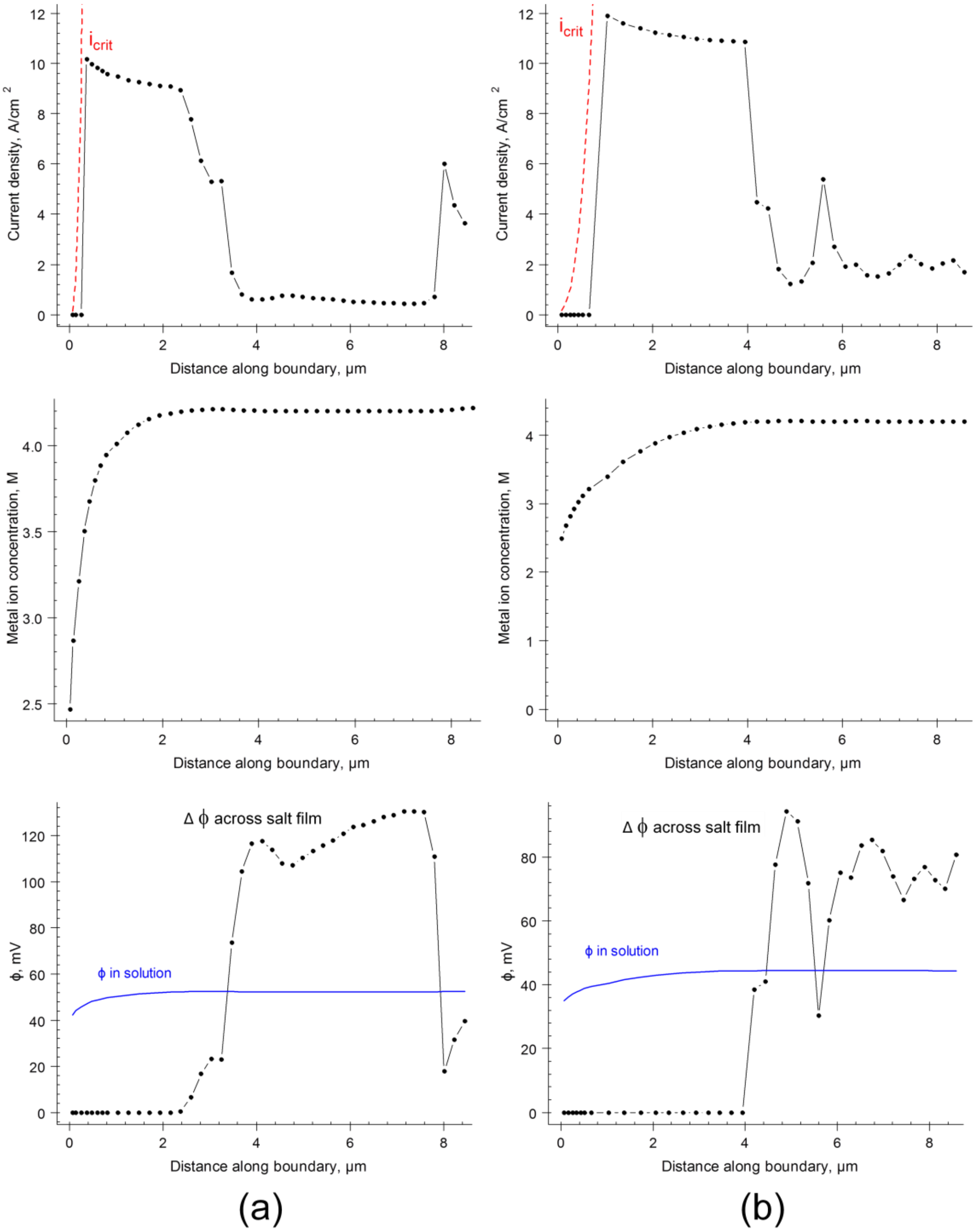

Figure 7-5- Distribution of anodic current density, i_a, and critical current density for passivation, i_{crit}, metal ion concentration at the pit surface, C_M, and potential drop (ϕ) in solution at the pit surface with respect to the reference electrode (infinity) and potential difference across the salt film ($\Delta\phi$) as a function of distance from the pit rim to the pit bottom for a 316 stainless steel pit simulated at 180 mV vs. SCE after growth for (a) 0.036 and (b) 0.369 s of its lifetime. The distance along the pit boundary ranges from the left rim of the pit (excluding the porous pit cover) to the middle of the bottom of the pit (the pit has mirror symmetry).

7.4 Sensitivity

There is some uncertainty associated with the literature values for several parameters in the model. In this section, the effects of changing input parameters on the results of the simulation are discussed. In order to do this, the effect of each parameter on the "stability" of pit growth is evaluated following the approach of Laycock and co-workers [7]. During the simulations, at relatively low potentials some pits grow for a short period of time before they repassivate. This behaviour is similar to the experimental observations of metastable pits which initiate spontaneously but then stop growing after a period of time. Also, the initial and boundary conditions set in this model ensure that pits will always grow for a finite time (~0.1 s) even for a very low applied potential. In this model, therefore, the minimum potential at which a pit can grow without undergoing repassivation during the time scale of simulation is identified as the stable potential (E_s). Below this potential, pits either do not grow or grow for a very short period before passivation. At potentials above E_s, pits can grow "indefinitely": this concept has been developed by Laycock and co-workers [7] who have demonstrated that potentiostatically-controlled pits remain stable once a salt film has formed. It was shown that within the metastable pits grown below E_s no salt film was present which was consistent with the suggestion made by Frankel and co-workers [72, 101, 102] that transition from metastable to stable growth is only possible for pits that have a salt film. Since Laycock and Newman [82] had also shown before that salt film formation potential is very close to the pitting potential, Laycock and White [7] concluded that E_s is effectively the pitting potential, E_{pit}.

In the following simulation results, the base parameters are as follows unless stated otherwise: diffusivity for all species, $D_i = 1\times10^{-5}$ cm^2/s, anodic reaction order with respect to hydrogen, n_i=0, anodic Tafel slope, b_a=100 mV, salt film precipitation rate, α=1 s^{-1}, subtended angle by the pit mouth, θ=15º, initial pit radius, r_{pit}=3 µm.

7.4.1 Anodic reaction order (n_a) with respect to hydrogen

One of the key input parameters in the model is the anodic reaction order with respect to H$^+$. Figure 7-6 shows the pit lifetime as a function of applied potential for different values of anodic reaction order, n_a, for a pit cavity of 3 µm radius and θ=15° that is modelled in 1 M NaCl. For potentials below E_s (indicated by an arrow in the figure), the pit is metastable and the time reported in the figure is the total lifetime that pit was active before passivation. Pits grown at potentials above E_s are stable and grow indefinitely. It can be seen that the increase in anodic reaction order results in a greater pit stability at a given applied potential. The effect of n_a on the surface current density can be observed in Figure 7-7 where the current density variation as a function of C_M for a simulation at 180 mV for different values of n_a is shown. The current density is modelled using the step algorithm described in Section 7.3.3. It can be seen that the higher values of n_a results in lower anodic current density at >80% surface concentration saturation. The decrease in current density is the result of increase in E_{corr} (through Equation 7-7 and Equation 7-4). Laycock and White [7] modelled the current density variation with surface saturation at 100 mV (similar to the shown in Figure 7-7) and compared it with experimental and choose n_a=0 for further simulations. Qualitative comparison of the pit propagation after 0.42 s of growth simulated with different n_a values is shown in Figure 7-8.

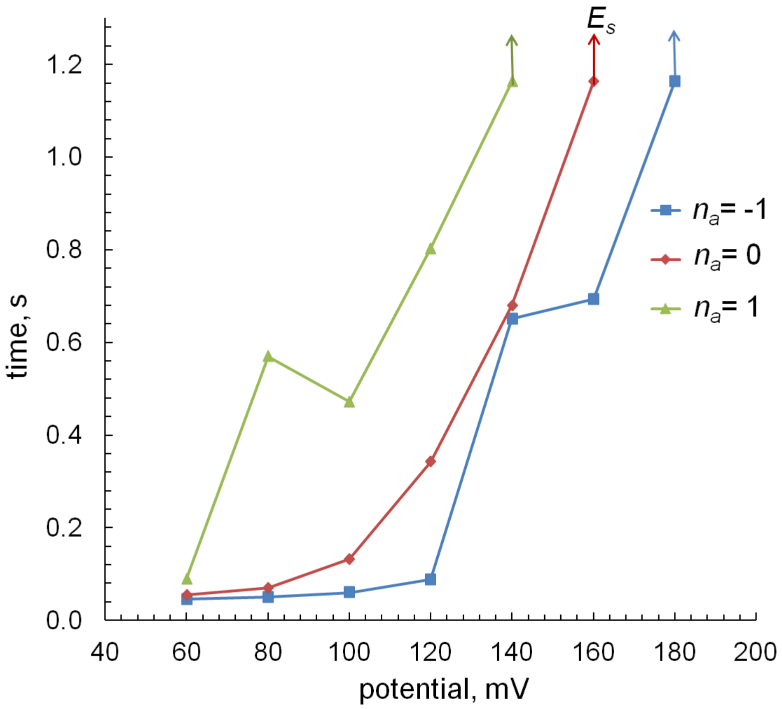

Figure 7-6- Pit lifetime as a function of applied potential at different values of anodic reaction order, n_a, for a 3 µm radius pit in 316 stainless steel pit modelled in 1 M NaCl solution. Arrows indicate the E_s value (stability potential) for each case.

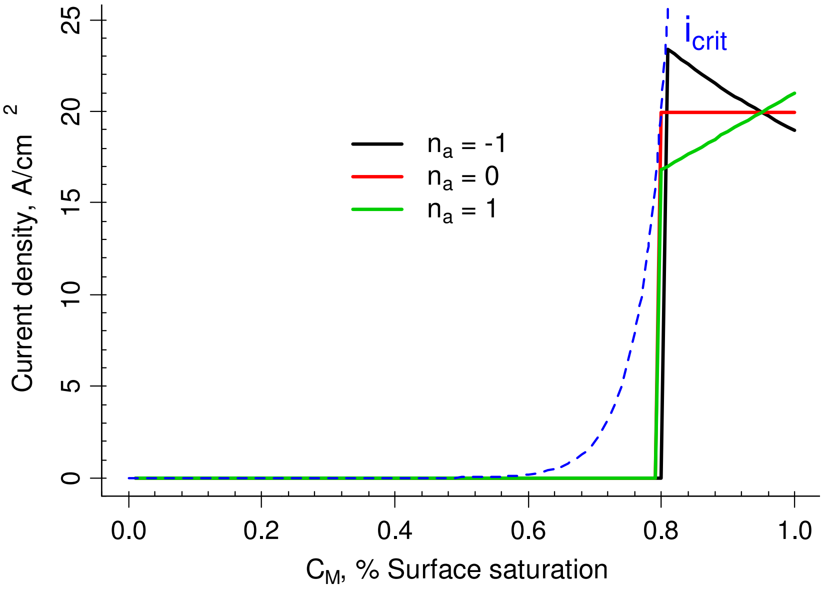

Figure 7-7- The modelled surface anodic current density, calculated for the anodic reaction order values indicated, as a function of C_M at 180mV applied potential for a pit in 316 stainless steel in 1 M NaCl.

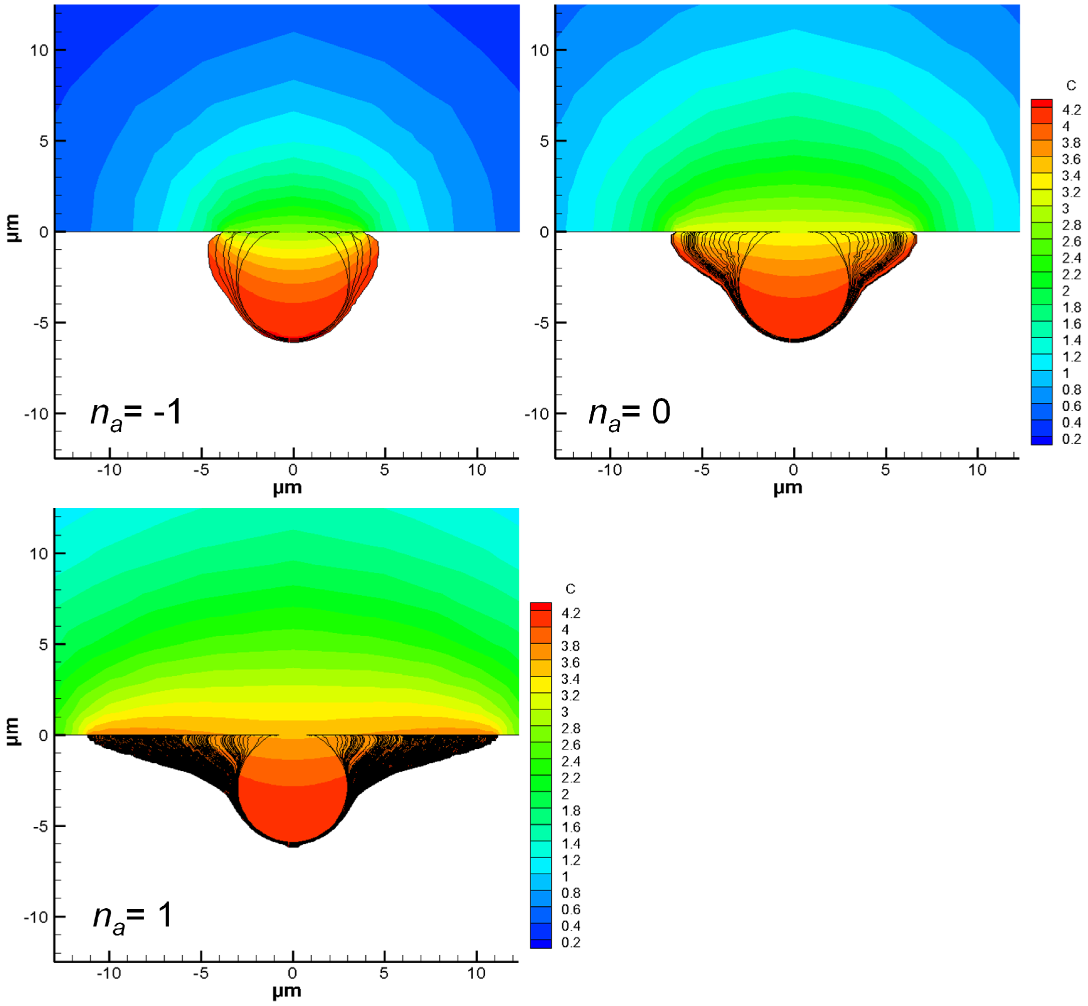

Figure 7-8- Cross sections through simulated pits after 0.42 s of growth lifetime modelled with different anodic reaction order values as indicated. The initial pit is a 3 µm radius cavity with 15° subtended angle by the pit mouth in 316 stainless steel 1M NaCl and at 240 mV vs. SCE applied potential. The black lines indicate the pit boundary at different time frames.

7.4.2 Diffusion coefficient

The effect of the diffusion coefficient parameter on the pit stability is shown in Figure 7-9. It can be seen that decreasing D_i results in greater pit stability through shifting E_s to lower potentials. This is as a result of the slower rate of metal ion transport towards the outside of the pit, which causes the metal ion concentration to reach the saturation value and form a salt film layer on the corroding surface more quickly, which lowers the current density to the diffusion-limited current density at most of the pit bottom. A slower diffusivity also ensures that a thicker salt film is present on the pit surface. Qualitative comparison of simulated pits with different diffusivity values grown at 200 mV are shown in Figure 7-10, which indicates that there is a smaller pit size and slower growth rate in pits modelled with a lower diffusion coefficient. Figure 7-11 shows the salt film thickness along the pit boundary of the modelled pits shown in Figure 7-10. Although the pit sizes are slightly different and some noise is seen at distances of 4-8 μm from the pit mouth (of unknown origin), a gradual increase in salt film thickness is seen towards the bottom of the pit modelled with a diffusion coefficient of 0.5×10^{-5} cm^2/s.

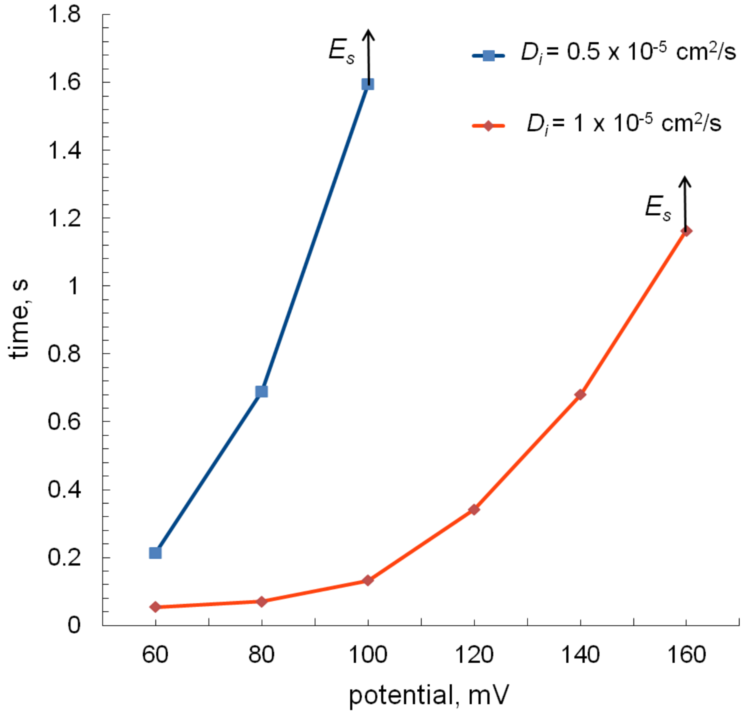

Figure 7-9- Pit lifetime as a function of the applied potential at different diffusion coefficient values, D_i, for a 3 μm radius pit in 316 stainless steel pit modelled in 1 M NaCl solution. Arrows indicate the E_s value (stability potential) at each case.

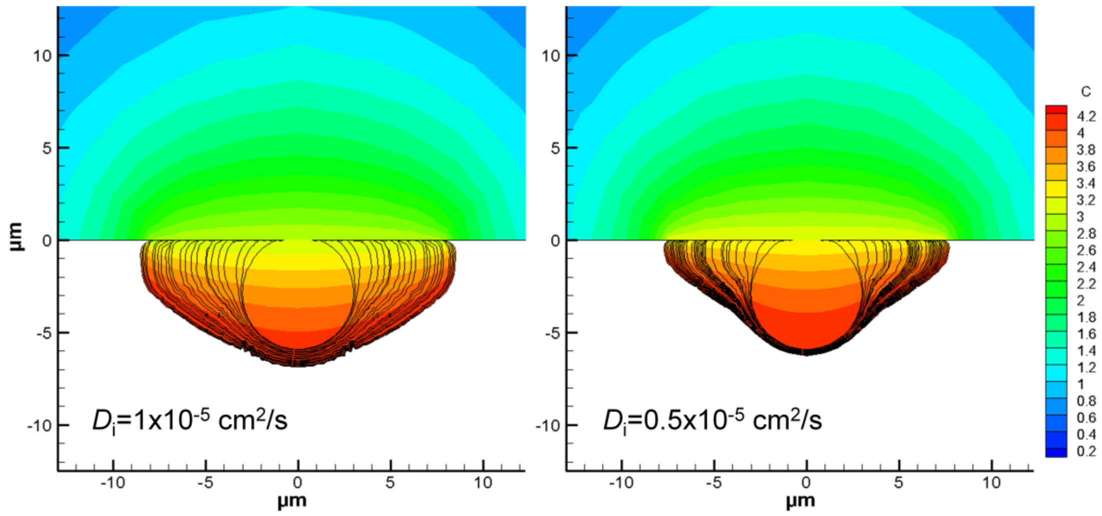

Figure 7-10- Cross sections through simulated pits after 1.16 s of growth lifetime modelled with different diffusivity values of indicated. The initial pit is a 3 µm radius cavity with 15° subtended angle by the pit mouth in 316 stainless steel 1 M NaCl and at 200 mV vs. SCE applied potential. The black lines indicate the pit boundary at different time frames.

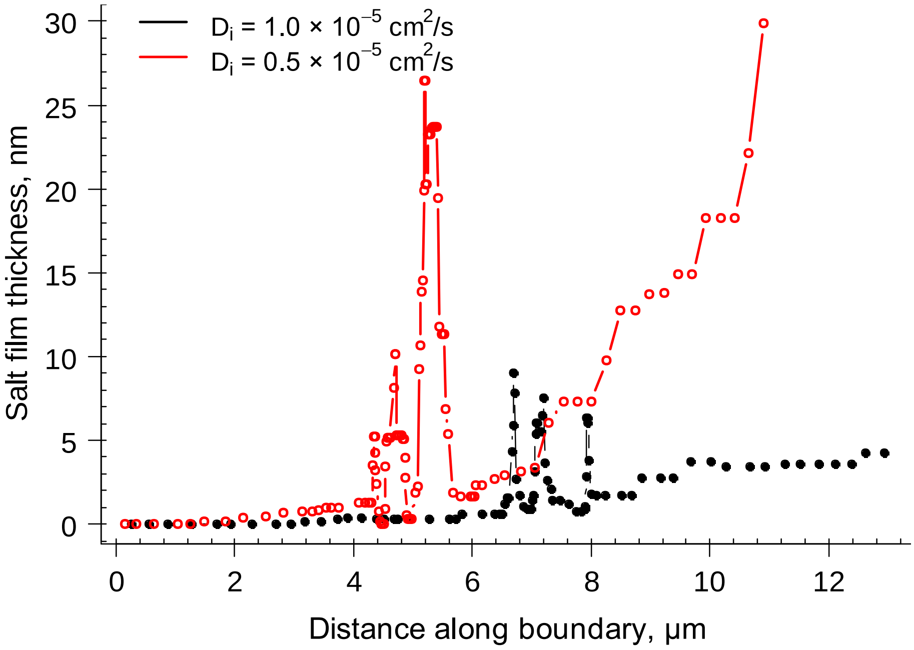

Figure 7-11- Salt film thickness along the pit boundary from the pit rim (0 µm) towards the middle of the pit bottom (right hand end of the lines) for the modelled pits shown in Figure 7-10. The pit has mirror symmetry.

7.4.3 Anodic Tafel slope

Figure 7-12 shows the pit lifetime as a function of the applied potential for various anodic Tafel slope values of 60, 80, 100 and 120 mV/decade for a pit of 3 µm initial radius in 316 stainless steel modelled in 1 M NaCl solution. It can be seen that as b_a increases then E_s increases too. The stability potential for the pits modelled with b_a

values of 60 and 80 mV/decade are seen at -40 and -20 mV, respectively. Whereas, for b_a= 100 and 120 mV, no stable growth is seen below 160 and 240mV, respectively.

It is worth noting that there is also a limitation in the maximum applied potential that can be successfully used to run the model. This is caused by the active-passive transition criterion (i_{crit}) that impedes the simulation above a certain potential. At any relatively high applied potential where i_a exceeds i_{crit} on any point on the pit surface, then the surface is assumed passive and model will not run. For the pits simulated with b_a values of 60, 80 and 100 mV/decade, the program stopped working at the first step at potentials higher than 80, 140 and 260 mV, respectively. However, these values do not appear on the graph as these potentials are above the stability point.

For b_a values of 120 mV/decade, no modelling was performed at potentials higher than 340 mV, up to which value the model operates successfully. Therefore, the effect of anodic Tafel slope is seen to shift the range of functional applied potentials through Equation 7-4 in combination with Equation 7-9.

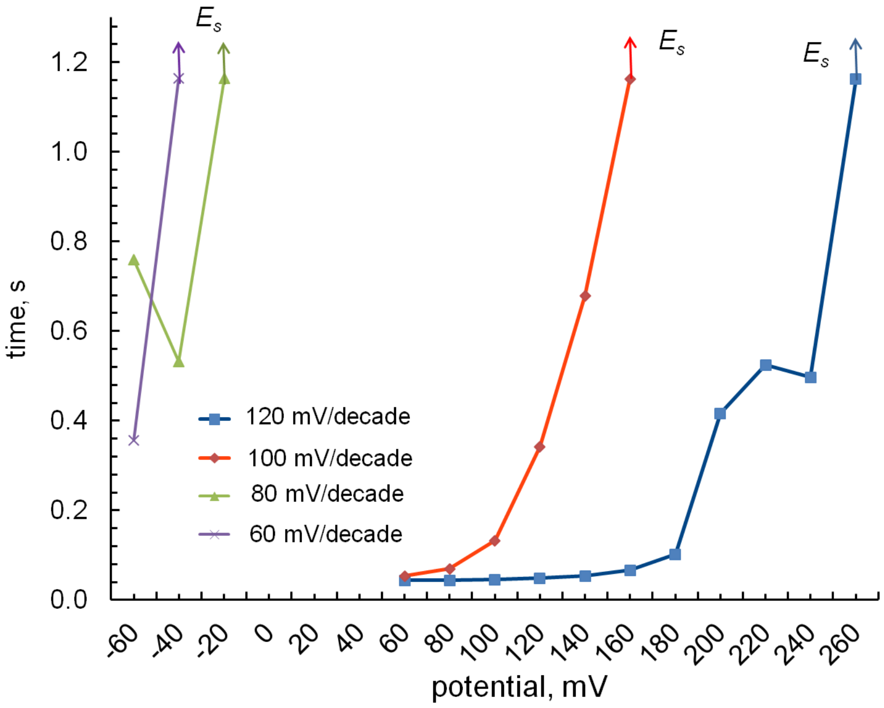

Figure 7-12- Pit lifetime as a function of the applied potential for different anodic Tafel slope values, b_a, for a pit with 3 µm initial radius in 316 stainless steel pit modelled in 1 M NaCl solution. Arrows indicate the E_s value (stability potential) for each case.

7.4.4 Salt film precipitation rate

The α parameter in Equation 7-1 is empirically chosen to adjust the salt film precipitation so that the concentration of metal ions on the pit surface does not exceed 110% of saturation. Figure 7-13 compares the cross sections of simulated pits at 220 mV in 1 M NaCl after 1.0 s of growth lifetime with α chosen as (a) 10 and (b) 1 s^{-1}. While the final shape of pits and the pit boudnaries seem very similar, a higher number of pit boundaries with jagged (rough) surfaces are seen for the pit modelled with an α value of 10 s^{-1}. The time resolution for the pit boundary movement at each case is *ca.* (a) 10^{-3} and (b) 10^{-2} s. The current density and salt film distribution along the pit boundary (from the pit rim to the pit bottom) after 1 s of the lifetime growth of the above pit are shown in Figure 7-14 where a smoother decrease is seen in the current density variation from the pit rim to the pit bottom for the pit modelled with an α value of 1 s^{-1}.

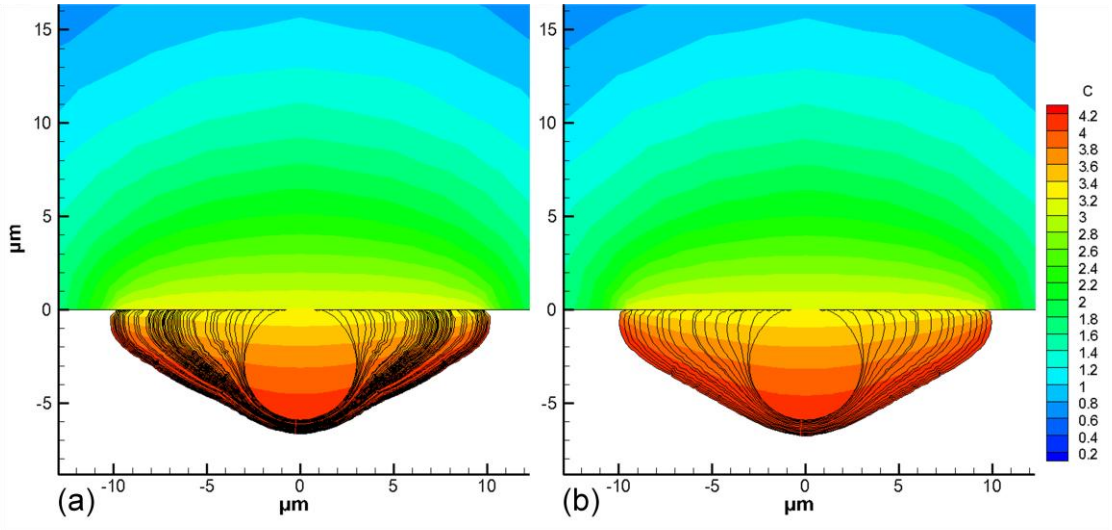

Figure 7-13- Cross sections through simulated pits after 1.0 s of growth lifetime modelled with α (a) 10 and (b) 1 s^{-1}. The initial pit is a 3 µm radius cavity with 15° subtended angle by the pit mouth in 316 stainless steel 1 M NaCl and at 220 mV vs. SCE applied potential. The black lines indicate the pit boundary at different time frames (The time resolution for the pit boundary movement at each case is *ca.* (a) 10^{-3} and (b) 10^{-2} s).

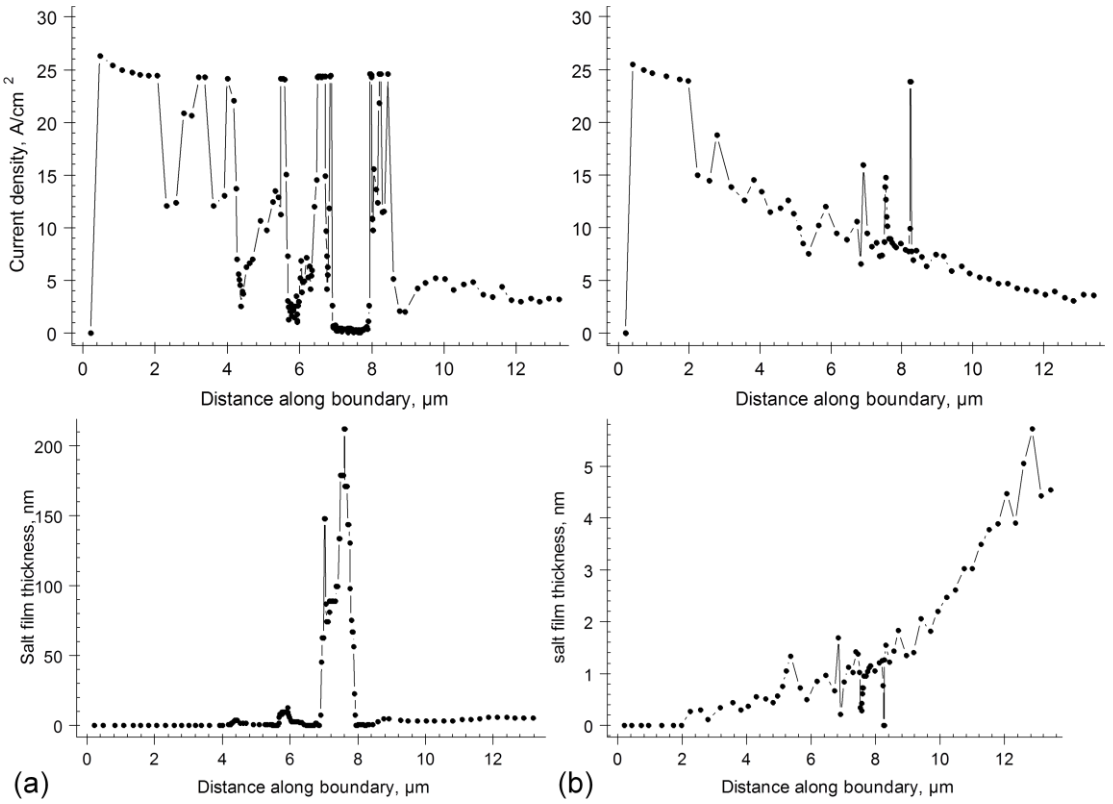

Figure 7-14- Current density and salt film thickness distribution as a function of distance from the pit left rim (0 µm) to the middle of pit bottom (~13 µm) for the simulated pits shown in Figure 7-13 at 1 s of growth lifetime modelled with α value of (a) 10 and (b) 1 s^{-1} in 316 stainless steel 1 M NaCl and at 220 mV vs. SCE applied potential. The pit has mirror symmetry.

7.4.5 Conductivity

The conductivity of the solution at each point is given by Equation 7-11, which is valid for dilute solutions [7]. However, the solution inside pit is concentrated in metal ions and may even exceed C_{sat} at the pit bottom. In order to evaluate the sensitivity of simulation results to conductivity, a factor of 0.5 has been applied to Equation 7-11 and simulations were performed for 1 and 0.01 M NaCl solutions. Figure 7-15 compares the pit lifetime as a function of the applied potential for different values of solution conductivity for a pit of 3 µm initial radius in 316 stainless steel pit modelled in 1 and 0.01 M NaCl solution. While the stability potential, E_s, has increased significantly for the pits modelled in 0.01 M compared with the pits simulated in 1 M, less sensitivity to the value of conductivity at each solution is observed.

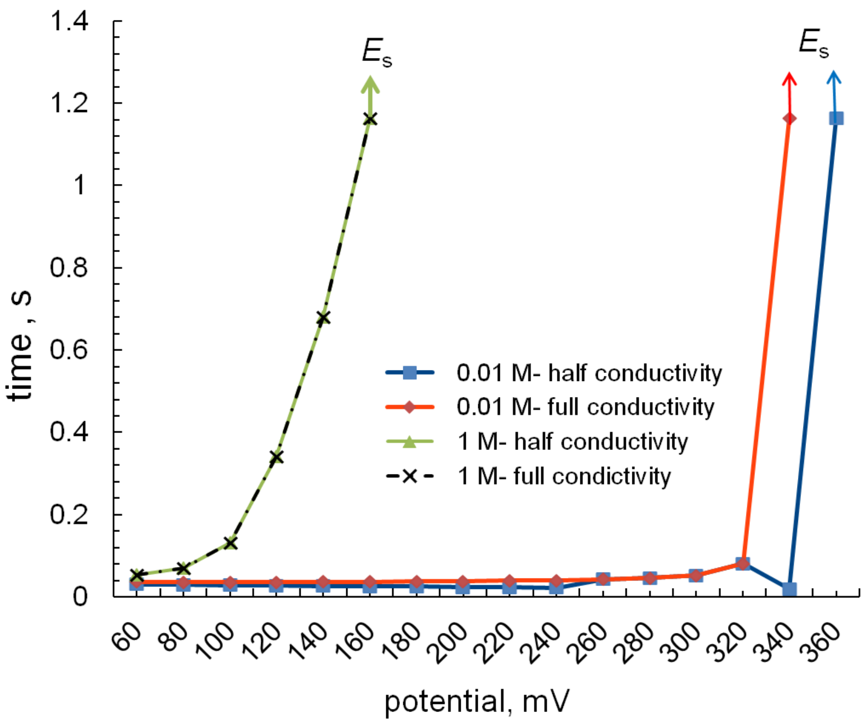

Figure 7-15- Pit lifetime as a function of the applied potential for different values of conductivity of 1 and 0.01 M NaCl solution for a 3 µm initial radius pit in 316 stainless steel pit modelled. Arrows indicate the E_s value (stability potential) at each case. A factor of 0.5 has been applied to Equation 7-11 which calculates the conductivity of solution at each point.

7.4.6 Pit cover

The effect of a perforated cover over the pit cavity on the ion transport from inside the pit to the bulk solution was shown in Chapter 6. It was shown that the lacy cover acts as a diffusion barrier to the transport process causing an increase in concentration of metal ions inside the pit solution and dilution around the pit mouth in bulk solution. Although the effect of remnant lacy layer on the transport process is considered in the simulation during pit development, the extent of perforation of the cover on the initial pit should also be addressed. In order to consider the effect of the cover on the pit growth, a cover with certain thickness is assumed over the pit cavity, through which the diffusivity of metal ions is adjusted separately from the value used within the bulk and pit solution. By applying a higher diffusivity value across the hypothetical cover, the transport of metal ions in the bulk electrolyte close to the pit mouth is accelerated, leading to local dilution close to the pit mouth.

The effect of higher diffusivity values across the hypothetical cover is examined as follows. Figure 7-16 shows the final shape of simulated pits after 10 s of growth lifetime. Pits with 30 μm initial radius were modelled in 0.1 M NaCl solution at an applied potential of 240 mV vs. SCE with a cover layer of 5 μm thick with diffusivity value of (a) 100, (b) 50 and (c) 1 times the diffusivity value of species inside and outside the pit (1×10^{-5} cm^2/s). Qualitative comparison illustrates the effect of the hypothetical cover on the formation of the perforated cover while the diffusivity across the cover was taken higher, (a) and (b), than the diffusivity inside the pit.

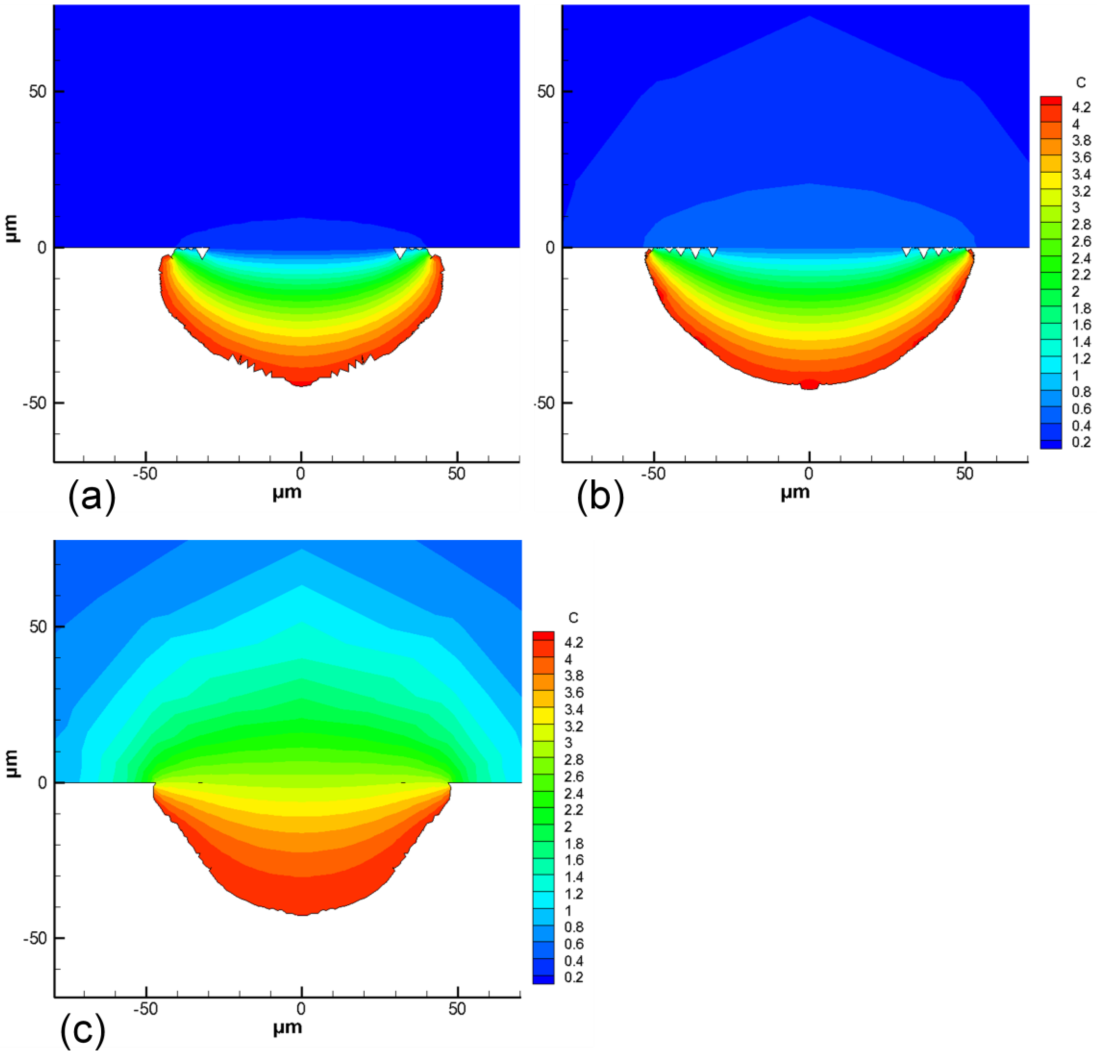

Figure 7-16- Cross sections through simulated pits after 10.0 s of growth lifetime modelled with the diffusivity in a 5 μm layer of solution just outside the pit mouth adjusted to (a) 100 (b) 50 and (c) 1 times the diffusivity value for ions inside and outside the pit (1×10^{-5} cm^2/s). The initial pit is a 30 μm radius cavity with 80° subtended angle by the pit mouth in 304 stainless steel in 0.1 M NaCl and at 240 mV vs. SCE applied potential. The black lines indicate the pit boundary at different time frames.

7.5 Modification to the model using experimental results from 2D pit growth radiographs

In this section, a modified version of the model is described, in which some of the parameters used in the original model are replaced with data extracted from the radiographs introduced in Chapter 6.

7.5.1 Passive-active transition criterion

One of the limitations of the model, as noted in Section 7.4.3, is the maximum potential that can be applied. This limitation is a result of the criterion set in the model to identify the active and passive regions. As described in Section 7.3.3, the model differentiates the status of the surface by comparing the actual anodic current density, i_a, with the critical passivation current density, i_{crit}. The i_a is calculated from the empirical version of Tafel Equation 7-4 by taking into account the applied potential, E_{corr}, i_{corr}, b_a and IR potential drop. Figure 7-17 shows the current density variation as a function of the surface saturation (C_M/C_{sat}) at different applied potentials given by the step algorithm described in Section 7.3.2. There is no limitation on the extent of i_a: the higher the applied potential, the higher i_a. However, i_{crit} is given by the empirical Equation 7-9 and is only dependent on the metal ion concentration, C_M. Thus, i_{crit} reaches its maximum value once C_M reaches to C_{sat}. At relatively high applied potential, even at $t = 0$, at any point on the pit surface i_a is greater than i_{crit}, therefore the model considers the whole pit passive and does not run at all. This is also because that within the time resolution of simulation, the rate of salt film precipitation is not high enough to precipitate required amount of salt film to absorb part of the applied potential so that i_a is decreased to values lower than i_{crit}.

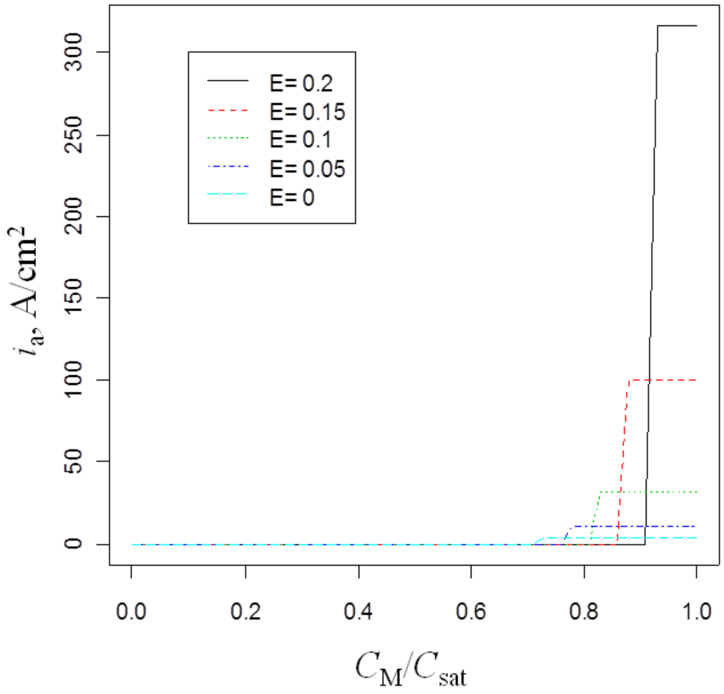

Figure 7-17- surface current density as a function of surface saturation (C_M/C_{sat}) at different interfacial potential (E) given by the step algorithm implemented in the original model

An alternative method is to establish a relationship between the surface current density, metal ion concentration and interfacial potential for the model. It is thus no longer necessary to use the idea of "i_{crit}". Instead, whether or not a region of the pit surface is active or passive is defined by the function $i_a(E,C_M)$, where E is the interfacial potential difference at the pit/solution interface. In order to do this, smooth curves were fitted to a series of the surface kinetics plots extracted from the experimental results, described in Section 6.9. Figure 7-18 shows $i_a(E,C_M)$ curves extracted from experimental pit growth data, and the smoothed curves that were derived from these data and implemented in the model.

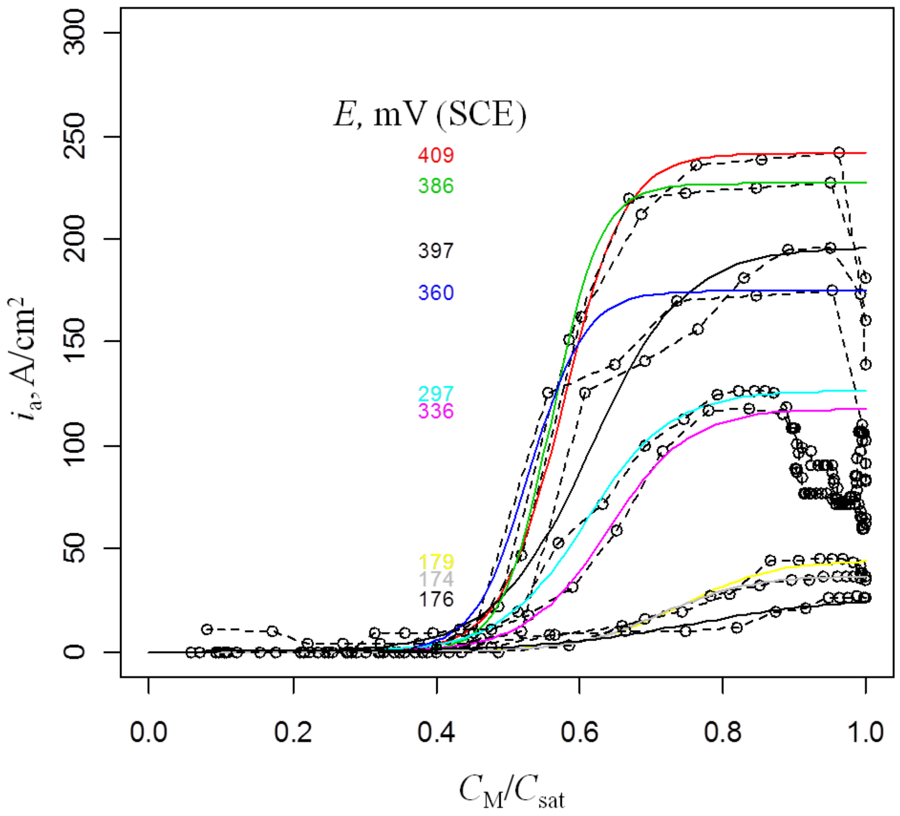

Figure 7-18- Surface current density as a function of surface saturation (C_M/C_{sat}) at different interfacial potential (E): the smoothed curves have been fitted to experimentally extracted surface kinetic plots shown in Chapter 6.

Figure 7-19 shows the pit lifetime as a function of the applied potential comparing the original and modified versions of the model. The growth of a 3 µm pit in 316 type stainless steel is simulated in 1 M NaCl. It can be seen that E_s is shifted from 160 mV in the original version to 220 mV in the modified version. As stated earlier, it has been shown by Laycock and White [7] that E_s is effectively the pitting potential, E_{pit}. Therefore, taking E_s as the pitting potential then the modified model looks slightly closer to the pitting potential of 316(L) reported in the literature shown in Table 7-2.

Table 7-2- literature pitting potential for 316(L) stainless steel

Alloy [Ref.]	E_{pit} (mV, SCE)	Conditions
316L [10]	160, 200, 220	0.5 M NaCl,22 °C, 600grit
316L [117]	~ 150	1 M NaCl, 20 °C, 220 grit
316 [82, 118]	~ 200	1 M NaCl, 20 °C, 220 grit

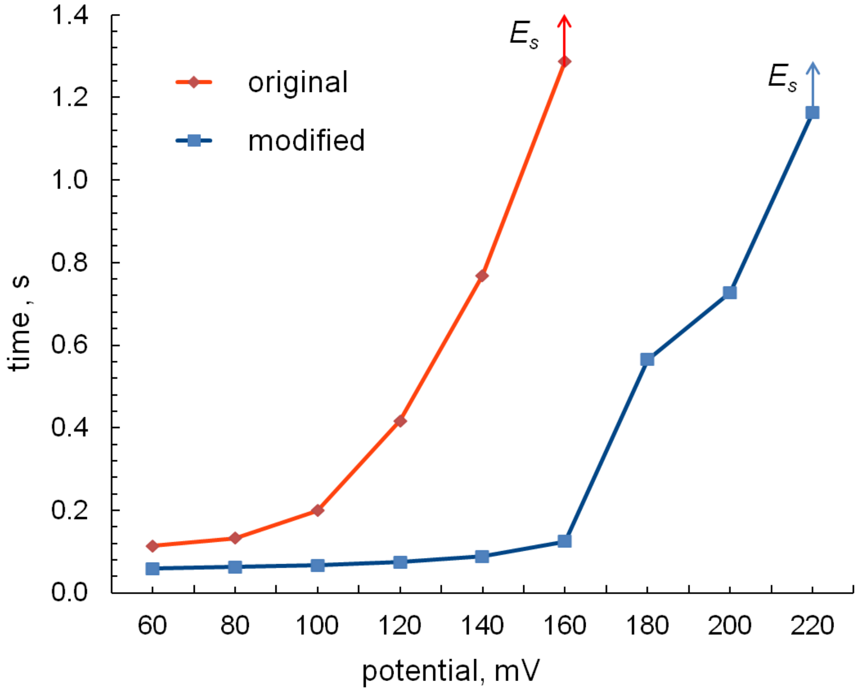

Figure 7-19- Pit lifetime as a function of the applied potential for the original and the modified version of the model simulated a 3 µm radius pit in 316 stainless steel in 1 M NaCl solution. Arrows indicate the E_s value (stability potential) at each case.

Figure 7-20 shows a qualitative comparison of an experimental pit with the simulated results from the original (using Equation 7-9) and modified versions (using input parameters from Figure 7-18) of the model under similar conditions (there is some uncertainty about the starting condition and the geometry of the electrolyte outside the experimental pit). The initial pit geometry in the model was selected to match that of the initial frame from the experimentally-measured pit. A series of cross sections through the pits simulated for 304 stainless steel with the (a) original and (b) modified version of the model is shown at different time stages of the growth lifetime of 19.8 s. The potential of 240 mV SCE was applied to a 30 µm initial pit cavity with θ=80° in 0.1 M NaCl with a salt film precipitation rate of 1 s^{-1}. A value of 1×10^{-3} cm^2/s was applied as the diffusivity of ions across the 5 µm thick hypothetical layer over the pit cavity to represent the effect of cover. A series of radiographs of a pit in 304 stainless steel foil grown in 0.1 M NaCl at 605 mV SCE for a period of ~ 57 s is shown in part (c). The total potential drop in solution (bulk and inside pit) of the experimental pit varies between ~350 to 400 mV whereas in the model, the potential drop between the pit mouth and the reference electrode (at infinity) is on the order of ~50 mV. This ensures that the potential at the pit mouth for both modelled and experimental pits is in the same range ±50 mV.

Qualitatively it can be seen that both versions have simulated the sideways growth lobe and the formation of a perforated cover. However, smoother pit boundaries and uniform dissolution over the pit bottom are seen during the pit growth generated by the modified version of the model while jagged edges and a small lobe at the middle of the pit bottom are rendered by the original version. The rounded and dish-shape pit simulated by the modified version looks much closer to the experimentally developed pit. It is notable that the timing between the modelled and experimental results is different, probably owing to the different pseudo-3D geometry of the model and 2D geometry of the experiment.

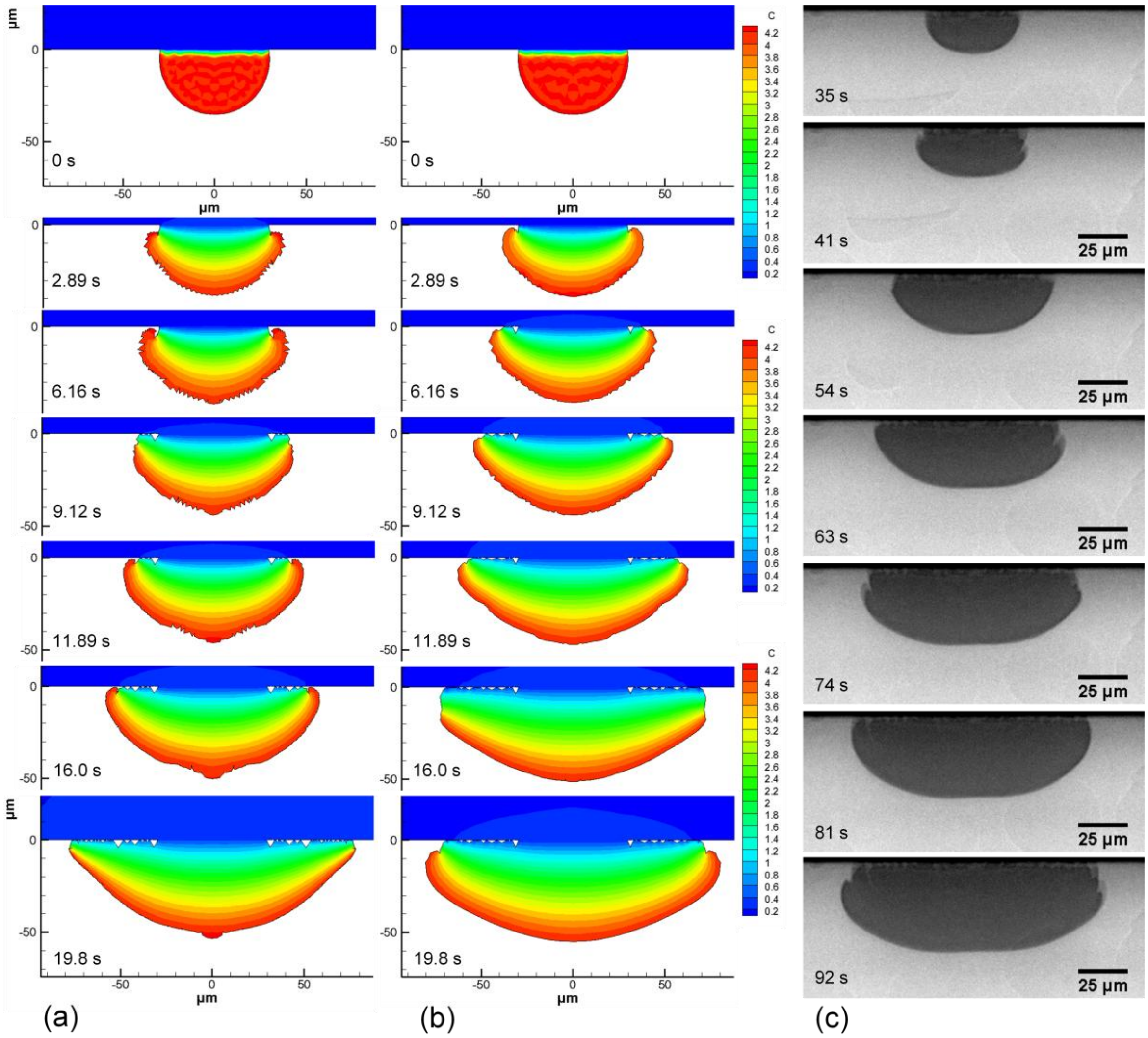

Figure 7-20- Cross sections through simulated pits at different stages of growth for a period of 19.8 s of growth lifetime generated with (a) the original and (b) the modified version of the model. The initial pit modelled is a 30 µm radius cavity with 80° subtended angle by the pit mouth in 304 stainless steel in 0.1 M NaCl and at 240 mV vs. SCE applied potential with a salt film precipitation rate of α=1 s^{-1} and a diffusivity value of 1×10^{-3} cm^2/s across the 5 µm hypothetical layer over the pit cavity. (c) A series of radiographs of a pit in 304 stainless steel foil grown in 0.1 M NaCl at 605 mV SCE for a period of ~ 57 s.

Figure 7-21 shows a quantitative comparison between the model parameters as a function of the distance along the pit boundary from the left rim to the middle of the pits shown in Figure 7-20 simulated with (a) the original and (b) the modified version of the model.

The top two plots in Figure 7-21 show the current density within the pit. For the original version of the model, the first few data points are zero, indicating the region where the pit surface is passive. For the modified version of the model, there is a current density of 20 Acm^{-2} seen in the regions that should perhaps be passive due to the low concentration of metal ions (this requires further investigation and possible refinement). Adjacent to the passive region, the original version of the model shows a very variable current density in the region of 2-5 Acm^{-2}, whereas the modified version shows a region of very high current density (up to 120 Acm^{-2}) for ~20 μm along the pit perimeter, followed by a lower current density that gradually decreases from ~20 Acm^{-2} to ~3 Acm^{-2}. It should be noted that the current densities determined here are substantially higher than those measured for the 2D pit (see, for example, Figure 6-10). This is likely to be a result of the fact that the pit simulation model has 3D geometry, whereas the experimental measurements and programme used to extract the metal ion concentration and potential distributions have 2D geometry.

The second pair of graphs shows the metal ion concentration in the solution adjacent to the pit surface. For the original version of the model, the solution concentration reaches the saturation value of 4.2 M immediately at the end of the passive region, suggesting that there is no region of active dissolution in the absence of a salt film (this may have been an issue of timing and has not been seen as a typical behaviour in the original model). In contrast, for the modified model, the metal ion concentration gradually increases through the active region with high current densities, and remains at 4.2 M in the region where the current drops and surface is covered with a salt film layer as can be deduced from the following potential drop plots.

For both versions, the potential drops in solution (with respect to the infinity) are almost the same, ~35 mV, and they increase from the pit rim (where $C_M \approx 0$) further down to the pit bottom as C_M reaches 4.2 M and salt film precipitates and then potential drops in solution remain constant all across the pit bottom. A fluctuating potential drop across the salt film (which is associated with the noise in current density and salt film thickness) is observed for the original model, while for the modified version, a gradual increase in potential drop across the salt film is seen as the salt film thickens towards the pit bottom.

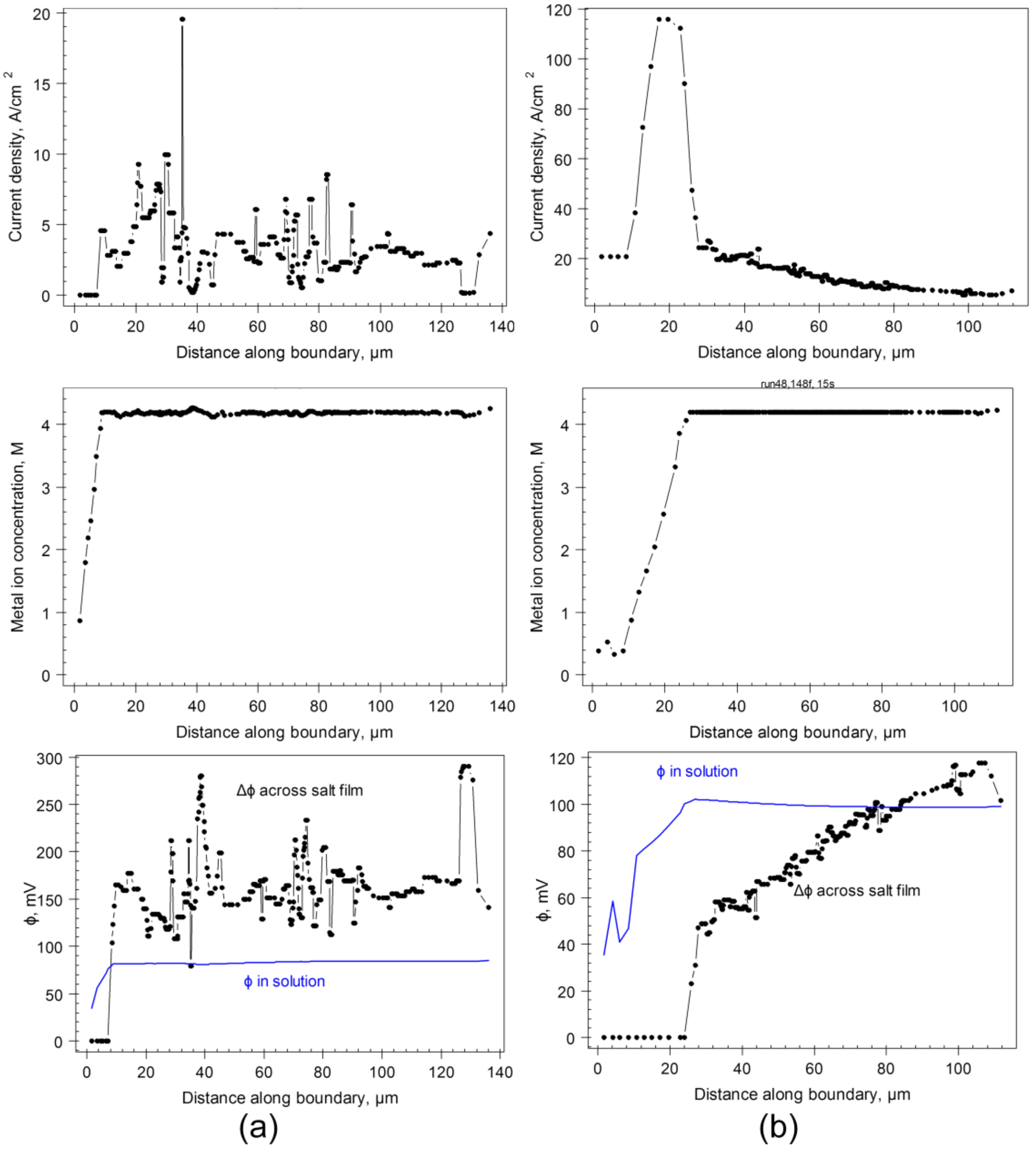

Figure 7-21- Distribution of anodic current density, i_a, metal ion concentration, C_M, and potential drop (ϕ) in solution and across the salt film as a function of distance from the pit rim to the pit bottom for a 304 stainless steel pit at 240 mV vs. SCE after 15.0 s of growth lifetime simulated with (a) the original and (b) the modified version of the model.

7.6 Discussion

The model described in this chapter simulates the propagation of single pits in 300 series stainless steels in NaCl bulk solutions under potentiostatic control. The model is based on a version of Tafel equation formulated for the anodic dissolution kinetics in the pit environments. It takes into account the transport of the ions by diffusion and electromigration outside the pit. The salt film precipitation and associated potential drop are explicitly considered. The sensitivity to the input parameters for the original model is discussed below.

The original version of the model developed by Laycock and co-workers used the empirical Equation 7-9 as the criterion to identify if the pit surface is active or passive. The model has subsequently been modified to replace this criterion with an experimentally-derived relationship between the local current density, interfacial potential drop and metal ion concentration, $i_a(E,C_M)$. The extraction of the required data is described in Chapter 6. Preliminary work has been carried out to explore the effect of the modification of the model on its ability to predict pit growth morphology: the result of this approach is discussed later in this section.

7.6.1 Anodic reaction order

The effect of the anodic reaction order, n_a, with respect to H^+ on the stability of pit growth, shown in Figure 7-6, is via the change in E_{corr} value. Higher n_a values increase E_{corr} (through Equation 7-7) and therefore, through Equation 7-4 the anodic current density is decreased, which results in a lower dissolution rate and lower pit stability. Laycock and White [7] determined that $n_a=0$ gave model values for the relationship between current density and concentration (at a fixed potential) that were closest to experimental results.

7.6.2 Diffusion coefficient

Changes in the diffusion coefficient directly affect the transport of species towards the exterior of the pit. A decrease in the diffusivity value slows down the metal ion transport (both diffusion and electrolytic migration) as per Equation 7-12 which leads to earlier salt film precipitation across a wider area of the pit surface. The precipitation of a salt layer decreases the local current density to the diffusion controlled value (i_{lim}) and dissolution continues beneath the salt film at a much lower rate compared with the salt-free area [94]. Therefore the salt film prevents the current density from reaching i_{crit} and stabilises the pit growth at lower applied potentials. This is consistent with the significant influence of salt film precipitation on the stability of the pit in transition from metastable conditions which was reported by Frankel and co-workers [72, 101, 102].

With a lower diffusion coefficient, a thicker salt film is observed in Figure 7-11 and only the area close to the pit mouth, where diffusion length is shorter, grows without a salt film with high rate of anodic dissolution ($i_a \gg i_{lim}$). Therefore, the pit tends to grow laterally close to the metal surface at a higher rate as can be seen in Figure 7-10.

7.6.3 Anodic Tafel slope

The anodic Tafel slope considerably shifts the range of potential over which pit propagation takes place. An increase in b_a increases the stability potential in the original version of the model. However, in the modified version there is no limit to the applied potential, and therefore, the effect of b_a is limited to the calculation of E_{corr} and i_{corr}.

7.6.4 Conductivity

In the original model, the conductivity is calculated from the Equation 7-11, which was developed for dilute solutions. However, the concentration of metal ions inside the pit reaches C_{sat}, which is far from the dilute limit. The main effect of conductivity in this model is in the potential drop in the pit solution close to the pit mouth or in the bulk solution outside the pit mouth. It can be seen, for example, that >80% of the potential drop in solution of 1 M shown in Figure 7-5 occurs outside the pit solution and the potential drop in pit solution only increases slightly from the pit rim towards the pit bottom. It was shown by Laycock and White [7] that the errors incorporated from the conductivity in the potential drop would be less than ~10 mV. This suggests that the impact on i_a should be negligible for a b_a value of 100 mV in Equation 7-4. This is consistent with the relatively small effect of the conductivity on the pit stability potential, E_s, shown in Figure 7-15. The change by a factor of 0.5 in conductivity value for 1 M NaCl has not changed E_s. However, E_s shows a small sensitivity to the change in conductivity for the lower concentration of 0.01 M NaCl.

The significant shift in the E_s value from 1 to 0.01 M NaCl is most likely due to the increased potential drop in solution, which is similar to the well known effect of chloride concentration on the pitting potential [57, 59, 77, 82]. However, at a chloride concentration of 0.1 M shown in Figure 7-21, where the increased diffusivity value on the hypothetical cover on the pit has decreased C_M at pit mouth to near zero, more than 50% of the potential drop is within the pit solution, although the significant increase in the potential drop in (b) is due to the unusual/ irregular high current density. The effect of sharp gradient of metal ion concentration within the pit cavity from the pit bottom towards the rim and its associated conductivity in occluded pit cavity grown in solutions of low chloride concentration (0.1-0.01 M NaCl) [107] needs further investigation.

7.6.5 Pit cover

Although the model has successfully shown formation of a perforated cover on the pit cavity where the initial cavity is occluded (θ=15) as shown in Figure 7-4, less success was observed for a higher initial θ, which was necessary for the purpose of comparison with experimental pits where larger pit size with higher θ were observed. Therefore, preliminary investigation has been carried out on simulating the effect with a separate diffusivity across a hypothetical layer over the pit cavity as shown in Figure 7-16. It can be seen that no lacy cover is formed while an equal diffusivity is set within the hypothetical layer (Figure 7-16(c)), which is due to the high C_M values around the pit mouth that dissolves the metal and leaves no remnant metal as cover. Increased diffusivity values have resulted in formation of perforated cover shown in Figure 7-16 (a) and (b). However, further investigation is required to find the optimum value for the purpose of comparison with experimental observations.

7.6.6 Modification of the model

In the original version of the model, the determination of whether regions of the pit are passive or active depends upon the i_{crit} criterion, explained in section 7.3.3.4 and 7.5.1. It operates through a step algorithm (as shown in Figure 7-17), i.e. below a certain concentration of metal ions required for continuation of dissolution, C_{crit}, the anodic current density is set to zero. Above C_{crit}, i_a is given by the Equation 7-4. Therefore, a sharp transition, (step function) in the current density value from i_a in the active to 0 in the passive region exists in the model. In contrast, a smoother transition in i_a-C_M behaviour is seen within the surface kinetics plots experimentally extracted from 2D pits (Figure 6-46 as explained in section 6.9) or 1D artificial pits [84].

The sharp threshold in the current density between the active and passive regions in the original version of the model also results in an increase in the processing time for the model, which solves the system of nonlinear equations by an iterative solution using Newton's method. However, implementing a function based on the fitted curves (Figure 7-18) to the experimentally obtained surface kinetics plots has resulted in qualitatively smooth and stable growth, as shown in Figure 7-20. The stability potential, E_s, has shifted from 160 mV (SCE) in the original model to 220 mV (SCE) in the modified version, which is close to the conventionally measured pitting potential, E_{pit}, of 316 stainless steel with 1200 grit surface finish in 1 M NaCl [82].

As a result of eliminating the i_{crit} criterion from the propagation process, the model is no longer limited to a maximum applied potential (internal observations).

In summary, both the original and modified versions of the model are based on the idea that there is a critical concentration required for propagation. This simple idea successfully leads to undercutting events that lead to perforation of the metal surface. Repetition of this cycle during growth eventually forms a porous pit cover. The model comprehensively takes into account all the substantial features of pit propagation including transport and electromigration of ions, the local anodic current density, salt film precipitation and the potential drop in solution and across the salt film. This enables the model to predict the stability of a pit at a given condition.

A significant limitation of the model has been the definition of the criteria for the active/passive transition. The modification introduced in this work, based on the experimentally extracted surface kinetic results, has shown clear improvements that can provide a basis for future development of the model. The modified model functions at all applied potentials, whereas the original model will not operate above an upper potential limit. Further refinement of the extracted surface kinetic data using more accurate calculation of concentration at the pit mouth and associated potential drop will lead to future improvement of the model.

7.7 Conclusion

1. A predictive model of pit propagation in stainless steel has been described. The model is based on the anodic dissolution kinetics and the requirement to maintain a critical chemistry for propagation. It takes into account the transport and migration of ions outside the pit, salt film precipitation, and the potential drop in solution and across the salt film. It successfully simulates the development of metastable and stable pits, the dish-shape of pits and the formation of lacy covers on the pits.
2. The model uses a step algorithm and an empirical criterion to differentiate the active and passive states. This criterion limits the applicable range of applied potential in which model will operate.
3. The surface kinetics plot extracted from radiography data presented in Chapter 6, which establishes the relationship between the anodic current density, metal ion concentration and interfacial potential, has been used to modify the model to replace the step algorithm used for predicting the kinetic status of the pit surface.
4. The modified model gives a smoother pit shape similar to the experimental observations compared with the original. Further refinement is required to improve the range of current densities and interfacial potentials for comparison with experimental results.

8 Discussion and Future Work

8.1 Characterisation of corrosion pits in 2D and 3D

X-ray microtomography has been used to observe the growth of pits in stainless steel *in situ* and in real time with a spatial resolution of 0.37 μm, and it has been shown that the pit growth mechanism by upward growth of lateral lobes with high active dissolution rates is the same in 3D as in the 2D pits that have been used to extract pit growth parameters in this study. However, the time to collect the tomograms is ~ 5 or 45 minutes (depending upon the resolution), which leads to blurring of the images. Faster imaging is possible, but with current detectors this can only be achieved with increased incident X-ray intensity, which may lead to beam damage.

As the micro-capillary approach was mainly designed for pit initiation studies, it has some limitations for pit propagation studies since there may be leakage and crevices underneath the micro-capillary tip when the radius of a growing pit exceeds the radius of micro-capillary. Moreover, the microtomography measurements carried out are very difficult to control, and this, combined with the blurring caused by growth of pits during the measurement, mean that this is not currently a viable method for obtaining quantitative pit growth parameters.

X-ray synchrotron radiography provides high resolution imaging (up to 0.37 μm) to study propagation of 2D pits *in situ* in real time. This approach builds on the work of Ernst and Newman [106, 107] who used video microscopy to view 2D pits. However, the use of higher resolution allows observation of smaller features (e.g. the formation of a small “pit-within-a-pit” (Figure 6-11) and surface roughening that are not visible with video microscopy. Furthermore, the local current density (real corrosion rate) along pit perimeter can be directly quantified from the movement of the pit boundary. However, the imaging conditions do not give enough contrast to image salt films, which would be highly desirable to confirm some of the assumptions that need to be made in the model.

8.2 Extraction of pit growth parameters from pit radiography

Measurement of the local dissolution rate within pits can be used to establish the key kinetic relationship for pit propagation, which is the local current density as a function of the local interfacial potential and metal ion concentration. In order to achieve this, it is necessary for the surface metal ion concentration and interfacial potential to be back-calculated using transport equations and assuming electroneutrality of the electrolyte. In this way, the surface kinetics can be established for “each single radiograph” of a growing pit rather than from the conventional 1D artificial pit experiments which required various measurements at different potentials and pit depths. However, the main limitation/weakness in the back-calculation process is the unknown extent of coveredness and its effect on the rate of ion transport which determines the concentration of metal ions and associated potential drop around the pit mouth.

In this study, the effect of a pit cover has been observed from (a) the diffusion-controlled behaviour of pits and (b) the stability products of pits. Both galvanostatic (low potential) and potentiostatic (high potential) pits have shown a diffusion controlled pit depth behaviour from which effective diffusion coefficients have been extracted (Table 6-1). The values show considerable variation, which reflects the difficulty in accounting for the effect of the pit cover. These values are less than those commonly obtained for 1D artificial pit measurements. The discrepancy can be attributed to the lacy cover which acts as a diffusion barrier. A similar effect of the pit cover has also been observed in studies of pit stability products. Furthermore, the pit cover introduced some uncertainty to the value of the metal ion concentration at the pit mouth and complicated the calculation of cell electrical resistance where the cover acts as a resistive barrier as well.

8.3 Modification to the pit growth model

The original model successfully simulates significant features of pit propagation including metastable growth, salt film formation, stable growth, porous cover formation and dish-shape pits. However, the model is very sensitive to the anodic Tafel slope and limited in the feasible range of applied potentials by the “i_{crit}” criterion set to differentiate the passive or active region. The modification introduced in this work, based on the experimentally extracted surface kinetic results, has shown some clear improvements (qualitatively and quantitatively) that can provide a basis for future development of the model.

The modified model functions at all applied potentials. Further modifications can be followed by refinement of the extracted surface kinetics data by more accurate calculation of concentration at the pit mouth and associated potential drop.

8.4 Future work: extending the model to atmospheric corrosion conditions

The great majority of work on the pitting corrosion of stainless steel has been carried out for full immersion conditions. This has also been the case for the present study, since the original model developed by Laycock and White [7] also applies to full immersion conditions. However, for a number of important applications, including developing corrosion prediction models for nuclear waste containers, it is necessary to extend the model to atmospheric pitting conditions, where corrosion occurs under thin layers or droplets of concentrated salt solutions under open circuit potential conditions. In order to do this, it will be necessary to develop the model geometry to take account of the confined solution phase and also explicitly consider the cathodic kinetics.

The present study focuses on the anodic kinetics, and these are dominated by the requirement of a critical metal ion concentration for propagation, C_{crit}, which was shown in this work to be ~65% of saturation, consistent with the reported ranges in the literature [67, 81, 84]. This critical chemistry is often considered to be a constant, applicable to different stainless steels over a wide range of environmental conditions [7, 107]. However, atmospheric pitting corrosion occurs at high chloride concentrations seen in the thin films or droplets of moisture [182-188] and recently Ernst and Newman [120] have shown a steep decrease in the value of $C_{\mathrm{crit}}/C_{\mathrm{sat}}$ for 316L stainless steel from ~65% at 1 M bulk chloride to as low as ~ 10% in solutions with more than 6 M chloride. This suggests further investigation of anodic dissolution kinetics at the conditions relevant to atmospheric pitting corrosion for future implementation of the model.

As noted above, the cathodic kinetics are a key aspect of atmospheric pitting corrosion, and the limitation of the cathodic current available from oxygen reduction outside the pit has led to an argument as to whether there is an upper bound on the maximum pit depth that can be reached in open-circuit atmospheric corrosion conditions [184-186]. This is in the line with the concept of “champion pit” where there is a competition among initiated pits for the limited current available for continuation of propagation (survival) [10, 138]. Based on the pit stability product, Chen and Kelly [184-186] argued that for hemispherical pit with the interfacial potential on its perimeter at the repassivation potential, there is a maximum available current, that can be supplied by the oxygen reduction reaction, below which a pit cannot propagate. As the anodic current cannot exceed the maximum available cathodic current supply, by assuming a certain value of repassivation potential for 304, they propose that there is an upper bound to the maximum pit depth that can be reached in atmospheric corrosion conditions. However as stated above, Ernst and Newman [120] have shown that the critical chemistry and consequently the critical anodic current required for propagation significantly drops for chloride concentration above ~1 M. Moreover, Laycock *et al.* [189] have shown that the critical potential, at which a pit can stably propagate (such as the repassivation potential), reduces linearly with chloride concentration from 0.01 to 1 M, but rapidly falls with further increases in chloride. These different observations need to be resolved in order to develop a robust predictive model for pit propagation.

From a geometrical aspect, it has been observed [120, 183, 190] that under droplets of concentrated $MgCl_2$ solutions, pits tend to propagate preferentially in the horizontal direction, producing relatively shallow dish-shaped pits without a significant cover. This at first may suggest that the Chen and Kelly’s [184-186] assumption of a hemispherical geometry is conservative. However, it has been observed that pits do not maintain an approximately hemispherical shape throughout their whole growth, and more tunnel-like morphologies can develop [13, 16] especially with roughening surface at relatively low potential [84] at the pit bottom as shown in this work. In such circumstances, the actively corroding area of the pit does not necessarily increase with depth, and so a cathodic current limitation would not necessarily lead to an upper bound on the pit depth. Thus this necessitates studying the pit shape development in details in conditions relevant to atmospheric pitting corrosion with limited available current.

The absence of a significant pit cover under atmospheric conditions is a considerable advantage from the modelling standpoint, as accounting for the cover was the most challenging aspect of the current model for full immersion conditions. However, it is likely that there may be inert particles from marine aerosol salts [191-193] on the metal surface under real atmospheric conditions, including those of relevance to storage of nuclear waste containers, and their effect on ions transport and solution resistance will need to be taken into account.

9 Conclusions

1. X-ray synchrotron imaging methods are very effective for *in situ* and in real time observation of corrosion processes in aqueous environments.

2. Using *in situ* synchrotron X-ray microtomography with a pixel size of 350 nm, pit propagation in stainless steels under electrochemical control in a capillary microcell was investigated. The perforation of the metal surface by upward growth of rapidly dissolving lobes from the main pit was observed, leading to formation to the classical "lacy cover" found for pits in stainless steel. It is shown that propagation of corrosion pits in stainless steel may be influenced by the presence of sulfide inclusions.

3. X-ray synchrotron radiography was used to study 2D pit propagation in stainless steel foil in chloride solutions. The local dissolution rate (anodic current density) was directly measured from the movement of pit boundary and found to vary between ~ 1 and 5 A/cm^2 during the pit growth. The pit surface chemistry (concentration of metal ions) and interfacial potential at each point on the pit surface were then calculated using transport equations and the assumption of electrolyte electroneutrality to give the relationship between local current density, interfacial potential and metal ion concentration.

4. The pit depth growth is controlled by diffusion for pits grown under either potential or current control. It is also observed that the pit depth growth rate is independent of the bulk chloride concentration, whereas lateral growth of pits is controlled by the potential for both potential- and current-controlled regimes.

5. An effective diffusion coefficient was extracted from the diffusion-controlled pit growth in depth. The values obtained for 2D pits are less than 1D pits and it is proposed that the deviation is attributed to the barrier effect of the perforated pit cover on mass transport. From this, a "coveredness factor" has been introduced into the calculation of metal ion concentration within the pit.

6. For pits grown under potential control (which were grown at high potentials in the current work), a concentration of metal ions close to the saturation value (4.2 M) was observed at the pit bottom, consistent with the existence of a salt film. Under

these growth conditions, the pit surface was smooth and well-defined. In contrast, under galvanostatic growth conditions (which grew at lower potentials in the current work), the surface concentration was found to fluctuate around the critical concentration for continued dissolution, ~2.5 M, and a transition from a smooth surface at the initial stages to an etched and rough surface was observed as the current density (and thus interfacial potential) decreased .

7. The relationship between local current density, interfacial potential and metal ion concentration extracted from the radiographic data, was incorporated into the predictive model developed by Laycock *et al.* [7, 140] to replace an empirical algorithm used for predicting the kinetics status of the pit surface. A smoother pit shape similar to the experimental results was obtained compared with the original model, which used a step function. Further refinement is required to improve the range of current density and interfacial potential for comparison with the experimental results.

References

1. Smart, N.R., C.C. Naish, and A.M. Pritchard, *Corrosion principles for the assessment of stainless steel radioactive waste containers*, in *Serco report*. 2006, *available from*: http://www.nda.gov.uk/documents/biblio/.
2. NDA, *UK radioactive higher activity wastes storage review*. 2009, *available from*: http://www.nda.gov.uk.
3. Smart, N.R., *Atmospheric pitting corrosion of stainless steel radioactive waste containers, a technical note produced for Nirex*, in *Serco report*. 2005, *available from*: http://www.nda.gov.uk/documents/biblio/.
4. Smart, N.R., A.M. Pritchard, and A. Turnbull, *Review of Environmental Conditions for Storage of Radioactive Waste Containers*, in *SERCO/TAS/E.2098/P3443* 2010, *available from*: http://www.nda.gov.uk/documents/biblio/.
5. Winsley, R.J. and N.R. Smart, *Resumption of 4 metre box monitoring programme*, in *Serco report*. 2009, *available from*: http://www.nda.gov.uk/documents/biblio/.
6. Frankel, G.S., *Pitting corrosion of metals - A review of the critical factors.* Journal of the Electrochemical Society, 1998. **145**(6): p. 2186-2198.
7. Laycock, N.J. and S.P. White, *Computer simulation of single pit propagation in stainless steel under potentiostatic control.* Journal of the Electrochemical Society, 2001. **148**(7): p. B264-B275.
8. Scheiner, S. and C. Hellmich, *Finite Volume model for diffusion- and activation-controlled pitting corrosion of stainless steel.* Computer Methods in Applied Mechanics and Engineering, 2009. **198**(37-40): p. 2898-2910.
9. Frankel, G.S. and N. Sridhar, *Understanding localized corrosion.* Materials Today, 2008. **11**(10): p. 38-44.
10. Suleiman, M.I. and R.C. Newman, *The use of very weak galvanostatic polarization to study localized corrosion stability in stainless-steel.* Corrosion Science, 1994. **36**(9): p. 1657-1665.
11. Sedriks, A.J., *Corrosion of Stainless Steels*. 1996: Wiley-Interscience.
12. Davis, J.R., *Corrosion - Understanding the Basics*. 2000: ASM International.
13. Revie, R.W., *Uhlig's Corrosion Handbook (2nd Edition)*. 2000, John Wiley & Sons.
14. Pourbaix, M., L. Klimzack-Mathieiu, C.M. Mertens, J. Meuneir, C. Vanleugenhaghe, L.D. Munck, J. Lalrreys, L. Neelemans, and M. Warzee, *Potentiokinetic and corrosimetric investigations of the corrosion behaviour of alloy steels.* Corrosion Science, 1963. **3**: p. 239-259.
15. Starr, K.K., E.D. Verink, and M. Pourbaix, *Significance of protection potential for fe-cr alloys at room-temperature.* Corrosion, 1976. **32**(2): p. 47-51.
16. Stockert, L., F. Hunkeler, and H. Bohni, *A crevice-free measurement technique to determine reproducible pitting potentials.* Corrosion, 1985. **41**(11): p. 676-677.
17. Szklarska-Smialowska, Z., *Pitting and Crevice Corrosion*. 2005: NACE.
18. Hunkeler, F. and H. Bohni, *The significance of pit induction times.* Corrosion, 1984. **40**(10): p. 559-560.
19. Baroux, B., in *Corrosion Mechanisms in Theory and Practice* P. Marcus, Editor. 2002, Dekker: New York. p. 311.
20. Hoar, T.P. and W.R. Jacob, *Breakdown of passivity of stainless steel by halide ions.* Nature, 1967. **216**(5122): p. 1299-&.
21. Szklarska-Smialowska, Z., *Pitting Corrosion of Metals*. 1986, Houston, TX: NACE
22. Green, C.L. and U.o.O.F.o.P. Sciences, *Pitting corrosion of stainless steel*. 1999: University of Oxford.
23. Newman, R.C., *2001 W.R. Whitney Award Lecture: Understanding the corrosion of stainless steel.* Corrosion, 2001. **57**(12): p. 1030-1041.
24. Frankel, G.S., R.C. Newman, and E.S.C. Division, *Proceedings of the Symposium on Critical Factors in Localized Corrosion*. 1992: Electrochemical Society.

25. Natishan, P.M. and E.S.C. Division, *Proceedings of the Symposium on Critical Factors in Localized Corrosion II*. 1996: Electrochemical Society.
26. Turnbull, A., *Corrosion chemistry within pits, crevices, and cracks: proceedings of a conference held at the National Physical Laboratory, Teddington, Middlesex, on October 1-3, 1984*. 1987: H.M.S.O.
27. Böhni, H. and S. Virtanen, *Critical factors in localized corrosion IV: a Symposium ; proceedings of the international symposium [as part of the 202nd meeting of the Electrochemical Society, Salt Lake City, October 20 - 24, 2002]*. 2003: Electrochemical Society.
28. Missert, N., *Critical Factors in Localized Corrosion 5: A Symposium in Honor of Hugh Isaacs*. 2007: Electrochemical Society, The.
29. Kelly, R.G., G.S. Frankel, P.M. Natishan, and R.C. Newman, *Proceedings of the Symposium on Critical Factors in Localized Corrosion III: A Symposium in Honor of the 70th Birthday of Jerome Kruger*. Vol. 98. 1999, Pennington: Electrochemical Society Inc.
30. Weidner, J., S. Fujimoto, G.S. Frankel, and T. Haruna, *Critical Factors in Localized Corrosion 6, in Honor of Professor Shibata*. Vol. 16. 2009: The Electrochemical Society.
31. Froment, M., *Passivity of metals and semiconductors: proceedings of the Fifth International Symposium on Passivity Bombannes, France, May 30-June 3, 1983*, ed. Société de Chimie Physique. 1983: Elsevier.
32. Natishan, P.M., E.S.C. Division, E. International Society of Electrochemistry. Corrosion, and S.T. Division, *Proceedings of the Symposium on Passivity and its Breakdown*. 1998: Electrochemical Society.
33. Ives, M.B., J.L. Luo, J.R. Rodda, and E.S.C. Division, *Passivity of metals and semiconductors: proceedings of the Eighth International Symposium*. 2001: Electrochemical Society.
34. Seo, M. and E.S.C. Division, *Passivity and localized corrosion: an International Symposium in Honor of Professor Norio Sato*. 1999: Electrochemical Society.
35. Schmuki, P., E.S.C. Division, E.S. Luminescence, D.M. Division, and E.S. Meeting, *Pits and pores II: formation, properties, and significance for advanced materials : proceedings of the international symposium*. 2001: Electrochemical Society, Inc.
36. Park, J.O., T. Suter, and H. Bohni, *Role of manganese sulfide inclusions on pit initiation of super austenitic stainless steel's.* Corrosion, 2003. **59**(1): p. 59-67.
37. Suter, T., T. Peter, and H. Bohni, *Microelectrochemical investigations of MnS inclusions.* materials Science Forum, 1995. **192-194**: p. 25-40.
38. Ryan, M.P., D.E. Williams, R.J. Chater, B.M. Hutton, and D.S. McPhail, *Why stainless steel corrodes.* Nature, 2002. **415**(6873): p. 770-774.
39. Schmuki, P., H. Hildebrand, A. Friedrich, and S. Virtanen, *The composition of the boundary region of MnS inclusions in stainless steel and its relevance in triggering pitting corrosion.* Corrosion Science, 2005. **47**(5): p. 1239-1250.
40. Meng, Q., G.S. Frankel, H.O. Colijn, and S.H. Goss, *Metallurgy (communication arising): Stainless-steel corrosion and MnS inclusions.* Nature, 2003. **424**(6947): p. 389-390.
41. Meng, Q., G.S. Frankel, H.O. Colijn, and S.H. Goss, *High-resolution characterization of the region around manganese sulfide inclusions in stainless steel alloys.* Corrosion, 2004. **60**(4): p. 346-355.
42. Ke, R. and R. Alkire, *Surface-analysis of corrosion pits initiated at mns inclusions in 304 stainless-steel.* Journal of the Electrochemical Society, 1992. **139**(6): p. 1573-1580.
43. Ke, R.R. and R. Alkire, *Initiation of corrosion pits at inclusions on 304 stainless steel.* Journal of the Electrochemical Society, 1995. **142**(12): p. 4056-4062.
44. Muto, I., Y. Izumiyama, and N. Hara, *Microelectrochemical measurements of dissolution of MnS inclusions and morphological observation of metastable and*

stable pitting on stainless steel. Journal of the Electrochemical Society, 2007. **154**(8): p. C439-C444.
45. Rossi, A., B. Elsener, G. Hahner, M. Textor, and N.D. Spencer, *XPS, AES and ToF-SIMS investigation of surface films and the role of inclusions on pitting corrosion in austenitic stainless steels.* Surface and Interface Analysis, 2000. **29**(7): p. 460-467.
46. Webb, E.G. and R.C. Alkire, *Pit initiation at single sulfide inclusions in stainless steel - I. Electrochemical microcell measurements.* Journal of the Electrochemical Society, 2002. **149**(6): p. B272-B279.
47. Webb, E.G. and R.C. Alkire, *Pit initiation at single sulfide inclusions in stainless steel - II. Detection of local pH, sulfide, and thiosulfate.* Journal of the Electrochemical Society, 2002. **149**(6): p. B280-B285.
48. Webb, E.G. and R.C. Alkire, *Pit initiation at single sulfide inclusions in stainless steel - III. Mathematical model.* Journal of the Electrochemical Society, 2002. **149**(6): p. B286-B295.
49. Webb, E.G., T. Suter, and R.C. Alkire, *Microelectrochemical measurements of the dissolution of single MnS inclusions, and the prediction of the critical conditions for pit initiation on stainless steel.* Journal of the Electrochemical Society, 2001. **148**(5): p. B186-B195.
50. Pistorius, P.C. and G.T. Burstein, *Metastable pitting corrosion of stainless-steel and the transition to stability.* Philosophical Transactions of the Royal Society of London Series a-Mathematical Physical and Engineering Sciences, 1992. **341**(1662): p. 531-559.
51. Alkire, R.C. and K.P. Wong, *The Corrosion Of Single Pits On Stainless-Steel In Acidic Chloride Solution.* Corrosion Science, 1988. **28**(4): p. 411-&.
52. Hoar, T.P., *The corrosion of tin in nearly neutral solutions.* Transactions of the Faraday Society, 1937. **33**(2): p. 1152-1166.
53. Schwenk, W., *Theory of stainless steel pitting.* Corrosion, 1964. **20**(4): p. T129-&.
54. Suzuki, T., M. Yamabe, and Y. Kitamura, *Composition of anolyte within pit anode of austenitic stainless-steels in chloride solution.* Corrosion, 1973. **29**(1): p. 18-22.
55. Wilde, B.E. and E. Williams, *Use of current/voltage curves for study of localized corrosion and passivity breakdown on stainless steels in chloride media.* Electrochimica Acta, 1971. **16**(11): p. 1971-&.
56. Galvele, J.R., *Transport Processes and Mechanism of Pitting Of Metals.* Journal of the Electrochemical Society, 1976. **123**(4): p. 464-474.
57. Newman, R.C., *Pitting corrosion of metals* Interface 2010. **19**(1): p. 33-38.
58. Pourbaix, M., *Atlas of Electrochemical Equilibria in Aqueous Solutions*. 1974, Houston: NACE.
59. Galvele, J.R., *Transport Processes in Passivity Breakdown .2. Full Hydrolysis of the Metal-Ions.* Corrosion Science, 1981. **21**(8): p. 551-579.
60. Gravano, S.M. and J.R. Galvele, *Transport processes in passivity breakdown .3. Full hydrolysis plus ion migration plus buffers.* Corrosion Science, 1984. **24**(6): p. 517-534.
61. Mankowski, J. and Z. Szklarskasmialowska, *Studies on accumulation of chloride-ions in pits growing during anodic polarization.* Corrosion Science, 1975. **15**(8): p. 493-501.
62. Mankowski, J. and Z. Szklarskasmialowska, *Effect of specimen position on shape of corrosion pits in an austenitic stainless-steel.* Corrosion Science, 1977. **17**(9): p. 725-735.
63. Tooru Tsuru, K.H., Arsushi Nishikata, Shiro Haruyama, *Mass Transport and Chloride Ion Complexes in Occluded Cell.* Materials Science Forum, 1989. **44-45**: p. 289.
64. Pickering, H.W. and R.P. Frankenthal, *Mechanism of localized corrosion of iron and stainless-steel. 1. Electrochemical studies.* Journal of the Electrochemical Society, 1972. **119**(10): p. 1297-&.

65. Pickering, H.W. and R.P. Frankenthal, *Mechanism of localized corrosion of iron and stainless-steel. 2. Morphological studies.* Journal of the Electrochemical Society, 1972. **119**(10): p. 1304-&.
66. Sato, N. in *Corrosion and Corrosion Protection* 1981: The Electrochemcial Society.
67. Sato, N., *The stability of localized corrosion.* Corrosion Science, 1995. **37**(12): p. 1947-1967.
68. Sato, N., *The stability of pitting dissolution of metals in aqueous-solution.* Journal of the Electrochemical Society, 1982. **129**(2): p. 260-264.
69. Sato, N., *Toward a more fundamental understanding of corrosion processes.* Corrosion, 1989. **45**(5): p. 354-368.
70. Rosenfel.Il and I.S. Danilov, *Electrochemical aspects of pitting corrosion.* Corrosion Science, 1967. **7**(3): p. 129-&.
71. Isaacs, H.S. and G. Kissel, *Surface preparation and pit propagation in stainless-steels.* Journal of the Electrochemical Society, 1972. **119**(12): p. 1628-&.
72. Frankel, G.S., L. Stockert, F. Hunkeler, and H. Boehni, *Metastable pitting of stainless-steel.* Corrosion, 1987. **43**(7): p. 429-436.
73. Hakkarainen, T., *Factors determining the dissolution rate in pitting corrosion of stainless steel* Materials Science Forum, 1986. **8**: p. 81.
74. Hakkarainen, T. *Anodic behaviour of stainless steel in simulated pit solutions* in *Corrosion Chemistry within Pits, Crevices and Cracks*. 1987. London HMSO.
75. Steinsmo, U. and H.S. Isaacs, *The dissolution and repassivation kinetics of Fe-Cr alloys in pit solutions.* Corrosion Science, 1993. **35**(1-4): p. 83-88.
76. Isaacs, H.S., *Behavior of resistive layers in localized corrosion of stainless-steel.* Journal of the Electrochemical Society, 1973. **120**(11): p. 1456-1462.
77. Newman, R.C., M.A.A. Ajjawi, H. Ezuber, and S. Turgoose, *An experimental confirmation of the pitting potential model of Galvele.* Corrosion Science, 1988. **28**(5): p. 471-477.
78. Hunkeler, F., A. Krolikowski, and H. Bohni, *A study of the solid salt film on nickel and stainless-steel.* Electrochimica Acta, 1987. **32**(4): p. 615-620.
79. Newman, R.C. and M.A.A. Ajjawi, *A microelectrode study of the nitrate effect on pitting of stainless-steels.* Corrosion Science, 1986. **26**(12): p. 1057-1063.
80. Moayed, M.H. and R.C. Newman, *The relationship between pit chemistry and pit geometry near the critical pitting temperature.* Journal of the Electrochemical Society, 2006. **153**(8): p. B330-B335.
81. Newman, R.C. and H.S. Isaacs, *Diffusion-coupled active dissolution in the localized corrosion of stainless-steels.* Journal of the Electrochemical Society, 1983. **130**(7): p. 1621-1624.
82. Laycock, N.J. and R.C. Newman, *Localised dissolution kinetics, salt films and pitting potentials.* Corrosion Science, 1997. **39**(10-11): p. 1771-1790.
83. Tester, J.W. and H.S. Isaacs, *Diffusional effects in simulated localized corrosion.* Journal of the Electrochemical Society, 1975. **122**(11): p. 1438-1445.
84. Gaudet, G.T., W.T. Mo, T.A. Hatton, J.W. Tester, J. Tilly, H.S. Isaacs, and R.C. Newman, *Mass-Transfer and Electrochemical Kinetic Interactions In Localized Pitting Corrosion.* AIChE Journal, 1986. **32**(6): p. 949-958.
85. Isaacs, H.S. and R.C. Newman. *Local electrochemistry of pitting corrosion in stainless steel* in *Corrosion Chemistry Within Pits, Crevices and Cracks*. 1987. London HMSO.
86. Hunkeler, F. and H. Bohni. *Mass-transport-controlled pit growth on stainless steels and nickel*. in *Corrosion Chemistry in Pits, Crevices and Cracks*. 1987. London: HMSO.
87. Steinsmo, U. and H.S. Isaacs, *Dissolution and repassivation kinetics of Fe-Cr alloys in pit solutions .1. Effect of the surface salt layer.* Journal of the Electrochemical Society, 1993. **140**(3): p. 643-653.

88. Enerhaug, J., U.M. Steinsmo, O. Grong, and L.R. Hellevik, *Dissolution and repassivation kinetics of a 12.3Cr-2.6Mo-6.5Ni super martensitic stainless steel - A comparative study.* Journal of the Electrochemical Society, 2002. **149**(6): p. B256-B264.
89. Kuo, H.C. and D. Landolt, *Rotating-disk electrode study of anodic dissolution or iron in concentrated chloride media.* Electrochimica Acta, 1975. **20**(5): p. 393-399.
90. Kuo, H.C. and D. Landolt, *Galvanostatic transient study of anodic film formation on iron in concentrated chloride media.* Corrosion Science, 1976. **16**(12): p. 915-922.
91. Kuo, H.C. and K. Nobe, *Electrodissolution kinetics of iron in chloride solutions . 6. Concentrated acidic solutions.* Journal of the Electrochemical Society, 1978. **125**(6): p. 853-860.
92. Grimm, R.D. and D. Landolt, *Salt films formed during mass-transport controlled dissolution of iron-chromium alloys in concentrated chloride media.* Corrosion Science, 1994. **36**(11): p. 1847-1868.
93. Grimm, R.D., A.C. West, and D. Landolt, *AC Impedance Study of Anodically Formed Salt Films on Iron in Chloride Solution.* Journal of the Electrochemical Society, 1992. **139**(6): p. 1622-1629.
94. Landolt, D., *Mass-transport processes in anodic metal dissolution.* Russian Journal of Electrochemistry, 1995. **31**(3): p. 206-211.
95. West, A.C., R.D. Grimm, D. Landolt, C. Deslouis, and B. Tribollet, *Electrohydrodynamic impedance study of anodically formed salt films on iron in chloride solutions.* Journal of Electroanalytical Chemistry, 1992. **330**(1-2): p. 693-706.
96. Beck, T.R. *Occurance and properties of anodic salt films in pitting corrosion* in *Advances in Localized Corrosion*. 1990. Houston, TX: NACE.
97. Vermilye, D.A., *Concerning critical pitting potential.* Journal of the Electrochemical Society, 1971. **118**(4): p. 529-&.
98. Isaacs, H.S., *The localized breakdown and repair of passive surfaces during pitting.* Corrosion Science, 1989. **29**(2-3): p. 313-323.
99. Burstein, G.T., P.C. Pistorius, and S.P. Mattin, *The nucleation and growth of corrosion pits on stainless-steel.* Corrosion Science, 1993. **35**(1-4): p. 57-62.
100. Pistorius, P.C. and G.T. Burstein, *Aspects of the effects of electrolyte-composition on the occurrence of metastable pitting on stainless-steel.* Corrosion Science, 1994. **36**(3): p. 525-538.
101. Hunkeler, F., G.S. Frankel, and H. Bohni, *On the mechanism of localized corrosion.* Corrosion, 1987. **43**(3): p. 189-191.
102. Frankel, G.S. *Pit stability in stainless steel: the transition from metastability* in *Advances in localised corrosion*. 1990: NACE.
103. Boehni, H. and F. Hunkeler. *Growth kinetics and stability of localised corrsion processes*. in *Advances in Localized Corrosion*. 1990. Houston: NACE.
104. K.J. Vetter, H.H.S. *Pitting corrosion in an early stage and its theoretical implications* in *Localised Corrosion*. 1974. Houston: NACE
105. Williams, D.E., G. Stewart, and P.H. Balkwill. in *Critical Factors in Localized Corrosion*. 1992: The Electrochemical Society, Pennington NJ.
106. Ernst, P. and R.C. Newman, *Pit growth studies in stainless steel foils. I. Introduction and pit growth kinetics.* Corrosion Science, 2002. **44**(5): p. 927-941.
107. Ernst, P. and R.C. Newman, *Pit growth studies in stainless steel foils. II. Effect of temperature, chloride concentration and sulfate addition.* Corrosion Science, 2002. **44**(5): p. 943-954.
108. Ernst, P., M.H. Moayed, N.J. Laycock, and R.C. Newman. *Shape of Corrosion Pits in Metals*. in *Proceedings of the International Symposium on Pits and Pores: Formation, Properties, and Significance for Advanced Luminescent Materials* 1997. Montreal: Electrochemical Society. Corrosion Division, Electrochemical Society.

109. Ernst, P., N.J. Laycock, M.H. Moayed, and R.C. Newman, *The mechanism of lacy cover formation in pitting.* Corrosion Science, 1997. **39**(6): p. 1133-1136.
110. Laycock, N.J. and S.P. White, *A model for pit propagation in stainless steels*. Proceedings of the Symposium on Critical Factors in Localized Corrosion Iii: A Symposium in Honor of the 70th Birthday of Jerome Kruger, ed. R.G. Kelley, et al. Vol. 98. 1999, Pennington: Electrochemical Society Inc. 469-484.
111. Ryan, M.P., N.J. Laycock, H.S. Isaacs, and R.C. Newman, *Corrosion pits in thin films of stainless steel.* Journal of the Electrochemical Society, 1999. **146**(1): p. 91-97.
112. Ryan, M.P., N.J. Laycock, R.C. Newman, and H.S. Isaacs, *The pitting behavior of iron-chromium thin film alloys in hydrochloric acid.* Journal of the Electrochemical Society, 1998. **145**(5): p. 1566-1571.
113. Laycock, N.J., M.H. Moayed, and R.C. Newman, *Metastable pitting and the critical pitting temperature.* Journal of the Electrochemical Society, 1998. **145**(8): p. 2622-2628.
114. Moayed, M.H., N.J. Laycock, and R.C. Newman, *Dependence of the Critical Pitting Temperature on surface roughness.* Corrosion Science, 2003. **45**(6): p. 1203-1216.
115. Moayed, M.H. and R.C. Newman, *Deterioration in critical pitting temperature of 904L stainless steel by addition of sulfate ions.* Corrosion Science, 2006. **48**(11): p. 3513-3530.
116. Moayed, M.H. and R.C. Newman, *Evolution of current transients and morphology of metastable and stable pitting on stainless steel near the critical pitting temperature.* Corrosion Science, 2006. **48**(4): p. 1004-1018.
117. Laycock, N.J., *Effects of temperature and thiosulfate on chloride pitting of austenitic stainless steels.* Corrosion, 1999. **55**(6): p. 590-595.
118. Laycock, N.J. and R.C. Newman, *Temperature dependence of pitting potentials for austenitic stainless steels above their critical pitting temperature.* Corrosion Science, 1998. **40**(6): p. 887-902.
119. Salinas-Bravo, V.M. and R.C. Newman, *An alternative method to determine critical pitting temperature of stainless steels in ferric chloride solution.* Corrosion Science, 1994. **36**(1): p. 67-77.
120. Ernst, P. and R.C. Newman, *Explanation of the effect of high chloride concentration on the critical pitting temperature of stainless steel.* Corrosion Science, 2007. **49**: p. 3705-3715.
121. Qvarfort, R., *Critical pitting temperature-measurements of stainless-steels with an improved electrochemical method.* Corrosion Science, 1989. **29**(8): p. 987-993.
122. Natishan, P.M., S.Y. Yu, W.E. O'Grady, and D.E. Ramaker, *X-ray absorption near edge structure and X-ray photoelectron spectroscopy studies of chloride in passive oxide films.* Electrochimica Acta, 2002. **47**(19): p. 3131-3136.
123. Virtanen, S., P. Schmuki, and H.S. Isaacs, *In situ X-ray absorption near edge structure studies of mechanisms of passivity.* Electrochimica Acta, 2002. **47**(19): p. 3117-3125.
124. Maire, E., J.Y. Buffiere, L. Salvo, J.J. Blandin, W. Ludwig, and J.M. Letang, *On the application of X-ray microtomography in the field of materials science.* Advanced Engineering Materials, 2001. **3**(8): p. 539-546.
125. Salvo, L., P. Cloetens, E. Maire, S. Zabler, J.J. Blandin, J.Y. Buffiere, W. Ludwig, E. Boller, D. Bellet, and C. Josserond, *X-ray micro-tomography an attractive characterisation technique in materials science.* Nuclear Instruments & Methods in Physics Research Section B- Beam Interactions with Materials and Atoms, 2003. **200**: p. 273-286.
126. Stock, S.R., *X-ray microtomography of materials.* International Materials Reviews, 1999. **44**(4): p. 141-164.
127. Van de Casteele, E., D. Van Dyck, J. Sijbers, and E. Raman, *A model-based correction method for beam hardening artefacts in X-ray microtomography.* Journal of X-Ray Science and Technology, 2004. **12**(1): p. 43-57.

128. Stampanoni, M., G. Borchert, P. Wyss, R. Abela, B. Patterson, S. Hunt, D. Vermeulen, and P. Ruegsegger, *High resolution X-ray detector for synchrotron-based microtomography.* Nuclear Instruments & Methods in Physics Research Section a- Accelerators Spectrometers Detectors and Associated Equipment, 2002. **491**(1-2): p. 291-301.
129. Marrow, T.J., L. Babout, B.J. Connolly, D. Engelberg, G. Johnson, J.-Y. Buffiere, P.J. Withers, and R.C. Newman. *High-resolution, in-situ, tomographic observations of stress corrosion cracking*. in *Environment-Induced Cracking of Metals*. 2004. Banff, Canada.
130. Connolly, B.J., D.A. Homer, S.J. Fox, A.J. Davenport, C. Padovani, S. Zhou, A. Turnbull, M. Preuss, N.P. Stevens, T.J. Marrow, J.Y. Buffiere, E. Boller, A. Groso, and M. Stampanoni, *X-ray microtomography studies of localised corrosion and transitions to stress corrosion cracking.* Materials Science and Technology, 2006. **22**(9): p. 1076-1085.
131. Marrow, T.J., L. Babout, A.P. Jivkov, P. Wood, D. Engelberg, N. Stevens, P.J. Withers, and R.C. Newman, *Three dimensional observations and modelling of intergranular stress corrosion cracking in austenitic stainless steel.* Journal of Nuclear Materials, 2006. **352**(1-3): p. 62-74.
132. Davenport, A.J., C. Padovani, B.J. Connolly, N.P.C. Stevens, T.A.W. Beale, A. Groso, and M. Stampanoni, *Synchrotron X-ray microtomography study of the role of Y in corrosion of magnesium alloy WE43.* Electrochemical and Solid State Letters, 2007. **10**(2): p. C5-C8.
133. Connolly, B.J., D.A. Horner, S.J. Fox, A.J. Davenport, C. Padovani, S. Zhou, A. Turnbull, M. Preuss, N.P. Stevens, T.J. Marrow, J.Y. Buffiere, E. Boller, A. Groso, and M. Stampanoni, *X-ray microtomography studies of localised corrosion and transitions to stress corrosion cracking.* Materials Science and Technology, 2006. **22**(9): p. 1076-1085.
134. Eckermann, F., T. Suter, P.J. Uggowitzer, A. Afseth, A.J. Davenport, B.J. Connolly, M.H. Larsen, F. De Carlo, and P. Schmutz, *In situ monitoring of corrosion processes within the bulk of AlMgSi alloys using X-ray microtomography.* Corrosion Science, 2008. **50**(12): p. 3455-3466.
135. Eckermann, F., T. Suter, P.J. Uggowitzer, A. Afseth, and P. Schmutz, *The influence of MgSi particle reactivity and dissolution processes on corrosion in Al-Mg-Si alloys.* Electrochimica Acta, 2008. **54**(2): p. 844-855.
136. Eckermann, F., T. Suter, P.J. Uggowitzer, A. Afseth, M. Stampanoni, F. Marone, and P. Schmutz, *In situ microtomographically monitored and electrochemically controlled corrosion initiation and propagation in AlMgSi alloy AA6016.* Journal of the Electrochemical Society, 2009. **156**(1): p. C1-C7.
137. Knight, S.P., M. Salagaras, A.M. Wythe, F. De Carlo, A.J. Davenport, and A.R. Trueman, *In situ X-ray tomography of intergranular corrosion of 2024 and 7050 aluminium alloys.* Corrosion Science, 2010. **52**(12): p. 3855-3860.
138. Krouse, D.P., P. McGavin, and N.J. Laycock. *Computer Simulation Of Pitting Corrosion: Multiple Interacting Pits*. in *Corrosion & Prevention* 2008. Wellington: Australian Corrosion Association.
139. Laycock, N., S. White, and D. Krouse, *Numerical Simulation of Pitting Corrosion: Interactions Between Pits in Potentiostatic Conditions.* ECS Transactions, 2006. **1**(16): p. 37-45.
140. Laycock, N.J., J.S. Noh, S.P. White, and D.P. Krouse, *Computer simulation of pitting potential measurements.* Corrosion Science, 2005. **47**(12): p. 3140-3177.
141. Laycock, N.J., S.P. White, and W. Kissling, *The shape of pits in stainless steel*. Passivity and Localized Corrosion: An International Symposium in Honor of Professor Norio Sato, ed. M. Seo, et al. Vol. 99. 1999, Pennington: Electrochemical Society Inc. 541-550.

142. Laycock, N.J., S.P. White, and D.P. Krouse. *The Distirbution of Pitting Potentials for Stainless Steel*. in *in Pits and Pores II: Formation, Properties and Significance for Advanced Materials*. 2000. Pennington NJ, USA The Electrochemical Society
143. Laycock, N.J., S.P. White, J.S. Noh, P.T. Wilson, and R.C. Newman, *Perforated covers for propagating pits.* Journal of the Electrochemical Society, 1998. **145**(4): p. 1101-1108.
144. Stampanoni, M., G. Borchert, P. Wyss, R. Abela, B. Patterson, S. Hunt, D. Vermeulen, and P. Ruegsegger, *High resolution X-ray detector for synchrotron-based microtomography.* Nuclear Instruments & Methods in Physics Research Section a-Accelerators Spectrometers Detectors and Associated Equipment, 2002. **491**(1-2): p. 291-301.
145. Suter, T. and H. Bohni, *Microelectrodes for corrosion studies in microsystems.* Electrochimica Acta, 2001. **47**(1-2): p. 191-199.
146. Feldkamp, L.A., L.C. Davis, and J.W. Kress, *Practical cone-beam algorithm.* Journal of the Optical Society of America a-Optics Image Science and Vision, 1984. **1**(6): p. 612-619.
147. Rasband, W.S. *ImageJ*. 1997 [cited 2010; Available from: http://rsb.info.nih.gov/ij/.
148. Yahalom, J., L.K. Ives, and J. Kruger, *Nature of films over corrosion pits in stainless-steel.* Journal of the Electrochemical Society, 1973. **120**(3): p. 384-386.
149. Wu, B., J.R. Scully, J.L. Hudson, and A.S. Mikhailov, *Cooperative stochastic behavior in localized corrosion.* Journal of the Electrochemical Society, 1997. **144**(5): p. 1614-1620.
150. Punckt, C., M. Bolscher, H.H. Rotermund, A.S. Mikhailov, L. Organ, N. Budiansky, J.R. Scully, and J.L. Hudson, *Sudden onset of pitting corrosion on stainless steel as a critical phenomenon.* Science, 2004. **305**(5687): p. 1133-1136.
151. Harb, J.N. and R.C. Alkire, *The effect of fluid-flow on growth of single corrosion pits.* Corrosion Science, 1989. **29**(1): p. 31-43.
152. Davenport, A.J. and e. al., *Unpublished results* 2010.
153. Beck, T.R. and R.C. Alkire, *Occurrence of Salt Films during Initiation and Growth of Corrosion Pits.* Journal of the Electrochemical Society, 1979. **126**(10): p. 1662-1666.
154. Frankel, G.S., *The growth of 2-d pits in thin-film aluminium.* Corrosion Science, 1990. **30**(12): p. 1203-1218.
155. Frankel, G.S., R.C. Newman, C.V. Jahnes, and M.A. Russak, *On the Pitting Resistance Of Sputter-Deposited Aluminium-Alloys.* Journal of the Electrochemical Society, 1993. **140**(8): p. 2192-2197.
156. Frankel, G.S., J.O. Dukovic, V. Brusic, B.M. Rush, and C.V. Jahnes, *PIT GROWTH IN NIFE THIN-FILMS.* Journal of the Electrochemical Society, 1992. **139**(8): p. 2196-2201.
157. Tang, Y.C. and A.J. Davenport, *Magnetic field effects on the corrosion of artificial pit electrodes and pits in thin films.* Journal of the Electrochemical Society, 2007. **154**(7): p. C362-C370.
158. West, A.C., *Comparison of Modeling Approaches for a Porous Salt Film.* Journal of the Electrochemical Society, 1993. **140**(2): p. 403-408.
159. Newman, R.C. and H.S. Isaacs, *Stability of localized corrosion under conditions of varying mass-transfer.* Journal of the Electrochemical Society, 1983. **130**(8): p. C317-C317.
160. Isaacs, H.S., J.H. Cho, M.L. Rivers, and S.R. Sutton, *In-situ x-ray microprobe study of salt layers during anodic-dissolution of stainless-steel in chloride solution.* Journal of the Electrochemical Society, 1995. **142**(4): p. 1111-1118.
161. Laboratoire Jacques-Louis Lions, U.e.P.e.M.C., *Freefem++*, in *Third Edition*. 2011: Paris.

162. Lide, D.R., *CRC Handbook of Chemistry and Physics*. 85th Edition ed. 2004: CRC Press
163. Ezuber, H. and R.C. Newman. *Growth-rate distribution of metastable pits* in *Critical Factors in Localized Corrosion*. 1992. Pennington NJ The Electrochemical Society.
164. Strehblow, H.H. and M.B. Ives, *On the electrochemical conditions within small pits.* Corrosion Science, 1976. **16**(5): p. 317-321.
165. Darwish, N.A., F. Hilbert, W.J. Lorenz, and H. Rosswag, *The influence of chloride ions on the kinetics of iron dissolution.* Electrochimica Acta, 1973. **18**(6): p. 421-425.
166. McCafferty, E. and N. Hackerman, *Kinetics of iron corrosion in concentrated acidic chloride solutions.* Journal of the Electrochemical Society, 1972. **119**(8): p. 999-&.
167. Shibata, T. and T. Takeyama, *Stochastic theory of pitting corrosion.* Corrosion, 1977. **33**(7): p. 243-251.
168. Williams, D.E., C. Westcott, and M. Fleischmann, *Stochastic-models of pitting corrosion of stainless-steels .1. Modeling of the initiation and growth of pits at constant potential.* Journal of the Electrochemical Society, 1985. **132**(8): p. 1796-1804.
169. Williams, D.E., C. Westcott, and M. Fleischmann, *Stochastic-models of pitting corrosion of stainless-steels .2. Measurement and interpretation of data at constant potential.* Journal of the Electrochemical Society, 1985. **132**(8): p. 1804-1811.
170. Baroux, B., *The kinetics of pit generation on stainless steels.* Corrosion Science, 1988. **28**(10): p. 969-986.
171. Laycock, P.J., R.A. Cottis, and P.A. Scarf, *Extrapolation of extreme pit depths in space and time.* Journal of the Electrochemical Society, 1990. **137**(1): p. 64-69.
172. Scarf, P.A., R.A. Cottis, and P.J. Laycock, *Extrapolation of extreme pit depths in space and time using the r-deepest pit depths.* Journal of the Electrochemical Society, 1992. **139**(9): p. 2621-2627.
173. Engelhardt, G. and D.D. Macdonald, *Deterministic prediction of pit depth distribution.* Corrosion, 1998. **54**(6): p. 469-479.
174. Engelhardt, G. and D.D. Macdonald, *Unification of the deterministic and statistical approaches for predicting localized corrosion damage. I. Theoretical foundation.* Corrosion Science, 2004. **46**(11): p. 2755-2780.
175. Scheiner, S. and C. Hellmich, *Stable pitting corrosion of stainless steel as diffusion-controlled dissolution process with a sharp moving electrode boundary.* Corrosion Science, 2007. **49**(2): p. 319-346.
176. White, S.P., D.P. Krouse, and N.J. Laycock, *Numerical Simulation Of Pitting Corrosion: Interactions Between Pits In Potentiostatic Conditions*, in *ECS Transactions*. 2006, The Electrochemical Society. p. 37-45.
177. Sharland, S.M., *A mathematical-model of the initiation of crevice corrosion in metals.* Corrosion Science, 1992. **33**(2): p. 183-201.
178. Isaacs, H.S. and R.C. Newman. *Dissolution Kinetics during Localised Corrosion*. in *Corrosion and Corrosion Protection*. 1981: The Electrochemical Society
179. Monir, M., *XANES Study of Chemistry of Localised Corrosion in Artificial Pits of 316L Stainless Steel and Titanium*, in *Metallurgy and Materials* 2012, University of Birmingham: Birmingham.
180. Elbasiouny, M.S. and S. Haruyama, *Polarization behaviour of Fe-Cr alloys in acidic sulphate-solutions in active region.* Corrosion Science, 1976. **16**(8): p. 529-540.
181. Keddam, M., O.R. Mattos, and H. Takenouti, *Mechanism of anodic-dissolution of iron chromium-alloys investigated by electrode impedances.1. Experimental results and reaction model.* Electrochimica Acta, 1986. **31**(9): p. 1147-1158.
182. Tsutsumi, Y., A. Nishikata, and T. Tsuru, *Initial stage of pitting corrosion of type 304 stainless steel under thin electrolyte layers containing chloride ions.* Journal of the Electrochemical Society, 2005. **152**(9): p. B358-B363.

183. Tsutsumi, Y., A. Nishikata, and T. Tsuru, *Pitting corrosion mechanism of Type 304 stainless steel under a droplet of chloride solutions.* Corrosion Science, 2007. **49**(3): p. 1394-1407.
184. Chen, Z.Y., F. Cui, and R.G. Kelly, *Calculations of the cathodic current delivery capacity and stability of crevice corrosion under atmospheric environments.* Journal of the Electrochemical Society, 2008. **155**(7): p. C360-C368.
185. Chen, Z.Y. and R.G. Kelly, *Computational Modeling of Bounding Conditions for Pit Size on Stainless Steel in Atmospheric Environments.* Journal of the Electrochemical Society, 2010. **157**(2): p. C69-C78.
186. Chen, Z.Y. and R.G. Kelly, *An analytical modeling method for calculating the maximum cathode current deliverable by a circular cathode under atmospheric exposure*, in *Simulation of Electrochemical Processes II*, V.G.B.C.A.A.R.A. DeGiorgi, Editor. 2007. p. 33-41.
187. Maier, B. and G.S. Frankel, *Pitting Corrosion of Bare Stainless Steel 304 under Chloride Solution Droplets.* Journal of the Electrochemical Society, 2010. **157**(10): p. C302-C312.
188. Frankel, G.S., M. Stratmann, M. Rohwerder, A. Michalik, B. Maier, J. Dora, and M. Wicinski, *Potential control under thin aqueous layers using a Kelvin Probe.* Corrosion Science, 2007. **49**(4): p. 2021-2036.
189. Laycock, N.J., D.P. Krouse, S.M. Ghahari, A.J. Davenport, and T. Rayment, *Localised dissolution kinetics from fast in-situ radiography of propagating pits in stainless steel and implications for modeling pitting corrosion over long time-scales*, in *ECS Transactions*. 2011, Electrochemical Society: Boston.
190. Mi, N., M. Ghahari, T. Rayment, and A.J. Davenport, *Use of inkjet printing to deposit magnesium chloride salt patterns for investigation of atmospheric corrosion of 304 stainless steel.* Corrosion Science, 2011. **53**(10): p. 3114-3121.
191. Tada, E. and G.S. Frankel, *Electrochemical behavior of AISI 304SS with particulate silica coating in 0.1 M NaCl.* Journal of the Electrochemical Society, 2007. **154**(6): p. C312-C317.
192. Tada, E. and G.S. Frankel, *Effects of particulate silica coatings on localized corrosion behavior of AISI 304SS under atmospheric corrosion conditions.* Journal of the Electrochemical Society, 2007. **154**(6): p. C318-C325.
193. Maier, B. and G.S. Frankel, *Pitting Corrosion of Silica-Coated Type 304 Stainless Steel Under Thin Electrolyte Layers.* Corrosion, 2011. **67**(3).